Indium Nitride: An Investigation of Growth, Electronic Structure and Doping

Phillip A. Anderson

A thesis submitted in partial fulfilment
of the requirements for the degree of
Doctor of Philosophy
in
Electrical and Electronic Engineering
at the
University of Canterbury,
Christchurch, New Zealand.

May 2006

ABSTRACT

The growth, electronic structure and doping of the semiconductor InN has been explored and analysed.

InN thin films were grown by plasma assisted molecular beam epitaxy. The significance of the relative fluxes, substrate temperature and buffer layers was explored and related to the electrical and structural properties of the films. An exploration of the effect of active nitrogen species on InN films found that excited molecular nitrogen was preferred for growth over atomic and ionic species. An optimised recipe for InN was developed incorporating all explored parameters.

The bandgap of InN was explored using the techniques of optical absorption, photoluminescence and photoconductivity. All three techniques identified a feature near 0.67 eV as the only dominant and reproducible optical feature measurable from InN thin films. No evidence for any optical features above 1 eV was discovered. The effect of the Burstein-Moss effect is discussed and the debate over the relative impact of the effect is related to problems with precisely measuring electron concentrations. Photoluminescence from mixed phase InN films containing significant zincblende content is presented, with tentative evidence presented for a zincblende band gap near 0.61 eV.

Native defects within InN were studied by near edge X-ray absorption fine structure spectroscopy. Nitrogen related defects were found to be unlikely candidates for the high as-grown n-type conductivity. The most likely candidate remains nitrogen vacancies. Ion implantation was shown to cause substantial damage to the InN lattice, which could not be fully repaired through annealing. The limitation on annealing temperatures may limit the use of implantation as a processing tool for InN. Mg was shown to exhibit great promise as a potential p-type dopant. Photoluminescence from Mg doped films was found to quench at high Mg concentrations, consistent with a depletion region near the surface.

The potential dilute magnetic semiconductor $In_{1-x}Cr_xN$ was explored. All of the $In_{1-x}Cr_xN$ films were found to be ferromagnetic at room temperature and exhibited saturated magnetic moments of up to 0.7 emu/g. An interesting correlation between

background electron concentration and remnant moment is presented and the consequences of theoretical exchange models discussed. The bandgap of chromium nitride was also investigated and found to be an indirect gap of 0.7 eV.

ACKNOWLEDGEMENTS

Firstly, I would like to thank my supervisor Dr Steve Durbin for his guidance, constant enthusiasm towards the topic, and valuable insights. I am also very grateful to Dr Roger Reeves for his significant contributions to the topic, and the coordination of the optical experiments presented in this thesis.

There have been many other researchers who have contributed to the InN results presented here. Chito Kendrick has been great to work with as our topics have significantly overlapped, and much of the growth chapter was undertaken as a combined effort. Daniel Lee, William Lee and Ian Farrell have also been very helpful in assisting with growth issues. The help of Helen Devereux and Gary Turner with experimental and engineering support is very much appreciated. Optical characterisation was largely undertaken by Wolfgang Diehl, Lyndon Williams and Dr Damian Carder, to whom I am each very thankful for their expertise and significant input. Dr Robert Kinsey has been of great assistance with magnetic characterisation and also on theoretical models. Ion implantation studies were made possible through the help of Professor Chennupati Jagadish and Dr Ho Tan, whose perspectives were very constructive. I am also very grateful to Dr Mladen Petravic for his valuable collaboration on the NEXAFS experiments. Professor Thomas Myers and Dr Craig Swartz are thanked for their collaboration with variable field Hall analysis and valued discussions. XRD measurements were performed with the assistance of Dr Alec Asadov and Professor Wei Gao, whose contributions were much appreciated. Professor Simon Ringer and Dr Zongwen Liu provided important TEM expertise, for which I am very grateful. Finally, I would like to thank Dr John Kennedy and Dr Andreas Markwitz for their important work on the ion beam analysis of InN.

This work has been supported by the MacDiarmid Institute for Advanced Materials and Nanotechnology, and the University of Canterbury.

Last but certainly not least, I would like to thank Mum and Dad for always being there for me, and supporting me in whatever pursuit I have chosen.

CONTENTS

LIST OF FIGURES

LIST OF TABLES

PUBLICATIONS

The following journal articles and peer reviewed conference proceedings have been published, which in part have related to study towards this thesis:

P.A. Anderson, C.E. Kendrick, T.E. Lee, W. Diehl, R.J. Reeves, V.J. Kennedy, A. Markwitz, R.J. Kinsey, and S.M. Durbin, *Optical and Microstructural Characterisation of InN Grown by PAMBE on (0001) Sapphire and (001) YSZ*, Material Research Society Symposium Proceedings, vol. 743 (2003) Y12.3.1–Y12.3.6
This proceedings presents one of the first demonstrations of (111) YSZ as a substrate for InN. The study is largely described in section 2.6.

Robert J. Kinsey, Steven M. Durbin, Phillip A. Anderson, Chito E. Kendrick and Roger Reeves, *Characteristics of InN Thin Films Grown Using a PAMBE Technique*, Journal of Crystal Growth, vol. 269 (2004) 167–172.
This paper describes the growth and optical properties of wurtzite InN films. The study is largely described in sections 2.5 and 3.5.

P.A. Anderson, C.E. Kendrick, T.E. Lee, W. Diehl, R.J. Reeves, V.J. Kennedy, A. Markwitz, R.J. Kinsey, S.M. Durbin, *Structural and optical properties of indium nitride grown by plasma assisted molecular beam epitaxy*, Proceedings of the SPIE, vol. 5277 (2004) 90-98.
This proceedings describes the influence of relative In:N flux ratio on InN growth and film properties. The study is largely described in section 2.5.

P.A. Anderson, C.E. Kendrick, R.J. Kinsey, L. Williams, R.J. Reeves, S. M. Durbin, *Towards quantifying the bandgap energy of indium nitride*, Proceedings of Conference on Optoelectronic and Microelectronic Materials and Devices (COMMAD 04), (8-10 December 2004, Brisbane), IEEE Press EX973.
This proceedings describes a range of optical evidence in support of a 0.7 eV bandgap, including the first report of photoconductivity from InN films. The study is largely described in chapter 3.

C.E. Kendrick, P.A. Anderson, R.J. Kinsey, V.J. Kennedy, A. Markwitz, A. Asadov, W. Gao, R.J. Reeves and S.M. Durbin, *Polycrystalline InGaN grown by MBE on fused silica glass*, Physica Status Solidi (c), vol. 2 (2005) 2236–2239.
This paper describes the growth and characteristics of polycrystalline InGaN alloys.

P.A. Anderson, C.E. Kendrick, R.J. Kinsey, A. Asadov, W. Gao, R.J. Reeves and S.M. Durbin, *(111) and (100) YSZ as substrates for indium nitride growth*, Physica

Status Solidi (c), vol. 2 (2005) 2320–2323.
This paper is the first report of using (100) YSZ to promote the growth of zincblende InN. The study is largely described in sections 2.6 and 3.8.

P.A. Anderson, R.J. Kinsey, S.M. Durbin, M. Markwitz, J. Kennedy, A. Asadov, W. Gao and R.J. Reeves, *Magnetic and optical characteristics of the InCrN system*, Journal of Applied Physics, vol. 98 (2005) 043903-1 to 043903-5.
This paper is the first comprehensive study concerning the magnetic and optical properties of the InCrN system. The study is largely described in chapter 5.

P.A. Anderson, R.J. Kinsey, C.E. Kendrick, I.F. Farrell, D. Carder, R.J.Reeves and S.M. Durbin, *Influence of nitrogen species on InN grown by PAMBE*, Material Research Society Symposium Proceedings, vol. 892 (2005) FF6.3.1–FF6.3.1.6
This proceedings outlines the critical role active nitrogen species can play in determining InN film properties. The study is largely described in section 2.7.

P.A. Anderson, C.E. Kendrick, T.E. Lee, W. Diehl, R.J. Reeves, V.J. Kennedy, A. Markwitz, R.J. Kinsey, S.M. Durbin, *Optical and compositional properties of indium nitride grown by plasma assisted molecular beam epitaxy*, Smart Materials and Structures, vol. 15 (2006) S87-S91.
This paper discuses the composition of InN films and the role oxygen may play in reconciling the bandgap discrepancy. The study is largely described in sections 2.5 and 3.7.

P.A. Anderson, R.J. Reeves and S.M. Durbin, *RF plasma sources for III-nitrides growth: influence of operating conditions and device geometry on active species production and InN film properties*, Physica Status Solidi (a), vol. 203 (2006) 106–111.
This paper discuses the influence active nitrogen species and film polarity have on stress accommodation within InN films. The study is largely described in sections 2.7.

M. Petravic, P.N.K. Deenapanray, M.D. Fraser, A.V. Soldatov, Y.-W. Yang, P.A. Anderson, and S.M. Durbin, *Direct observation of defect levels in InN by soft x-ray absorption spectroscopy*, Journal of Physical Chemistry B, vol. 110 (2006) 2984–2987.
This paper discuses native defects within InN. The study is largely described in sections 4.2.

P.A. Anderson, R.J. Kinsey, C.E. Kendrick, L. Williams, R.J. Reeves, A. Asadov, W. Gao, V.J. Kennedy, A. Markwitz and S.M. Durbin, *Room temperature ferromagnetism in the $In_{1-x}Cr_xN$ system: a magnetic and optical study*, Current Applied Physics, vol. 6 (2006) 579–582.
This paper demonstrates ferromagnetism in an InN based diluted magnetic semicon-

ductors and shows that Cr is highly mobile within the InN lattice. The study is largely described in chapter 5.

S.M. Durbin, P.A. Anderson, R.J. Kinsey and R.J. Reeves *Perspectives on the properties of InN*, International Journal of Modern Physics B, (in press).
This paper describes a number of aspects of InN growth and presents optical data in support of a 0.7 eV bandgap. The study is largely described in sections 2.6, 3.5 and 3.8.

S.M. Durbin, P.A. Anderson, A. Markwitz and J. Kennedy *Oxygen Uptake of InN Thin Films as Determined by Ion Beam Analysis*, Thin Solid Films, (in press).
This paper presents ion beam analysis of InN films with particular emphasis placed on the role of oxygen within the layers. The study is largely described in sections 3.7.

Chapter 1

BACKGROUND TO THE III-NITRIDE SEMICONDUCTORS

1.1 SEMICONDUCTOR TECHNOLOGY

Semiconductors have revolutionised many aspects of life over the past 50 years. Techniques which have led to low cost, high density processing of silicon have resulted in silicon integrated circuits becoming ubiquitous within modern society. The astonishing progress which has been achieved in the processing of silicon is encompassed by Moore's law. In 1965, only 5 years after the first planar integrated circuit was produced, Gordon Moore noted that the density of transistors being fabricated on silicon integrated circuits was doubling approximately every 2 years (see Figure 1.1) [1]. Remarkably this trend has continued to the present day and the latest generation of microprocessors now pack more than half a billion transistors onto a square centimeter.

While the ability of semiconductors to rapidly process information may be the most visible application, semiconductors are used in applications as wide reaching as solid state lighting, power distribution, photovoltaics and high speed communications. When considering which semiconductor is preferred for a given application a number of material properties must be considered. High frequency devices rely on high peak carrier drift velocities along with compatibility with high-k dielectrics. For light emitting applications, the size and nature of the electronic bandgap must be considered. High power operation requires the material to be relatively insensitive to moderate changes in temperature. With many different material properties influencing the choice of semiconductor for a given application, there is constant effort towards realising novel

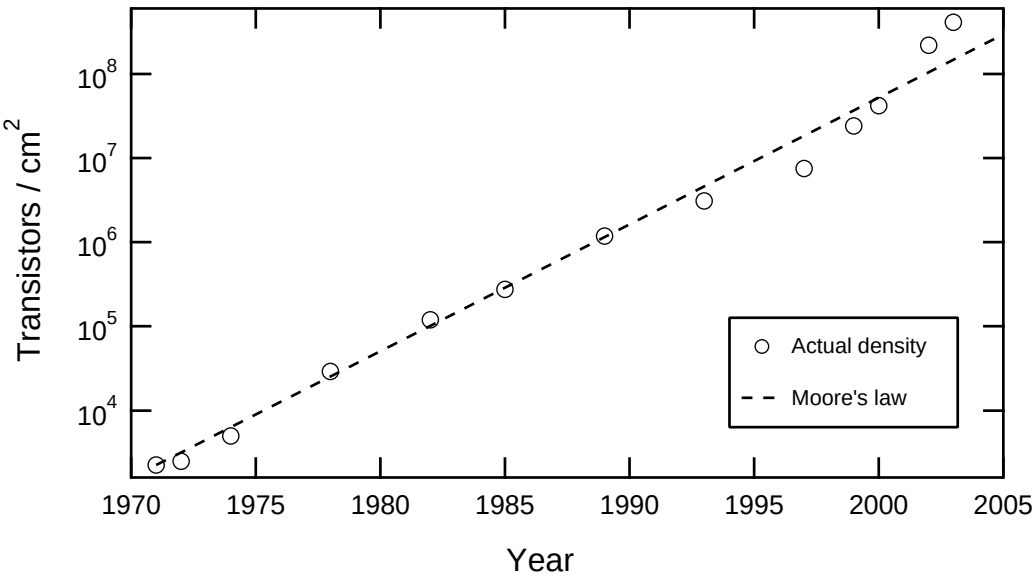

Figure 1.1 The transistor density achieved in state of the art consumer microprocessors. [Intel Corporation, http://www.intel.com/technology/silicon/mooreslaw/, accessed: 24th April 2006]

materials.

1.2 HISTORY OF THE III-NITRIDES

An area of much recent interest has been the III-nitride semiconductors: AlN, GaN, InN and their alloys. Ga-rich $In_xGa_{1-x}N$ alloys are now the material of choice for commercially produced green, blue and near ultraviolet (UV) light emitting diodes (LEDs) and laser diodes. Additionally, nitride based high electron mobility transistors (HEMTs) are under intense development as promising candidates for high frequency and high power operation. These devices open up applications in a wide range of areas including full colour displays, high density optical information storage, solid state lighting, sensors and diagnosis, RF amplifiers and power electronics [2].

The first report of III-nitrides synthesis was in 1938 by Juza *et* al. who synthesized GaN and InN crystallites [3]. The GaN was formed by flowing ammonia over hot gallium, and the InN from $InF_6(NH_4)_3$ reduction. The purpose of this initial study was to measure lattice parameters of the materials and there was little interest in their optical properties at that stage. It was 30 years later, when Maruska *et* al. first grew GaN layers by vapour phase deposition on sapphire substrates, that interest

in the nitrides increased [4]. Following this report, blue LEDs based on GaN:Zn/n-GaN structures were produced by Pankove *et* al. on vapour phase grown GaN. These structures relied on hot carrier injection from avalanche breakdown to generate holes. Despite subsequent advances in growth, p-type GaN proved elusive and it was not until 1989 when Amano *et* al. succeeded in reliably producing p-type GaN by Mg doping [5]. Research carried out at Nichia Chemical Industries by Nakamura *et* al. utilised Mg doping to form p-n junctions, and at the time, the brightest blue LEDs made from any material system [6]. Blue and green LEDs were then commercialised by Nichia Chemical Industries and others. Akasaki *et* al. and Nakamura *et* al. subsequently produced the first laser diodes based on the material system [7, 8]. Progress has continued at a remarkable rate, with the number of research groups studying the III-nitrides ballooning. Recent efforts have focused on improving the efficiency of nitride based LEDs and laser diodes and extending the range of wavelengths over which they operate. Added effort has also been applied to HEMTs based on nitride heterojunctions [9]. For a thorough account of the historical developments in the GaN field see the reviews by Jain *et* al. [2] and Pankove *et* al. [10].

Much of the progress in the nitrides field has been driven by metal organic vapour phase epitaxy (MOCVD), and the related technique, metal organic vapour phase epitaxy (MOVPE). Molecular beam epitaxy (MBE) has also been heavily used in nitrides research and has been the most common technique used for InN growth. MBE also has the advantage of being able to precisely control interfaces, which has made it the preferred technique for quantum dots and quantum wells. Particularly in GaN applications, MOCVD has benefitted from higher achievable growth temperatures and the subsequent gains in material quality. A drawback of MOCVD has been the tendency of doped films to suffer from hydrogen passivation of acceptors, which MBE can avoid through the use of non-ammonia nitrogen sources [2].

The success of the nitride system for light emitting devices has been somewhat of an enigma. Other commercially successful LED and laser diode technologies incorporate the use of native substrates for epitaxy, which the nitrides lack. Native substrates are a distinct advantage as they provide a perfect lattice match for growth of epitaxial layers.

This avoids the problem of misfit dislocations which inevitably form when growing on a lattice mismatched substrate. Dislocations are known to act as non-radiative recombination centres in III-V semiconductors. For example, GaAs and InP devices containing 10^8–10^9 dislocations/cm^2 (the common level of dislocations found in nitride based devices) would have luminescence quenched almost entirely by recombination at the dislocations. One theory used to describe the tolerance of nitrides for high levels of dislocations has been in terms of compositional fluctuations. Indium rich regions within the active quantum well regions can act as quantum dots, localising electrons and holes spatially and enhancing the probability they will recombine radiatively. Once trapped in the quantum dot, carriers are also prevented from moving to dislocation sites and recombining non-radiatively [11, 12].

A typical III-nitride LED or laser diode structure is shown in figure 1.2. The laser diode structure differs from the LED by the presence of an optical cavity in the laser diode. The cavity serves to trap light of a certain wavelength and promote stimulated emission at that wavelength. The LED structure is effectively the pump component of a laser diode.

Initially most nitride growth was on sapphire substrates, which provided a cost-effective hexagonal template for c-axis nitride growth. More recently there has been increased growth on SiC, which although being far more expensive, has an improved lattice and thermal expansion match. Still, a buffer layer is a critical component for nitride based devices grown on both sapphire and SiC. As the lattice mismatch with such substrates is extreme (14% in the case of sapphire/GaN and 3.5% for SiC/GaN) a strain accommodating layer (commonly called a buffer layer) is required. This AlN, AlGaN or GaN layer is typically grown at much lower temperature than the rest of the structure, which promotes the termination of threading dislocations and relaxation of the lattice [13]. Wetting of the substrate is also enhanced at low temperature and this prevents the film from adopting an islanded growth mode. When current flows through the devices, holes and electrons are injected across the GaN spacer layers and are then trapped in the quantum wells. Due to their spatial localisation within the wells, carriers recombine more efficiently than in a simple p-n junction diode. Unintentional In-rich

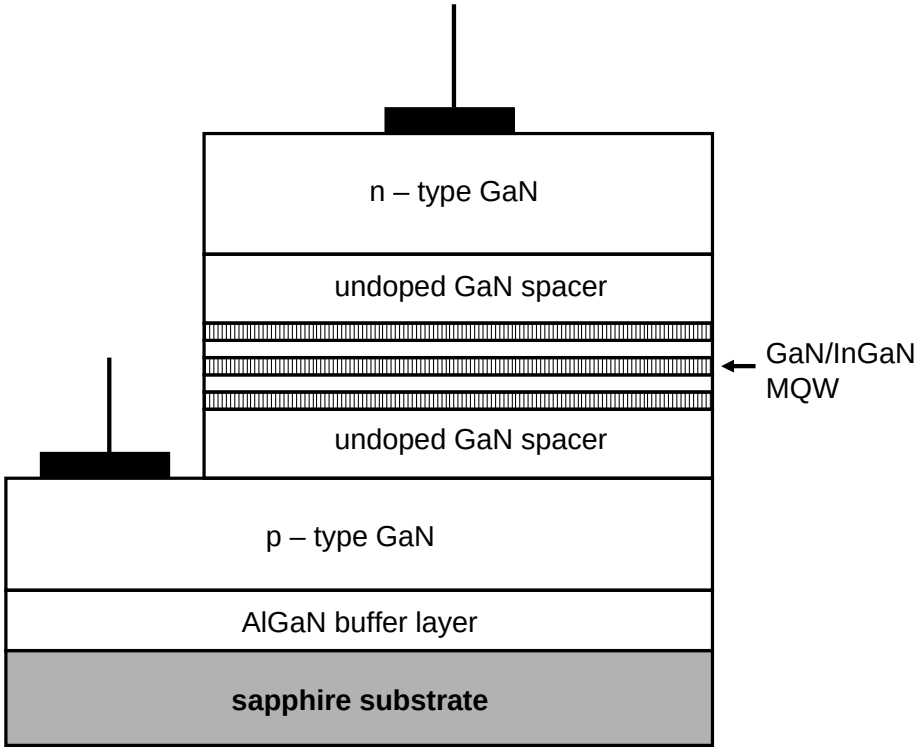

Figure 1.2 The typical structure used in nitride based blue and green LEDs and laser diodes.

regions within the active region operate on the same principle, causing further carrier localisation. The spacer layers are required to separate charged impurities within the p-type and n-type regions from the active region. Stray fields from such impurities can dissociate excitons and hence degrade performance.

1.3 THE INDIUM NITRIDE BANDGAP DEBATE

Until recently, the interest in indium nitride has been restricted to its role as a binary endpoint of InGaN alloys. However, over the last 5 years a fascinating debate has taken place over the true band gap energy of intrinsic InN. Historically the bandgap of InN has been accepted to be 1.9 eV. This value was determined in 1986 by Tansley and Foley after studying absorption spectra from radio frequency (RF) sputtered InN films [14]. A bandgap near 2 eV was confirmed by other groups also using sputtering techniques for the film growth [15, 16]. As the thin film techniques of MOCVD and MBE have increased in sophistication, the growth of epitaxial InN films became feasible. In 2001

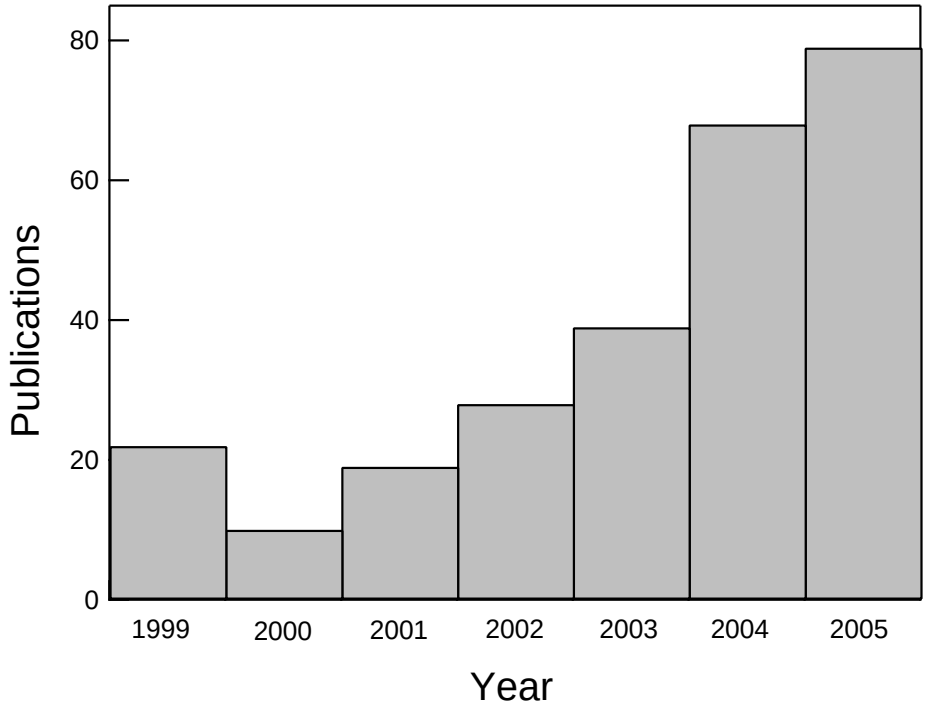

Figure 1.3 InN publications in recent calender years. Publications were counted if they included the words "indium nitride" in the title. [Web of Science, http://isiknowledge.com/, accessed: 4th January 2006]

Davydov *et* al. reported the observation of both a strong absorption onset and bright photoluminescence (PL) located below 1 eV for InN films grown by MBE [17]. This was quickly followed by other reports from Wu *et* al. and Matsuoka *et* al. who confirmed that MBE and MOCVD grown InN was showing evidence for a bandgap near 0.7 eV [18, 19].

The prospect of a bandgap near 0.7 eV generated much interest as it raised the possibility that the nitrides could be used to make optical devices which operated from the UV to the infrared (IR), somewhat of a holy grail for optoelectronic applications. Publications concerning the material increased sharply after the initial publication by Davydov *et* al., as shown in figure 1.3. Many other MBE and MOCVD groups confirmed the presence of the 0.7 eV feature as debate continued over the merits of PL and absorption in determining the bandgap in the InN case.

GaN and AlN are both known to exhibit PL and absorption features which arise from deep traps within the bandgap [20]. In some cases these effects can dominate op-

tical measurements, so the occurrence of a similar effect seemed very plausible within InN. Metallic indium clusters were detected within some InN films and Shubina *et* al. showed that the luminescence from InN films was greatly enhanced in regions around these clusters [21]. This raised the possibility that the 0.7 eV emission could be a result of Mie resonances. Specht *et* al. used valence electron energy loss spectroscopy (VEELS) to show that InN could exhibit an apparent gap near 1.7 eV, although questions have since been raised about the effects that electron damage induced by VEELS could have on the samples [22]. Butcher *et* al. have shown that the stoichiometry of InN films can sometimes be far from unity. They have suggested that the wide variety of results could possibly be explained as In_xN_y alloys with varying composition [20, 23]. Davydov *et* al. and Wu *et* al. have argued that the higher absorption features observed can be explained in terms of the Burstein-Moss effect [24, 25]. The Burstein-Moss effect describes the shift in the absorption edge of a degenerately doped material as the Fermi energy moves higher into the conduction band. This can lead to an absorption edge and PL peak of very different energy. The effect was shown to describe the behaviour of some MBE grown films very effectively using a two band Kane model [24].

Indium oxide is an indirect gap material with a bandgap near 3.75 eV [26]. The role of oxygen contamination within InN films has been a contentious issue. InN films are know to suffer from considerable oxidation at the surface but the effect of this layer on measured electrical and optical properties remains unclear. It has often been argued that the inherently higher oxygen contamination that results from sputtering can be used to explain the higher observed bandgap, as InN–In_2O_3 alloys would exhibit a wider absorption edge than InN [25, 27, 28]. Indeed, polycrystalline films were shown to exhibit a strong correlation between oxygen content and absorption onset by Yoshimoto *et* al. [27]. Additionally, Bhuiyan *et* al. used different growth techniques to produce films of variable oxygen content and absorption edges that again appeared to correlate with oxygen composition [28]. However, as noted by Monemar *et* al., the measured oxygen content in these films appears to be inadequate to account for a shift from 0.7 eV to 1.9 V assuming common levels of bandgap bowing. It is also noted by Monemar *et* al. that other reports show that In_2O_3 appears to segregate within the

InN lattice and not alloy. In this case the additional absorption feature should occur near 3.75 eV and not 1.9 eV.

Debate over the true bandgap of InN continues. To an extent, the number of different explanations proposed have served to confuse the topic as much as shed light on it. What is clear from the literature is that the only reliable optical feature that is reproduced in laboratories around the world is the 0.7 eV feature. It is this value that most of the InN community now seem to place more weight behind, but the matter is by no means settled. The observation of exitonic peaks in PL would be a big step towards resolving the matter but to achieve this would require growth of non-degenerate InN layers.

1.4 HIGH ELECTRON MOBILITY TRANSISTORS

High electron mobility transistors (HEMTs) based on GaN/AlGaN heterostructures are now manufactured commercially for applications in high power and high frequency operation [29]. The wide bandgap of the system is ideal for maintaining stable operation over a range of temperatures which is commonly demanded in power devices. Interestingly, Foutz *et* al. identified InN as having the highest peak drift velocity of all the nitrides (4.2×10^7 cm/s) and exceeding that of GaAs for electric fields greater than 5 kV/cm [30]. Despite the controversy over the bandgap — which could ultimately determine the suitability of the material for many optical applications — the material remains a very promising candidate for high frequency/high power devices.

Figure 1.4 shows a common structure for a GaN based HEMT. In principle an InN/AlGaN device could be based on the same structure, but with InN replacing the GaN layer. The devices rely on the formation of a high mobility electron accumulation layer at the GaN/AlGaN (or InN/AlGaN in the case of an InN HEMT) interface. The conductivity of this high mobility layer can be modulated very quickly by the gate voltage. The origin of this charge accumulation layer is two-fold. Firstly, because of the conduction band line up between AlGaN and GaN, it is energetically favorable for electrons to migrate to the GaN side of the interface (band bending induced quantum

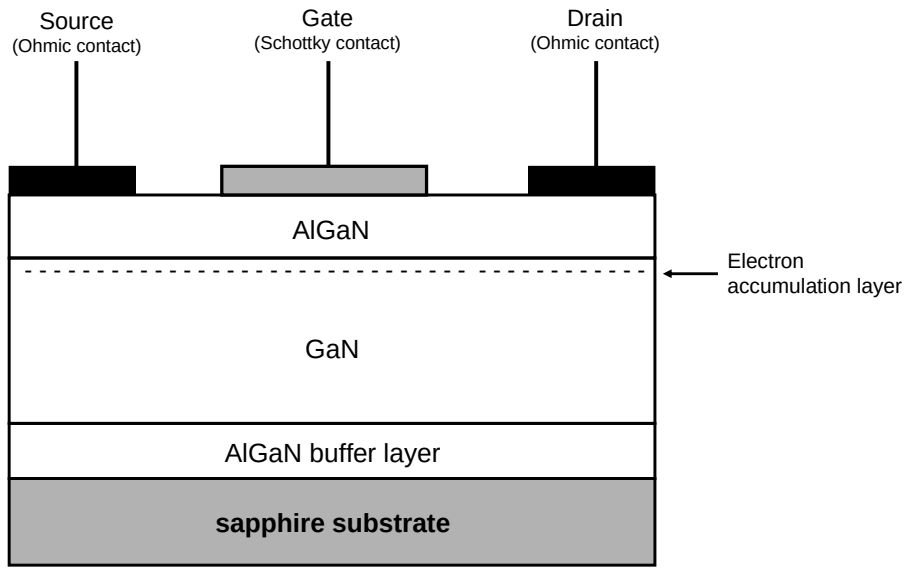

Figure 1.4 A possible structure for an InN based high electron mobility transistor (HEMT).

well). Secondly, the spontaneous polarisation differential between GaN and AlGaN requires that there is a charged layer to satisfy Poisson's equation.

An InN HEMT can be expected to benefit from similar accumulation due to both of these effects. However, recent investigations of InN thin films have revealed that InN may lend itself to high sheet concentrations at the surface [31, 32]. Sheet concentrations as high as 4×10^{13} cm^{-2} have already been identified at InN surfaces. This compares to sheet carrier concentrations of only 1×10^{13} cm^{-2} which are already used to produce commercial high power GaN based HEMTs. Although sheet charge is not the only consideration in determining HEMT suitability of a material, a large sheet charge is very desirable for high current applications. The origin of this high sheet concentration has been proposed to result from surface states acting as donors for InN [33]. Should this be the case, the polarity and termination of the surface could be expected to influence the level of this sheet density. Little is currently known about the termination of InN surfaces.

1.5 INDIUM NITRIDE AS A DILUTE MAGNETIC SEMICONDUCTOR

The area known as spintronics has attracted significant attention in recent years as groups strive to develop an efficient spin alignment and injection technology [34]. One approach is to use a semiconductor with a fraction of the atoms substituted by a transition metal, known as a diluted magnetic semiconductor (DMS). The use of a DMS as a spin polarising layer avoids the obstacle of injecting spin-polarised electrons across a metal-semiconductor interface — a process which has hampered progress using conventional ferromagnets [35]. $Ga_{1-x}Mn_xAs$ and $In_{1-x}Mn_xAs$ were the first ferromagnetic DMS materials to be explored extensively, although their low Curie temperatures make them undesirable for practical applications [36, 37]. A theoretical study by Dietl *et* al. [38] predicted higher Curie temperatures for wide bandgap semiconductors, and experimental studies confirmed room temperature ferromagnetism in a number of materials including $Ga_{1-x}Mn_xN$ [39], $Ga_{1-x}Cr_xN$ [40], $Al_{1-x}Cr_xN$ [41], $Zn_{1-x}Co_xO$, $Ti_{1-x}Co_xO_2$ [42] and $Sn_{1-x}Co_xO_2$ [43].

Figure 1.5 shows the Curie temperatures predicted by Dietl *et* al. for various semiconductors doped with 5% manganese and containing 3.5×10^{20} holes/cm^3. Of these materials, the nitride semiconductors have the advantage of an existing and rapidly developing technology base, which to date has been driven by blue and UV optical device applications. Despite the important role of InN in this industry, and recent interest regarding the value of the bandgap [17, 18], there have been few reports on its use as a DMS host. Chen *et al.* observed hysteresis at 1.7 K in an $In_{0.9}Mn_{0.1}N$ film [44]. A related study by the same group identified above room temperature ferromagnetism in an $In_{0.98}Cr_{0.02}N$ film [45]. Many questions remain over the origin of this ferromagnetism and whether it is the result of true DMS behaviour. Apparent higher Curie temperatures in the III-arsenide system has been shown to be the result of clustering of magnetic dopants [46], ferromagnetism resulting from such a mechanism does not rely on carriers mediating the magnetic exchanges. As such, there is no magnetic polarisation of the carrier spin, and the material is useless as a spin injection

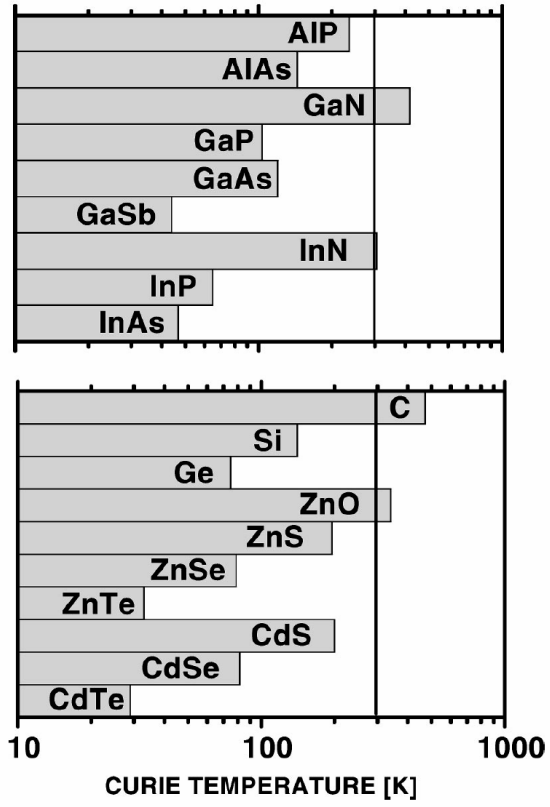

Figure 1.5 Curie temperatures evaluated for various III-V (top panel) as well group IV and II-VI semiconducting compounds (lower panel) containing 5% of Mn per cation (or 2.5% per atom) in 2+ charge state and 3.5×10^{20} holes/cm^3. [Dietl *et* al. Phys. Rev. B, 63, 195205 (2001)]

layer. Considerable investigation into the origins of magnetism in chromium doped InN is required before the suitability of the material as a spin injection layer can be determined.

1.6 THESIS MOTIVATION AND SCOPE

The prospect of InN having a bandgap near 0.7 eV has caused much excitement as people have envisioned devices based on the $In_xGa_{1-x}N$ system spanning the entire visible spectrum and much of the infrared. Such a material system would hold a great deal of promise for applications in solar cells and optoelectronics. Regardless of the bandgap, InN remains a promising material for applications in high electron mobility transistors, and dilute magnetic semiconductor applications. HEMTs offer a particularly achievable near term application; the device structure is simple and it was

one of the first devices realised in GaN technology.

Despite the prospect of applying InN in these ways, the material is still in its infancy in terms of our understanding of processing and preparing the material. The highest quality epitaxial layers still have high dislocation densities and heavy n-type conductivity. Understanding the origins of this n-type conductivity and eventually producing p-type InN will be a major step forward. Additionally, resolution of the bandgap question will reveal the suitability of the material for infrared optics and high power HEMTs. InN offers an interesting perspective on dilute magnetic semiconducting behaviour. The way this highly n-type material behaves when doped with transition metals may lend insights towards whether p-type conductivity is needed to mediate the exchange interaction and how clusters affect magnetism in the nitrides.

This thesis considers all of these topics in depth. Particular emphasis is paid towards the growth of InN using molecular beam epitaxy. The University of Canterbury has internationally competitive facilities for nitride MBE, the technique which leads InN growth technology. The bandgap question is examined in terms of the traditional techniques of absorption and PL. Photoconductivity measurements are also presented and discussed which provide a unique perspective on the bandgap question, and complement the PL and absorption data. Possible origins of the n-type conductivity of InN thin films is examined, and the presence of native defects at the surface is related to electron accumulation. In-situ doping and ion implantation are explored as a means of doping the material. Promising results are presented on the potential of magnesium acting as an acceptor. The magnetic and optical properties of the InCrN system are investigated. The magnetic and electronic role of different chromium sites is investigated and the origins of an interesting relation between n-type conductivity and ferromagnetism is discussed.

Chapter 2

GROWTH OF INDIUM NITRIDE BY PLASMA ASSISTED MOLECULAR BEAM EPITAXY

2.1 III-NITRIDE THIN FILM GROWTH TECHNIQUES

The electrical and optical properties of semiconducting materials can be greatly influenced by low levels of dopants or contaminants. Contaminant levels of one part in a hundred thousand (10^{17}cm^{-3}) or even one part in a million can have a significant influence on semiconductor properties. Accordingly, the need to use high purity growth and processing techniques is critical. The current lack of affordable bulk nitride substrates also means that III-nitride films are almost exclusively grown by heteroepitaxy. Although a number of companies and research groups are currently pioneering the growth of bulk nitride substrates, they are yet to become widely available and cost competitive [2]. The common techniques for III-nitride thin film growth are molecular beam epitaxy (MBE), metal organic chemical vapour deposition (MOCVD) and to a lesser extent, sputtering and pulsed laser deposition (PLD).

Sputtering (RF or DC) is usually performed in a high vacuum (HV) environment ($\sim 10^{-6}$ Torr) and typically uses argon to sputter a target and produce the constituents for film growth. Often nitrogen is leaked into the chamber separately to provide extra nitrogen species, which are often difficult to incorporate into films stoichiometrically. Sputtering generally produces films of lower structural quality and purity than the other common III-nitride techniques, and for this reason is not used widely for electronic applications. In the late 1980s, sputtering was the only technique available to grow InN reliably, hence much of the early InN literature concerns sputtered films (for example

see the work of Tansley and Foley [14, 47]).

Pulsed laser deposition has received the least attention of the four techniques. This is largely due to the cost and complexity of a PLD system, which typically incorporates a basic MBE system with the addition of a sophisticated laser. The technique utilises an ultra high vacuum (UHV) environment ($<10^{-9}$ Torr) and as such is capable of achieving high purity films. PLD has been used to grow nitride thin films with electrical and optical properties close to that of state-of-the-art MOCVD. However, the already well established technologies of MBE and MOCVD have resulted in the technique being largely passed over (for example see the work of Vispute *et* al. [48]).

Metal organic chemical vapour deposition (MOCVD) and the closely related technique of metal organic vapour phase epitaxy (MOVPE) lead the commercial nitrides industry. Thin films are grown by decomposing organic species as they pass over a hot substrate. The organic species can be chosen so that they incorporate a desired constituent without incorporating themselves into the film. Typical organic species which are used for III-nitride MOCVD are trimethylgallium, trimethylindium and trimethylaluminium (or TMIn, TMGa and TMAl) as the group-III sources, and ammonia as the nitrogen source. GaN MOCVD technology is now quite mature, however InN has proved considerably more difficult to produce by the technique. The low dissociation temperature of InN ($\sim$600°C) has reduced the efficiency of the technique to decompose ammonia and hampered progress. However, groups now appear to be circumventing the problem by carefully selecting the III:V ratio and the technique now produces InN films with electrical and optical properties close to the best MBE grown InN films.

The leading technique for high quality InN film growth is molecular beam epitaxy (MBE). Although MOCVD is used heavily for commercial GaN growth, MBE also finds many applications in the GaN field. MBE has several advantages in that abrupt interfaces can be easily formed, and the ultra high vacuum (UHV) environment allows accurate control over dopant species. The UHV environment of MBE also permits the use of in-situ monitoring techniques such as RHEED. As this thesis concerns films grown by MBE, the next section gives an overview of the technique and key process parameters. A comprehensive review of III-nitride MBE is given by Wang *et* al. [49].

2.2 MOLECULAR BEAM EPITAXY

2.2.1 System overview

Figure 2.1 shows the major components and schematic layout of the nitride MBE system at the University of Canterbury. The system is a Perkin-Elmer model 430. The water cooled chamber is fitted with ion and cryo pumps (cryo pumped exclusively during film growth) which results in a base pressure of $\sim 5 \times 10^{-11}$ Torr. Active nitrogen is supplied by a radio frequency inductively coupled plasma source, and all metallic species are supplied by standard or high temperature effusion cells. Samples can be transferred in and out of the system using a three chamber load-lock. Growth can be monitored in-situ by a Staib Instruments reflection high energy electron diffraction (RHEED) system, and also a custom built laser interferometer. Substrates are mounted on 78 mm molybdenum blocks via indium or indium-tin solder. The growth temperature can be controlled by a high temperature substrate manipulator heater capable of temperatures greater than 1200°C. The substrate manipulator temperature is monitored by a thermocouple touching the back side of the molybdenum block. Growth temperatures were calibrated using a silicon/aluminium eutectic.

2.2.2 Effusion cells and metallic flux

Standard effusion cells were used to supply indium, gallium, calcium, magnesium and manganese flux. A water cooled high temperature effusion cell was used to supply chromium flux. All metal ingots used in the cells had purities of at least 99.9999%. Crucibles were pyrolytic boron nitride and prior to having metal loaded were outgassed at 1200°C in the case of the standard cells, and 1600°C in the case of the high temperature cell. Once loaded with metal, all effusion cells were again outgassed to approximately 10% above the maximum intended operating temperature.

The flux from effusion cells is well understood; as such, the flux is easily quantified by a quartz crystal microbalance (QCM). A QCM is a water cooled quartz crystal which can be lowered into the growth position of the MBE system. Once there, the change in the characteristic oscillation frequency of the crystal can be measured as

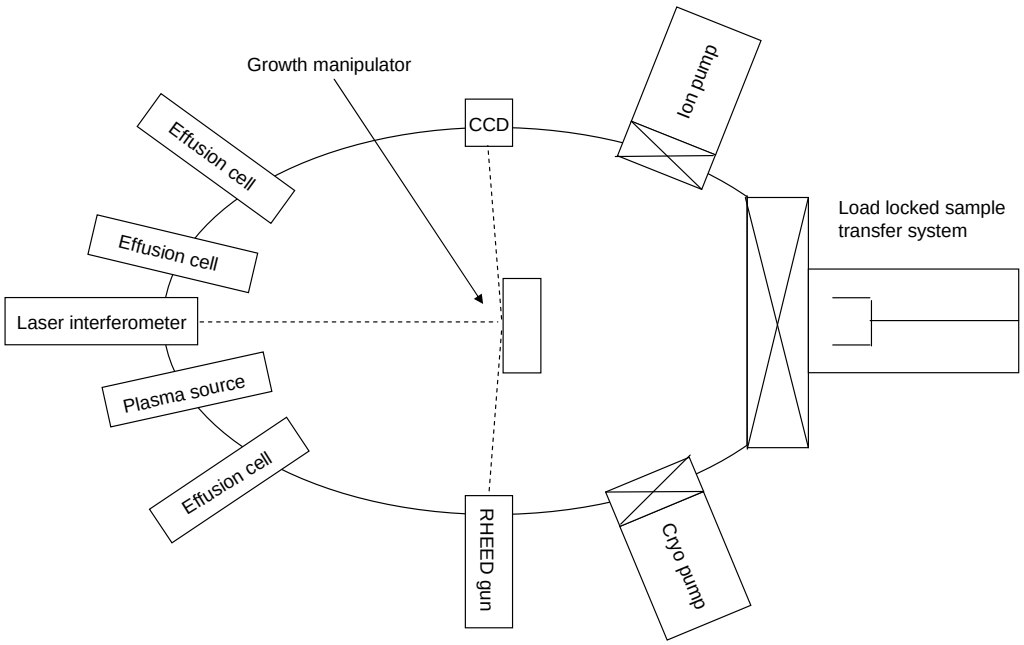

Figure 2.1 Major components and layout of the nitrides molecular beam epitaxy system at the University of Canterbury.

material is deposited onto the crystal. By assuming that all incident species stick to the crystal, the flux can be calculated. This technique was used to quantify fluxes for In, Ga, Mn and Cr in this system. The flux from Ca and Mg cells was small and difficult to measure by QCM. As such, theoretical flux curves were relied upon along with the existing compositional analysis techniques of ion beam analysis.

2.2.3 The radio frequency inductively coupled plasma source

As the common form of nitrogen is inert at achievable growth temperatures, a plasma or ion source is required to activate the N_2 molecule. The primary source used in this work was an Oxford Applied Research HD-25 radio frequency inductively coupled plasma source (RF-ICP). An earlier plasma source model, the MDP-21, was used for initial studies. Unless otherwise stated, results refer to growth with the HD-25. All nitrogen which flowed into the RF-ICP was filtered by a Aeronex Gate Keeper nickel inert gas filter, and flow was moderated by a 0–5 sccm mass flow controller. The basic structure of an RF-ICP is shown in figure 2.2. Nitrogen is controllably leaked into the

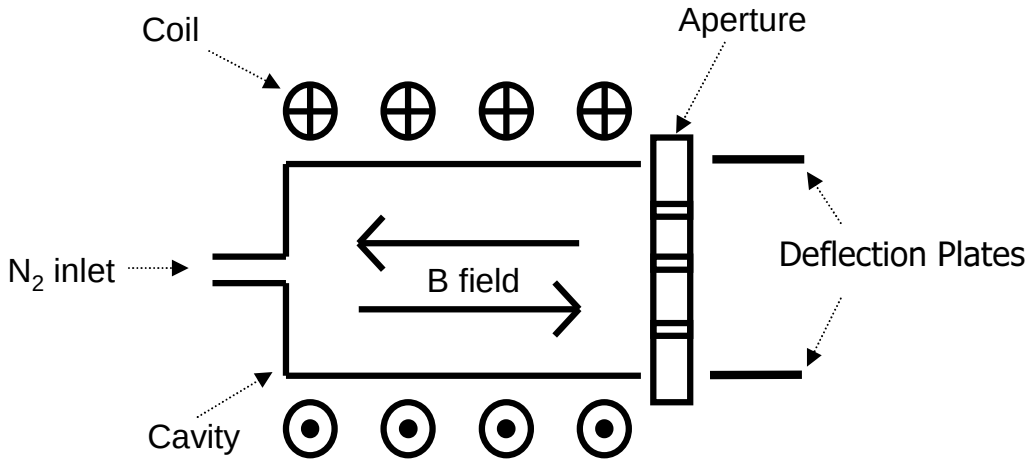

Figure 2.2 The main features of a radio frequency inductively coupled plasma source.

cavity via the inlet. A water cooled coil couples the RF signal into the cavity via a magnetic field which is most intense at the centre of the cavity. The alternating field accelerates charged particles which collide further with other species and a plasma is formed. Typically the source (both HD-25 and MDP-21) was operated at RF powers of 150–350 W and a flow rate of 1.3 sccm for film growths. The species generated by an RF-ICP can vary substantially at different plasma operating conditions and also from different source geometries. Section 2.7 considers the different species produced by RF sources and the effect that they can have on film properties.

2.2.4 Reflection high energy electron diffraction

RHEED is a very powerful tool for in-situ growth monitoring and is commonly used for MBE. When applied fully, RHEED can yield growth rate, surface structure and strain relaxation information. The technique utilises a grazing angle high energy electron beam (∼20 keV) in which the wavelength of the electrons is comparable to typical atomic spacings (0.1–1 nm). The electrons reflect off different atomic planes within the first several nanometres of the film and interfere constructively and destructively to form a diffraction pattern on a phosphor screen. From this diffraction pattern (or RHEED pattern) one can infer properties about the growing crystal. There has been much research into understanding how different features within RHEED patterns re-

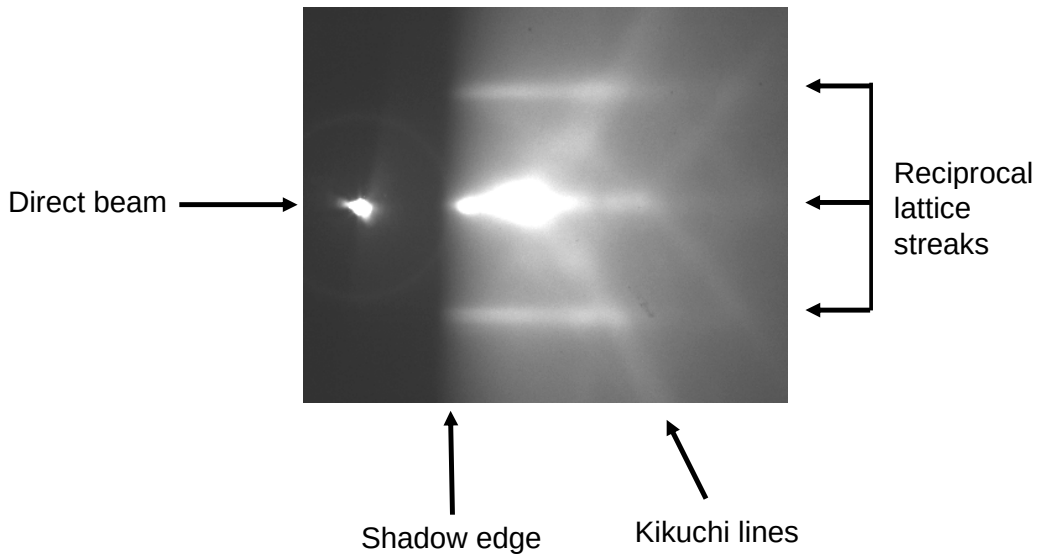

Figure 2.3 A RHEED image from a GaN film showing the direct beam, shadow edge, Kikuchi lines and parallel streaks.

late to film properties; a very thorough review is given by Braun [50]. Typical nitride RHEED patterns are dominated by a combination of reciprocal lattice streaks and Kikuchi lines as shown in figure 2.3. The shadow edge signifies where the beam is blocked by the film/substrate, and the separation of this and the direct beam represent the angle of incidence of the beam impinging on the film. Typical spot sizes for the electron beam are $\sim$100 μm. As the name suggests, the spacing of the reciprocal lattice streaks is inversely proportional to the spacing of the atomic planes taking part in diffraction. Whether the streaks appear continuous or broken can be used to assess the roughness of the growth front. Streaky reciprocal lattice features indicate that the film is smooth on a nm scale and the patterns are due solely to reflection/diffraction. If however, the reciprocal lattice features appear spotty then it indicates there is roughness on the nm scale. In this case some electrons are transmitted through surface features and cause an interference pattern (spotty reciprocal lattice features). In this thesis RHEED is primarily used to determine the crystalline nature of the film surface, e.g. poly or single crystal, atomically flat or rough, and to study how strain is accommodated as growth progresses. A Staib RH20 RHEED gun was used with a KSA capture and analysis system. The electron gun was typically operated at 20 kV and 1.5 A.

2.2.5 Heteroepitaxial growth on lattice mismatched substrates

Nitride thin films occur commonly in two different phases. The lowest energy, and thermodynamically stable crystal structure for InN, GaN and AlN is the wurtzite structure. The zincblende structure is closely related and of very similar energy. Consequently, by using a suitable template it is possible to grow the zincblende structure by non-equilibrium techniques such as MBE. Other crystal structures, such as rocksalt [51], have been explored by a number of groups under high pressure environments but these phases are not discussed in this thesis. Figure 2.4 shows a unit cell for the wurtzite and zincblende structures.

The most common growth direction for wurtzite III-nitrides is the (0001) direction, also known as the c-axis. The c-axis is a polar direction which means that the crystal has an inherent electric field along this axis. The polarity arises from the lack of inversion symmetry in the wurtzite crystal which results in some charge separation along the c-axis. This can have consequences for surfaces and thin layers where the phenomena is most noticeable. Film polarity and its influence on surface chemistry is discussed in detail in section 4.2.2.

As no bulk nitride substrates are commonly available, growth has been performed on a number of different substrates and crystal orientations. The majority of this thesis considers growth on (0001) sapphire with the use of buffer layers. However, growth on quartz, (100) and (111) yttrium stabilised zirconia (YSZ) and (0001) GaN templates is also explored and discussed. Growing heteroepitaxially introduces a number of complications. Epitaxial growth requires a substrate to be chosen which has a surface template that matches the growth crystal symmetry. In the case of growing c-axis oriented wurtzite nitride thin films, this demands hexagonal symmetry on the substrate surface. The next major consideration is lattice mismatch. Any mismatch between the lattice constants of the substrate and the film can lead to misfit dislocations. Dislocations can propagate through III-V thin films and significantly degrade the optical properties of the layer. Many techniques such as nitriding and inserting buffer layers

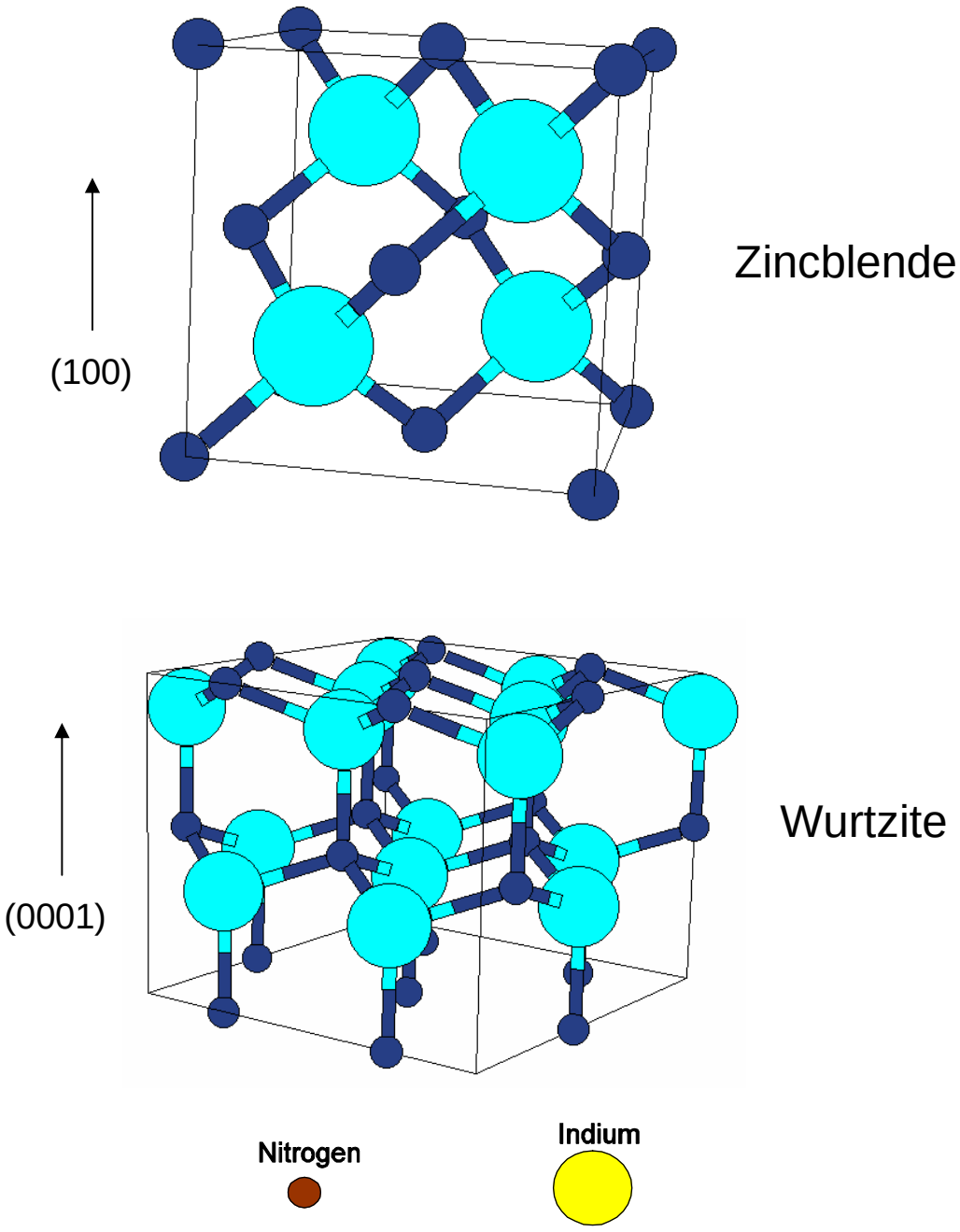

Figure 2.4 The wurtzite and zincblende crystal structures. The two most common phases of the III-nitride semiconductors. [US Naval Research Laboratory, http://cst-www.nrl.navy.mil/lattice/struk/, accessed: 25th April 2006]

have been developed to accommodate misfit strain but it remains one of the foremost problems. A close match between thermal expansion coefficients is also important. As a film cools down from the growth temperature both the substrate and film will contract. If there is a significant difference in the thermal expansion coefficients then this may cause the film to crack. Cracks can result in regions of the film becoming electrically isolated from each other, rendering the film useless for devices.

Figure 2.5 shows the lattice constants and thermal expansion coefficients for common substrates and III-N semiconductors. The plot gives an indication of how various substrates match indium nitride in terms of lattice constant and thermal expansion coefficient. For the cubic crystal structures (YSZ and Si), effective a-plane lattice constants are derived from the hexagonal (111) face. It is interesting to note that the most common III-N substrate, sapphire, has the worst lattice and thermal expansion match to InN. The success of sapphire substrates for InN growth to date has been due to the use of buffer layers and nitridation. (111) Si has a relatively good match to InN in terms of both lattice constant and thermal expansion coefficient. However, Si surfaces are often not stable under typical processing conditions, and Si is also an efficient n-type dopant of the III-nitrides. This has prevented widespread use of silicon substrates for InN growth, although recently progress has been made using AlN buffer layers [52].

Many groups have reported that GaN films grown on sapphire are actually rotated in the a-plane with respect to the substrate. It has been shown that such an arrangement actually produces a smaller lattice mismatch between the two crystals. In our experience we have not observed a similar effect occurring with InN growth. When quoting lattice mismatches in this thesis, unless otherwise stated, the unrotated mismatch is assumed.

2.3 CHARACTERISATION TECHNIQUES

A number of post growth characterisation techniques are discussed within this chapter. It is not feasible to give a comprehensive overview of each technique, so only a brief

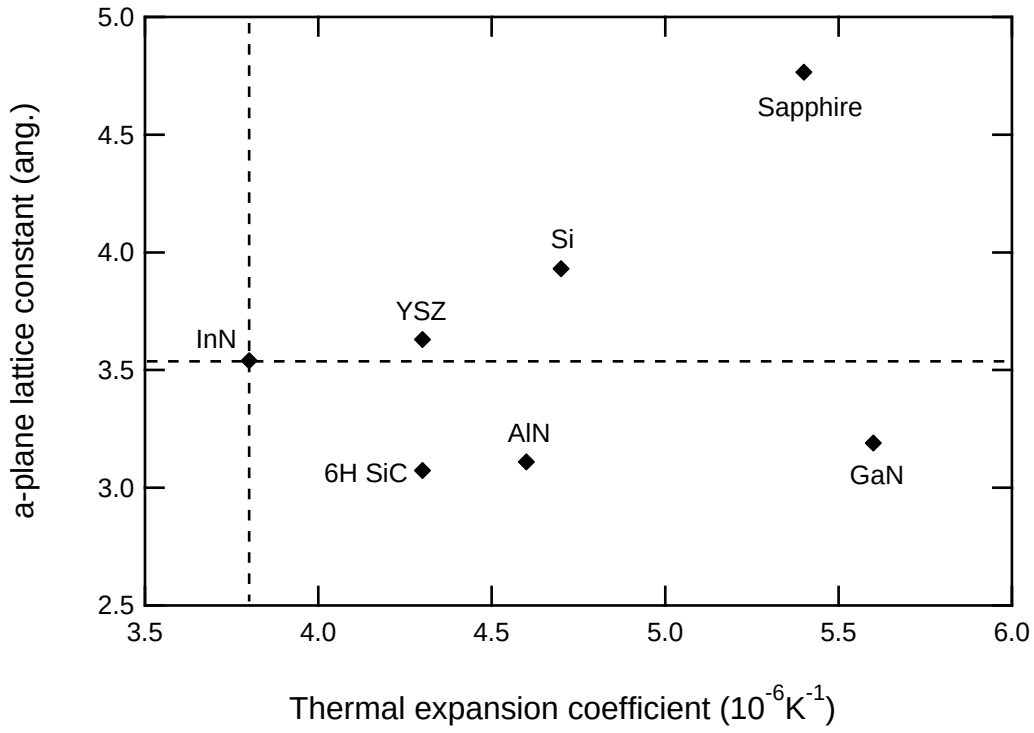

Figure 2.5 The a-plane lattice constant and a-plane thermal expansion coefficient for common indium nitride substrates and III-N semiconductors. For Si and YSZ the effective a-plane values are derived from the (111) face.

technique summary is given here along with key operating parameters. The reader is directed to the thorough review of semiconductor characterisation techniques by Cahn [53] for further information. All measurements were carried out at the University of Canterbury unless otherwise stated.

Atomic force microscopy (AFM) used a Digital Instruments Nanoscope IIIa operating in tapping mode. The system was mounted on a vibration isolation table and was capable of lateral resolution of $\sim$ 10 nm and vertical resolution of $\sim$ 1 nm. Image processing included only the basic routines included with the Nanoscope IIIa software.

Scanning electron microscopy (SEM) utililised a Raith 150 electron beam lithography system. The system included a Leica field emission electron microscope which was operated at 10 kV with a 30 μm aperture.

Transmission electron microscopy (TEM) was performed using a JEOL 3000F electron microscope at the Australian Key Centre for Microscopy and Microanalysis, University of Sydney, Australia. Standard ion milling techniques were used to prepare samples. The system was equipped with a secondary X-ray detector which allowed compositional information to be obtained through the complementary technique of **electron probe X-ray microanalysis** (EPXA).

Hall effect measurements used an EGK 2000, 0.5 T system. All measurements made at the University of Canterbury were single field only and no allowance was made for non-uniformity of the carrier concentration. Samples were contacted in the van der Pauw geometry. Silver paste was used to form ohmic contacts to the InN layers, while platinum with a silver capping layer was used to form an ohmic contact to GaN layers. A limited number of samples were studied by variable field Hall effect through a collaboration with Professor Tom Myers of West Virginia University; full details of this technique are given in section 4.2.2.

Ion beam analysis (IBA) was carried out at the Institute of Geological and Nuclear Science, Lower Hutt, New Zealand. The three IBA techniques employed were **Rutherford backscattering spectrometry** (RBS), **nuclear reaction analysis** (NRA) and **particle induced X-ray emission** (PIXE). Together these 3 techniques were capable of determining the stoichiometry of nitride layers within 10% (including depth profiles), and dopant profiles to 50 ppm within 10%.

2.4 GALLIUM NITRIDE GROWTH

Gallium nitride technology is the most well developed of the III-nitrides. Understanding the important aspects of GaN growth is beneficial when developing InN growth processes as many of the growth issues also apply to InN. Additionally, the use of GaN buffer layers is often employed to grow InN on sapphire substrates. One of the most important considerations when growing GaN by MBE is the level of Ga metal which is allowed to accumulate at the surface during growth. It is well understood in

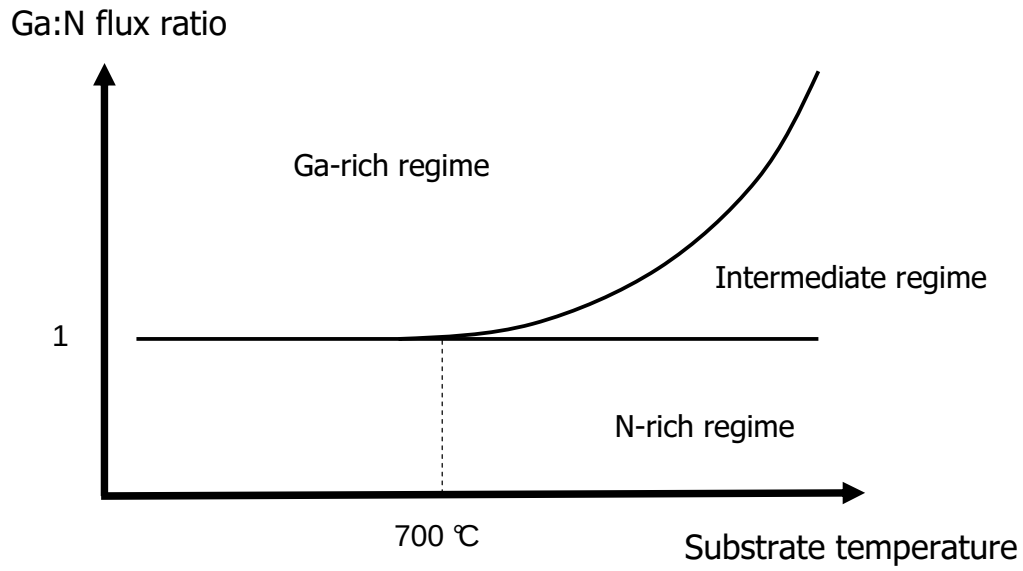

Figure 2.6 The GaN growth diagram indicating the three conditions which MBE grown GaN can be produced.

GaN technology that three separate gallium accumulation regimes exist [54, 55]. The relative Ga:N flux ratio and substrate temperature determine the regime as shown in figure 2.6. In the "N-rich" regime, less than a monolayer of Ga metal exists on the surface. In the "intermediate" regime, a bilayer of Ga exists at the surface which is believed to act as a surfactant and provide a low energy diffusion pathway for N species [56]. In the "Ga-rich" regime Ga accumulates as droplets on the surface which also have a surfactant effect. The intermediate and Ga-rich regimes are preferred for high quality film growth as the surfactant effect of the Ga metal improves the ability of nitrogen adatoms to find a suitable lattice site.

The growth rate of GaN has been shown to saturate as the Ga-rich regime is approached. A simple way to determine the boundaries between different growth regimes is to measure the growth rate at fixed nitrogen flux and various gallium fluxes. This was achieved using a custom built laser interferometer system. Laser interferometry measures the interference of a laser beam reflected from both the substrate and the film surface as a film grows. The period of the interference signal then gives the growth rate as described by:

$$GR = \frac{\lambda}{2nT} \tag{2.1}$$

where GR is the growth rate, λ is the wavelength of the laser, n is the refractive index of the material at λ (2.3 for GaN at 670 nm), and T is the oscillation period.

In order to map out the different growth regimes for the Canterbury MBE system, two GaN films were grown with the Ga flux varied in discreet steps. The nitrogen plasma conditions were unchanged during growth and the growth rate was measured at the various flux ratios by laser interferometry using a semiconductor laser operating at 658 nm. The films were both grown on sapphire substrates at 700°C with a low temperature GaN buffer grown at 500°C. Figure 2.7 shows the growth rate of the two GaN films grown at RF powers of 350 W and 150 W, respectively. A constant nitrogen flow rate of 1.3 sccm was used for both films. As we can see from figure 2.6, no intermediate regime exists at growth temperatures of 700°C. This indicates that the saturation in growth rate in both figures 2.7(a) and 2.7(b) marks the transition between N-rich and Ga-rich conditions. Increasing the RF power shifts the transition between the two regimes to higher Ga flux. By using these plots it was possible to choose a Ga flux that was slightly into the Ga-rich regime. This corresponded to a Ga flux of 2.1 and 1.5×10^{14} atoms.cm^{-2}s^{-1} for the 350 and 150 W plasma measurements, respectively. This Ga flux was then used for future optimised GaN films and buffer layers. It should be noted that the laser interferometry technique became available only towards the end of this thesis and originally the transition to the Ga-rich regime had been determined by observing the presence of Ga droplets on film surfaces. This original approach yielded a Ga flux within 5% of the laser interferometry determined Ga flux for the boundary between the two regimes.

The polarity of GaN films has been shown to strongly influence film properties. Typically GaN films grown on sapphire by MBE are N-polar, while films grown on sapphire by MOCVD are Ga-polar. The Ga-polar surface has been shown to be the preferred surface for high quality GaN growth [2]. Often AlN buffer layers are employed

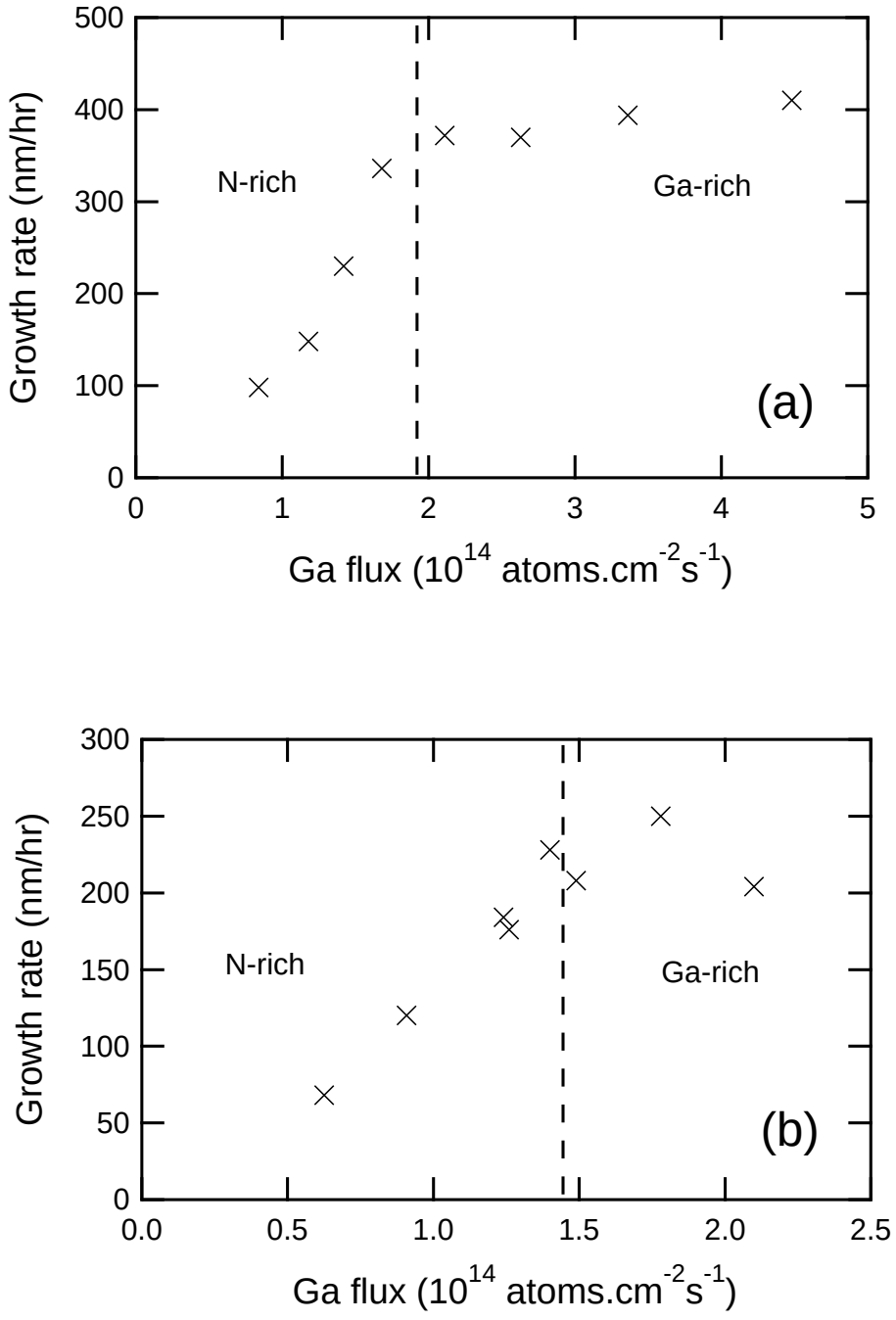

Figure 2.7 The growth rate of GaN layers at various Ga fluxes. (a) Ga-polar GaN with plasma RF power of 350 W and flow rate of 1.3 sccm. (b) N-polar GaN with plasma RF power of 150 W and flow rate of 1.3 sccm. The dashed line represents the Ga flux where the growth rate begins to saturate, this point marks the transition between the N-rich and Ga-rich regimes.

to achieve the Ga-polar growth mode in MBE growth [57]. The other common technique used to achieve Ga-polar growth by MBE is to use an MOCVD grown GaN template as the substrate. In this work GaN layers were grown on sapphire and MOCVD GaN templates to achieve N-polar and Ga-polar layers, respectively. Films were grown on both substrates under Ga-rich and N-rich flux conditions. No nitridation step was used. Films had a 50 nm low temperature buffer layer grown at 500°C, and then a 400 nm high temperature layer grown at 700°C. Figure 2.8 shows AFM images of the four films, along with the root mean square (rms) roughness of each film. Clearly the films grown on the GaN templates have much flatter morphologies, a result of the films growing homoepitaxially on an already relaxed GaN template. The films grown on sapphire, on the other hand, are highly strained due to the large lattice mismatch of GaN on sapphire. Additionally, the films grown on sapphire are expected to be N-polar as opposed to the preferred Ga-polarity of the MOCVD templates. The films grown in the Ga-rich regime show a small improvement in surface roughness, although the effect is small compared to the effect of the polarity and lattice mismatch.

From an InN perspective, the interest in GaN growth extends only as far as it can assist in producing improved InN films. As a buffer layer for InN, the GaN must be of high structural quality, indicating that growth in the Ga-rich regime with Ga-polarity should be preferred. We also want the GaN to be as electrically insulating as possible so that the buffer layers do not distort electrical measurements we make on InN layers. Hall effect measurements on all GaN films revealed that the GaN layers had high resistivity. It was often difficult to obtain reliable Hall data as the currents achieved through the GaN layers were small. Carrier concentrations below 10^{18} cm^{-3} were common. Hall mobilities <10 cm^2/Vs were measured for non-optimised films, and up to 150 cm^2/Vs for optimised growth.

2.4.1 Low temperature buffer layers and sapphire nitridation

Two common techniques that are often employed to improve the properties of GaN films are low temperature buffer layers and nitridation. A low temperature GaN buffer

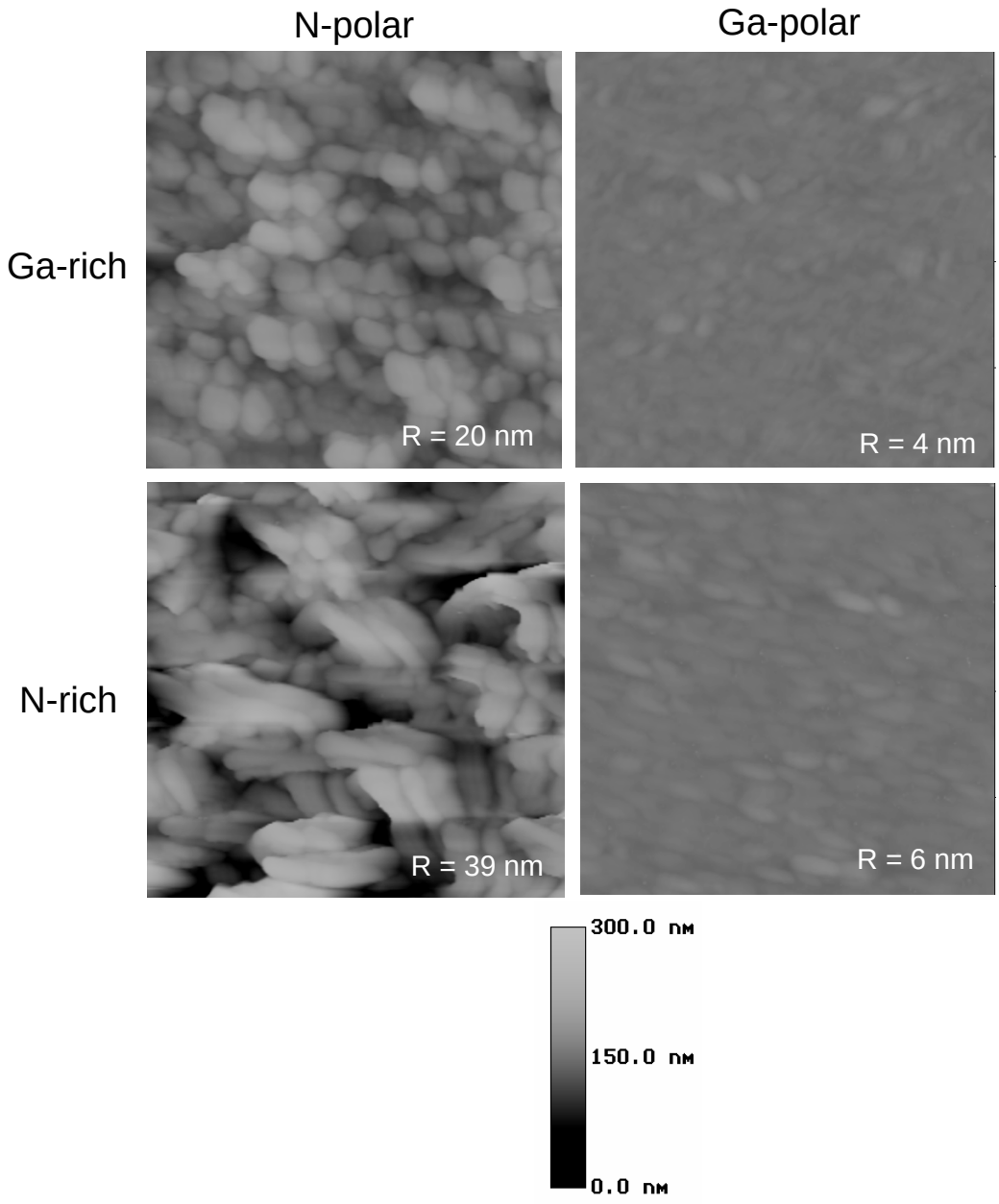

Figure 2.8 AFM images of N-polar and Ga-polar GaN films grown in both the Ga-rich and N-rich regimes. R is the root mean square surface roughness.

layer 10–200 nm thick has been shown to assist in strain accommodation on lattice mismatched substrates. Additionally, at lower temperatures (∼500°C), adatoms are less mobile and this leads to more complete wetting of the substrate surface, resulting in enhanced film uniformity. The lower mobility of adatoms also prevents them from diffusing away from dislocations and thus promotes the annihilation of dislocations. Nitridation is a technique used on sapphire substrates. By exposing the sapphire to active nitrogen, a thin AlN layer can be formed at the sapphire surface. This AlN layer helps reduce the lattice mismatch with GaN and also acts as a barrier between the oxygen-rich substrate and the GaN film. Common nitridation temperatures are near 700°C although some researchers have argued that a longer nitridation at lower temperatures is more favorable for GaN growth [58]. Both nitridation and low temperature buffer layers are used in this work; full details of the optimised growth recipe is given in section 2.8.3.

2.4.2 Indium surfactant assisted growth of GaN

When GaN films were used as a buffer layer for InN, it was often the practice to have both the indium and gallium effusion cells heated simultaneously. This meant that while the GaN buffer layer was being grown, the indium cell would be producing a substantial flux. In theory this flux should have been entirely blocked by the indium shutter. However, in practice this was not the case. Figure 2.9 shows a RHEED pattern taken at end of growth from two GaN films grown under identical conditions except the temperature of the indium effusion cell. Clearly the film where the indium cell was hot has a much streakier RHEED pattern indicative of a smoother surface morphology. This effect has been studied by Kruse *et* al. [59] who found that indium metal can act as a surfactant for GaN growth without incorporating within the film. The indium metal is believed to form a thin layer at the surface which provides a low energy diffusion pathway for Ga adatoms, similar to the self surfactant effect of Ga adatoms. As the indium cell was always hot when GaN was used as a buffer layer all of the GaN buffer layers discussed in this thesis have benefitted from this effect.

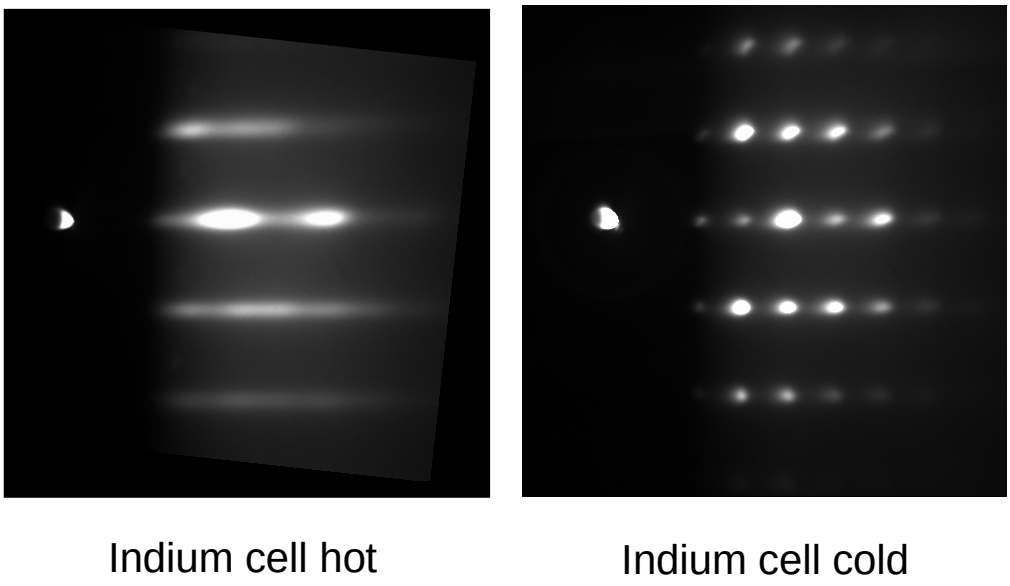

Figure 2.9 RHEED image along the $(\overline{1}\overline{1}20)$ azimuth of two GaN layers grown under identical conditions other than the temperature of the indium effusion cell (indium shutter closed).

2.5 GROWTH REGIMES OF INDIUM NITRIDE

After studying the growth dynamics of GaN, it may seem logical that a similar growth diagram will exist for InN. However, the In–N bond is weaker than the Ga–N bond and as a consequence the material dissociates at a lower temperature. The lower sustainable growth temperature means that unlike GaN, it is difficult to maintain a stable accumulation of metal species on the film surface during growth. Gunshor *et* al. observed that InN dissociates readily above 430°C [60]. The InN studied in this case was presumably In-polar as the films were grown on MOCVD GaN templates. Xu *et* al. found that growth of In-polar InN was limited to below 500°C, while N-polar InN could be reliably produced up to 600°C [61]. In either case, the growth of InN at temperatures above 600°C is not feasible. Figure 2.10 shows a proposed growth diagram for the InN material system. A constant active nitrogen flux of 1.5×10^{14} atoms.cm^{-2}s^{-1} is assumed (equivalent to the HD-25 operating at 1.3 sccm and 150 W as shown in figure 2.7(b)). The boundary between the In-rich and N-rich regimes is assumed to occur when the active nitrogen and indium fluxes are equal. The transition from the In-rich to intermediate regime is possible only when there is significant In flux desorbing

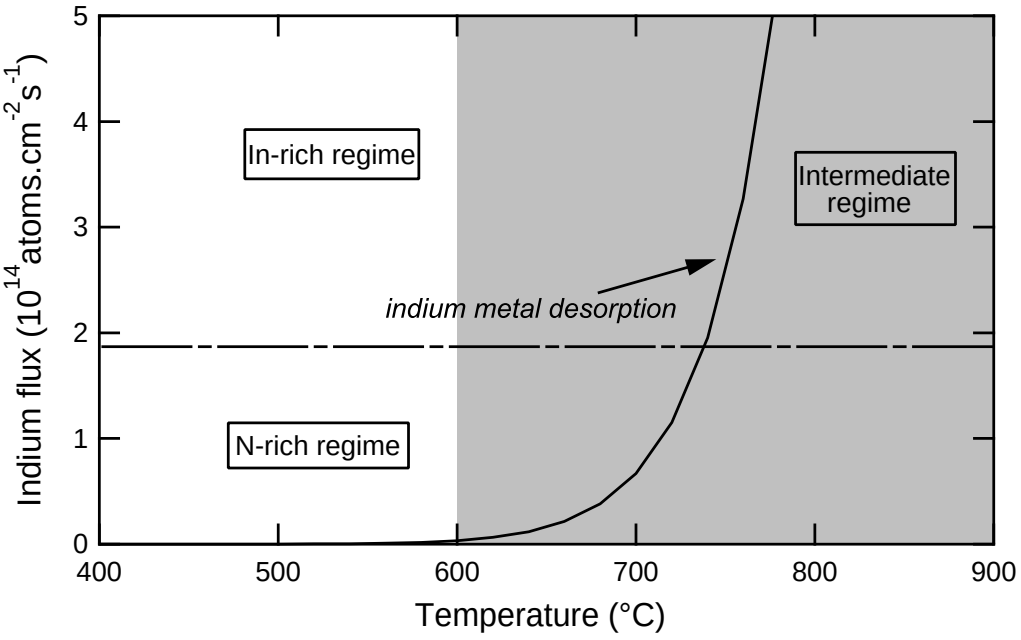

Figure 2.10 A proposed growth diagram for InN. The diagram assumes an active nitrogen flux equivalent to the HD-25 operated at 150 W and 1.3 sccm as calculated in figure 2.7(b). The boundary between the In-droplet and intermediate regimes was determined from the indium metal desorption curve. The shaded region marks unattainable growth temperatures due to the decomposition of InN.

from the surface, such that an equilibrium metal accumulation can be achieved. This curve has been estimated from the desorption of indium from indium metal as described by the Hertz-Knudsen equation [62]. This is not entirely accurate as the desorption of In from InN will vary from that of a metallic surface, although this approach yields a reasonable approximation for In desorption from GaN; Dimakis *et* al. have studied the desorption of In from a GaN surface and found an activation energy of 1.94 eV [63], which compares with an activation energy of 2.51 eV for indium metal. Both values result in a growth diagram where the intermediate regime lies above 600°C. The requirement that the substrate temperature must be below 600°C for InN growth means that there are only two accessible growth regimes of InN: In-rich or N-rich.

In order to explore the effect different growth regimes have on film properties, a series of InN films were grown on GaN buffers at 550°C. GaN buffers were grown directly on sapphire by MBE, so that both the GaN and InN layers are expected to be N polar. Sapphire substrates were nitrided for 15 min at 650°C prior to the GaN deposition. The buffer layers were 150 nm thick and grown at 650°C in the Ga-rich

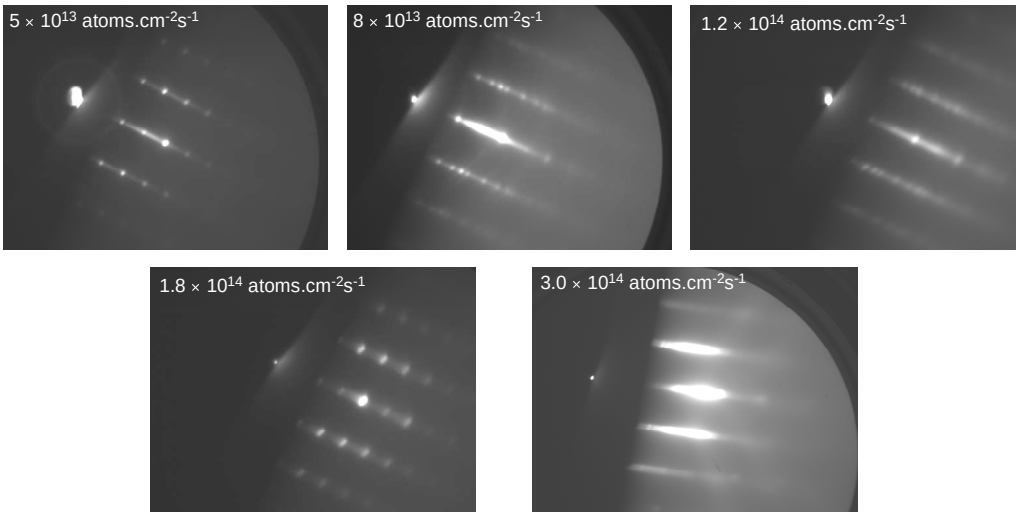

Figure 2.11 RHEED images after growth of InN films grown with various In fluxes (inset) and fixed plasma operating conditions of 350 W and 1.3 sccm. Images are taken along the $(\overline{1}\overline{1}20)$ azimuth.

regime as indicated in section 2.4. The plasma conditions were kept constant at 350 W and 1.3 sccm, while the In flux was varied from 0.5–3.0$\times 10^{14}$ atoms.cm^{-2}s^{-1}. All films were grown for 3 hrs.

Figure 2.11 shows the RHEED images from the end of growth of five films grown at various In:N flux ratios along the $(\overline{1}\overline{1}20)$ azimuth. The $(\overline{1}\overline{1}20)$ RHEED pattern is consistently the brightest pattern which we observe during growth of InN. At an indium flux of 3.0×10^{14} atoms.cm^{-2}s^{-1} the growth is in the In-rich regime and indium metal is expected to accumulate on the surface of the film. It is in this regime that the RHEED pattern adopts a bright and streaky appearance suggesting that the short range crystal order is high and that the surface is flat on an atomic level. The fact that the RHEED pattern remains bright when indium metal is expected to accumulate on the film surface suggests that the indium is forming droplets and occupies only a small fraction of the total surface area. Examining the film under an optical microscope confirms the presence of fractional surface coverage by indium droplets. The other four RHEED images all represent films grown in the N-rich regime and there seems to be little influence on the pattern as we move further into the N-rich regime. All four films from the N-rich regime show a pattern which consists of spots and streaks superimposed, representative of a single crystal film with a partially roughened surface.

During GaN epitaxy gallium metal can form ordered arrangements on the surface during GaN growth known as surface reconstructions. These surface reconstructions are visible through additional RHEED symmetry [64]. At no time during InN epitaxy did we observe stable surface reconstructions in the RHEED pattern. This may indicate that indium metal tends not to form layers of metallic adatoms as is common in GaN growth. It is also interesting to note that estimating the transition between the N-rich and In-rich regimes based on the equivalent flux of Ga in the GaN growth diagram has produced a good match with the change in RHEED pattern observed in this experiment.

Figure 2.12 shows SEM images of a film grown in the N-rich regime (indium flux = 0.5×10^{14} atoms.cm^{-2}s^{-1}) and a film grown in the In-rich regime (In flux = 3×10^{14} atoms.cm^{-2}s^{-1}). Both films have a partially coalesced island morphology. The higher In flux appears to have promoted a greater degree of island coalescence, but this film is over twice as thick as the N-rich regime film and the islands will naturally coalesce more as the film gets thicker. A significant point to note is that although growth in the In-rich regime appears to result in improved crystal order as determined by RHEED and SEM, growth in this regime is highly non-uniform. Film delamination at high indium flux is a severe problem and causes large areas of the substrate film to peel off or adopt rough morphologies. The streaky RHEED pattern and delamination observed in the film grown at high indium flux are likely related. When a film adopts a two dimensional growth mode (streaky RHEED pattern) the layer will have often have few dislocations which can help to relieve strain. As a result the layer remains highly strained and once it reaches a critical thickness the strain can cause the film to delaminate from the substrate.

2.5.1 Influence of growth temperature on film morphology

To assess the influence of growth temperature on film properties, InN layers were grown directly onto sapphire substrates in the N-rich regime (In flux = 0.5×10^{14} atoms.cm^{-2}s^{-1}) at growth temperatures of 200, 400 and 550°C, respectively. Prior to growth the sapphire substrates were nitrided at 200°C for 60 min. All films were ∼300 nm thick as measured by cross sectional SEM. Figure 2.13 shows AFM images from the three

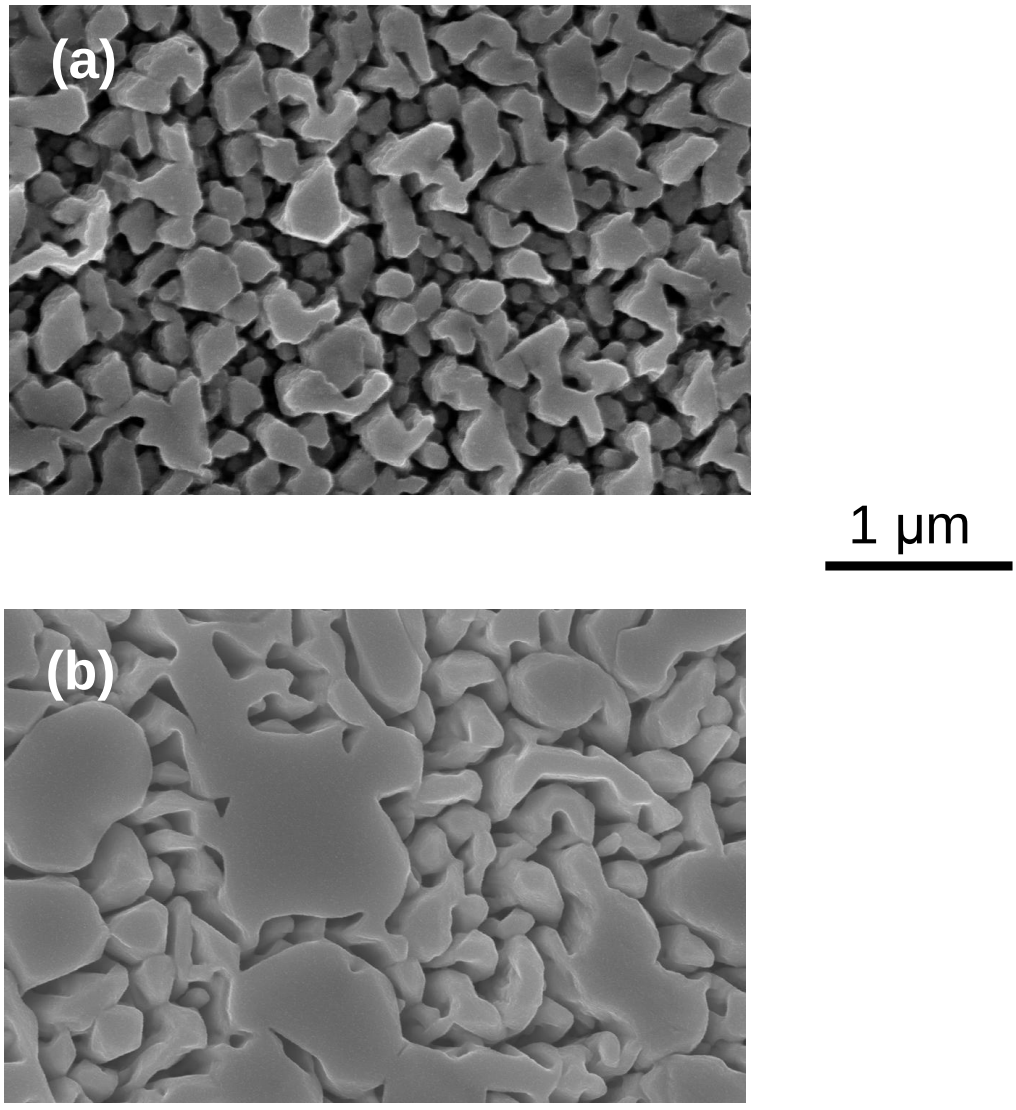

Figure 2.12 SEM images of InN films grown with various indium flux (a) N-rich regime indium flux = 0.5×10^{14} atoms.cm^{-2}s^{-1}, (b) In-rich regime In flux = 3.0×10^{14} atoms.cm^{-2}s^{-1}. All other film parameters remain unchanged.

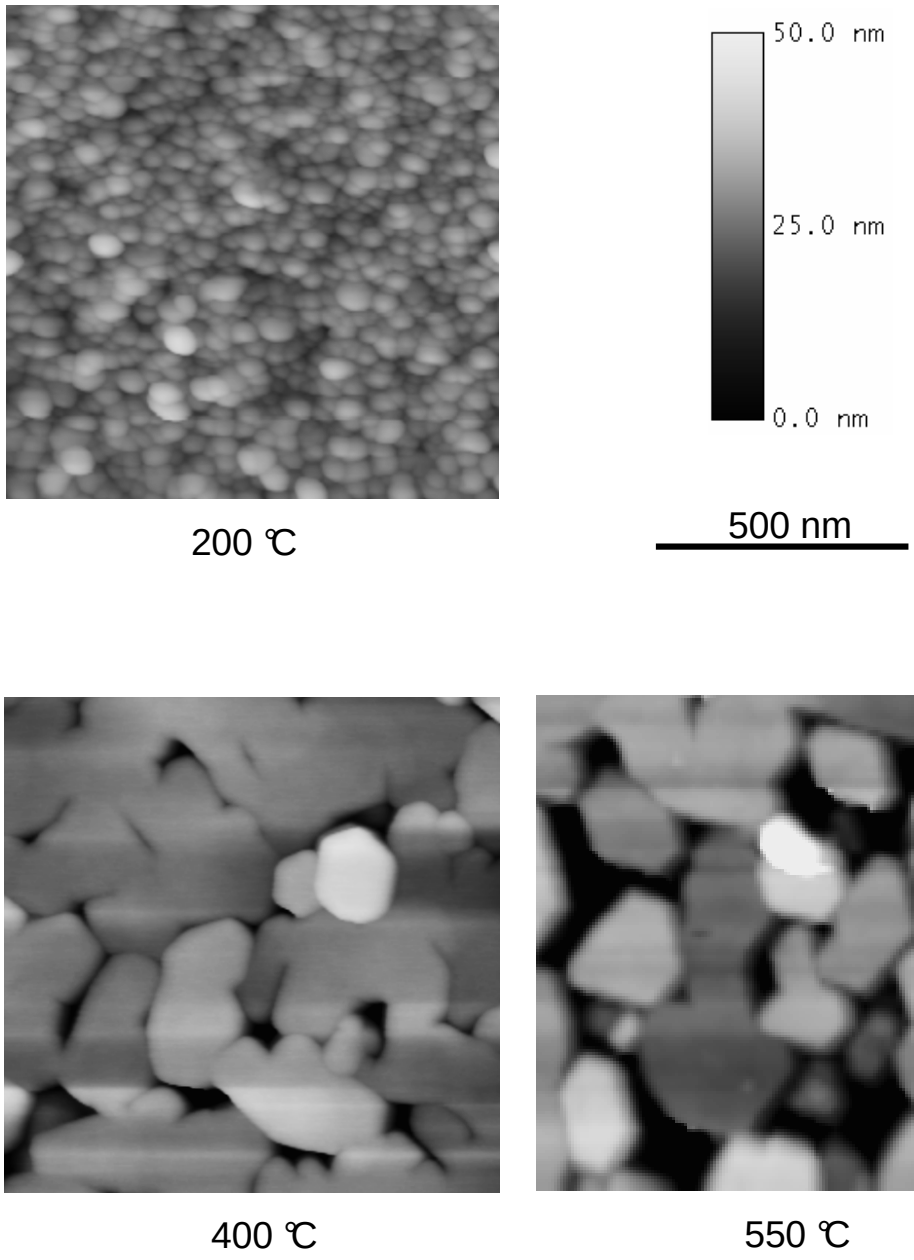

Figure 2.13 AFM images of three InN films grown directly on nitrided sapphire at various growth temperatures.

films. As with the film growth at 550°C on GaN buffers of figure 2.12, the films grown directly onto sapphire at 400 and 550°C have a coalesced island morphology with clear hexagonal symmetry visible. At 550°C the islands are more distinct while at the lower temperature the coalescence is further progressed. A growth temperature of 200°C results in flatter granular morphology with no hexagonal symmetry. The temperature dependence of the morphology can be explained in terms of the mobility of adatoms on the film surface. At low temperatures adatoms have less potential to migrate far from where they impinge on the growth front. This leads to many of the adatoms incorporating into the film at less energetically favourable sites than at higher temperature. For example, indium and nitrogen adatoms appear to adopt lower energy states on an InN face than they do on a (0001) sapphire face. The morphology of the films described in figure 2.13 is more heavily islanded at higher growth temperatures. This suggests that adatoms impinging on the sapphire substrate are more likely to migrate off the sapphire and onto the InN islands at higher temperature. This is a natural consequence of adatoms adopting the lowest energy state available given the activation energy of achieving that state and the available thermal energy.

2.5.2 Electrical characteristics from different regimes

As is evident from figures 2.12 and 2.13, growing at a substrate temperature of 550°C leads to an island morphology. If the islands are not sufficiently coalesced this can cause problems when making electrical measurements, as the films are not always continuous. This proved to be the case for the films grown with In flux of 1.2 and 1.8×10^{14} atoms.cm^{-2}s^{-1} as outlined in section 2.5. The carrier concentration and Hall mobility of the other three films in this series are shown in figure 2.14. The higher In flux clearly results in significantly improved Hall mobility and reduced n-type carriers. The reasons for this are likely to be a surfactant effect caused by the increased surface coverage of In which will arise on the surface, although it has not had a significant effect on surface morphology as is clear from figure 2.12. This indicates the self-surfactant effect of indium metal leads to improved short range crystal order (e.g. less point defects) but is not influencing the overall morphology greatly. The improved

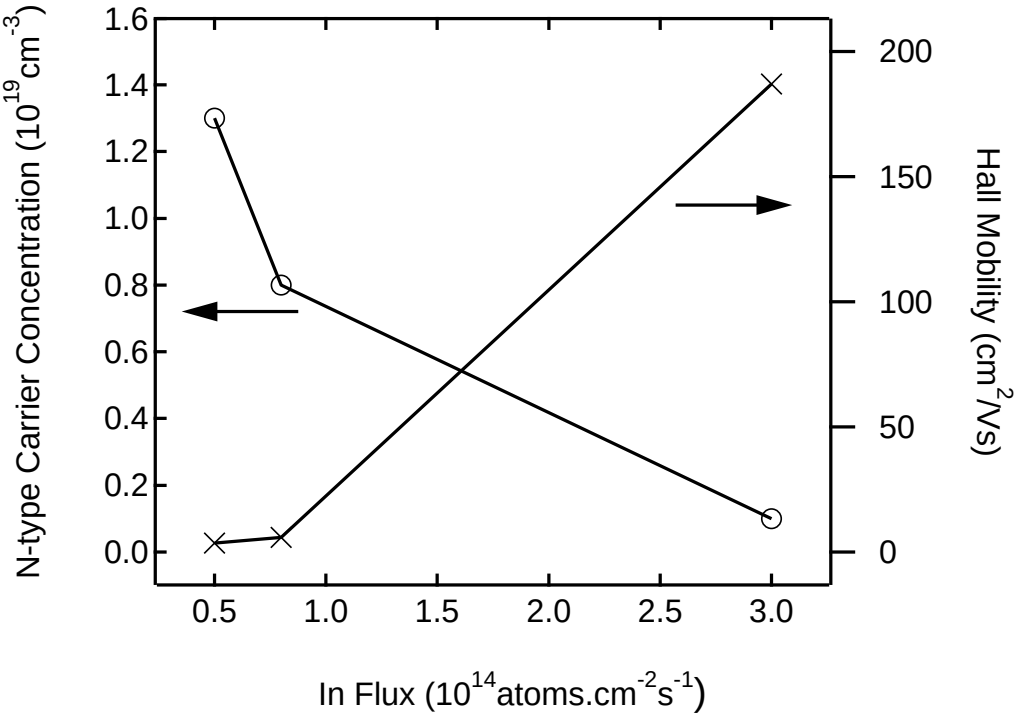

Figure 2.14 N-type carrier concentration and Hall mobility of InN films grown on GaN buffer layers as a function of In flux.

electrical properties of the film grown in the In-rich regime suggests that although the RHEED pattern indicated a polycrystalline surface (likely to be indium metal), the film continues to grow single crystal below the surface.

2.5.3 Effect of GaN buffer layer

This section has considered the effects of different In:N flux ratios on InN growth directly on nitrided sapphire, and on GaN buffer layers (grown on sapphire). Although the general trends of relative In:N flux ratio are found to be preserved on both nucleation surfaces, a GaN buffer layer is found to be preferred for a number of reasons. Firstly, delamination of InN becomes problematic when thick films (>300 nm) are grown directly on nitrided sapphire. Films have been grown up to 1 μm thick on GaN buffer layers with no problem of delamination. This is clearly a product of the reduced lattice mismatch between GaN/InN. Secondly, higher growth temperatures can be maintained on GaN before the surface morphology becomes heavily islanded. As

is evident from figure 2.13, growth at 400°C on sapphire already leads to a heavily islanded morphology. When growth is performed on GaN we find this transition does not occur until ∼480°C. Finally, the electrical properties of films grown on GaN are superior to a comparable film grown on nitrided sapphire. Typical Hall mobility for films grown near the In-rich regime on GaN buffers and nitrided sapphire at 400°C are 200 and 40 cm^2/Vs, respectively.

2.6 (100) AND (111) YSZ AS ALTERNATIVE SUBSTRATES

Many of the problems associated with InN epitaxy stem from the large lattice mismatch with commonly used substrates. Identification of a nearly lattice matched substrate suitable for InN heteroepitaxy would be a large step forward for the technology. (0001) sapphire with an optional GaN buffer layer is the most widely used substrate for InN growth. The lattice mismatch of sapphire with unrotated InN is 26%, while a GaN buffer layer reduces this to 8%. In contrast, (111) YSZ has a mismatch of only 2.5% and has been used to demonstrate films with reduced X-ray diffraction (XRD) full width half maximum (FWHM) compared to films on sapphire substrates grown by pulsed laser deposition [65]. The (100) face of YSZ provides a cubic template for the metastable zincblende phase of InN. In many optical applications the zincblende phase is preferred because of the absence of built-in electric fields that can act to separate carriers. Little is known about the properties of zincblende InN, and successful characterisation of this phase could also assist in answering questions regarding the wurtzite phase. Other groups have used r-plane sapphire [66] and GaAs with an InAs buffer [67] as substrates for zincblende InN, although electrical and optical characterisation of these films was limited. This section discusses the use of both (111) and (100) YSZ as substrates for epitaxial InN growth.

2.6.1 Growth and structural characteristics

Figure 2.15 shows AFM images and RHEED patterns of films grown on (111) and (100) YSZ at 550 and 450°C, respectively. Growth on (111) YSZ was generally much

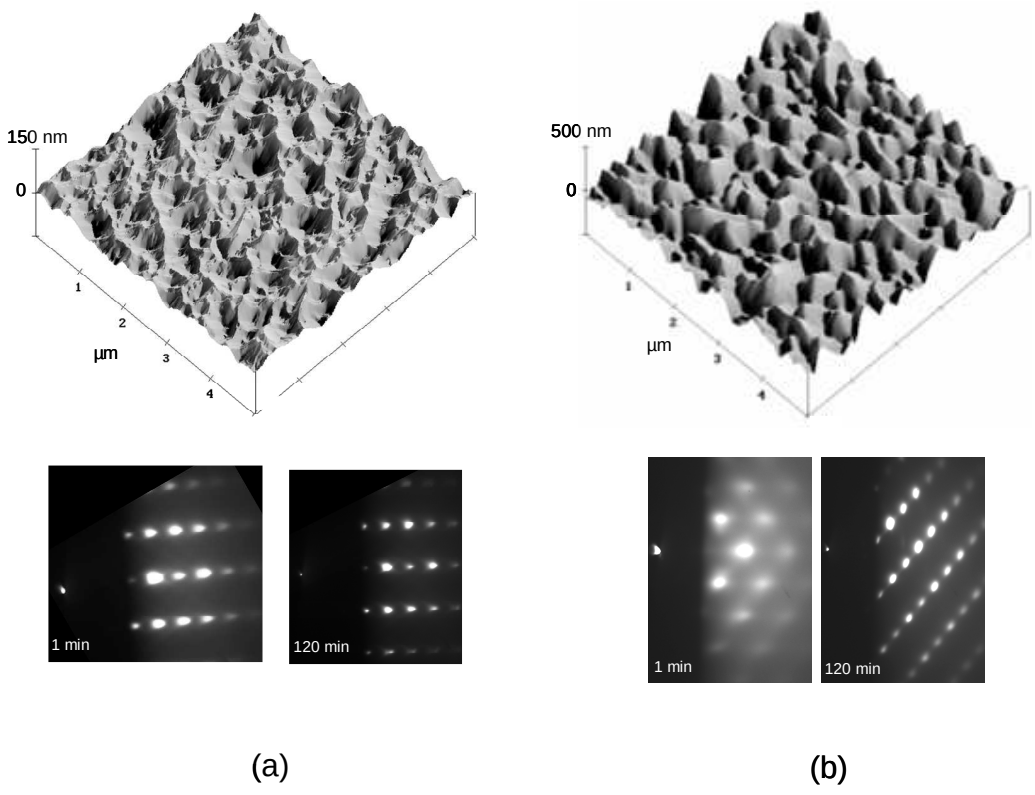

Figure 2.15 AFM and RHEED images taken from InN films grown on (a) (111) YSZ and (b) (100) YSZ. RHEED images from the film grown on (111) YSZ are along the $(\overline{1}\overline{1}20)$ azimuth; the film grown on (100) YSZ lacks obvious RHEED symmetry.

smoother than on (100) YSZ, and adopted a crater-like morphology, with hexagonal symmetry visible within the crater outlines. Hexagonal symmetry in the RHEED pattern from films grown on (111) YSZ confirmed c-axis oriented wurtzite films. The RHEED pattern also confirmed that the wurtzite growth mode was adopted within the first minute (1 min RHEED image, figure 2.15) of growth and continued throughout (120 min RHEED image, figure 2.15). The rougher films on (100) YSZ showed a heavily islanded surface, with no obvious symmetry visible in AFM or under RHEED pattern rotation. The 1 and 120 min RHEED images show the film grown on (100) YSZ initially adhering to the cubic template, but as growth progresses intermediate features appear, suggesting the formation of a secondary phase. The pattern also adopts a crosshatched appearance with brighter spots appearing on diagonal lines from the shadow edge, indicative of a strongly faceted surface.

The evolution of the crystal phase from majority zincblende to majority wurtzite as growth continues is confirmed by TEM. Figure 2.16(a) shows a high resolution image of the interface where epitaxial growth is clearly observed from (100) YSZ to (100) InN. Studying regions further from the interface revealed significant quantities of both phases present. Boundaries between zincblende and wurtzite phases were observed with varying crystallographic orientations as shown in figure 2.16(b). Interestingly, the surface and interface of the samples both tended to be zincblende, suggesting that some bulk transformation to the wurtzite phase may take place upon the zincblende phase reaching a critical thickness. The nucleation of the zincblende phase and then gradual formation of the wurtzite phase is consistent with observations of RHEED patterns by Tabata *et* al. and Cimilla *et* al. [66, 67]. XRD was performed on films grown on (100) YSZ in order to further confirm the TEM findings. The two-theta scan revealed peaks associated with both the wurtzite and zincblende phases as shown in figure 2.17.

2.6.2 Electrical properties of InN grown on YSZ substrates

Hall measurements revealed carrier concentrations as low as 3×10^{18} and 2×10^{19} cm^{-3} for films grown on the (111) and (100) faces, respectively, with peak Hall mobility of 200 cm^2/Vs achieved on both substrates. These values compare favourably to films

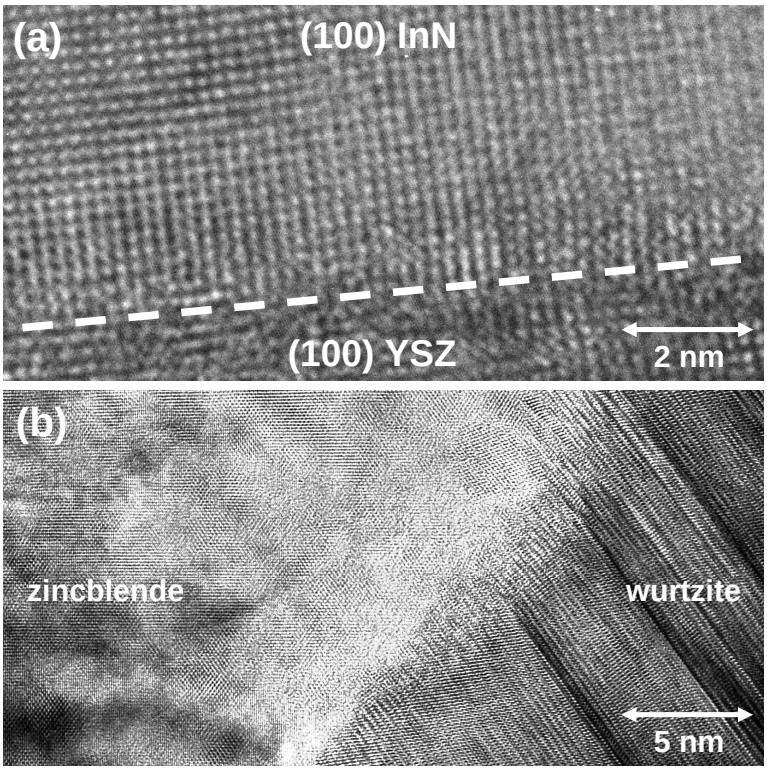

Figure 2.16 TEM images showing: (a) epitaxy of zincblende InN at the (100) YSZ interface, (b) a phase boundary between a wurtzite and zincblende region.

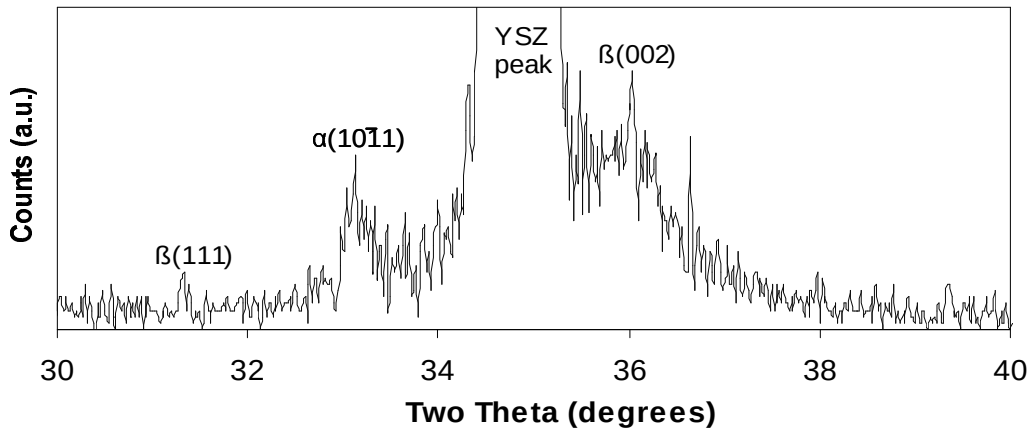

Figure 2.17 Two-theta scan for a film grown on (100) YSZ with wurtzite (α) and zincblende (β) features labeled.

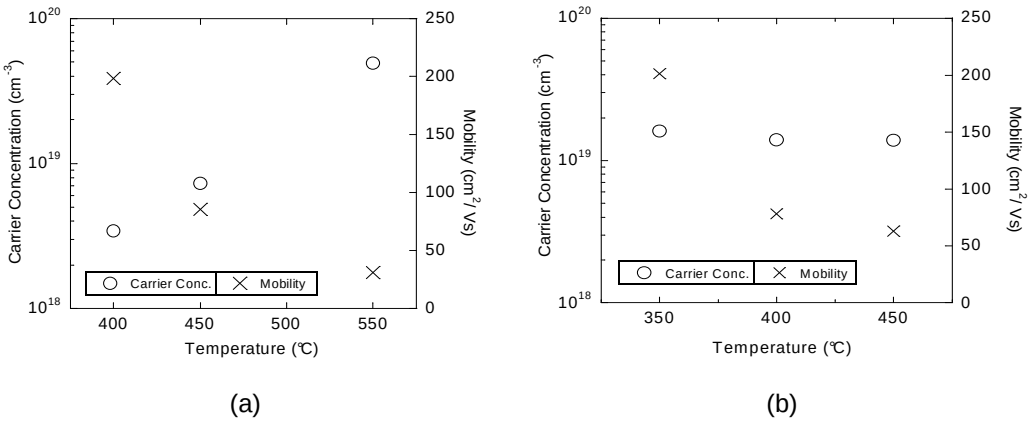

Figure 2.18 Growth temperature dependence of the electrical characteristics of InN films grown on (a) (111) YSZ and (b) (100) YSZ.

grown directly on sapphire under similar conditions, which typically exhibit a Hall mobility of 100 cm^2/Vs and carrier concentrations near 10^{20} cm^{-3}. Figure 2.18 shows the carrier concentration and Hall mobility for films grown on (111) and (100) YSZ as a function of substrate temperature. Surprisingly, films grown on both orientations show an increase in Hall mobility for reduced substrate temperature. This may signal that there is some buffer layer effect from growing at lower temperatures. As has been covered in section 2.4, lower growth temperatures promote substrate wetting and dislocation annihilation, and hence such dependencies are sometimes observed. Another possibility is the stability of the substrate. Nitridation of sapphire is thought to provide an effective diffusion barrier to stop the sapphire and nitride film mixing, but no such step was attempted on the YSZ substrates. At higher temperatures mixing of the film and substrate is more likely.

2.7 ACTIVE NITROGEN SPECIES

As mentioned in section 2.2.3, the active nitrogen produced by a plasma source can vary substantially depending on the source design and operation. Consequently, identifying the species which is preferred for growth can assist in choosing an optimal source and operating conditions. The two competing inductively coupled plasma sources which have previously been studied in detail are the radio frequency inductively coupled plasma

(RF-ICP) [68, 69, 70], and the electron cyclotron resonance plasma sources (ECR) [71]. The RF-ICP has become the most common choice for MBE nitride growth, as films produced with this technique have been shown to have superior electrical, optical and structural properties [72, 73]. Active nitrogen species produced by both these sources typically consists of a combination of atomic nitrogen, varying series of excited molecular nitrogen and ionic forms of both species. Studying the optical emission from both sources has proved a useful tool in determining the relative composition of active species produced by the plasmas [68, 69, 74, 75, 76]; a complete description of all optical transitions involving atomic and molecular nitrogen is given by Wright *et* al. [77]. Optical emission spectroscopy can provide qualitative information about species produced within the cavity but does not necessarily represent the active species which survive long enough to leave the cavity and take part in growth. The technique of quadrupole mass spectrometry (QMS) provides a direct way of measuring which species leave the cavity and arrive at the growth position [78]. Typically ECR sources are found to produce a high content of 2nd-positive series excited molecular nitrogen and ionic species [71, 72, 76]. In contrast, the RF-ICP typically produces mainly 1st-positive series excited molecular nitrogen and atomic nitrogen [72, 75].

Although the decision to use an RF-ICP for nitride growth may be relatively straightforward, a number of different RF-ICP products are available, with the Veeco UNI-Bulb and the Oxford Applied Research HD-25 among the most commonly noted. A number of groups have shown that the active nitrogen species produced by different RF-ICPs can vary substantially and can have a profound influence on nitridation effectiveness [79, 80], electrical characteristics [78], and optical properties [74]. Furthermore, studies of the optical spectra of nitrogen plasmas at different RF powers and flow rates have shown that the relative amounts of active species can change quite dramatically depending on the plasma operating conditions [75]. Although this section considers only active species produced by the Oxford Applied Research HD-25 RF-ICP, it is important to note when comparing results from the literature that the different plasma sources may be significantly influencing the active nitrogen make-up.

2.7.1 Influence of plasma operating conditions on active species production

Figure 2.19(a) shows an optical emission spectrum measured from an HD-25 RF-ICP operated at 400 W and 1.3 sccm. The characteristic atomic nitrogen peaks are visible at 745, 821 and 869 nm. The emission from 1st-positive molecular series is visible as broader bands centred at 590, 660, 760 and 820 nm [72, 76]. The spectral region examined in this study includes emission only from the atomic nitrogen and the 1st-positive molecular series; the content of the 2nd-positive molecular series and ions is not explored. However, previous studies have identified atomic and 1st-positive molecular species as the dominant species produced by RF-ICPs [72]. By monitoring how the relative intensity of these peaks change as a function of flow rate and RF power, we can gain an understanding of how the relative composition of the active nitrogen species changes with plasma operating condition. Figure 2.19(b) shows the ratio of the 822 nm atomic nitrogen peak to the 651 nm molecular nitrogen peak as a function of RF power at a constant nitrogen flow rate of 1.3 sccm. As the RF power is increased, the relative amount of atomic nitrogen produced within the cavity increases approximately linearly. The flow rate dependence was also investigated and it was found that lower flow rates resulted in higher relative atomic species content.

Although optical emission spectroscopy is a useful technique for examining how the species production changes within the cavity, when it comes to growing thin films we are concerned with what species leave the source and reach the growth location. For this reason we have studied the mass spectra using a quadrupole mass spectrometer (QMS). Figure 2.20(a) shows a QMS spectrum measured in line-of-sight from an HD-25 operated at 400 W and 1.3 sccm. The atomic and molecular peaks are located at 14 and 28 amu, respectively. The QMS was operated at an ionising voltage of 25 V, which produced some ionisation of ground state N_2 but no double ionisation. Figure 2.20(b) shows the partial pressure (PP) ratio of atomic nitrogen (14 amu) and molecular nitrogen (28 amu) as a function of RF power at a constant flow rate of 1.3 sccm. The trend again shows enhanced relative atomic production at higher RF powers, in agreement with that of figure 2.19(b) This suggests that although there may

be some change in the ratio of the two species as they exit the aperture, the general trends are preserved. It must be noted that the molecular species in this measurement includes some ground state N_2 as well as activated N_2, as separating the two was not possible with the ionising restrictions imposed by the residual gas analyser.

2.7.2 Dependence of electrical characteristics on active species and polarity

A series of four indium nitride films were grown on (0001) sapphire substrates with gallium nitride buffer layers at RF powers of 110, 150, 250, and 350 W, respectively. The nitrogen flow rate for these films was 1.3 sccm, which corresponded to a chamber pressure of 1×10^{-5} Torr. It was found that the plasma would self-extinguish if the power was reduced below 110 W at this flow rate. All four films exhibited streaky RHEED patterns throughout growth and a flat surface morphology with rms roughness less than 5 nm. Figure 2.21 shows the carrier concentrations for these films as a function of the active nitrogen species as determined in figure 2.19. Clearly the films where molecular nitrogen is the dominant active species during growth have lower n-type carrier concentrations. The Hall mobility of these films was found to correlate strongly with the carrier concentration, as has been observed by other groups studying indium nitride [81, 82], with a maximum Hall mobility of 377 cm^2/Vs achieved for the film grown at 150 W. As the RF power is reduced the ratio of active molecular nitrogen to atomic nitrogen changes but the total amount of active nitrogen also decreases. This results in the effective III:V flux ratio increasing as the plasma power is reduced and may complicate interpretation of figure 2.21. The III:V flux ratio is known to have a profound influence on GaN quality [83, 54], although this has not been established as definitively for indium nitride growth.

Three indium nitride films were grown on (111) YSZ at RF powers of 150, 250 and 350 W, respectively. YSZ has a lattice mismatch of 2.5% with indium nitride, as opposed to 8% with gallium nitride, and has been used to grow indium nitride films with relatively low carrier concentrations [84]. Hall effect measurements revealed that films grown on YSZ were relatively insensitive to active nitrogen species as shown in

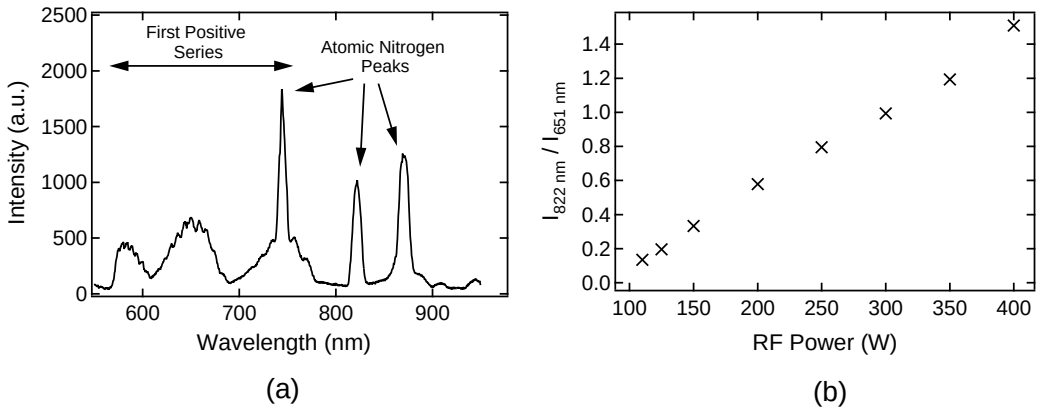

Figure 2.19 (a) Optical emission spectrum measured from an HD-25 nitrogen RF-ICP operating at 400 W and 1.3 sccm. Characteristic features can be attributed to transitions from atomic species or first positive series molecular species as labeled. (b) The ratio of the 822 nm peak to the 651 nm peak as a function of RF power at a constant flow rate of 1.3 sccm.

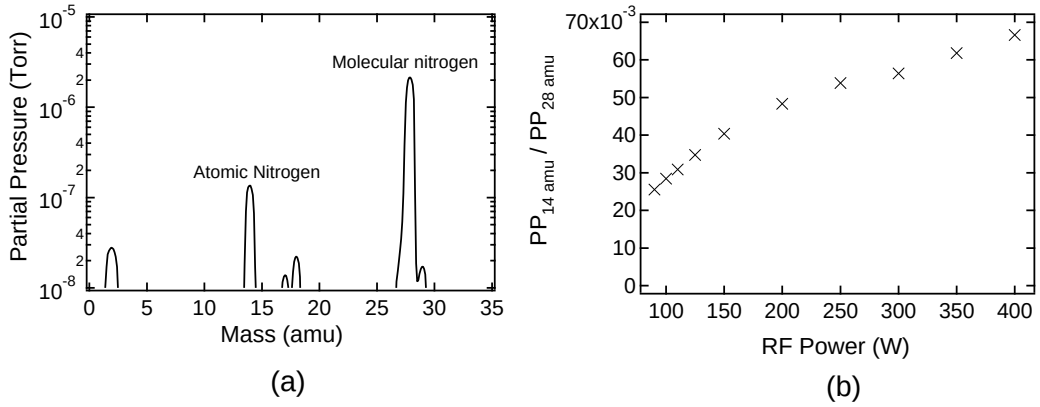

Figure 2.20 (a) Line-of-sight mass spectrum measured from an HD-25 nitrogen RF-ICP operating at 400 W and 1.3 sccm. (b) The ratio of the atomic and molecular nitrogen partial pressures (PP) as a function of RF power with a constant flow rate of 1.3 sccm. This ratio gives an indication of the relative amounts of atomic and molecular species emitted from the source.

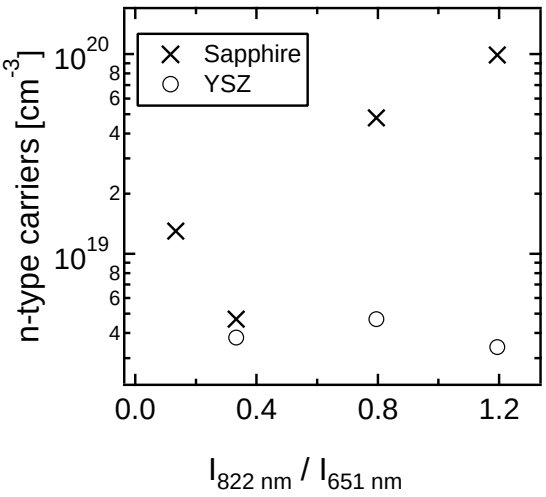

Figure 2.21 Carrier concentrations of InN films grown on (0001)Sapphire/(0001)GaN and (111)YSZ as a function of active species generated by the plasma. Emission intensity is monitored at 822 nm (atomic nitrogen) and 651 nm (1st-positive series molecular nitrogen) at various RF powers and a constant flow rate of 1.3 sccm.

figure 2.21. The contrasting results from the two substrates were surprising, as although the lattice mismatch with YSZ is smaller than it is with GaN, it is still large by epitaxial growth standards. Thus, a weaker but similar trend was expected. This prompted a closer investigation of the crystal structure of films in the two series, as polarity is known to significantly influence surface reactions. It was suspected that a similar effect may have been observed here for InN, as the two sets of films appear to respond differently to different active species. Muto *et* al. have shown that KOH etching can be used to distinguish between N-polar and In-polar InN films [85]. A similar approach was used here with InN films being etched for 2 hrs in a 10 mol/L KOH solution. SEM micrographs were taken before and after etching as shown in figure 2.22. The formation of pyramids is clearly visible on the films grown on sapphire/GaN, which is indicative of N-polar films. Alternatively, for films grown on (111) YSZ, the etching profile is much smoother and although there appears to be some change in morphology there is an absence of pyramids, indicating an In-polar film. Thus films grown on sapphire/GaN are revealed to be N-polar, and films grown on (111) YSZ are found to be In-polar. The film polarity appears to have a significant influence on how a layer responds to different active nitrogen species.

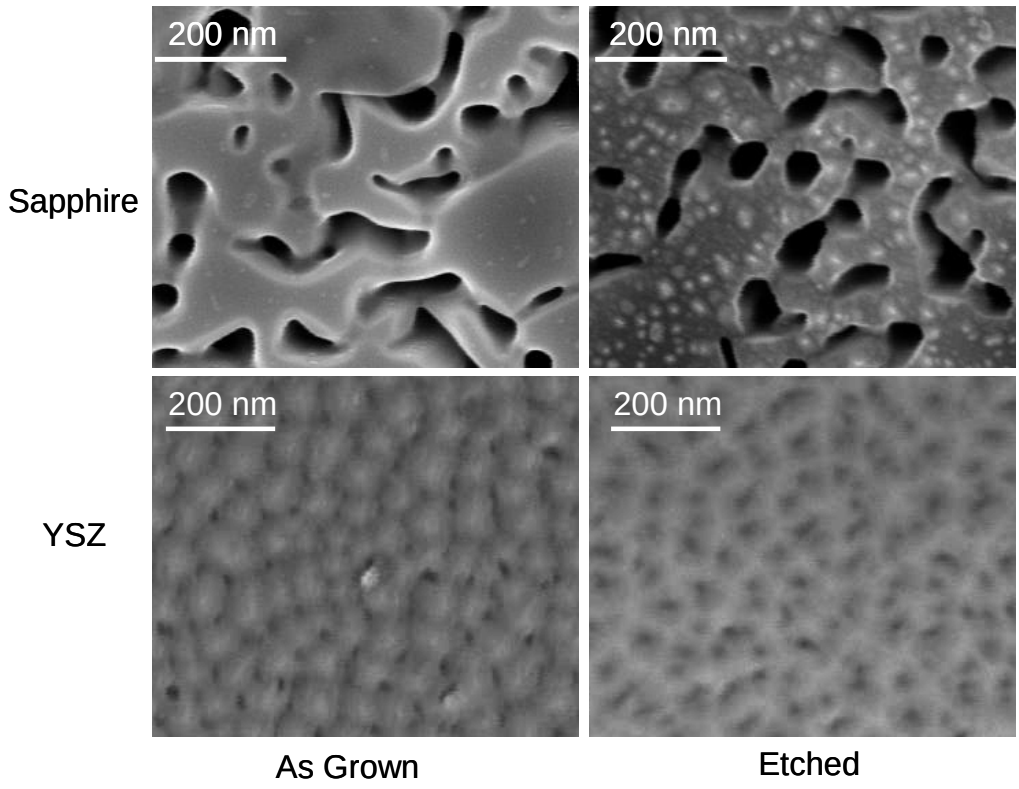

Figure 2.22 SEM images of InN films grown on GaN/sapphire and YSZ before and after etching in 10 mol/L KOH for 2 hrs.

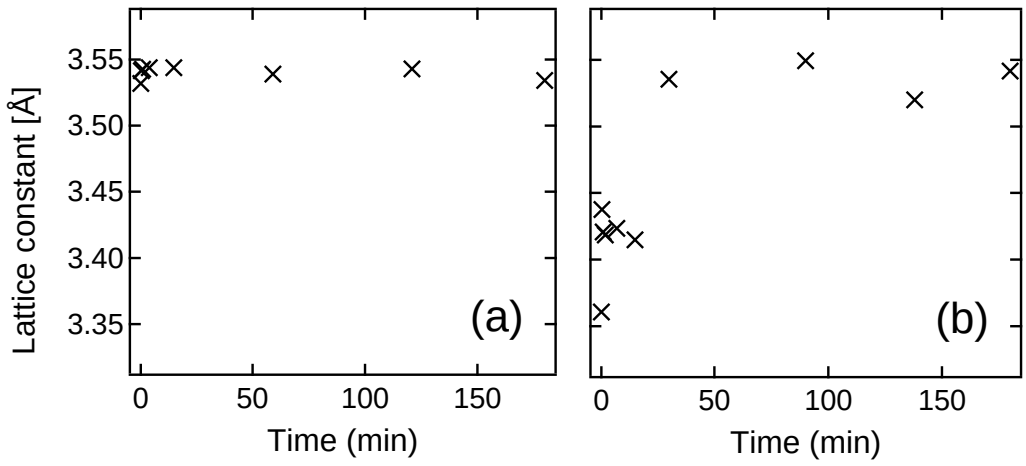

Figure 2.23 InN a-plane lattice constant during InN growth on (0001) GaN/Sapphire with different active nitrogen species ratios: (a) low atomic nitrogen content; (b) high atomic nitrogen content.

2.7.3 Strain accommodation and active nitrogen species

Ng *et* al. have observed that indium nitride relaxes fully within the first several bilayers of growth as measured by RHEED spacing. The plasma operating conditions were not mentioned in their study [86]. We have studied the RHEED spacing throughout growth to determine how the active nitrogen species influence the strain relaxation in indium nitride. Figure 2.23(a) shows the a-plane lattice constant during growth for an indium nitride film grown on gallium nitride with an RF power of 350 W (high atomic nitrogen content). The profile in this case is typical for all films we have examined grown with RF powers of 250 and 350 W on gallium nitride. The lattice relaxes to that of bulk indium nitride within the first 30 s of growth (1 nm), in agreement with the measurements of Ng *et* al. [86].

Figure 2.23(b) shows the a-plane lattice spacing of indium nitride film grown on gallium nitride with an RF power of 150 W (low atomic nitrogen content). A similar profile is observed for films grown at an RF power of 110 W. Interestingly in this case the lattice takes far longer to relax to that of bulk indium nitride, which is not achieved until a film thickness near 50 nm is reached. There is also evidence that the relaxation takes place in discreet steps after ∼30 s and ∼20 min. Measurements of the a-plane lattice constant on YSZ revealed that the lattice seemed to relax immediately

at all RF powers, but the much lower mismatch and noise in the measurement make interpretation difficult. This observation reinforces the significant influence that active nitrogen species has on N-polar InN growth. The films which relax gradually as growth progresses are found to have superior electrical properties. It has been proposed by Ptak *et* al. that the higher quality of films achieved with excited molecular nitrogen compared with atomic nitrogen can be explained in terms of the preference of atomic nitrogen to form N_2 [78]. As the bond energy in N_2 is large atomic nitrogen is thought to "scavenge" nitrogen from the growing crystal at the expense of the crystallinity of the growing semiconductor. This process is postulated to relate in an increased level of point defects.

2.8 OPTIMISATION OF INDIUM NITRIDE

When it comes to choosing a recipe for optimised InN growth, it is important to determine which parameters are most desired in an optimised film. The influence that the relative In:N ratio, growth temperature, active nitrogen species and substrate have on the structural and electrical properties of InN have been discussed. Of the parameters considered, a high content of active molecular nitrogen is clearly preferable. The GaN buffer atop a sapphire substrate is also found to be the most desirable template. The choice of In:N flux ratio is less simple. Although there is motivation for growing in the In-rich regime where indium metal accumulates on the surface (improved electrical properties of figure 2.14), this regime was also found to be highly non-uniform across 2 cm substrates. It was found that by growing just on the N-rich side of this regime with the high molecular content active nitrogen flux, (see figure 2.10), a combination of improved electrical characteristics and uniformity over the substrate could be maintained. The substrate temperature is the other parameter which has been found to have mixed effects on film properties. Figure 2.24 summarises structural and electrical properties of optimised InN layers grown at 450°C and 550°C. Growing at high temperature (550°C) has been found to lead to superior electrical properties, but also to rough films which lack uniformity across the substrate. On the other hand, lower growth temperatures lead to smooth surfaces with streaky RHEED patterns, and uniformity over the

entire substrate. However, electrical properties at the lower temperature are typically inferior.

2.8.1 Low temperature InN buffer layers

Given the contrasting attributes of the InN films grown at varying growth temperatures, a logical step may seem to be the use of a low temperature layer as a buffer layer for a high temperature film. This approach is commonly used for GaN and has been studied by Dimikas *et* al. for InN growth [63]. The motivation for a low temperature buffer layer is that the film may take the morphology of the low temperature layer, while achieving the electrical characteristics of a high temperature layer. Two InN films were grown on sapphire with a GaN buffer and a low temperature (300°C) 30 nm InN buffer layer to test this hypothesis. The high temperature InN layers were grown at 500 and 550°C, respectively. The film grown at 500°C was found to be flat and continuous in agreement with the work of Dimikas *et* al. The resulting InN layer grown at 550°C was found to have the coalesced island morphology. However, the coalescence was clearly further advanced than the corresponding film without the low temperature InN buffer. The result suggests that it is difficult to maintain the fully coalesced flat morphology at high temperatures. Above 500°C decomposition of InN becomes significant and this is likely playing a role in the promotion of the islanded growth mode. Lu *et* al. have reported that growing above the dissociation temperature results in a roughening of InN surfaces as films become thick, which is supportive of this hypothesis [81]. Dimikas *et* al. did not investigate high temperature InN layers above 500°C, likely due to the fact they were growing on Ga-polar templates, and In-polar growth is not believed to be sustainable in that region [61].

2.8.2 InN grown on Ga-polar MOCVD grown templates

As determined by etching experiments (see figure 2.22) all InN films grown directly on sapphire and on GaN buffer layers have been confirmed to be N-polar. It is generally accepted that when using a GaN buffer layer for growth, the polarity of the resulting InN layer is determined by the polarity of the underlying GaN layer. For instance, Ga-

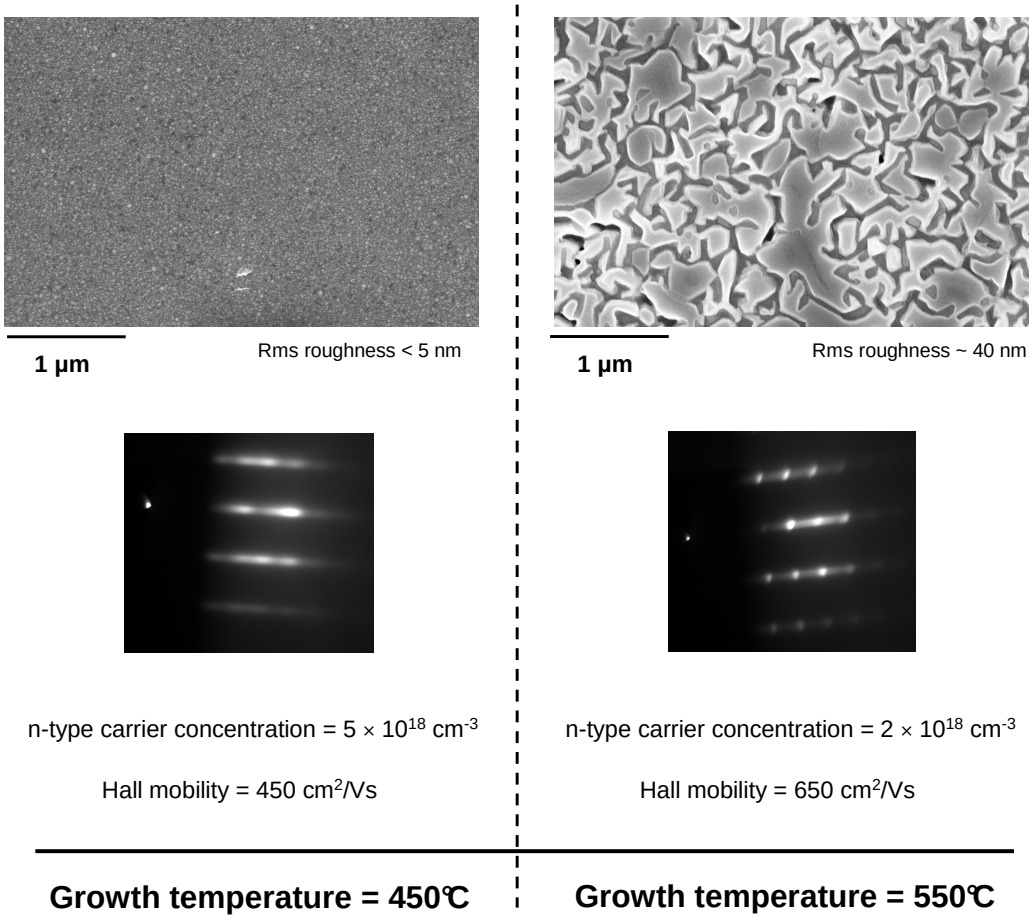

Figure 2.24 The contrasting electrical and structural properties of InN film grown at 450 and 550°C, respectively. The AFM image (top), RHEED pattern along the $(\overline{1}\overline{1}20)$ azimuth (centre), and Hall effect results (bottom) are shown. Both films were grown with In flux of 1.8×10^{14} atoms.cm^{-2}s^{-1}, RF power = 150 W, N flow rate = 1.3 sccm and a 150 nm GaN buffer layer.

polar GaN leads to In-polar InN, while N-polar GaN leads to N-polar InN. Additionally MOCVD grown GaN is typically structurally superior to layers that are currently produced by MBE at the University of Canterbury. In order to determine if the polarity and structural quality of the GaN layer was significantly influencing growth dynamics of the InN, an InN film was grown on MOCVD Ga-polar GaN and the morphology and electrical properties examined. Plasma operating conditions for the film were 150 W and 1.3 sccm, and indium flux was 1.8×10^{14} atoms.cm^{-2}s^{-1} (slightly N-rich conditions). The film was grown at 450°C. The morphology of the film as measured by SEM was found to be very similar to that of the corresponding film grown on an N-polar MBE grown GaN layer, with an rms roughness <5 nm. The electrical characteristics were also very similar, with the In-polar InN having a carrier concentration and mobility of 6×10^{18} cm^{-3} and 420 cm^2/Vs, respectively, while the comparable N-polar film exhibited Hall effect results of 5×10^{18} cm^{-3} and 450 cm^2/Vs, respectively. These results show that at least for the lower temperature of 450°C, the film polarity and GaN quality was not greatly influencing growth. However, as mentioned earlier, the polarity has been shown to influence the maximum attainable growth temperature. This effect was not investigated during this work but clearly it may prevent the growth of indium polar InN layers at elevated temperatures where electrical characteristics improve.

2.8.3 Optimised recipe and comparison with literature

The optimised recipe for N-polar InN growth on a sapphire substrate with GaN buffer is shown in figure 2.25. This process produces an InN film $\sim$ 600 nm thick with carrier concentration of 2×10^{18} cm^{-3} and Hall mobility of 650 cm^2/Vs. The morphology is that of coalesced islands. If a flatter, more homogenous, film is desired then the growth temperature of the final step can be lowered to 470°C, which results in significant improvement in the film smoothness (rms roughness less than 5 nm compared to $\sim$ 30 nm) and also improved homogeneity over the wafer.

It is well known that growing thicker InN films leads to improved electrical properties. Lu *et* al. have grown InN films up to 7.5 μm thick by MBE. This resulted in a Hall mobility of 2100 cm^2/Vs and n-type carrier concentration of 3×10^{17} cm^{-3},

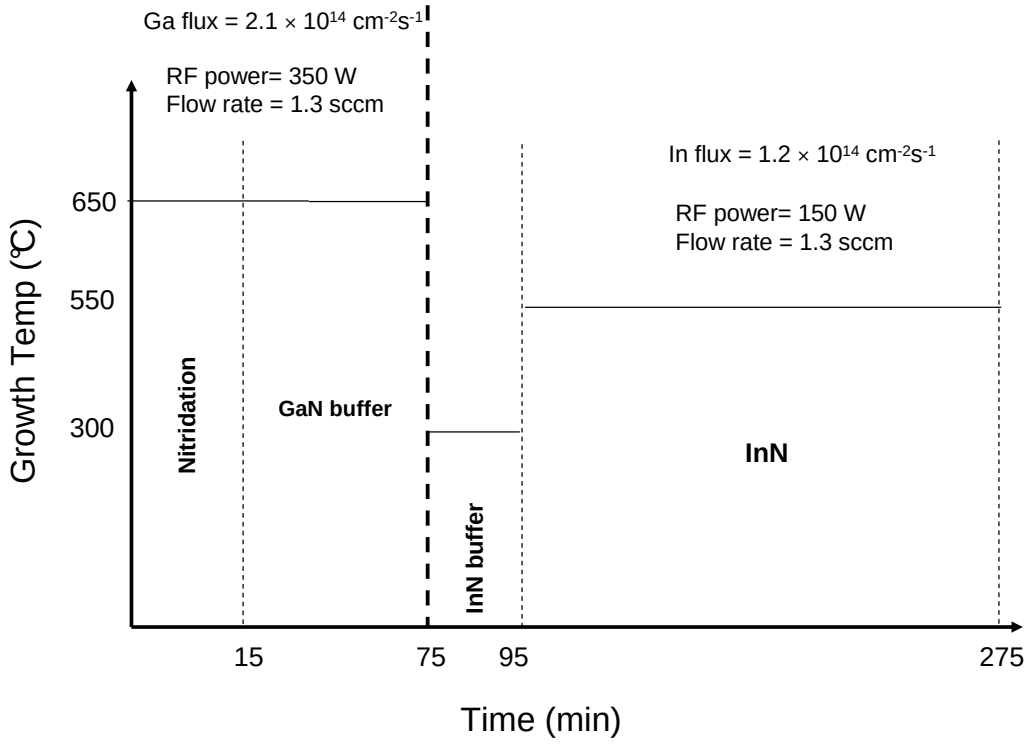

Figure 2.25 The optimised recipe developed to grow InN on sapphire substrates with a GaN buffer layer by molecular beam epitaxy. RF power and flow rate refer to the plasma operating condition for the different processes.

the record electrical properties reported to date. The single layer carrier concentration and Hall mobility are often used as a yardstick to compare the quality of InN films. Other groups to achieve high quality InN layers by this standard include: Dimikas *et* al. [63] (who significantly use the same RF-ICP as Canterbury), with n-type carriers of 1.6×10^{19} cm^{-3} and Hall mobility of 860 cm^2/Vs by MBE; Saito *et* al. produced InN directly on nitrided sapphire with n-type carriers as low as 1×10^{19} cm^{-3} and Hall mobility of 830 cm^2/Vs by MBE [87]; and Yoon *et* al. who grew InN on AlN buffers by MBE to achieve carrier concentrations of 5×10^{18} cm^{-3} and Hall mobility of 482 cm^2/Vs. There are are also a number of other groups producing InN with Hall mobility near 1000 cm^2/Vs and carrier concentrations below 10^{19} cm^{-3}. A good recent summary is given by Butcher *et* al. [20]. Most of these groups grow by MBE but progress has recently been made with MOCVD: for example see the review of Butcher *et* al. and references therein [20].

It is important to take the thickness of films into account when comparing electrical data between groups. With this accounted for, the n-type carrier concentration of 2×10^{18} cm^{-3} achieved in this thesis compares very well for a 500 nm thick film, among the lowest reported for such a thickness. The Hall mobility of 650 cm^2/Vs is not as impressive however, being towards the middle of the group for mobilities reported from optimisation studies for films 500 nm thick. Typically, a low mobility for a given carrier concentration is attributed to carrier compensation. The background chamber pressure achieved in this work was below 10^{-10} Torr, making the possibility of contamination low. However, a higher concentration of native defects remains a possible source of compensation. Many different plasma sources are used to generate active nitrogen for InN research. Section 2.7 showed that different nitrogen species could have a significant effect on the resulting film properties. The varying species produced by different sources is a possible explanation for the apparent varying levels of compensation reported among research groups.

Chapter 3

THE ELECTRONIC BANDGAP OF INDIUM NITRIDE

3.1 BAND STRUCTURE OF INDIUM NITRIDE

As discussed in section 1.3, the optical band gap of InN has been the subject of much debate over recent years. The bandgap of a material, however, represents only one aspect of its wider band structure, namely, the smallest separation between the valence band maximum and conduction band minimum. Like most other III-V semiconductors, InN is believed to have a direct band gap. A direct gap semiconductor has no separation in momentum space between the valence band maximum and conduction band minimum. This attribute means that electrons and holes can recombine across the bandgap minimum without the need for phonons to participate in the process. This makes direct gap materials efficient emitters of light.

Theoretical techniques can predict the shape of the band structure of many materials very effectively. Density functional theory (DFT) in combination with the local density approximation (LDA) is commonly used in modern band structure calculations [88, 89]. Although the LDA is effective at predicting the shape of electronic bands, the offset between the valence and conduction bands is often underestimated. A correction factor is typically applied to compensate for this error. Various LDA based methods have been applied to InN to show that the material has a bandgap near either 0.7 eV [90, 91] and 1.9 eV [92] (depending on the method used). The ionic nature of InN bonds has been cited as a source of the complication, as accurate simulations generally require the consideration of a high number of electron interactions in ionic materials [90]. Bechstedt *et* al. have used a corrected DFT-LDA technique to calculate the band

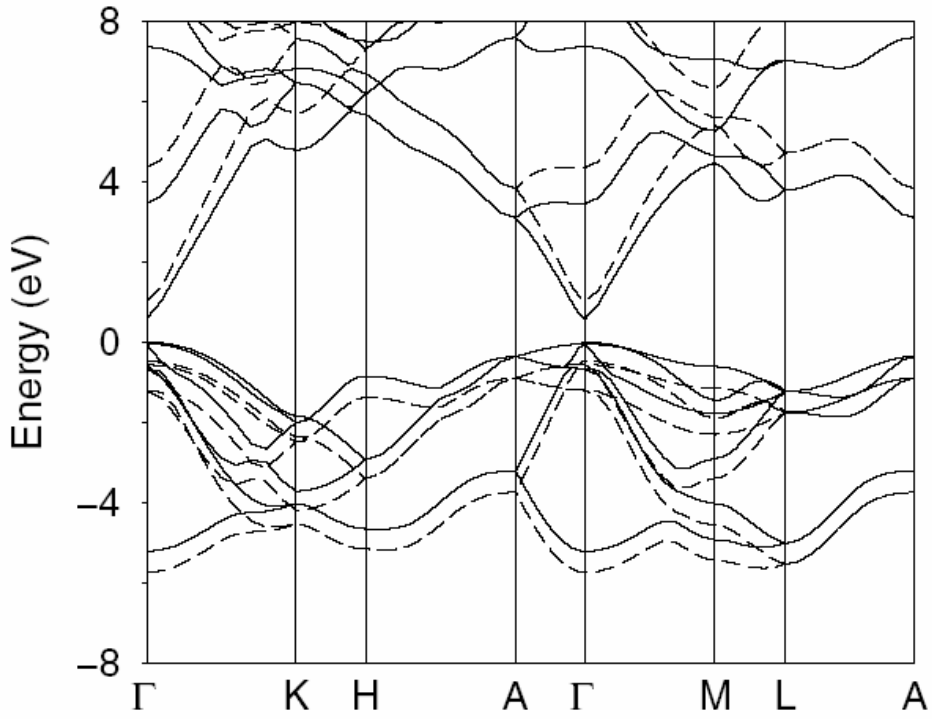

Figure 3.1 Energy band structure of wurtzite InN. Solid lines: DFT-LDA, dashed lines: including quasiparticle corrections. [Bechstedt *et* al. Phys. Stat. Sol. (a), 195 (2003) 628]

structure around the 1st Brillouin zone as shown in figure 3.1 [93]. The solid curve shows the DFT-LDA result while the dashed curve includes a quasiparticle correction. The main effect of the correction is to shift the relative offset between valence and conduction band and not to alter the location of features in momentum space. For this reason we can have confidence that InN is indeed a direct gap semiconductor, and that the features described by figure 3.1 do, for the most part, represent the band structure of InN in momentum space.

Although much progress has been made in simulating the band structure of InN, there has also been a considerable effort made to determine the bandgap of the material through experimental means. Much of the InN bandgap debate has centred on interpreting varying experimental results. This chapter also focuses primarily on the experimental determination of a bandgap. The following section outlines the key techniques used.

3.2 DETERMINING THE BANDGAP OF A SEMICONDUCTOR

3.2.1 Optical absorption

Historically, the most widely used technique to determine the bandgap of a semiconductor has been optical absorption. The technique relies on the fact that a photon will travel through a material unabsorbed as long as there are no available electronic transitions of the same energy as the photon. If there are available transitions for an electron, then there is a finite probability that the photon will be absorbed and the electron excited. Therefore, by measuring the absorption of different wavelength photons transmitted through a slab of the material, an understanding of the possible electronic transitions within the material can be gained. If we apply this theory to a semiconductor, photons with less energy than the band gap of the semiconductor will be transmitted, while photons with an energy greater than the bandgap may be absorbed according to:

$$P_{abs}(E) = 1 - e^{-\alpha(E)x} \tag{3.1}$$

where $P_{abs}(E)$ is the probability the photon of energy E will be absorbed, $\alpha(E)$ is the absorption coefficient, and x is the path length of the photons within the slab. The absorption coefficient for photons of above bandgap energy in a semiconductor with parabolic bands is described by:

$$\alpha(E) = A(E - E_g)^{1/2} \tag{3.2}$$

where E is the energy of the photons, E_g is the bandgap of the material and A is a constant related to the effective mass of carriers in the material [94]. Although recent studies have produced evidence that the conduction band of InN is indeed a perturbed parabola, the perturbation does not significantly distort this model [24]. From this

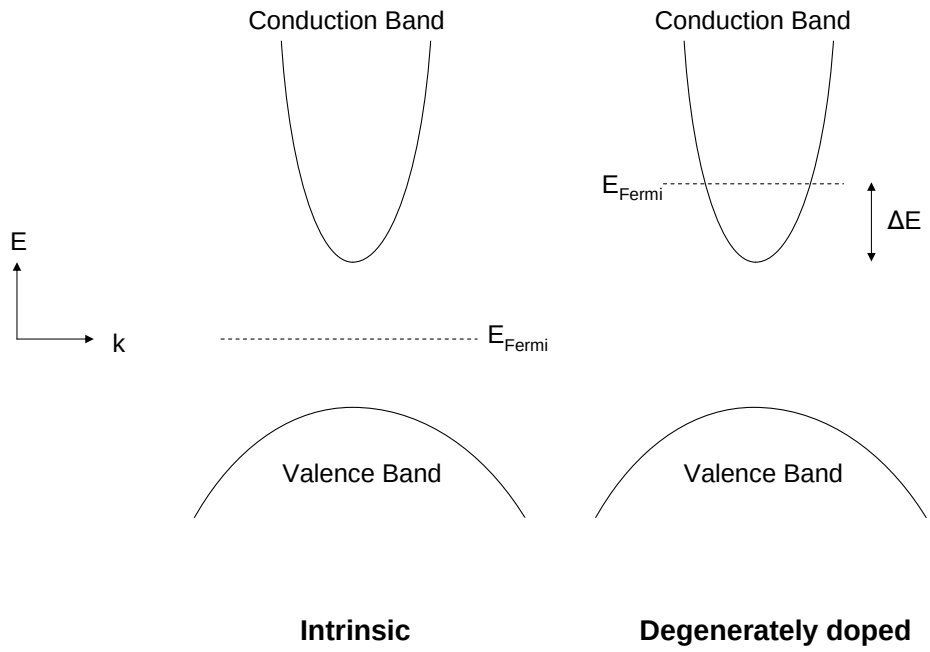

Figure 3.2 The energy band diagram shows how the location of the Fermi level in a degenerately doped direct gap semiconductor can increase the apparent bandgap measured by optical absorption. E_{Fermi} is the Fermi Energy, and ΔE is the Burstein-Moss shift.

expression we see that the square of the absorption coefficient is linear with E, and the intercept with the energy axis of an $\alpha^2(E)$ vs E plot marks the bandgap of the material in question. This is the procedure used to commonly determine the bandgap of a semiconductor via optical absorption.

Equation 3.2 holds true for non-degenerate semiconductors but under the degenerate condition the analysis is not as simple. Figure 3.2 shows the energy band diagram of a direct gap semiconductor under two different doping conditions. The intrinsic case represents no doping and the Fermi energy lies essentially at mid gap. The degenerate case represents heavy n-type doping where the Fermi energy is pushed into the conduction band. This causes most states below the Fermi energy to become occupied. For an electron to then be optically excited from the valence band, the photon needs energy $E_g + \Delta E$ where ΔE is known as the Burstein-Moss shift and is labeled in figure 3.2. As even the highest quality InN thin films currently produced are believed to be degenerately n-type, the Burstein-Moss shift normally needs to be accounted for when examining the bandgap through absorption. Whereas the non-parabolic nature of the

conduction band can be ignored in equation 3.2, it becomes more significant when calculating the Burstein-Moss shift. This will be discussed further in section 3.6.2 where modeling of the conduction band is explored.

3.2.2 Photoluminescence

The other technique commonly used to interrogate the bandgap of materials is luminescence. Luminescence can occur when a non-equilibrium carrier distribution is created within a material. This chapter discusses only photoluminescence (PL), which generates the luminescence via an above bandgap optical pump (in this case a laser). Electrons and holes created by the pump recombine through either non-radiative or radiative recombination. If the semiconductor has a direct gap and is of sufficiently high crystal quality, there will be substantial radiative recombination. Emitted photons can then be collected and analysed. There are a number of different transitions that can lead to luminescence; in general the rate a particular transition will proceed (R_{UL}), is governed by:

$$R_{UL} = N_u \cdot N_l \cdot P_{ul} \tag{3.3}$$

where N_l and N_u is the density of carriers in the upper and lower energy levels, respectively, and P_{ul} is the transition probability. Unlike absorption, PL signals do not always shift substantially to higher energy if the material is degenerately doped. Although a Burstein-Moss shift can influence the line shape of PL emission, recombination often takes place at localised states within band tails [95]. Figure 3.3 shows a typical density of states profile for an imperfect semiconductor. The presence of defects near the band edges causes the density of states to tail exponentially into the forbidden gap in what is known as an Urbach tail [96]. Although the density of carriers in these states is low compared to deeper in either band, the localised nature of carriers in the tail states can lead to a high transition probability. If this outweighs the influence of the low carrier density, luminescence will be dominated by recombination from the Urbach tails. This

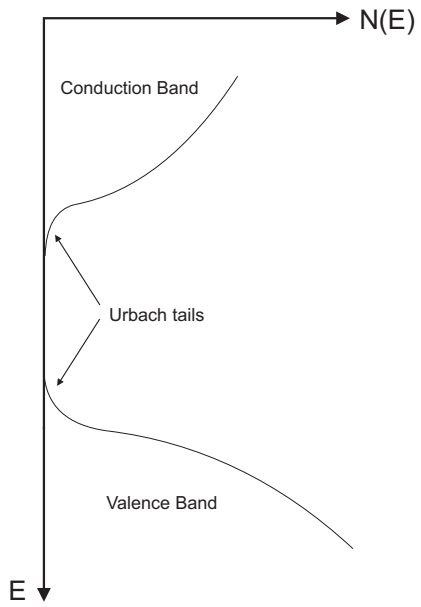

Figure 3.3 Energy (E) vs density of states (N(E)) diagram for a typical defective semiconductor in which shallow donors and acceptors lead to a broadening of the band edges (Urbach tails).

effect can lead to PL underestimating the bandgap of a material.

Just as a low density of states within a band tail sometimes leads to high transition probabilities, so too can low density deep levels. GaN is well known for the "yellow band" luminescence which, in low quality material, can be orders of magnitude brighter than the band edge PL. The origins of the yellow luminescence in GaN are still debated, and many different transitions have been suggested which could account for the signal [97, 98, 99]. A common explanation for the phenomenon involves donor-acceptor pairs (DAP). A donor-acceptor complex occurs when a donor and an accepter are located spatially close to each other. As donor and acceptor lattice sites are charged, they cause some carrier localisation. The resulting localisation of electrons and holes leads to increased transition probability for the donor-acceptor pair. As there are many different donors, acceptors and complexes that can commonly occur in a semiconductor, predicting whether a particular deep level will dominate PL is not trivial. The deep level argument has been at the centre of much of the InN bandgap debate.

3.2.3 Temperature dependence of photoluminescence

Studying the temperature dependence of PL signals can yield information about the origins of the transitions causing the luminescence. Band edge luminescence usually red shifts and loses intensity with increasing temperature. As a lattice expands when heated, this causes a narrowing of the reciprocal lattice, and hence widening of the bandgap (from the dispersion relation). An empirical relationship known as Varshni's equation [100, 101] is commonly used to describe the temperature dependence of semiconductor bandgaps as:

$$E_g = E_0 - \frac{\alpha T^2}{T + \beta} \tag{3.4}$$

where E_0 is the gap at absolute zero, and α and β are constants. While the location of PL resulting from traps is less easy to predict, the intensity as a function of temperature usually reveals a characteristic activation energy. As carriers thermalise according to Fermi-Dirac statistics [102], the PL intensity related to such a state decays exponentially as described by:

$$\frac{I(T)}{I_0} = \frac{1}{1 + Ae^{(-E_a/kT)}} \tag{3.5}$$

where $I(T)$ and I_0 are the PL intensity as a function of temperature and the 0 K PL intensity, respectively, A is a constant relating radiative and non-radiative lifetimes, E_a is the activation energy of the trap, k is the Boltzmann constant and T is the temperature.

3.2.4 Photoconductivity

The other technique considered in detail in this chapter is photoconductivity. Photoconductivity relies on measuring how the conductivity of a sample changes when it is illuminated with photons of varying energy. When a photon is absorbed and an

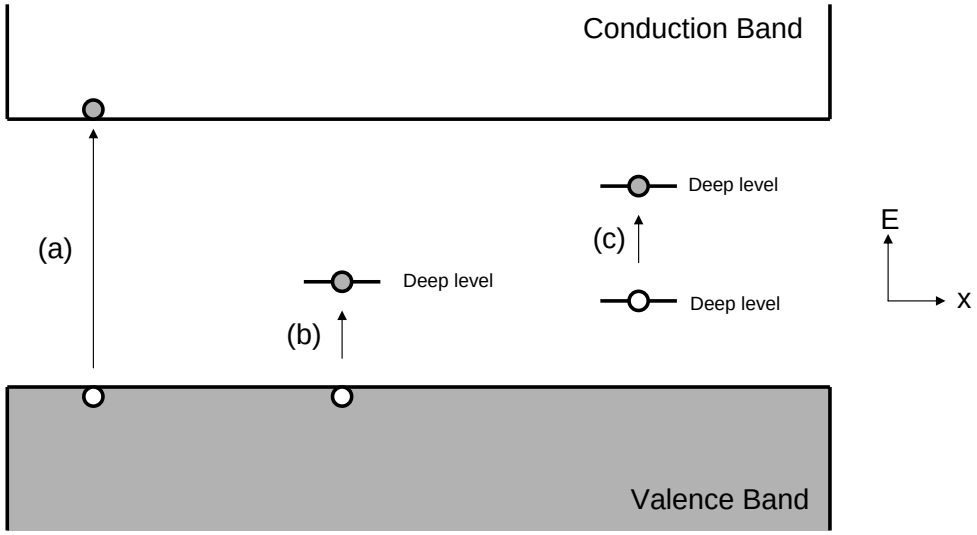

Figure 3.4 The band diagram depicts three different absorption processes which have different effects on the conductivity of a sample: (a) Valence band–conduction band; (b) Valence band–deep level; (c) Deep level–deep level.

electron excited into a higher energy state, the electron may be able to take part in conduction. Whether the excited electron is electrically active or not depends on the nature of the initial and final states. If either the valence or conduction band is involved in the transition, then there will be some additional contribution to the conductivity of the material. If both the initial and final states are deep levels then any contribution to conductivity is unlikely, with hopping conduction providing the only possible conduction mechanism. Figure 3.4 shows a band diagram with three possible transitions which have different effects on the conductivity of the absorbing material. Transition (a) shows a valence band edge to conduction band edge transition that generates both an electron and hole which are free to take part in conduction. Transition (b) shows a valence band to deep level transition which contributes only a free hole. Transition (c) shows a deep level to deep level transition which contributes no free carriers. Clearly the three effects will each make a different contribution to the conductivity of the material. The additional conductivity of a unipolar change in free carriers has on conductivity, according to Drude theory [103], is given by:

$$\Delta\sigma = \Delta n \cdot \mu . q \tag{3.6}$$

where $\Delta\sigma$ is the change in conductivity, Δn is the change in density of the carrier, μ is the mobility of the carrier and q is the charge of the carrier. If it is assumed that all impinging light is absorbed and that the absorption is dominated by a single transition then Δn can be calculated. q is simply the charge of an electron and $\Delta\sigma$ is measured so the mobility of the additional carriers can then be implied. Another approach to distinguish between different contributions in a PC experiment is to measure the temperature dependence of the PC. This approach is particularly useful for identifying shallow traps. As a sample is heated, the amount of thermal energy available to electrons increases from 0 meV at 0 K to ∼26 meV at 300 K; this additional thermal energy allows shallow traps to thermalise. Consequently, any carrier excited into shallow traps will contribute additional conduction at high temperatures.

3.3 EXPERIMENTAL DETAILS

Absorption measurements were performed at Industrial Research Ltd, Lower Hutt, New Zealand using a custom built system incorporating a tungsten lamp and lead sulphide detector. All of the photoluminescence and photoconductivity measurements in this chapter have been performed in the Department of Physics and Astronomy at the University of Canterbury.

Figure 3.5 shows the general experimental setup used during PL. An argon laser operating at 488 nm and a spot diameter of ∼0.5 mm was used as the optical pump. Either an indium antimonide, lead sulphide or germanium detector was used to detect the luminescence. The choice of detector is very significant for InN studies. Although germanium is by far the most sensitive detector below 1 eV, its sensitivity falls off quickly around 0.7 eV. This is the area of interest for most InN luminescence signals and consequently the germanium detector often distorts results. Although lead sulphide and indium antimonide detectors have a relatively flat response below 0.5 eV,

the sensitivity of the materials is between 3 and 5 orders of magnitude lower than that of the peak germanium sensitivity in the infrared. The luminescence was focused using quartz lenses into the spectrometer and filtered with a Newport 515 filter to remove any residual laser content. Sample temperature was varied using an Oxford Instruments MicrostatHe helium flow cryostat between 4 and 300 K during PL measurements. Samples were mounted using silver paste onto the cryostat cold finger, which provided good thermal contact between the cold finger and sample. The laser was chopped at ∼10 Hz to generate an AC pump and a lock-in amplifier was then used to detect the AC luminescence signal. This arrangement allowed background noise to be largely removed. The PL was detected in a backscattering geometry using a SPEX minimate spectrometer with a grating blazed at 2400 nm. The entry/exit slit width configuration of the aperture was 300/500 μm, which resulted in a spectral resolution of ∼2 nm. For a thorough description of the experimental techniques employed here see the work of Lyndon Williams [104].

A diagram of the typical photoconductivity experimental setup is shown in figure 3.6. The excitation source for the PC experiment was an Oriel 1000W FEL 6315 quartz tungsten halogen (QTH) lamp. The QTH lamp has significant spectral content from 0.5-4 eV. The lamp emission was passed into a Spex 500M spectrometer with a 600 line grating blazed at 1250 nm. The configuration allowed the light to be dispersed with a resolution of ∼3 nm. The dispersed light was then focused through quartz lenses into an optical chopper of adjustable frequency. As with the photoluminescence setup, the chopping of the excitation source accompanied by a lock-in amplifier allows the signal to be more easily extracted from background noise. However, more care must be taken when using this approach for photoconductivity as it is common for some conduction processes to persist long after the excitation has ended. For example optical excitation of GaN has been shown to lead to enhanced conductivity many hours after the illumination has been stopped [105]. For this reason different chopping frequencies have been explored in the range of 1-1000 Hz.

Electrical contact was made to the InN layer via silver contacts. A 4 point contact system was used as shown in figure 3.6. Using separate pairs of contacts for the voltage

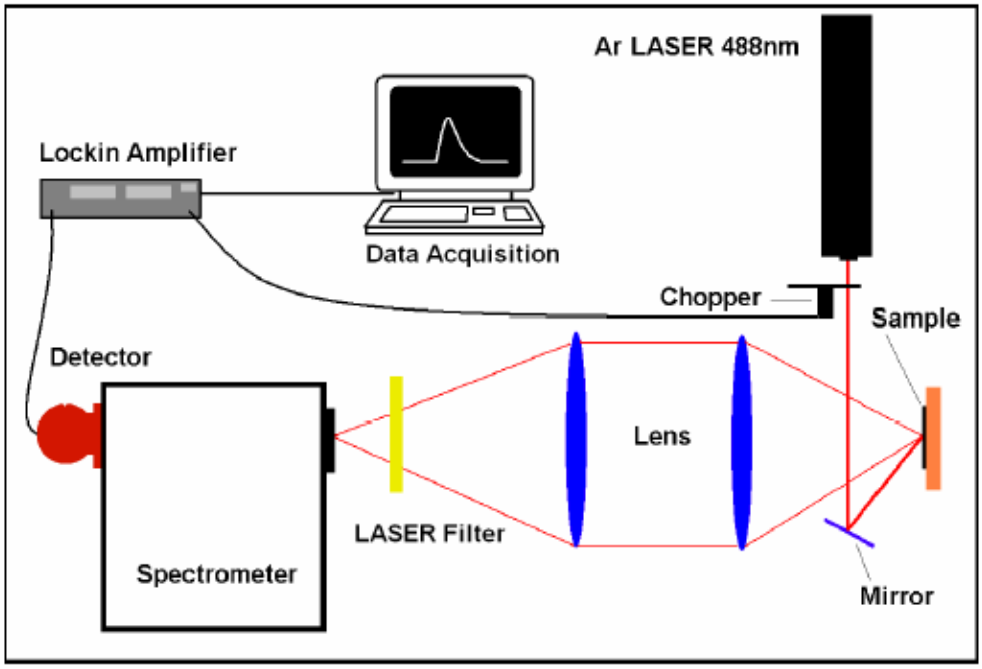

Figure 3.5 The experimental setup used to measure photoluminescence from InN films.

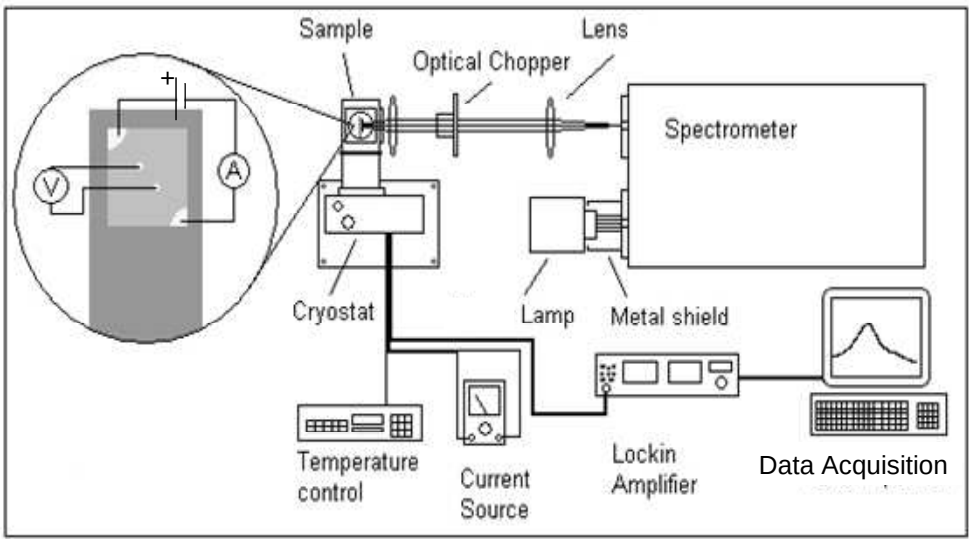

Figure 3.6 The experimental setup used to measure photoconductivity from InN films.

measurement and current supply was found to lead to better noise performance. For temperature dependent measurements an Oxford Applied Research closed cycle He cryostat was used. As with photoluminescence the samples were mounted on the cold finger using silver paste. An important point to note is that the spectral power from the quartz tungsten lamp is not flat. As such a varying PC signal may be expected due simply to the difference in spectral power at different wavelengths. Also, the spectrometer response disperses different wavelengths with varying efficiencies. When these two responses are convolved they can distort a PC spectrum. Attempts have been made to measure the spectral response of the lamp/spectrometer system but the measurement has not yet been sufficiently accurate to apply as a correction. The presence of this distortion must be noted when reviewing results.

3.4 POLYCRYSTALLINE INDIUM NITRIDE

The originally accepted gap of 1.9 eV determined by Tansley *et* al. [14] was measured by optical absorption on polycrystalline InN, which makes the technique a logical place to begin an exploration of the current controversy. Figure 3.7 shows the original absorption coefficient squared vs energy plot used by Tansley *et* al. to determine the bandgap of InN. The InN films studied in this case were 0.1–2 μm thick polycrystalline films grown by RF sputtering on glass substrates. Typical grain sizes of the polycrystalline material were 10–30 nm, and the grains were c-axis oriented (c-axis perpendicular to the substrate surface). Surprisingly these polycrystalline layers were reported to have the lowest electron concentration (1.6×10^{16} cm^{-3}) and highest Hall mobility (2600 cm^2/Vs) ever measured from InN thin films.

Early on during the InN research programme at the University of Canterbury polycrystalline InN was deposited on a quartz substrate as an initial investigation of InN growth by MBE. The film was grown at 400°C in the N-rich regime and was ∼300 nm thick. The RHEED pattern and the corresponding SEM image from the film are shown in figure 3.8. The clear arcs visible in the RHEED image confirm that, as expected, the film is polycrystalline. The continuous nature of the arcs also indicate that there is little or no texturing of the polycrystalline grains in the growth plane. However, the

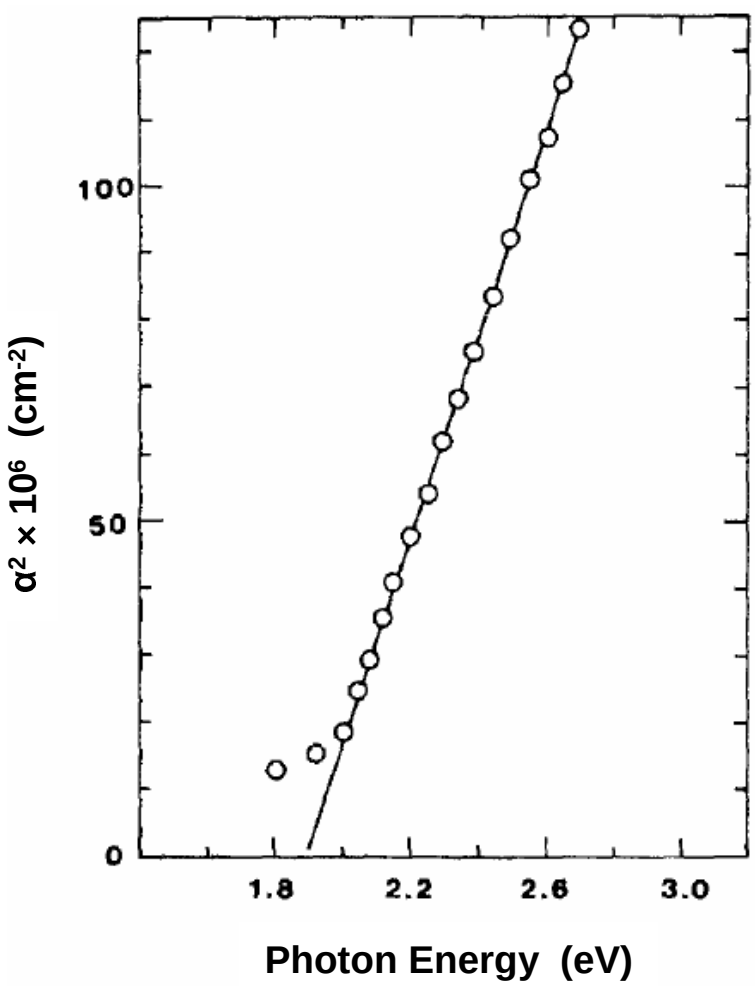

Figure 3.7 The square of the absorption coefficient as a function of photon energy for indium nitride with electron concentration 1.6×10^{16} cm^{-3}. [T. L. Tansley and C. P. Foley, J. Appl. Phys. 59 (1986) 3241]

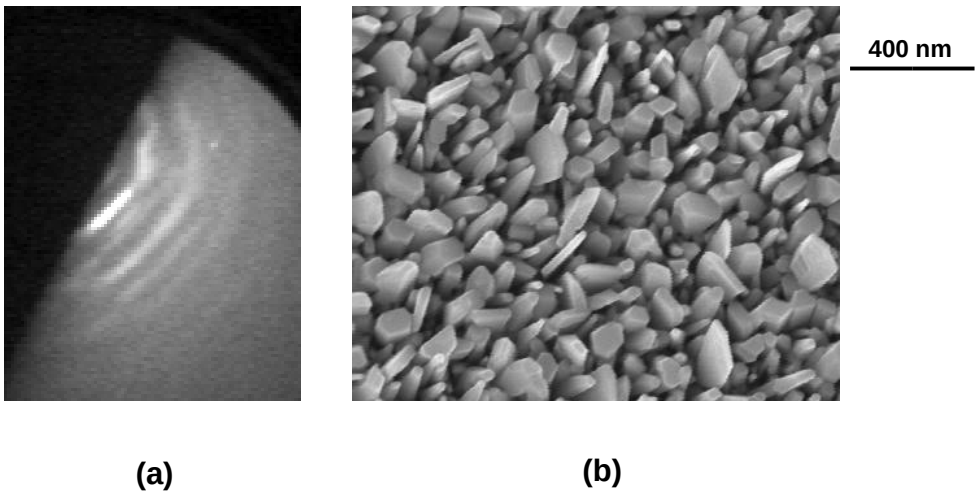

Figure 3.8 (a) RHEED pattern and (b) SEM image from a polycrystalline InN layer grown on a quartz substrate by MBE.

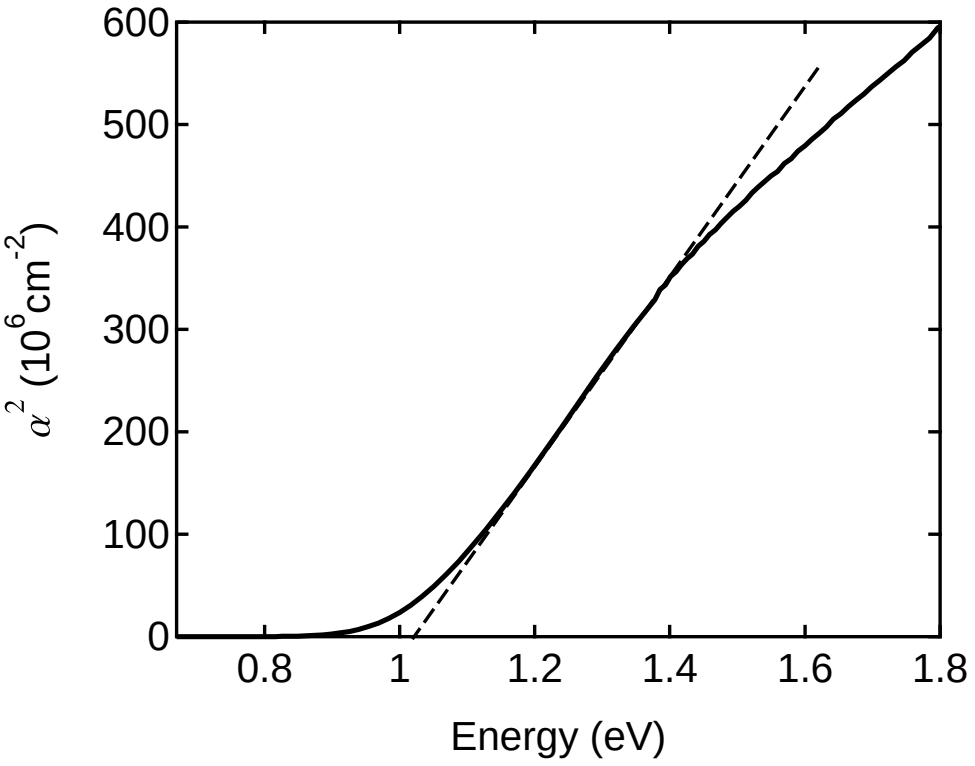

Figure 3.9 Absorption coefficient squared (solid curve) as a function of photon energy for a polycrystalline InN film grown by MBE. The dashed line extrapolates the linear segment of the curve to the energy axis intercept.

SEM image reveals clear hexagonal symmetry within many of the grains. This suggests that as was observed by Tansley *et* al. the grains are generally c-axis oriented. This is a common trait of the III-nitride semiconductors with the c-axis often being the preferred growth direction [2]. An analysis of this layer reveals a wide variety of grain diameters and shapes. Larger grains have diameters of up to ∼150 nm and are typically faceted structures. Smaller grains have diameters as small as ∼10 nm, and have high aspect ratios while exhibiting strong hexagonal symmetry. Single field Hall effect measurements on this layer revealed an n-type carrier concentration of 7×10^{19} cm^{-3} and Hall mobility of 3 cm^2/Vs. Figure 3.9 shows the absorption coefficient squared as a function of photon energy for the polycrystalline InN film grown by MBE. The linear segment of the plot is extrapolated to the energy axis revealing that the absorbing feature in this case involves an energy transition of ∼1.02 eV.

3.4.1 Quantum size effects

The contrasting plots of figures 3.7 and 3.9 are typical of the conflict between MBE grown and sputtered film properties. However, the interesting aspect of this comparison is the structural similarity between the two layers. Both are polycrystalline films with grain sizes as small as 10 nm, although the MBE grown layer also contains a significant quantity of larger grains. One of the recurring arguments used to describe the discrepancy between MBE/MOCVD and sputtered materials has been quantum size effects [20, 25]. As grain sizes approach the wavelength of free carriers in a material, energy levels become discrete and shift to higher energy. Therefore quantum confinement of carriers in the conduction band (or the valence band) could lead to an effective widening of the apparent bandgap. The quantum size effect argument has assumed the bandgap of InN is 0.7 eV, and that confinement effects shift the apparent gap to higher energy. Absorption data can be expected to be dominated by the lowest energy absorbing feature. Therefore, although the MBE polycrystalline film described in figure 3.8 contains grains as small as 10 nm, in the quantum size effect model the larger grains can be expected to absorb at 0.7 eV. This low energy absorption will mask any higher energy absorption which may occur from the smaller grains. This view has

be used to argue that the true bandgap of InN is 0.7 eV. The smaller maximum grain size of 30 nm in the material grown by Tansley *et* al. can be seen as a possible explanation of the higher absorption onset. However, no definitive correlation has been shown between grain size and absorption onset. Chemical origins and other electronic phenomenon can also be used to explain the phenomena.

A study by Lan *et* al. identified 1.9 eV luminescence from InN nanowires with diameters of 30-50 nm, while 0.7 eV luminescence was observed from larger wires with diameters of 50-100 nm [106]. The possibility of quantum confinement playing a role in this result has been suggested. The maximum nanowire diameter reported by Lan *et* al. (50 nm) is somewhat larger than that reported by Tansley *et* al. (30 nm), but both studies report optical features of comparable energy. The size and distribution in size of grains/wires should be expected to strongly influence the location and profile of optical features. As Lan *et* al. pointed out, although the small effective mass of electrons in InN does lend the material to influence by quantum size effects, this contribution does not appear to be adequate to explain a shift of over 1 eV. A simple one dimensional quantum well analysis suggests features around 5 nm in diameter would be required to achieve this.

Although absorption is dominated by low energy features, PL can be expected to have the opposite behaviour. The quantum confinement of electrons and holes typically enhances the ability of carriers to recombine radiatively. This effect is exploited in LED structures to enhance efficiency. Should quantum effects be influencing luminescence from InN films then PL should reveal the confinement; recombination in the confined regions should be enhanced and occur at a longer wavelength. Figure 3.10 shows the temperature dependent PL signal obtained from the polycrystalline MBE grown film described by figures 3.8 and 3.9. In this case the PL was measured by a germanium detector as it offers the greatest sensitivity for the weak signal strength expected from polycrystalline layers. The 0.85 eV feature with FWHM of 0.15 eV was the only signal detected. The dip in the PL near 0.92 eV is due to atmospheric water absorption. An effort was made to look for higher energy luminescence but nothing could be separated from background noise. This suggests that quantum confinement

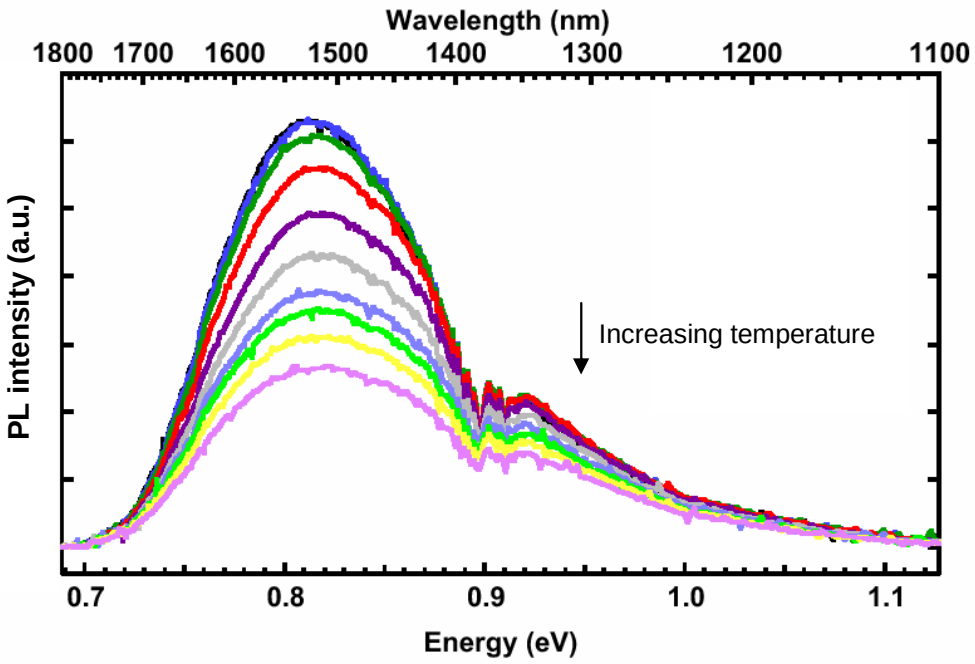

Figure 3.10 Temperature dependent PL from a polycrystalline InN film grown by MBE. The various temperature curves range from 4 K (greatest intensity) to 284 K (weakest intensity) in 30 K steps.

is not the origin of the higher energy optical features detected in the other cases. The MBE grown polycrystalline film contains a wide range of grain sizes which encompass the range of feature sizes reported by Tansley *et* al. and Lan *et* al. [47, 106]. Should quantum confinement be leading to the higher energy features then luminescence at higher energy should be detected in this sample. The temperature dependence of the luminescence in figure 3.10 shows a blue shift with increasing temperature which is not consistent with well behaved band edge transitions. However, the low energy cutoff of the germanium detector is known to distort signal shape in this region and for this reason the temperature dependence must be considered with caution.

3.5 DIAGNOSING THE 0.7 ELECTRON VOLT FEATURE

As shown in section 3.4 ostensibly similar films can exhibit drastically different optical properties. Depending on the growth method and conditions used, layers with band-like features in the range of 0.6–2 eV have been produced by different research groups. Although all films studied in this thesis are grown by the same technique, significant

variation in optical properties of films are also observed. Figure 3.11 shows PL signals measured from four different InN films grown at the University of Canterbury with the corresponding n-type carrier concentrations of the films indicated. Films (a), (c) and (d) were grown on sapphire substrates (all N-polar) and film (b) on (111) YSZ (In-polar). Films (a) and (c) have a GaN buffer layer. All films are single crystal as indicated by the presence of reciprocal lattice features in the RHEED pattern. The growth temperature, relative III:V ratio and buffer layers were altered between growth of the four films.

The PL signals portrayed here are representative of the majority of films studied by PL. All unintentionally doped InN films studied exhibited PL in the 0.5–1 eV range. Film (a) consists of a relatively sharp peak centred at 0.68 eV; there is also a weak low energy shoulder accompanying the peak. This was a common profile for N-polar films. PL from film (b) consists of a peak at 0.67 eV accompanied by a low energy shoulder at 0.61 eV, a number of In-polar films exhibited profiles similar to this. Film (c) was among the narrowest and lowest energy PL features measured, with a single PL peak with FWHM of 30 meV located at 0.63 eV. Interestingly, the FWHM of this film is similar to film (a) although the carrier concentration is 2 orders of magnitude lower. Several high carrier concentration films exhibited sharp PL features, suggesting the increasing of FWHM is not solely due to the raising of the Fermi energy into the conduction band as has been suggested in recent reports [25]. This effect has been studied theoretically in InN and proposed to result in broadening of the PL FWHM and skewing of the PL lineshape [107]. Film (d) exhibits a single feature located at 0.78 eV, with a FWHM of 180 meV. This was the broadest and highest energy PL peak observed from single crystal InN in this study (note figure 3.10 shows higher energy PL from a polycrystalline InN film).

These four films illustrate the vastly different PL peak locations and line shapes which can occur from films grown with the same system. Such variation in the luminescence location and line shape are not typically characteristic of band edge signals. Band edge luminescence from other common III:V systems usually occurs at a well defined energy and has a FWHM of only several meV. It can be argued that the nature

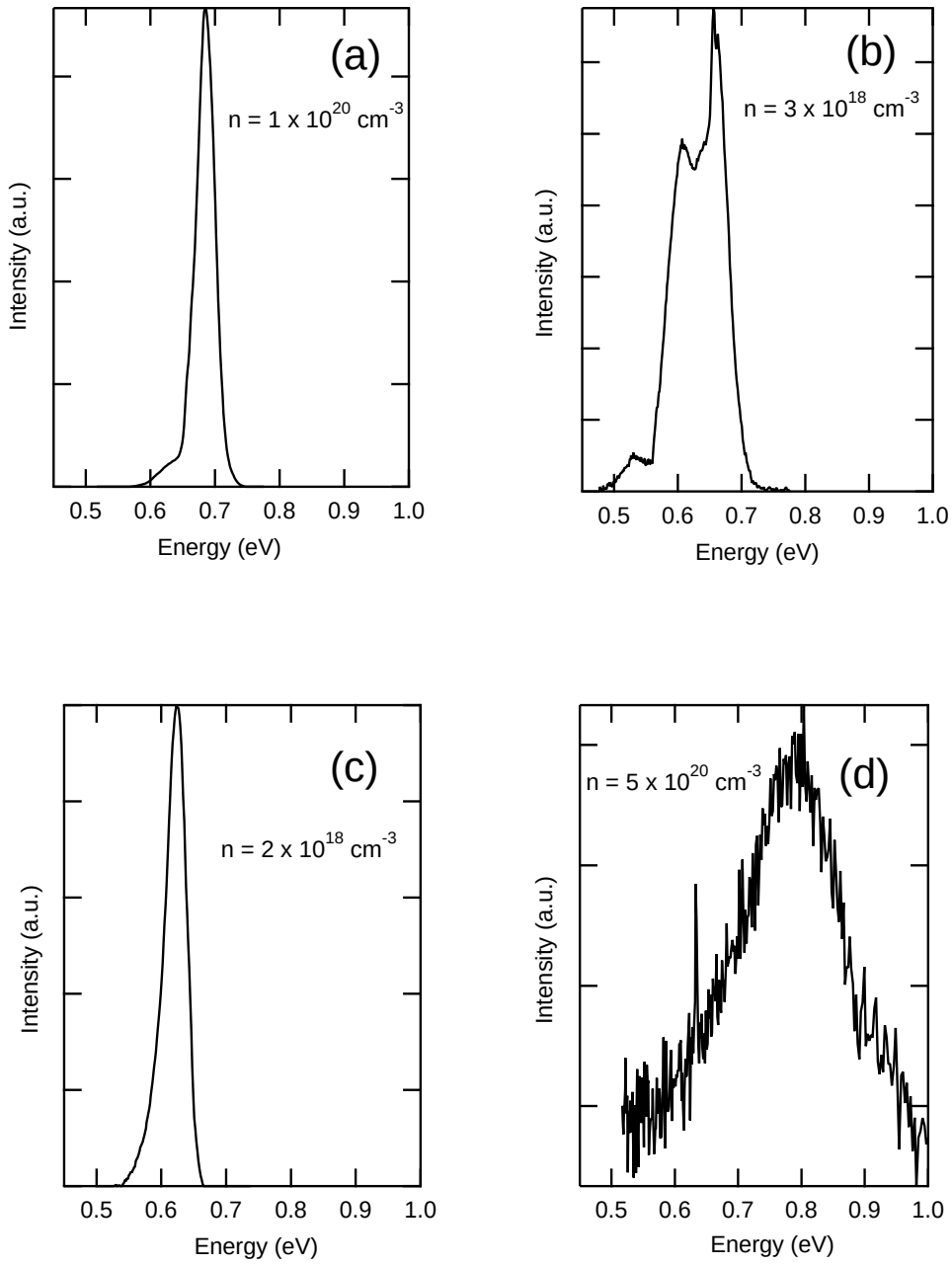

Figure 3.11 The 4 K PL signals obtained from 4 different single crystal InN thin films as measured with an InSb detector. (a) N-polar InN grown on (0001) sapphire/GaN, (b) In-polar InN grown on (111) YSZ, (c) N-polar InN grown on (0001) sapphire/GaN, (d) N-polar InN grown on (0001) sapphire.

of the low energy PL signals described by figure 3.11 is more easily paralleled with the so called "yellow band" observed in GaN PL [99]. However, multiple peak structure, such as that shown by film (b), is not common in GaN yellow band PL. Also, although yellow band PL from GaN may be several orders of magnitude brighter than the band edge signal, the band edge signal is always present. We have made considerable effort to detect PL from InN in the 1-2 eV range but nothing above background noise has been detected.

Whenever PL measurements were made, an effort was made to measure the signals with the same experimental setup. Slit widths, laser power and filters were all unchanged between runs so that meaningful comparisons could be made between the observed PL intensities. Figure 3.12 shows the peak intensity as a function of peak location for many of the InN films grown at the University of Canterbury. Despite the scatter in the data, it is clear that there is a correlation: greater intensity PL occurs at lower peak energy. If it is assumed that the observed PL is band related, it can be argued that the increase in intensity at lower energy is due to improved crystal quality and the resulting reduction in non-radiative pathways. The red shift of the PL as intensity increases may be related to a reduced level of degenerate doping which is discussed further in section 3.6.

3.5.1 Temperature dependent photoluminescence

Films (a) and (b) from figure 3.11 were studied by temperature dependent photoluminescence as shown in figure 3.13. As discussed in section 3.5.1 the temperature dependence of photoluminescence is a useful tool for determining the origins of PL signals. In general, non-radiative pathways grow to dominate recombination processes as the temperature is raised. This is the case for both film (a) and film (b) from figure 3.13 as the PL intensity is approximately an order of magnitude lower at room temperature compared to that at 4 K. The lineshape of the two curves as a function of temperature reveals contrasting behaviour. The lineshape of film (a) shows little dependence on temperature, with the peak red shifting and weakening as the temperature is raised. The profile of film (b), in contrast, alters substantially between 4 K and 290 K. This is

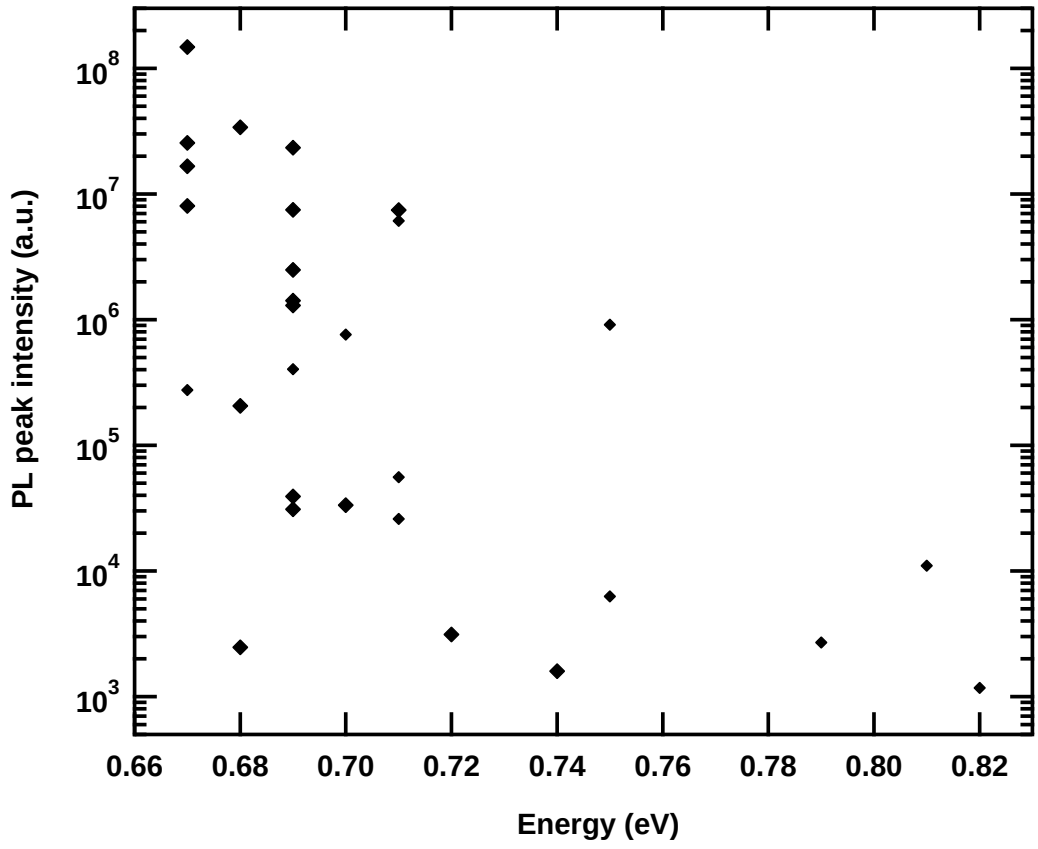

Figure 3.12 The PL intensity as a function of peak location for InN films grown at the University of Canterbury. Measurements were made with an InSb detector.

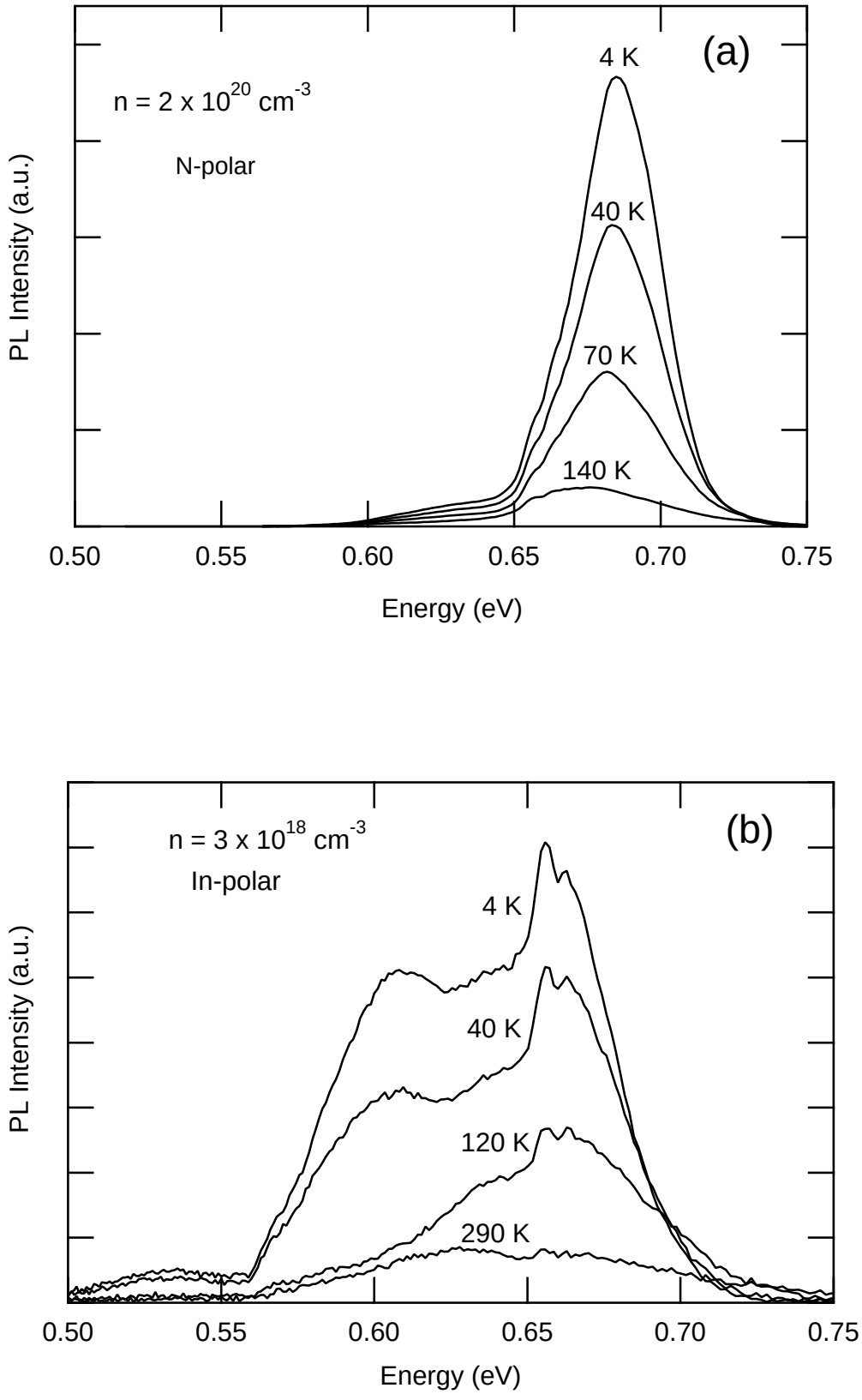

Figure 3.13 The temperature dependent PL from InN films with (a) N-polarity and 1×10^{20} cm^{-3} carriers and (b) In-polarity and 3×10^{18} cm^{-3} carriers.

due to differing behaviour of the two major peaks which constitute the PL of film (b). The low energy peak located at ∼0.61 eV fades quickly as the temperature is raised, leaving the ∼0.67 eV peak to dominate at room temperature. There is also a hint of a weak ∼0.64 eV peak which becomes more noticeable at high temperature.

Gaussian curve fitting was used to monitor the peak locations and peak intensities of the major PL components from both films. A single gaussian was found to provide a good fit for PL from film (a), while 2 gaussian curves were found to provide a good fit to PL from film (b). Gaussian fits were calculated with a least squares approach. Figure 3.14 shows the temperature dependence of the PL peak location for film (a) and the high energy (∼0.67) peak of film (b). The Varshni temperature dependence profile as outlined in equation 3.4 has been fitted (also using a least squares approach) and is represented by the solid curves. The Varshni parameters of the two dependencies are shown inset. As is expected for band edge related transitions, both PL signals red shift as the temperature is raised. The temperature dependence of film (a) is found to correspond very well with the fitted Varshni equation. These parameters of $\alpha = 0.4442$ meV/K and $\beta = 690$ K agree well with the results of Wu *et* al. who obtained $\alpha = 0.414$ and 0.481 meV/K and $\beta = 454$ and 865 K for two films with n-type carriers of 3.5×10^{17} cm^{-3} and 1.2×10^{19} cm^{-3} , respectively [108]. The bandgap of these films was measured by optical absorption.

Varshni parameters for related III:V semiconductors are shown in table 3.1. The temperature dependence of the PL peak location of film (a) also agrees well with common values measured from similar materials. This agreement with other similar III:V materials and the effectiveness of the Varshni equation in fitting the experimental data is consistent with the feature originating from a band to band transition. The temperature dependence of PL from film (b) is not described as effectively by the Varshni equation, although it does provide a loose fit. The Varshni parameters extracted for film (b) also fall outside the range of common values for the parameters outlined in table 3.1. The failure of the Varshni equation to provide an effective description of the bandgap for film (b) is surprising given the good agreement achieved from film (a). A likely source of the discrepancy is the multi-peak fitting used to separate the ∼0.67 eV

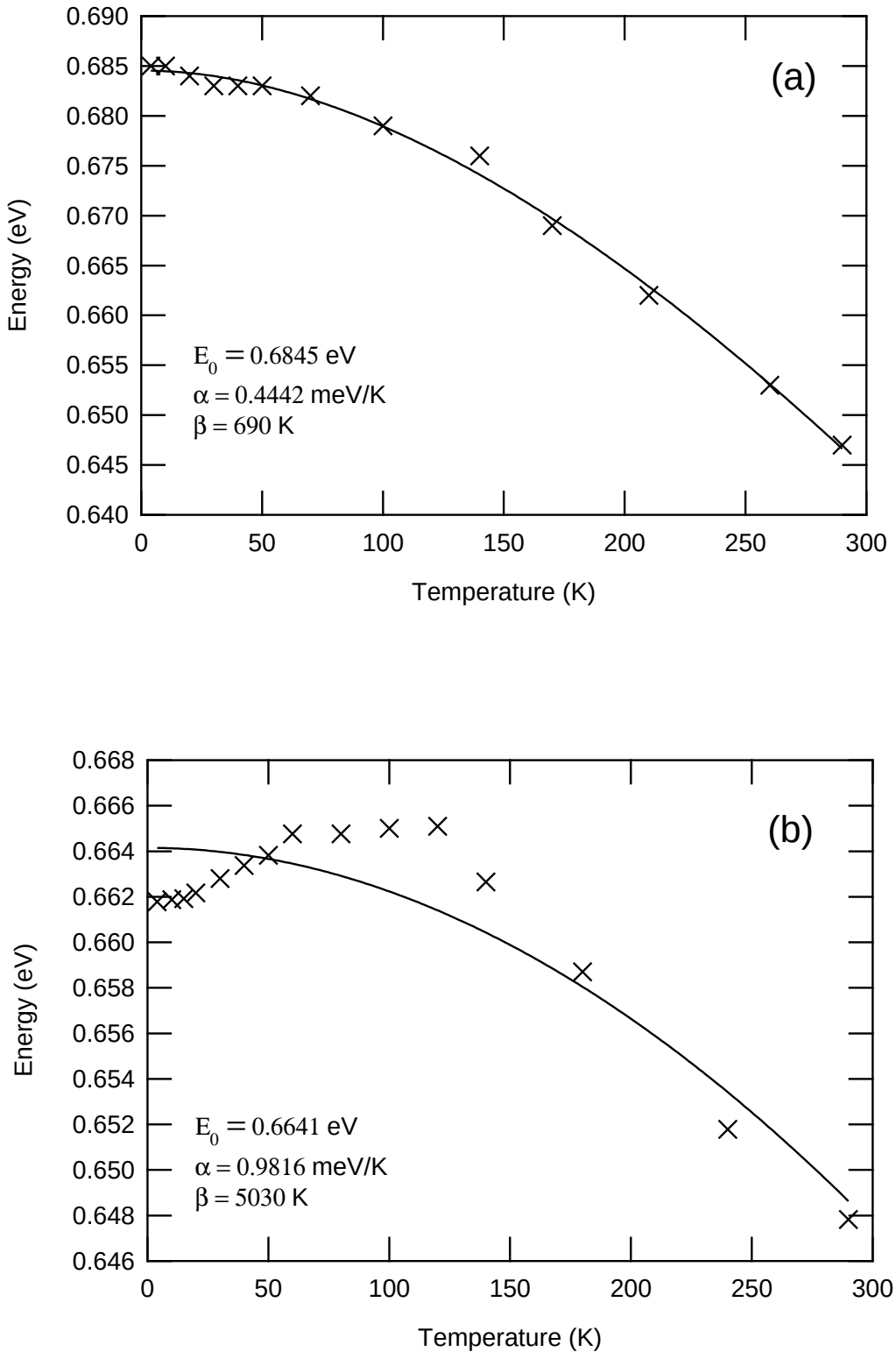

Figure 3.14 The temperature dependence of the PL peak location for the two films described in figure 3.13. The crosses represent the experimental data; the solid lines represent the least squares fit of the Varshni equation as described in equation 3.4. The calculated Varshni parameters are shown inset. (a) N-polar film with 1×10^{20} cm^{-3} n-type carriers and (b) In-polar film with 3×10^{18} cm^{-3} n-type carriers.

Table 3.1 The Varshni parameters for selected III:V semiconductors with an anion or cation in common with InN. All values have been extracted from the review article of Vurgaftman *et* al. [109].

	E_g (eV)	α (meV/K)	β (K)
GaN	3.507	0.909	830
AlN	6.23	1.799	1462
InAs	0.417	0.276	93
InP	1.4236	0.363	162

peak from the $\sim$ 0.61 eV peak. Due to the overlap between the two peaks, the location of the fitted peaks influence each other, and they must be deconvolved to extract the peak locations. This added source of error may explain the deviations observed from the theoretical shift.

The location and intensity of the $\sim$0.61 eV peak from figure 3.13(b) as a function of temperature is shown in figure 3.15. As can be seen from figure 3.15(a) the temperature dependence of the peak shows regions of substantial blue and red shifting. This is not characteristic for a band edge transition and suggests the transition may be defect related. Klochikhin *et* al. [110] and Arnaudov *et* al. [111] have identified a similar transition in low carrier concentration InN and assigned the peak to conduction band edge to deep acceptor transition. Figure 3.15(b) shows a plot of the peak intensity as a function of temperature. The least squares fit of the trap related intensity profile as outlined in equation 3.5 is shown by the solid curve. The thermalisation of carriers from a trap with activation energy of 12.6 meV describes the behaviour of the intensity very well. Klochikhin *et* al. have suggested the trap lies 50 meV above the valence band which agrees well with the separation of the two peaks in figure 3.13(b). The extraction of a much smaller activation energy could be related to the presence of other states near the valence band edge. The activation energy is then reduced to the largest energy gap between different acceptor states.

3.5.2 Density of states and photoconductivity

One of the major limitations of the techniques of optical absorption and photoluminescence is that both measurements can be dominated by low density defects or impu-

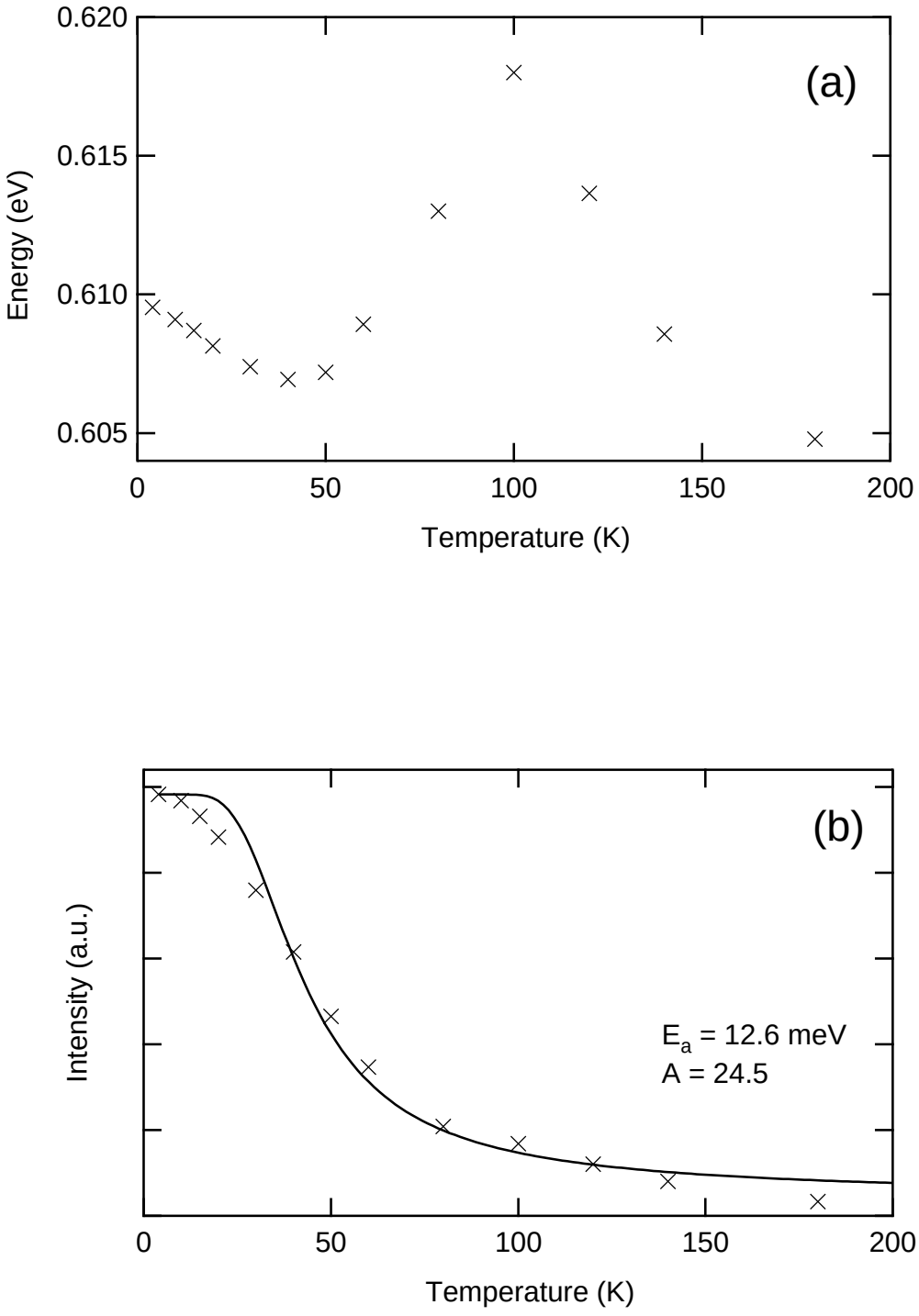

Figure 3.15 The temperature dependence of the low energy peak from figure 3.13(b). The PL peak location as a function of temperature is shown in (a) and the peak intensity as a function of temperature in (b). The solid curve in (b) represents the least squares fit of the trap related intensity profile as outlined in equation 3.5.

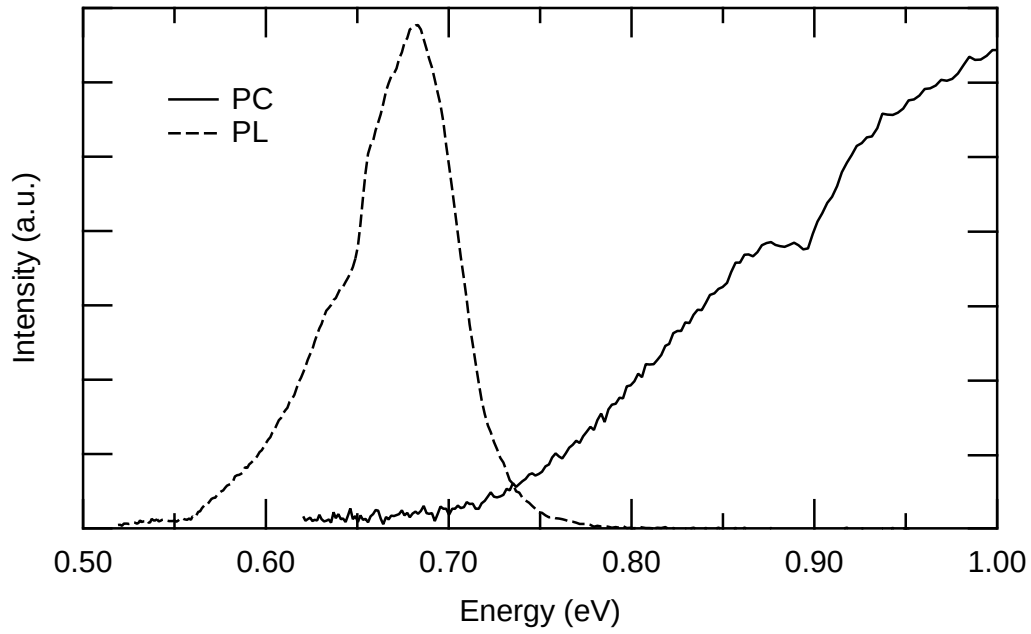

Figure 3.16 The 10 K photoconductivity signal obtained from an InN film with n-type carrier concentration of 3×10^{19} cm^{-3}. The 4 K PL signal from the same film is also shown.

rities. An example of this is the red luminescence obtained from GaN after low level doping with erbium [112]. Photoconductivity (PC) can offer a different perspective for analysing an optical feature. Only carriers which are excited into a conducting level contribute to photoconductivity. This allows isolated defect levels which may dominate PL to be distinguished from high density levels, which can take part in conduction. Figure 3.16 shows the PC and PL signals obtained from an InN film on sapphire with an n-type carrier concentration of 3×10^{19} cm^{-3}. Three films were studied in detail by PC, all grown on sapphire. All films exhibited similar PC onsets and figure 3.16 is representative of the set. The onset of the PC conduction near 0.70 eV corresponds well with the PL peak location at 0.67 eV. PC is expected to be influenced by the Burstein-Moss shift and it can explain the 30 meV shift observed here. The PC onset accompanying the PL peak provides strong evidence that the transition resulting in the 0.67 eV feature is related to band like conduction levels. Unfortunately the power output of the lamp/filter/spectrometer combination could not be monitored accurately during the experiment. This has prevented determination of the average mobility of carriers contributing to the photoconductivity as outlined in equation 3.6. This mea-

surement has the potential to confirm if the valence band, conduction band, or both are involved in the conduction. It must be remembered that a deep level to conduction band, or a valence band to deep level, transition will also contribute to conduction. For this reason the PC by itself does not provide unequivocal evidence for a narrow band gap. It does however confirm that at least one of the bands, or a band like defect state, is taking part in the transition. The 0.7 eV feature is not due to a deep level to deep level transition as described in figure 3.4(c).

In order to investigate the contribution to the PC from hopping conduction and trap activation, the temperature dependence of the PC signal was measured. As hopping conduction relies on carriers tunneling between states, this process is greatly enhanced at high temperatures. The proposed defect states which hopping could possibly take place between are randomly distributed. Theoretical models to describe this form of hopping mechanism are described as variable range hopping (VRH). The two common models of VRH conduction are Mott and Efros-Shklovskii [113]. The temperature dependence of both conduction mechanisms can be described by:

$$\sigma(T) = \sigma_0 e^{(-A/T)^B} \tag{3.7}$$

where σ_0 is the conductivity at 0 K, A is the Mott or Efros-Shklovskii temperature, and B is 1/2 for Mott VRH, or 1/4 for Efros-Shklovskii VRH.

Figure 3.17 shows the intensity of the PC (measured from the same film described in figure 3.16) as a function of temperature. The PC intensity was measured with illuminating photons of 1.01 eV. Photons of 0.8 and 0.9 eV were also used and produced similar profiles. The temperature dependence of the PC rules out hopping as being a dominant contribution to the photoconductivity. Both the Mott and Efros-Shklovskii models of hopping conduction predict significant enhancement in conductivity as temperature is increased, which is clearly not the case. There are two regions of the curve which show small enhancement of the PC at 40 and 110 K. However, orders of magnitude greater conductivity are typically expected over this temperature range for VRH

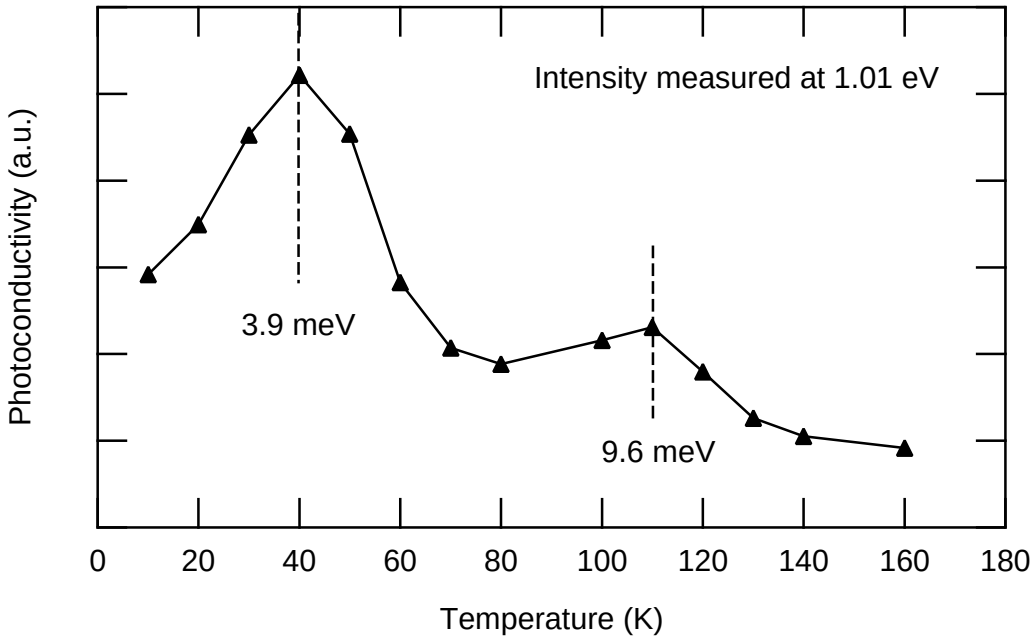

Figure 3.17 The temperature dependence of the PC intensity measured at 1.01 eV as a function of temperature. The measurements were made on the film described in figure 3.16. This film has an n-type carrier concentration of 3×10^{19} cm^{-3}.

conduction in other semiconductors [114, 115]. It is more likely that these features are due to shallow traps thermalising with the conduction or valence band. The energy of these traps has been inferred from the thermal energy available at the local maxima and equate to 3.9 and 9.6 meV, respectively.

3.6 DEGENERATELY DOPED INDIUM NITRIDE LAYERS

Most as-grown InN thin films have high n-type carrier concentrations. There has been a single report of as grown InN being p-type; Feiler *et* al. reported p-type InN with carrier concentrations up to 6.5×10^{20} cm^{-3} in films grown by PLD [116]. However, this report is an exception and has not been reproduced by other research groups. As-grown electron concentrations are typically so high that the films are believed to be exclusively degenerately doped. This means that the Fermi level lies within the conduction band of the material and even at low temperatures there remains a conducting free electron gas. Temperature dependent electrical measurements are a common tool for determining if the Fermi level lies within a band or not. If a material is degenerate, then little change in

carrier concentration is expected with temperature. Carrier mobility may be expected to improve at low temperature as phonon scattering is reduced (pure metallic type conduction). However, in defective materials phonon scattering is often a relatively small effect [117]. Therefore, resistivity is expected to decrease or remain constant with decreasing temperature.

Contrastingly, for a non-degenerate semiconductor the carrier concentration can be expected to decrease as temperature is reduced. This is a result of donor sites no longer having the thermal energy to ionise at low temperatures (carrier freeze out). Also, any intrinsic conduction from band to band thermal excitations is reduced greatly at low temperatures. Consequently, the resistivity of a non-degenerate semiconductor should increase with decreasing temperature. To confirm that the samples studied in this work were, as expected, degenerately doped, temperature dependent resistivity measurements were made on selected samples. Figure 3.18 shows the temperature dependent resistivity of two InN films with different carrier concentrations. Figure 3.18(a) describes an InN film with an n-type carrier concentration of 3×10^{19} cm^{-3} and exhibits two areas of contrasting temperature dependence. From room temperature down to $\sim$130 K the resistivity decreases, suggesting metallic like conduction. Below $\sim$130 K the resistivity increases, suggesting there is some carrier freeze out happening. However, both these effects are very small and the resistivity must be considered largely temperature independent. The invariance of the resistivity with temperature indicates that carrier scattering is limited by defect related scattering, and not phonons.

Figure 3.18(b) describes an InN film with an n-type carrier concentration of 1×10^{20} cm^{-3}. The behaviour of resistivity as a function of temperature in this case is far more metallic like. The resistivity decreases steadily from room temperature to low temperatures with no evidence for any semiconductor like carrier freeze out. The decrease in conduction is much larger (as a percentage change) than observed in figure 3.18(a). This suggests that at higher carrier concentrations phonon scattering becomes the dominant mechanism limiting carrier mobility. Both films examined here show trends characteristic of degenerately doped semiconductor films. These results are in good agreement with the work of Swartz *et* al. who also studied the temperature dependence of carriers

in InN films [118].

3.6.1 Burstein-Moss shifts and photoconductivity

As discussed in section 3.2.1, degenerate doping of a material can significantly influence band to band optical absorption processes (and hence also photoconductivity). The Burstein-Moss shift has been shown by Wu *et* al. to provide a good fit to some experiential data from MBE grown films [119]. On the other hand, Butcher *et* al. have argued that many other absorption measurements on InN films fail to agree with this model and that an alternative explanation is required. The work in this thesis has not focused significantly on absorption measurements, however, photoconductivity provides an alternative approach to study the Burstein-Moss shift in degenerate materials. If it is assumed that each absorbed photon generates a single free carrier, and that the PC is small relative to the total conductivity of the sample, then the PC is proportional to the absorption coefficient. Consequently, a PC squared vs energy plot can be used to infer the location of the Fermi level as shown in equation 3.2.

Figure 3.19 shows the photoconductivity squared vs energy plots for three films with various carrier concentrations. It must be noted that the lamp/spectrometer response will distort this measurement, but the small wavelength over which the measurement is considered should ensure that this distortion is small. Also, the linear nature of the PC squared onsets in figure 3.19 gives confidence that the approach is valid. All three films show strong photoconductivity onsets in the 0.65–0.8 eV range. The linear segments of the plots have been extrapolated to the energy axis to estimate the energy of the absorbing feature as described in equation 3.2. Using this approach the carrier concentration can be correlated with the apparent bandgap, as plotted in figure 3.20. The plot includes the three films studied by PC, as well as three polycrystalline InN films grown on quartz that were studied by optical absorption. As seen, there is a trend for a higher measured bandgap with increasing carrier concentration, although the progression is not as smooth as may be expected if the Burstein-Moss effect is the dominant influence. The relation of these points to theoretical Burstein-Moss shifts is discussed in the following section.

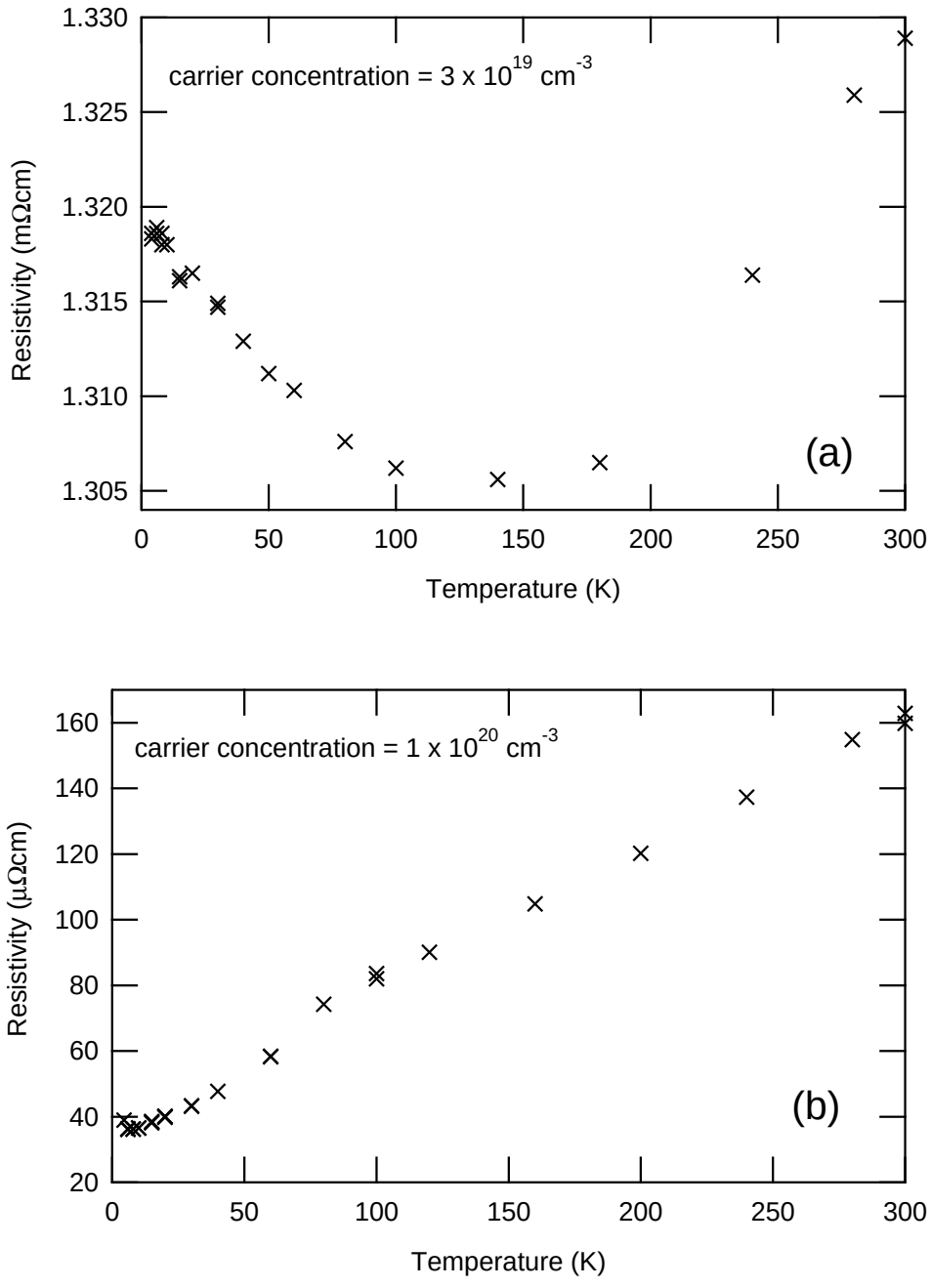

Figure 3.18 The temperature dependent resistivity of two InN films with the corresponding n-type carrier concentrations inset.

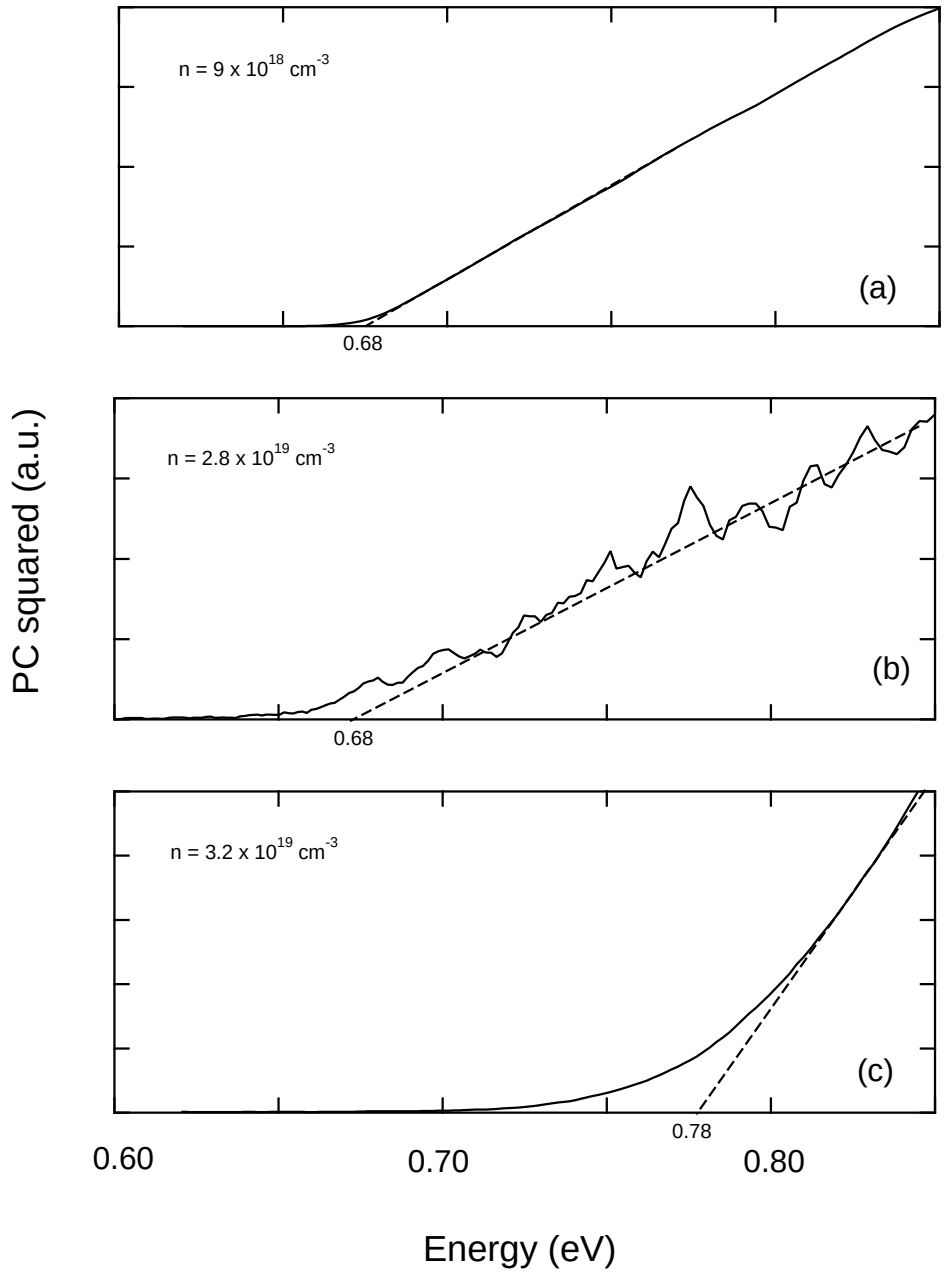

Figure 3.19 The photoconductivity squared (solid curve) vs photon energy for three InN films which showed measurable PC responses. The dashed line shows an extrapolation of the linear section of the response to the energy axis intercept as described in equation 3.2.

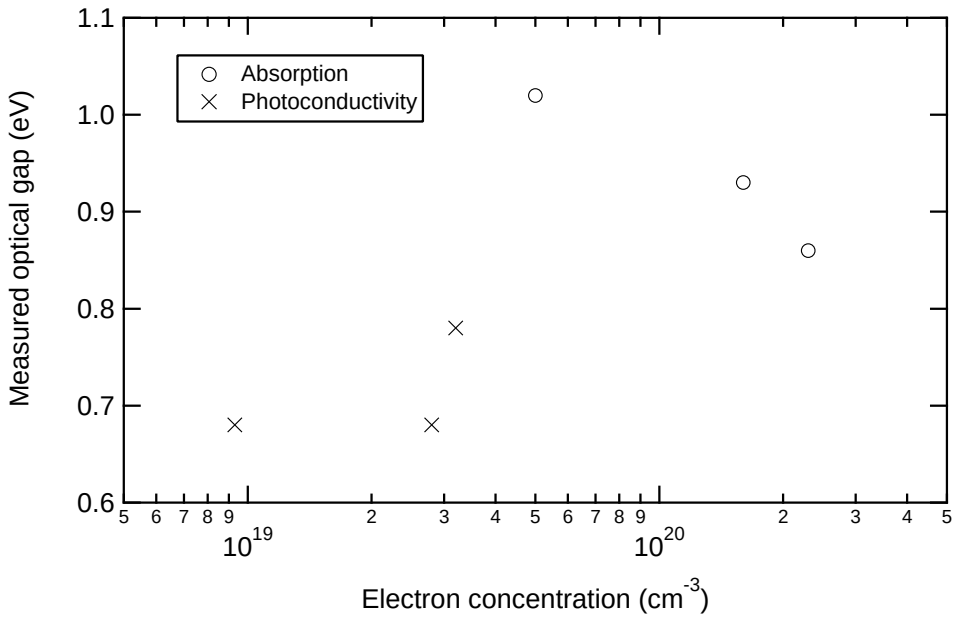

Figure 3.20 The apparent bandgap of InN films measured by optical absorption and photoconductivity as a function of electron concentration.

3.6.2 Parabolic and non-parabolic conduction band models

The theoretical Burstein-Moss shift has been calculated using two approaches. Firstly the standard parabolic band was calculated with an assumed effective mass of $0.11m_e$ [120]. When the shape of the conduction band is discussed in this section the reference is to the energy-wavevector profile of the band. In the parabolic approximation the apparent bandgap of the material is given by evaluating equation 3.8 at the Fermi wave vector for a free electron gas, of carrier density N, given by $k_f = (3\pi N)^{1/3}$.

$$E_{cb}(k) = E_g + \frac{\hbar^2 k^2}{2m^*} \tag{3.8}$$

where k is the wave vector, E_g is the bandgap of the material, and m^* is the effective mass of electrons in the material. The parabolic band approach considered here has been used by Davydov *et* al. to describe a series of single crystal InN films effectively [121]. However, there have been experimental and theoretical studies which have concluded that the conduction band of InN differs substantially from a parabola [24, 122].

As a result, equation 3.8 may overestimate the Burstein-Moss effect in the material.

Wu *et* al. have used the two band Kane model for narrow gap semiconductors to estimate the Burstein-Moss effect [119, 123], and also achieved good agreement with experimental results. The dispersion relation for the conduction band under the two band Kane model is described by:

$$E_{cb}(k) = \frac{1}{2}E_g + \frac{\hbar^2 k^2}{2m_e} + \frac{1}{2}\sqrt{E_g^2 + 4E_p\frac{\hbar^2 k^2}{2m_e}} \tag{3.9}$$

where k is the wave vector, E_g is the bandgap of the material, m_e is the free electron mass, and $E_p = 2m_e P^2/\hbar^2$, where P is the interband momentum matrix parameter. Typical values for E_p in III-N semiconductors are ∼10 eV, which is used in this work. Wu *et* al. have discussed the influence of various values of E_p on the calculated Burstein-Moss shift in InN; for further details see their study [119].

Figure 3.21 shows the calculated parabolic and non-parabolic Burstein-Moss shifts for InN and the experimental points derived from photoconductivity and absorption. Both methods in this case seem to overestimate the extent of the shift presented in the experimental data. This apparent failure of the Burstein-Moss effect to accurately describe the shifting absorption onsets exhibited by InN thin films has continued to provide controversy over the origins of the 0.7 eV feature. Wu *et* al. have shown very good agreement between the non-parabolic band shift and experimental data [119]. However, Davydov *et* al. have shown equally convincing fits between a theoretical parabolic shift and experimental data [121]. Also, Butcher *et* al. have shown that many other InN samples fail to be reconciled by the Burstein-Moss shift [20].

While the Burstein-Moss shift may not have yet provided a definitive explanation of all absorption onsets observed from InN films, all the measurements are consistent in that larger absorption onsets are generally observed in heavily doped films. This gives us confidence that the effect is indeed playing a significant role. An obvious source of discrepancy between measurements is the determination of the carrier concentrations. Single field Hall effect measurements — as are commonly employed — produce an aver-

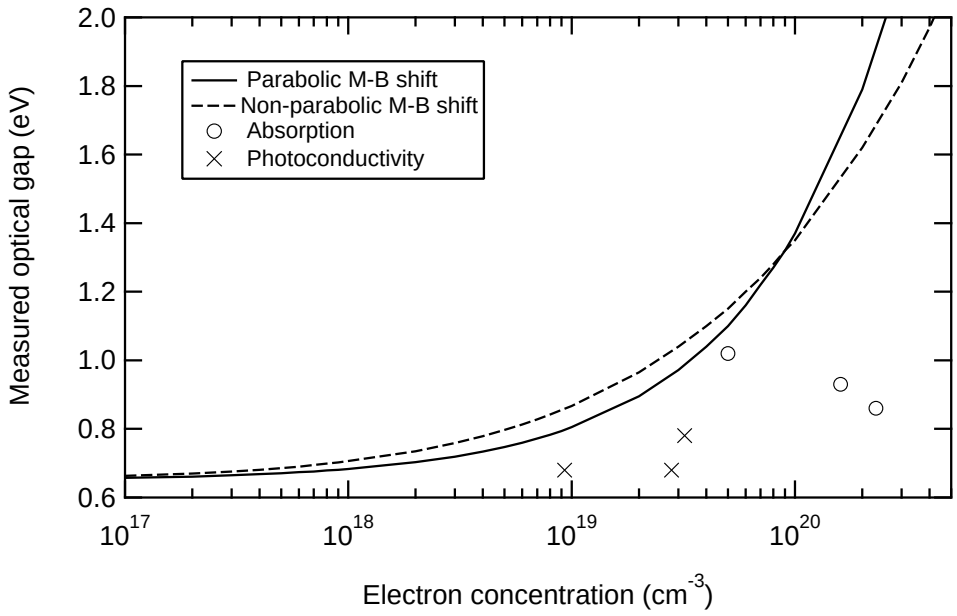

Figure 3.21 The calculated apparent bandgap according to the Burstein-Moss for a parabolic (solid curve) and non-parabolic (dashed curve) conduction band. The experimental points described in figure 3.20 are also displayed.

age electron concentration for a layer. The interpretation of Hall effect measurements, and the significant effect non-homogenous electron distributions could have should be considered when reconciling the Burstein-Moss effect with experimental data.

3.6.3 Surface charge accumulation and Hall effect measurements

All Hall effect measurements discussed up to now have assumed that the studied layers are homogeneous. This assumption allows the use of a simple single field Hall apparatus to determine the carrier concentration and Hall mobility of a layer. This approach is commonly used when calculating InN carrier properties. However, as discussed in section 1.4, InN has been found to exhibit substantial electron accumulation at the film surface. Lu *et* al. have reported electron accumulation at the surface and possibly the interface as high as 5 $\times 10^{13}$ cm^{-2} [31]. Variable field analysis by Swartz *et* al. revealed that there were two distinct conducting layers [118]. A high mobility layer with a mobility of >1000 cm^2/Vs was assigned to bulk conduction, while a low mobility layer of ∼200 cm^2/Vs was assigned to surface and/or interface conduction. We have

studied several of our wurtzite films by variable field Hall effect and found accumulation comparable to these results.

The presence of this electron accumulation layer can have significant implications for single field Hall effect measurements. In the study by Swartz *et* al. the reported surface sheet density and mobility should correspond to 7% of the current in a single field Hall measurement flowing through the surface layer. This calculation was made for a 600 nm thick InN layer; as film thickness is reduced further this fraction will increase. Single field Hall measurements will result in a weighted average of the two layers according to how much current flows through each layer. This result offers an explanation for the apparent offset in carrier concentration between the measured Burstein-Moss shifts of figure 3.21 and the calculated shift according to the conduction band models. The films considered in this figure range between 100–500 nm in thickness. Hall effect measurements on films of this thickness can all expected to be significantly influenced by the accumulation layer. An attempt was made to correct the single field measurements for a fixed accumulation layer of density 3 $\times 10^{13}$ cm^{-2} and mobility 200 cm^2/Vs but the results were unreasonable for some of the layers; several films had apparent p-type bulk conductivity after the correction. This suggests that the nature of the accumulation layer may be changing substantially between films.

It may seem surprising that the studies of Wu *et* al. [119] and Davydov *et* al. [121] achieved good agreement between experimental results and the Burstein-Moss effect, when the same approach failed to achieve good consistency here. The answers to the discrepancy likely lies in the influence of the accumulation layer. The films studied by these other groups were all single crystal and had thicknesses >500 nm. In this regime the surface accumulation layer will be influencing the Hall effect results by at most 10%. Compare this to the results here where films of various thickness were studied and the maximum thickness of the layer was 500 nm. It is likely that the electron accumulation layer is the dominant mode of conduction in many of the films considered in this work. The film morphology must be considered as an additional factor influencing the electron accumulation within films. The inherent high surface area of polycrystalline films could result in the surface accumulation having a larger

effect in these films. This varying influence of the electron accumulation layer on films of varying thickness, and potentially varying morphology, may also help to explain the results presented by Butcher *et* al. [20]. In their report a range of sputtered and single crystal films, presumably of various thickness and morphology are presented, and it is argued the Burstein-Moss effect provides an inadequate description of the results.

3.7 CHEMICAL ORIGINS OF THE BANDGAP DISCREPANCY

Chemical differences in film composition have been a much discussed possibility for the bandgap discrepancy. Oxygen has been the most widely studied impurity which has been suspected as alloying with InN to alter the bandgap. In_2O_3 is a wide gap semiconductor with a bandgap near 3.75 eV, so InN/In_2O_3 alloys would be expected to have a bandgap in the 0.7-3.75 eV range. Bhuiyan *et* al. studied a range of films grown from different techniques and identified a correlation with high oxygen content and high bandgaps [28], although the Burstein-Moss effect was also suspected to play a significant role. Yoshimoto *et* al. reported that oxygen contaminated polycrystalline films showed PL peak shifting towards the blue with increasing oxygen content [27]. For example, an absorption onset at 1.55 eV was reported for an oxygen content of 1%, and an onset of 2.27 eV was reported for an oxygen content of 6% (cation percentage).

We have already shown that polycrystalline films grown on quartz have exhibited 0.8 eV PL and 0.8-1 eV absorption onsets (section 3.4). To explore the effect of oxygen contamination we studied one of these films using ion beam analysis techniques of Rutherford backscattering spectrometry (RBS) and nuclear reaction analysis (NRA). RBS and NRA are not ideal techniques for studying the oxygen content as common substrates for InN also contain oxygen and this can interfere with the measurements. However, by combining the techniques, stoichiometry and oxygen content can be determined to within several percent accuracy. All films studied by this technique appeared stoichiometric, with no measurable oxygen content in the bulk of the film, although, there was evidence for oxidation of a surface layer up to 40 nm thick. The fact that the InN film shows a low energy absorption onset and PL gives further confidence that the polycrystalline films are largely oxygen free within the bulk.

This result viewed in parallel with the work of Yoshimoto *et* al. [27], does suggest that the large variations observed in the apparent bandgap of InN may be able to be partially explained in terms of oxygen contamination. However, the oxygen contents reported in this study were low if alloying is to account for the shift. Assuming linear bandgap bowing of the InO_xN_{1-x} alloy, the predicted bandgap shift is less than 100 meV. It is possible that the correlation with the oxygen content is coincidental or secondary. Butcher *et* al. have proposed an interesting argument in that non-stoichiometry of InN films may effectively produce an alloying effect and shift the apparent band gap of the material [23]. Again, the question arises as what magnitude of deviation from 1:1 stoichiometry is required to produce a shift to around 2 eV in bandgap. Many MBE grown films have been shown to have close to 1:1 stoichiometry. There has yet to be a demonstration of a meaningful correlation between this effect and the measured bandgap of "InN" films.

3.8 MIXED PHASE INDIUM NITRIDE THIN FILMS

Much of the interest in InN has been on the thermodynamically stable wurtzite phase of the material. However, studying the zincblende phase of InN can also shed light on the bandgap debate, as the zincblende bandgap typically lies at a slightly lower energy than the wurtzite bandgap. For example α-GaN (wurtzite) and β-GaN (zincblende) have bandgaps of 3.4 and 3.2 eV, respectively, while α-AlN and β-AlN have gaps of 6.2 and 5.1 eV, respectively. The metastable InN zincblende phase has been successfully produced by MBE using InAs [67] and r-plane sapphire [66] as substrates, although it has always been detected along with the wurtzite phase. PLD growth on c-plane sapphire produced mixed phase InN which exhibited a bandgap near 1.9 eV as measured by optical absorption [124]. Section 2.6 discusses the growth of zincblende InN using (100) YSZ substrates as part of this work. Until now, no photoluminescence (PL) has been reported from films containing significant quantities of zincblende InN.

Hall effect measurements revealed that films grown directly on (100) YSZ had electron concentrations of 1-3 $\times 10^{19}$ cm^{-3} and Hall mobilities of 50-200 cm^2/Vs. A non-optimised wurtzite InN film grown on a GaN buffer with 2 $\times 10^{19}$ cm^{-3} electrons

and a Hall mobility of 150 cm^2/Vs was used to compare the PL from a purely wurtzite film against PL from mixed phase films grown on (100) YSZ. Figure 3.22(a) shows the temperature dependent PL from the non-optimised wurtzite InN film with comparable electron concentration to the films grown on (100) YSZ substrates. As expected the PL intensity is greatly reduced at high temperatures as non-radiative recombination dominates. The peak red shifts with increasing temperature, consistent with the Varshni fit applied in figure 3.14. The temperature dependent PL from a mixed phase InN film grown on (100) YSZ is shown in figure 3.22(b). This signal profile is characteristic of many of the InN films grown on (100) YSZ, although often the intensity of the PL varies greatly between samples. A low temperature 0.68 eV feature similar to the PL signal from figure 3.22(a) is again measured, however there is also an accompanying low energy peak located near 0.61 eV. The low energy peak near 0.61 eV does seem to correspond with the proposed deep acceptor level reported from wurtzite InN films as discussed in section 3.5.1 [111, 110]. However, the peak assigned to deep acceptors was found to quench when the carrier concentration of the films was greater than $\sim 10^{18}$ cm^{-3} in a study by Klochihkin *et* al. [110]. In this case the carrier concentration is an order of magnitude greater than the quenching level, suggesting that this peak could be of different origin, possibly related to the zincblende phase.

The temperature dependence of the two peaks is shown in figure 3.23. The peak locations were calculated by least square fitting of gaussians to the peaks. Above 200 K the signal was too noisy to obtain a reliable fit. Both peaks show red shifts with increasing temperature with the higher energy feature being broadly consistent with the temperature dependence of the peak studied in figure 3.22(a). The shift of the low energy feature, although adopting a slightly different profile to the high energy peak, shifts by a similar amount ($\sim$ 12 meV) between 4 and 200 K. The deconvolving of the peaks again presents some difficulties when analysing temperature dependence, and small variations in the profiles of the temperature dependence must be treated with caution. Power and temperature dependence of the intensity of the two PL peaks (from figure 3.22(b) are shown in figure 3.24. The temperature dependence of the two peaks is very similar. This excludes any shallow traps taking part in the transitions

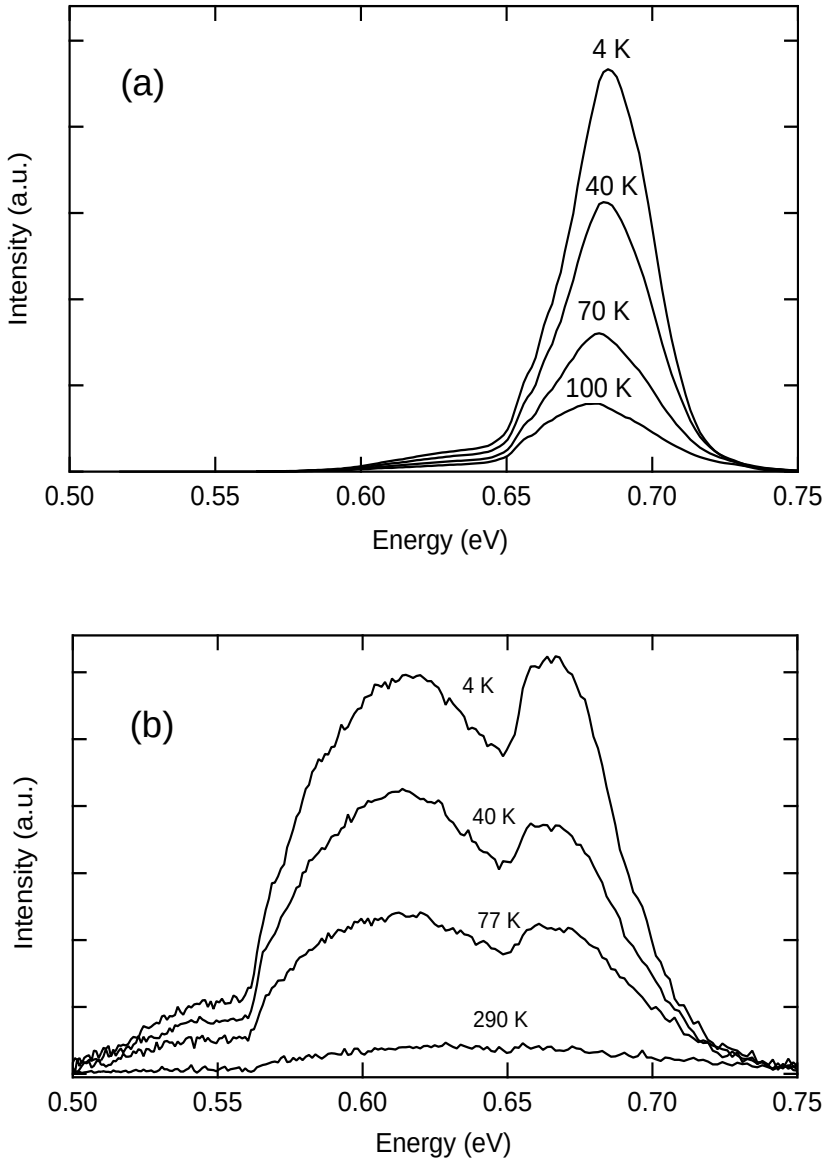

Figure 3.22 Temperature dependent PL measured from (a) wurtzite InN, and (b) mixed phase InN films of similar electron concentration.

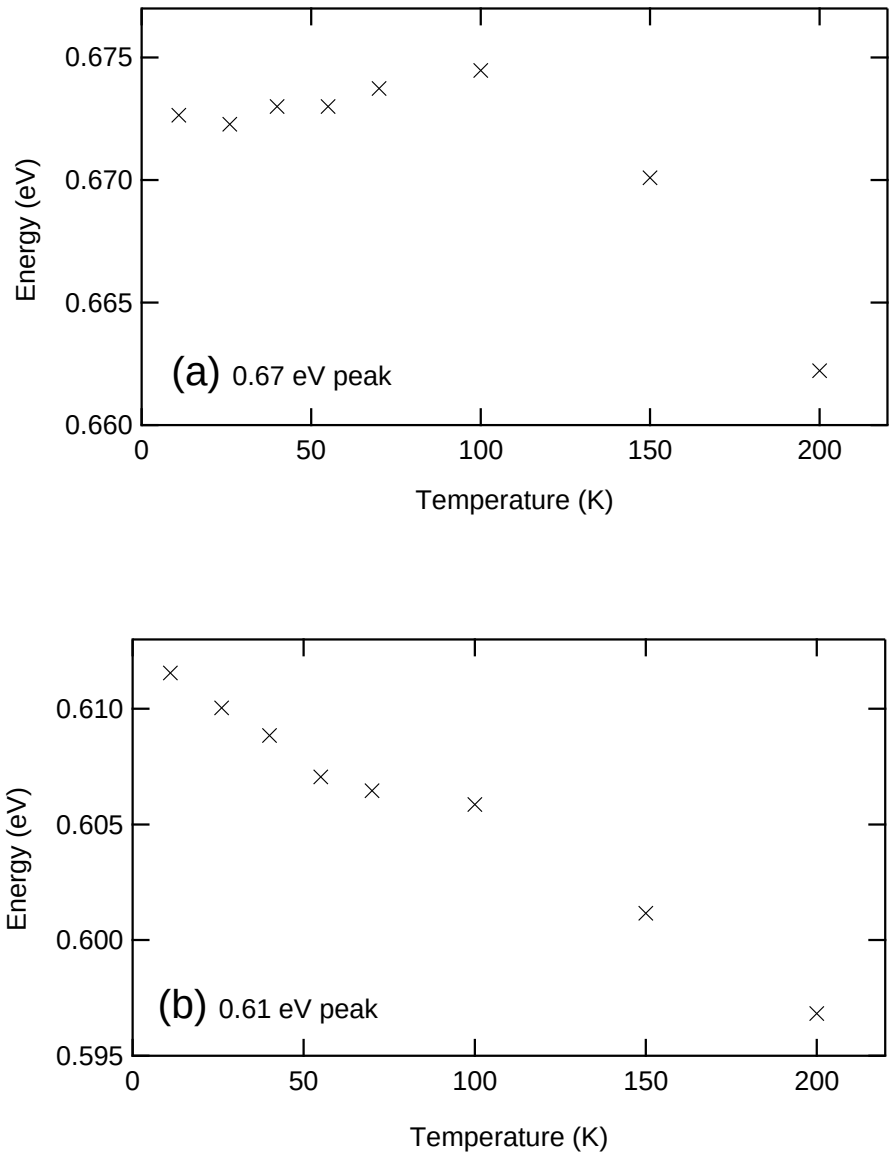

Figure 3.23 Location of the two major PL peaks as a function of temperature from a mixed phase InN film grown on (100) YSZ. (a) ∼0.67 eV peak, (b) ∼0.61 eV peak.

as traps within 26 meV of the bands should thermalise before the temperature reaches 300 K. It does not, however, exclude a deep acceptor taking part in the recombination. The power dependence of both peaks is also very similar, with both peaks saturating at an excitation power of ∼300 mW/cm^2. If the low energy peak was due to a deep acceptor it could be expected to saturate at much lower power, as the density of such a state would be small compared to the density of states in the valence and conduction bands. However, the probability of such transitions must also be taken into account.

Although the cubic and zincblende phases are distinct materials, they differ only in second nearest neighbour orientation. It is therefore reasonable to expect many of the fundamental properties of the material to be similar. The PL from mixed phase InN films grown on (100) YSZ have been studied and compared to PL from wurtzite InN. PL from mixed phase InN contains an additional bright peak near 0.61 eV accompanying the usual ∼0.68 eV feature. Temperature and power dependencies of the low energy peak are similar to those of the high energy peak. This suggests the 0.61 eV (4 K) feature may represent the bandgap of zincblende InN.

3.9 THE BANDGAP OF INDIUM NITRIDE

There now exists such a range of studies concerning the nature of the InN bandgap, that it is possible to construct almost any argument you wish from the wide array of often conflicting results. In such a situation it makes sense to step back and examine the recurring themes within the data. The only reliably reproduced optical feature from InN thin films is the ∼0.67 eV absorption and PL transition. Although films are still produced exhibiting higher energy features, they occur over a wide range of energies which is not characteristic of a band edge feature. In materials such as GaN where deep levels may dominate the photoluminescence from a material, the band edge transition — although often many orders of magnitude weaker — is still visible. We have made a substantial effort to look for higher energy PL but have never detected anything above background noise.

The observation of photoconductivity from near 0.7 eV is further evidence that

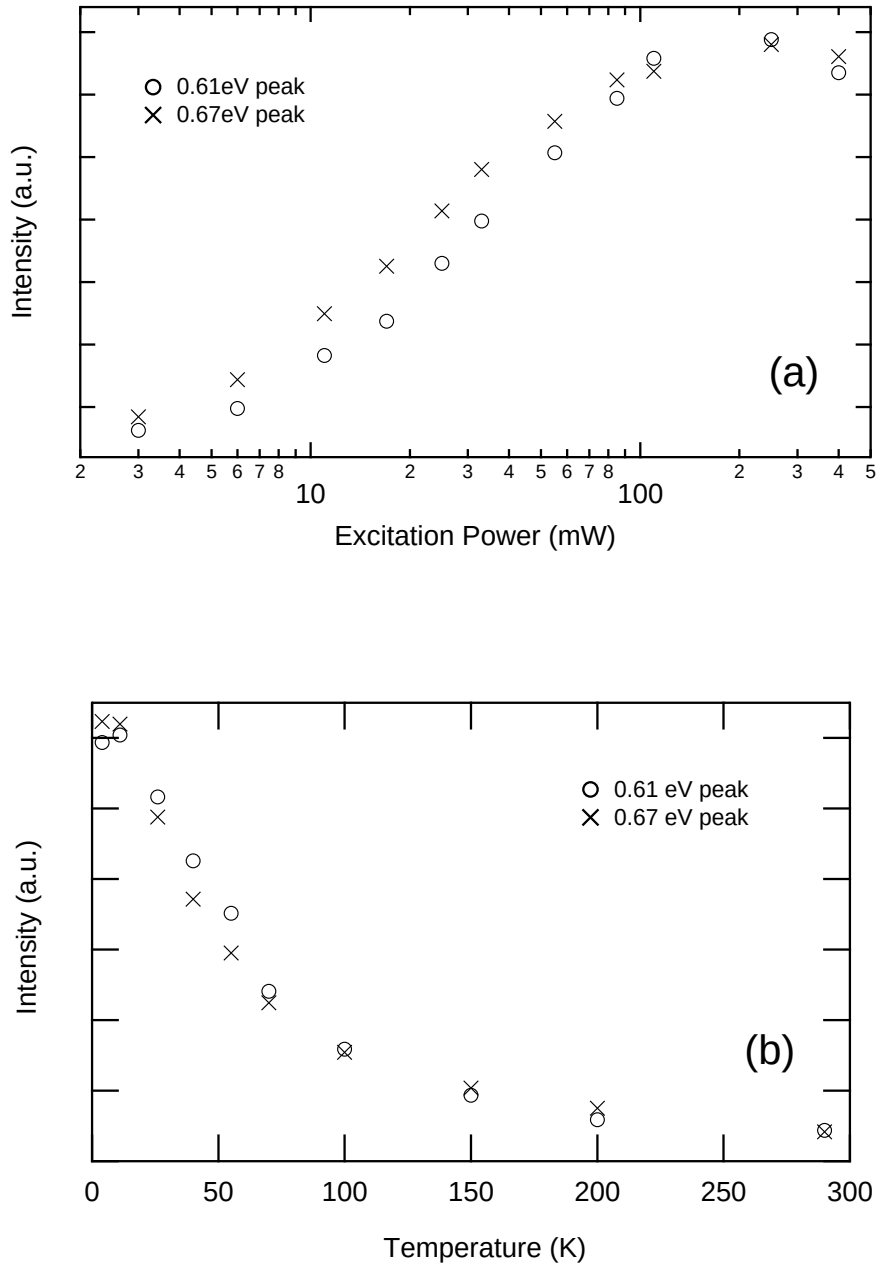

Figure 3.24 (a) temperature dependence and (b) power dependence of the 0.67 and 0.62 eV PL peaks measured from a mixed phase InN nitride film grown on (100) YSZ.

the feature is bandgap related, as the temperature dependent PC data clearly rules out hopping conduction as the origin. The suggestion that the bandgap of cubic InN lies near 0.61 eV, as observed from PL from mixed phase InN films, is also consistent with a 0.67 eV wurtzite InN bandgap. The separation in energy between the two phases corresponds well with the relation of the two phases in GaN and AlN. The Burstein-Moss effect goes part way to describing the observed higher energy bandgaps. Although, carrier concentration calculations must be treated with cation when dealing with thin or polycrystalline films. It also seems likely that alloying with oxygen or non-stoichiometry plays a role in the describing some of the apparent higher energy bandgaps.

Chapter 4

DOPANTS AND DEFECTS IN INDIUM NITRIDE

4.1 FOUNDATIONS FOR DOPING

4.1.1 Donors and acceptors in semiconductors

The reason that semiconductors are of such great technological importance is due to the easily manipulated electronic properties of the materials. For instance, an intrinsic semiconductor is not a greatly exciting material. The interesting and technologically valuable phenomena occur when we use dopants, light, heat, electric fields or another external parameter to vary the electronic properties of the material. It is this wide array of methods to manipulate the electronic properties which permit integrated circuits, laser diodes, sensors and other devices to be produced from semiconductors.

One of the most important ways of altering the properties of a semiconductor is doping. Doping can be used to produce materials where electrical conduction is dominated by the conduction band (n-type), or the valence band (p-type). Combining p-type and n-type doping to make a p-n junction is central to many device concepts. The doping effect an impurity has on a semiconductor is determined by the propensity of the impurity to contribute or remove electrons from a band. The likelihood that an impurity will adopt such a role is determined by the location of acceptor or donor impurity states relative to the band edges. Figure 4.1 shows the locations of donor and acceptor states relative to the band edges for n-type and p-type material, respectively. Donors near the conduction band edge easily lose electrons to the conduction band, making a material n-type. Acceptors near the valence band edge easily remove an electron from the valence band, making the material p-type. The closer these states

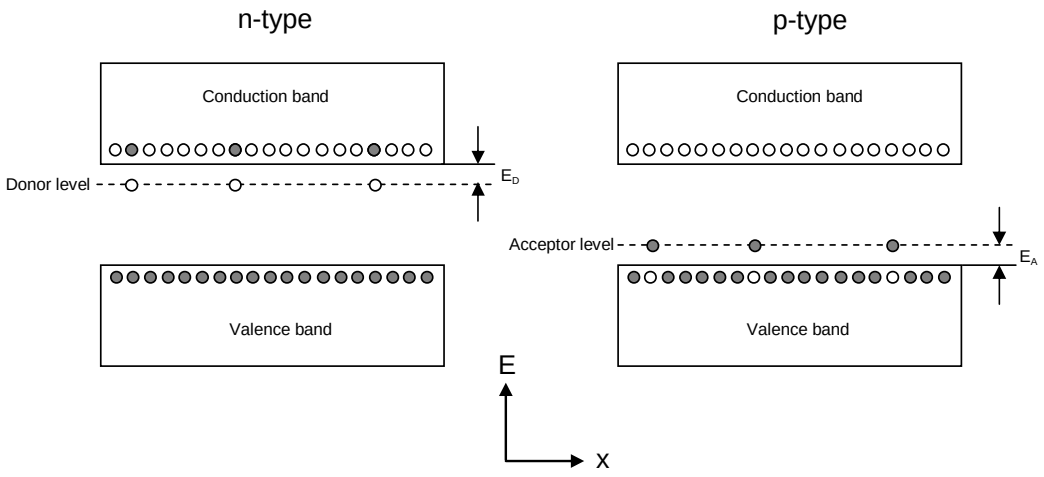

Figure 4.1 The location of donor and acceptor levels relative to the conduction and valence band edges. In this simplified diagram occupied electronic states are represented by filled circles, while unoccupied states are represented by unfilled circles.

are to their respective band edges, the more readily they will adopt a charged state and contribute to doping. The separation in energy between acceptor states and the valence band edge, or donor states and the conduction band edge, is known as the ionisation energy (labeled as E_A and E_D, respectively). If the ionisation energy is less than the amount of thermal energy available to electrons, most of the dopant states will ionise. If however, the ionisation energy exceeds the available thermal energy, few dopant states will ionise. At 300 K the thermal energy available to electrons is $\sim$26 meV.

4.1.2 Chemical and structural nature of dopants

Dopant states are introduced into a semiconductor by defects or impurities. Most semiconductors are n-type or p-type as-grown, without any intentional incorporation of impurities. This is because despite our best efforts to grow perfect crystalline semiconductors, there always exists a finite level of defects within a crystal. These defects may act as donors or acceptors. In the III-nitrides, common defects include vacancies, antisites, interstitials and dislocations [125]. The III-nitrides are almost exclusively n-type as-grown, indicating that on average, these native defects act as donors. In order to controllably make a semiconductor p-type or n-type, impurities are incorporated into the lattice. If an impurity substitutes onto a lattice site which previously

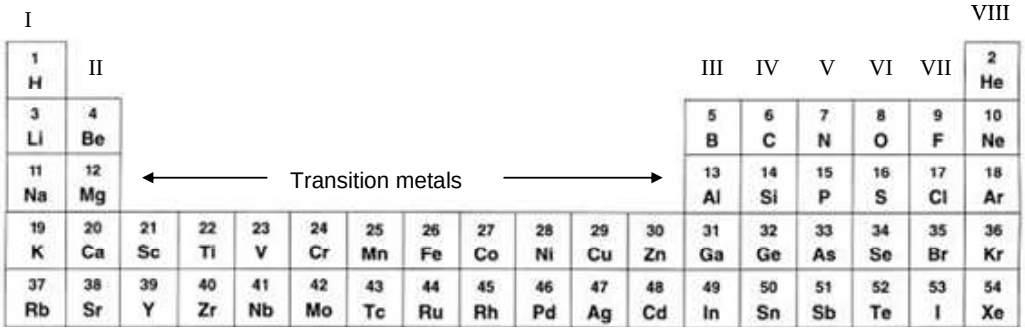

Figure 4.2 The first 54 elements of the periodic table, grouped according to electron valency.

had more valence electrons than the impurity, the impurity will likely be an acceptor. Similarly if the impurity has more valence electrons, the impurity will probably be a donor. Using this model it is possible to anticipate the likely behaviour of specific impurities from the periodic table. For instance, consider the first 54 elements of the periodic table shown in figure 4.2. As is common, the table is grouped in terms of the electron valency of each element. Indium, gallium and aluminium are group three metals. So if in a III-nitride semiconductor one of the group three metals is replaced by a group two metal, the group two metal will behave as an acceptor; magnesium is a common acceptor used to dope GaN and AlGaN. It also follows that a group four element substituted onto the group three site will act as a donor; silicon is a common donor for III-nitrides. As can be seen from figure 4.2 there exists many more potential dopants than just Mg and Si for the III-nitrides. Be, Ca and Sr are other potential p-type dopants; C, Ge and Sn are potential n-type dopants. Substitution with the nitrogen lattice position presents a new array of group four and six elements for p-type and n-type doping, respectively.

Although it may appear relatively simple to select dopants for a particular semiconductor, the practicality of incorporating the dopant into the lattice plays a large role in determining the suitability of a dopant. Figure 4.3 describes three possible arrangements which impurities may adopt when incorporating in a host lattice. Substitution is normally the desired incorporation location, which typically results in dopants behaving as expected by the valency of the atom. Interstitial incorporation is common

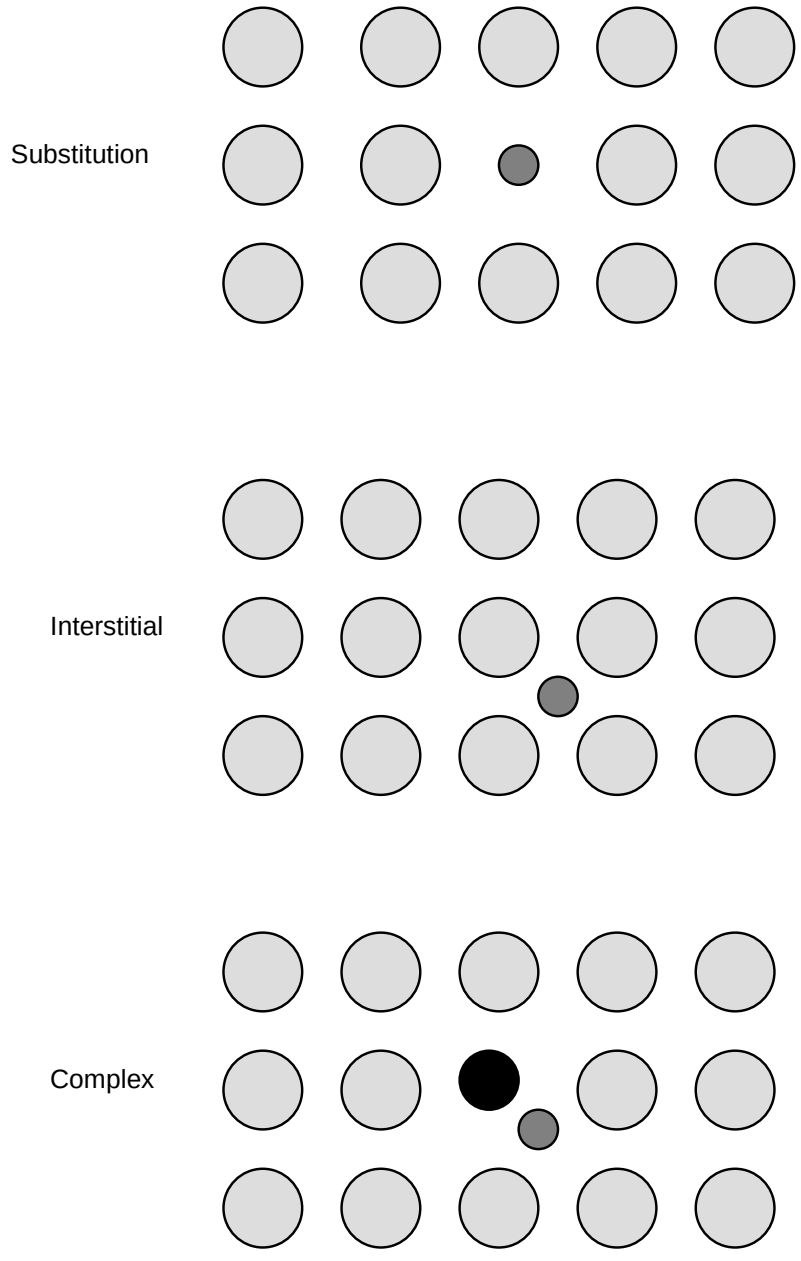

Figure 4.3 Three possible incorporation arrangements for impurities into a hypothetical 2 dimensional semiconductor lattice.

for atoms with small atomic radii relative to the host lattice constant. Complexes are formed when two or more impurities bond in some way within the host semiconductor. For example, magnesium acts as an acceptor in GaN if it substitutes onto a gallium lattice site. However, if the Mg incorporates interstitially it can behave as a donor [126]. Additionally, magnesium tends to attract residual hydrogen, and this can lead to acceptor sites being passivated as the hydrogen forms a complex with the magnesium [127]. So, the task of controllably doping a semiconductor becomes much more complicated than choosing a suitable dopant. The method of dopant incorporation also plays a major role in determining the adopted lattice location, and hence must also be considered carefully. In practice, experimental investigations of how potential dopants behave within a semiconductor are the most common way for determining the suitability of a particular dopant.

4.1.3 Compensation effects

Many native defects within semiconductors can behave as either acceptors, donors or traps. For instance, a dangling bond, as is common at dislocations and surfaces, can donate an electron to the conduction band, or accept an electron to form a hole. The state which the defect adopts is determined by the Fermi energy. The Fermi energy is also sometimes referred to as the "crystal energy". This is because the Fermi energy determines whether electronic states within the crystal at a given energy will likely be occupied or vacant. States below the Fermi energy will likely be occupied, while states above the Fermi energy will probably be vacant.

The influence of the Fermi energy location on dopant polarity can cause complications during doping. For example, doping a semiconductor with acceptors moves the Fermi energy lower, however, as the Fermi energy is reduced, some states that were previously below the Fermi energy are now above it, and hence switch from being mostly occupied to unoccupied. The opposite also holds when doping a semiconductor n-type. This effect is known as compensation. Compensation by a crystal can mean that the effect of doping is largely canceled out by native defects adopting a different polarity. Compensation is particularly severe in highly defective semiconductors where there are

a lot of states close to the Fermi energy. As the III-nitrides are grown heteroepitaxially, they typically have high levels of such defects and hence are highly susceptible to compensation effects. There have been many studies on compensation in Mg doped GaN of which the work of Eckey *et* al. provides a good summary [128].

4.1.4 Methods for doping

Arguably, the simplest and most cost effective way of doping a semiconductor is by diffusion. Diffusion doping involves transferring a dose of the dopant onto the surface of a semiconductor and then heating the sample. The dopant then migrates into the lattice and produces a doped region near the surface. This process is commonly used for large scale manufacture of silicon integrated circuits. Often diffusion will result in a mixture of substitutional and interstitial dopant lattice locations. A drawback of diffusion doping is the often high temperatures required to make some dopants mobile within a specific lattice. This can exclude many potential dopants, particularly for semiconductors with low dissociation temperatures such as InN.

Another important tool for doping is ion implantation; this technique relies on a particle accelerator to produce high energy dopant ions which bombard the host semiconductor and imbed themselves in the lattice. Although a much more expensive process than diffusion, ion implantation has several key advantages. Firstly it allows buried layers to be created which are often very useful for device processing. Secondly, it is relatively easy to produce a wide range of ions for implantation, as most elements can be implanted with this technique. Obviously the major drawback is the damage caused by the high energy ions. A post implantation annealing step is often employed to attempt to repair damage.

In-situ doping involves incorporating impurities into the semiconductor host as the crystal grows. As the atoms are not required to diffuse, the process is not limited by the dissociation temperature of the semiconductor like diffusion doping. In-situ doping does require a source of the dopant species, which is not always easily generated. In molecular beam epitaxy the dopant atoms are typically supplied by a separate effusion cell. The added complexity of incorporating an additional source into a growth system

is a major drawback of this technique. However, many initial investigations of dopants are carried out using this technique. For a general review of semiconductor doping see the work of Guk and Shmidt [129].

4.2 NATIVE DEFECTS IN INDIUM NITRIDE

Since all as-grown InN nitride films have high n-type carrier concentrations, a reasonable question is, what is the source of the electrons? In fact, both GaN and AlN have also suffered from this problem of high electron concentrations in as-grown films [125]. It has long been argued that the nitrogen vacancy is the likely source of this background carrier concentration in GaN [4, 125]. With the similarity of the materials and the growth processes used, one might argue that the nitrogen vacancy is also a likely candidate for the high electron concentrations observed in InN. A study by Look *et* al. considered dopants in InN and used glow discharge mass spectrometry (GDMS) to quantify impurities within unintentionally doped InN epilayers [130]. The dopants studied were carbon, silicon, oxygen, aluminium, sulphur and hydrogen; this group includes the elements which commonly contaminate layers during thin film growth. Of the species studied only hydrogen was present in sufficient concentrations to account for the electron concentration. This result suggests that the dominant donor in InN is either hydrogen or native defects.

4.2.1 Synchrotron based studies of defects

InN layers have been studied by near-edge X-ray absorption fine structure (NEXAFS) spectroscopy in order to investigate if native defects could account for the high electron concentrations. This work was carried out through a collaboration with Dr Mladen Petravic at the Australian National University. There has been one previous study of InN by NEXAFS by Lee *et* al. [131]. However, that study focused on the crystallographic make-up of InN films as they became thicker and not on defect levels.

NEXAFS is a synchrotron based technique which utilises the precise control of soft X-ray energy possible with a synchrotron to study core electron absorption spectra.

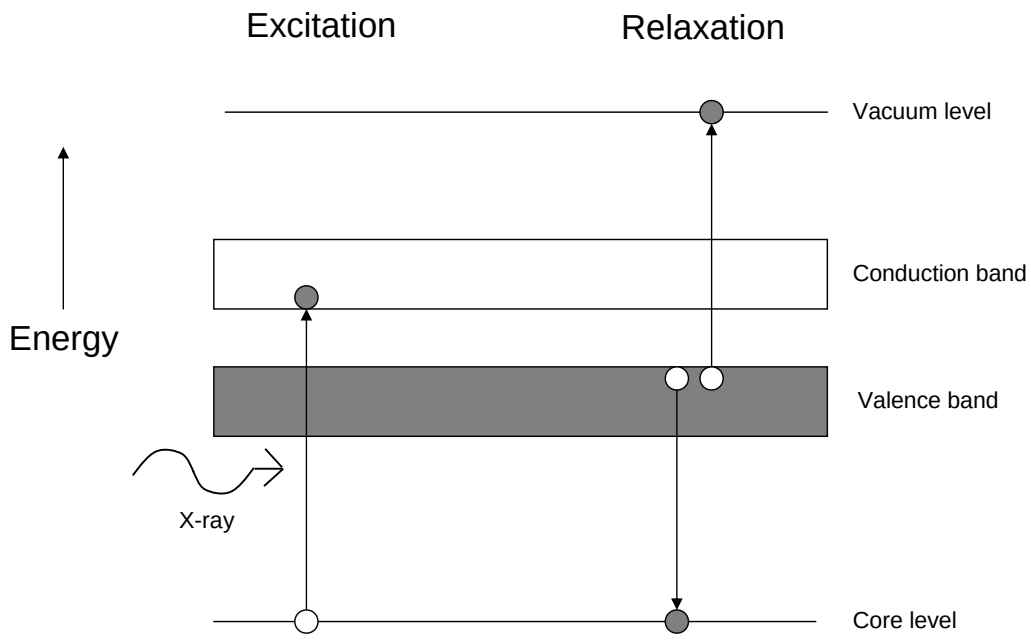

Figure 4.4 A description of the transitions exploited by the NEXAFS experimental technique. The excitation process shows an X-ray being absorbed which leads to the promotion of a core electron to the conduction band. The relaxation process then shows how energy conservation requires a spectator electron to be excited to the vacuum level as a valence band electron fills the recently emptied core level.

For an X-ray to be absorbed, an electron must be excited from the core level to the conduction band, or a vacant energy level near the conduction band. After an electron is excited into the conduction band from the core level, another electron will relax back into the core level. This process of relaxation always triggers a secondary electron to be emitted from the crystal. It is this process which is exploited to measure the absorption coefficient of the incident X-rays in NEXAFS. Figure 4.4 shows a soft X-ray exciting an electron from a core level to the conduction band and the subsequent relaxation which leads to the emission of a secondary electron. In this case, the secondary electron is emitted when an electron falls from the valence band to the core level; this is known as "spectator" emission. If the electron transition is from the conduction band to the core level, the emitted electron is known as "participator" emission. Finally, if the exciting X-ray has sufficient energy to excite the core level directly to the vacuum level, the emitted electron is known as an "Auger" electron. Adding the total current from these three processes together gives the total electron yield (TEY). The TEY from the sample is found to be proportional to the absorption coefficient, and is the common quantity

measured during NEXAFS. Also often measured is the partial electron yield (PEY). The PEY measurement applies a retarding voltage to the gathered electrons and hence measures electrons only over a critical energy. This results in the PEY measurement being more surface sensitive than TEY.

In this study we examine only the nitrogen K edge. This requires that all the identified transitions have a final state which contains a contribution from p orbitals [132, 133]. The result of this is that indium antisites, indium vacancies, indium interstitials and nitrogen vacancies cannot be identified by this technique. The common defects which are detected by nitrogen K edge NEXAFS are interstitial nitrogen and nitrogen antisites.

Figure 4.5 shows the TEY and PEY measurements from a 700 nm thick wurtzite N-polar InN film grown on (0001) sapphire/GaN. The PEY measurement used a retarding voltage of 100 V and scans were taken with a photon impact angle of 40°. All measurements were made at the Elettra beam line, Italy. Two scans are shown; the first an as grown InN film, and the second the same film after bombardment with 5 keV N_2^+ ions for 15 min. Features were fitted with sigmoidal and gaussian line shapes, as described in the report by Petravic *et* al. [132]. The fitted peak locations are identified by the numbers 1-7 in figure 4.5. The locations of all the peak energies are summarised in table 4.1. The conduction band edge (CBE) appears at 397.5 eV and is identified as the inflection point of the yield onset in the as-grown sample. It is noted that the examined layer is degenerately n-type and so the absorption edge should be shifted by the Burstein-Moss effect. However, the carrier concentration of this layer is $\sim 2\times10^{18}$ cm^{-3} and this level of electrons has been shown to result in a Burstein-Moss shift of <0.1 eV in section 3.6. Four resonances (labeled 1-4) are identified above the conduction band onset in the as-grown sample. These transitions are in good agreement with the work of Lee *et* al. and are characteristic of states associated with In–N bonds in the a-plane (peaks 1, 2 and 4) and c-axis (peak 3) [131, 132]. Interestingly, the PEY measurement shows little difference in line shape, suggesting that the near surface region adopts a similar bonding profile to the bulk.

After bombarding with the N_2^+ ions a single feature is detected below the absorption

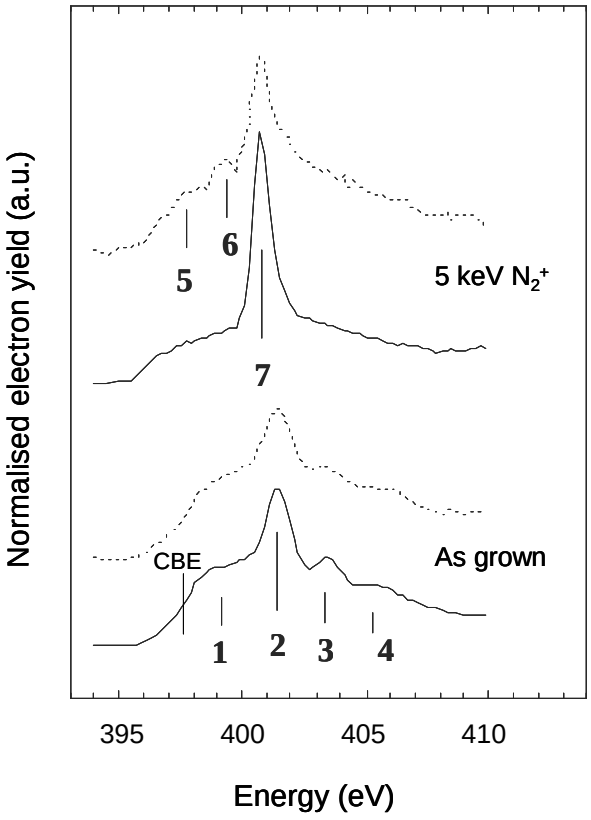

Figure 4.5 The total electron yield (solid curve) and partial electron yield (dotted curve) for nitrogen K edge NEXAFS measurements made on N-polar InN samples. The as-grown sample has not been subjected to ion bombardment, while the 5 keV sample has been bombarded by 5 keV N_2^+ ions for 15 min.

Table 4.1 The locations of p-state bonding and defect levels in InN thin films as determined by NEXAFS.

Peak	CBE	1	2	3	4	5	6	7
Energy (eV)	397.5	399.7	401.5	403.4	405.3	397.2	399.2	400.7

edge (5) and two other resonances are detected above the absorption edge (6 and 7). The emergence of these peaks after bombardment indicates that they are likely due to defects within the lattice. It has previously been established that the likely sources of observed defects in nitrogen K-edge NEXAFS are interstitial nitrogen and nitrogen antisites [132, 134]. Petravic *et* al. have attributed peak 7 to molecular nitrogen and demonstrated that the fine structure of the peak contains the signature of molecular nitrogen vibrations [132]. By then reconciling the remaining two peaks with theoretical predictions, peaks 5 and 6 were assigned to interstitial nitrogen and nitrogen antisites, respectively [134]. The interstitial location supported by theoretical studies is the split interstitial [125, 134]. This arrangement has the interstitial bound to a host nitrogen atom; the pair then jointly occupy the lattice position.

The relative magnitude of peaks 5 and 6 is much greater in the PEY measurement than TEY. This gives an indication that interstitial nitrogen and antisite nitrogen defects are more prevalent close to the surface than in the bulk, consistent with the ion bombardment causing more damage near the surface. The close proximity of peaks 5 and 6 to the conduction band edge suggest that both defects should be donors in InN. The fact that neither of these features are visible in the as grown sample indicates that the formation energy of the defects during growth is quite high. This is in agreement with the theoretical study of Van de Walle and Neugebauer [125]. For that reason it seems unlikely that the high n-type carrier concentrations observed in InN can be attributed to interstitial nitrogen or nitrogen antisites. This leaves indium related native defects (including the nitrogen vacancy) and hydrogen as the likely origins of the high electron concentration.

4.2.2 Surface states as a source of electron accumulation

The electron accumulation layer discussed in section 3.6.3 provides an interesting perspective on the source of the background n-type conductivity in InN. A number of reports have shown that this electron accumulation layer is strongly localised within several nanometers of the film surface [31, 32]. The magnitude of the electron accu-

mulation layer appears too high to be accounted for by polarity effects, and hence is likely due to a high density of donors near or at the surface. At any surface a material is forced to adopt a plane of vacancies, the nature of which is determined by how the surface of a film is terminated. If the film is indium terminated then the surface will effectively consist of nitrogen vacancies; if however, the film is nitrogen terminated, the surface will consist of indium vacancies. A mixture of the two is also possible. To the authors knowledge there are no reported studies of how InN films terminate. There have however, been several reports of film polarity. Film polarity may provide a good indication of surface termination as the bonding arrangements at the surface vary substantially with polarity.

Figure 4.6 shows the crystal structure of wurtzite InN. When viewed along the c-axis — the common growth direction for InN — the crystal consists of a series of polar hexagonal planes of indium and nitrogen atoms, each bonded to three other atoms within the plane. Each atom is also bonded to one other atom in a separate plane. The indium and nitrogen atoms within a plane are slightly displaced from each other along the c-axis; this is what determines the polarity of a layer. If the nitrogen atoms within the plane are closer to the film surface, the film is N-polar; if the indium atoms are closer to the film surface, the film is In-polar. As there is only a single bond between planes, the energy of the system can be minimised by terminating the crystal between planes (surface occurs at an inter-plane lattice location). If the crystal terminates intra-plane then there will be three times as many dangling bonds than the inter-plane case. For this reason it is often assumed that N-polar films are nitrogen terminated and In-polar films are indium terminated [135].

We have used variable field Hall effect measurements to study how the various conduction channels in an InN layer vary with polarity. This work was carried out at West Virginia University through a collaboration with the research group of Professor Thomas Myers. The advantage of variable field Hall effect measurements is the ability of the technique to separate different conduction channels within a layer. While single field measurements provide an average value for the layer, variable field measurements can distinguish inhomogeneities in conduction within a layer. The variable field Hall

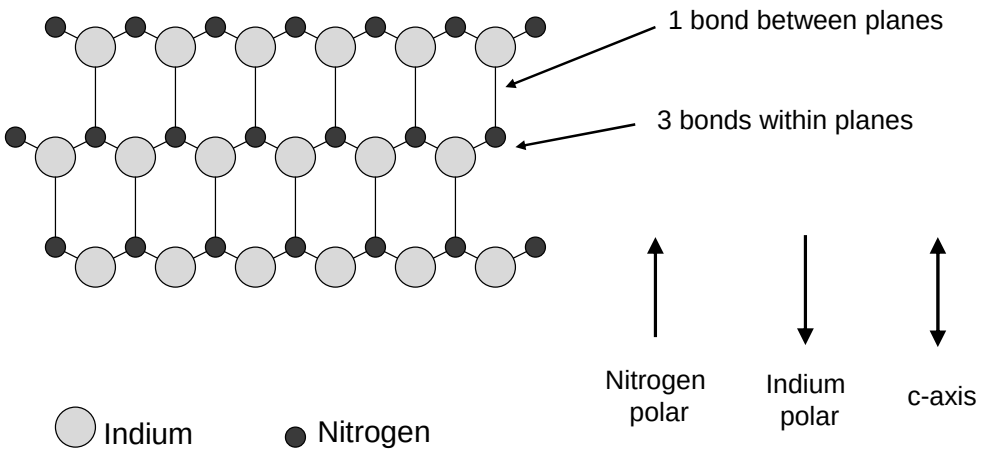

Figure 4.6 A 2D representation of the wurtzite InN lattice structure. Each atom has three bonds within the hexagonal planes (only 2 shown), and 1 bond between hexagonal planes.

effect data in this case was processed using quantative mobility spectrum analysis (QMSA) [136]. QMSA does not rely on any prior assumptions regarding the number of carrier channels such as the other widely used technique of multiple carrier fitting (MCF). QMSA essentially results in a spectrum of the density of carriers versus the carrier mobility; full details of the experimental details and techniques used here are available in a report by Swartz *et* al. [118].

As described in section 2.7.2, the polarity of films grown on sapphire/GaN and YSZ were found to be N-polar and In-polar, respectively. Samples from both these sets were studied by variable field Hall effect analysis. Figure 4.7 shows the calculated QMSA spectrum for a N-polar InN film grown on (0001) sapphire/GaN and for an In-polar InN film grown on (111) YSZ. Commonly, two distinct conduction layers are observed in InN layers: A high mobility layer which has been associated with "bulk" InN, and a low mobility layer associated with the InN surface and possibly the substrate interface [118]. The N-polar InN sample agrees well with this model, with a high mobility layer centered around 1000 cm^2/Vs, and a low mobility layer around 250 cm^2/Vs. There is also a low density hole layer visible near 500 cm^2/Vs. This hole layer is likely an artefact of the data processing during QMSA analysis, which sometimes results in a low density hole layer accompanying an electron layer [136]. The techniques used in these measurements cannot resolve the mobility of carriers below $\sim$200 cm^2/Vs and for

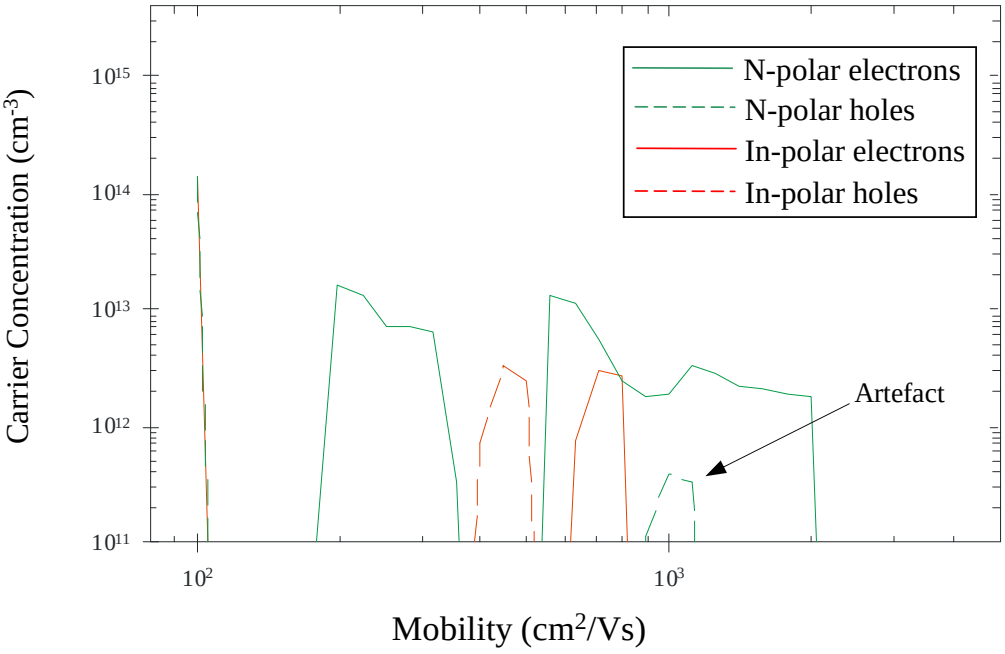

Figure 4.7 The QMSA spectrum calculated from variable field Hall effect measurements on N-polar and In-polar InN films. The N-polar films were grown on (0001) sapphire/GaN. and the In-polar films were grown on (111) YSZ.

this reason only the conductivity of carriers from this regime can be measured. The In-polar film, however, is not reconciled with the two electron conduction model. The dominant features are an electron layer with a mobility of ∼700 cm^2/Vs, and a hole layer with mobility of ∼400 cm^2/Vs. There is no resolvable low mobility electron layer. The hole layer in this case does not overlap an electron peak and for this reason may resemble a real feature.

The absence of the low mobility electron layer in the In-polar film — which is widely believed to result from the electron accumulation at the film surface — suggests that the film polarity plays a role in the origin of electron accumulation. The effect of film polarity in creating electron or hole accumulation layers in GaAs and GaN is well understood. Polar materials have an internal electric field; any changes in this internal field require the presence of an electric charge, as determined by Poisson's equation. It is this charge accumulation effect which is exploited at heterojunctions to make modulation doped HEMTs. Explaining the presence of electron accumulation in InN as polarity induced, does offer a good qualitative description of the surface layer, and

the changing nature of accumulation with polarity. However, using Poisson's equation to examine the problem more closely reveals that the calculated accumulation layer is insufficient to account for the observed concentrations. This indicates that surface donor states offer a more likely origin of the phenomenon.

The likely difference in surface termination between the two film polarities of figure 4.7 could explain the contrasting levels of electron accumulation. The N-polar film is anticipated to be N-terminated, while the In-polar film is expected to be In-terminated, If, as seems likely, the accumulation is due to surface states acting as mainly donors, then the nature of the film surface should strongly influence this effect. The varying chemical nature of the surface under different termination conditions may also account for the observed hole conduction layer. Although, more work is required to establish if this is indeed a real effect and not a product of the data analysis. It is noted that the observed hole mobility observed in figure 4.7 is much greater than common theoretical hole mobility in InN. However, often confined conduction channels can exhibit carrier mobility up to an order of magnitude greater than the free carrier mobility.

4.3 ION IMPLANTATION OF POTENTIAL ACCEPTORS

In order to explore the effectiveness of a range of different dopants within InN, an ion implantation study was undertaken. This work was carried out as a collaboration with the research group of Professor Chennupati Jagadish at the Australian National University. As discussed in section 4.1.4, ion implantation is capable of doping a semiconductor with a wide range of impurities, the main drawback being the large amount of lattice damage caused by the implanted species. For this reason, rapid thermal annealing steps are typically used to repair lattice damage in implanted samples.

In order to assess the impact of rapid thermal annealing on InN samples, non-implanted InN was annealed at 500 and 650°C and the changes in electrical properties of the film measured. Figure 4.8 shows the carrier concentration and single field Hall effect mobility after rapid thermal annealing at different temperatures. The annealing steps lasted for 45 s and were performed in a nitrogen flow of 15 L/s. Both annealing steps

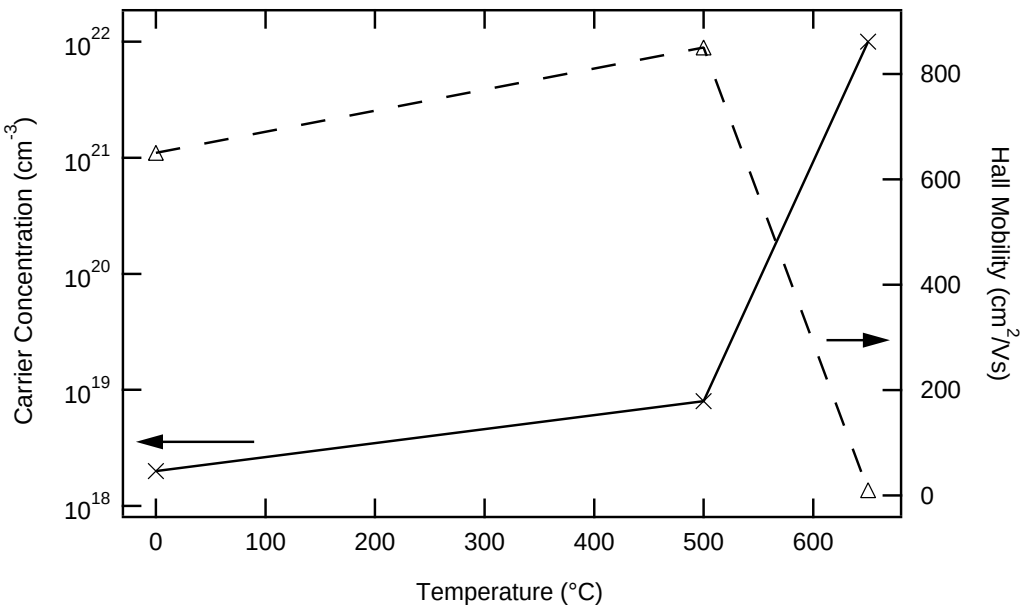

Figure 4.8 The carrier concentration and Hall mobility of an undoped N-polar InN layer grown on sapphire/GaN after annealing for 45 s in nitrogen atmosphere at various temperatures.

increased the n-type carrier concentration, with a dramatic degradation in electrical properties observed after the 650°C anneal. The behaviour of the Hall mobility shows a slightly different trend. A small enhancement in mobility is observed after a 500°C anneal, but the mobility dropped to only 10 cm^2/Vs for a 650°C anneal. The improved mobility after annealing at 500°C does give some confidence that there is some lattice healing taking place under these conditions. Higher temperature anneals were also investigated but the electrical properties were found to degrade severely above 650°C, making it difficult to make reproducible Hall effect measurements. Complete desorption of the InN layer was observed near 900°C. It was therefore decided to perform a rapid thermal anneal on all implanted films at both 500°C and 650°C.

4.3.1 Implantation of carbon, zinc and cadmium

The elements chosen to explore in this study were zinc, cadmium and carbon. Zinc and cadmium could be expected to behave as acceptors when incorporating on indium lattice sites, while carbon is expected to act as an acceptor when incorporating on the nitrogen lattice site. The depth to which ions are implanted is determined by the

Table 4.2 A summary of the the ion implantation conditions and species used during this study.

Species	Implantation Energy (keV)	Dose (atoms.cm^{-2})	Peak Content (cm^{-3})
C	100	1.25×10^{16}	5×10^{20}
C	100	2.5×10^{15}	1×10^{20}
C	100	5×10^{14}	2×10^{19}
Zn	400	5×10^{15}	2×10^{20}
Zn	400	1×10^{15}	5×10^{19}
Zn	400	2×10^{14}	1×10^{19}
Cd	650	5×10^{15}	2×10^{20}
Cd	650	1×10^{15}	5×10^{19}
Cd	650	2×10^{14}	1×10^{19}

acceleration energy, host lattice make-up, and implanted species. In order to select suitable implantation energies, simulations were carried out using the SRIM simulation package [137]. From this, the required implantation energies to achieve a concentration peak ∼250 nm below the surface were determined as 100, 400 and 650 keV for carbon, zinc and cadmium, respectively. Appendix B shows the simulated implantation profiles for the three elements in InN. In order to verify the calculated implantation profiles a carbon implanted sample was studied by secondary ion mass spectroscopy (SIMS). Although the lack of an InN standard prevented quantative analysis, the measured carbon profile was consistent with the simulated profile. Three different implantation doses were carried out for each dopant; a summary of the implantation conditions and species is shown in table 4.2. After implantation, the samples were cleaved and subjected to rapid thermal annealing at 500 and 650°C as previously discussed.

Figures 4.9, 4.10 and 4.11 show (a) the carrier concentration and (b) the Hall mobility of the implanted samples under different annealing conditions. A general trend visible in the three implantation runs is the degradation of electrical properties with increasing implantation dose: the carrier concentration typically increases with increasing dose, while the Hall mobility decreases. The only significant departure from this trend is the 2.5×10^{14} cm^{-2} carbon dose sample annealed at 650°C. This sample shows a notable improvement in Hall mobility and decrease in electron concentration over the lower doped film. However, this point is an exception, and is likely to be an experimental outlier.

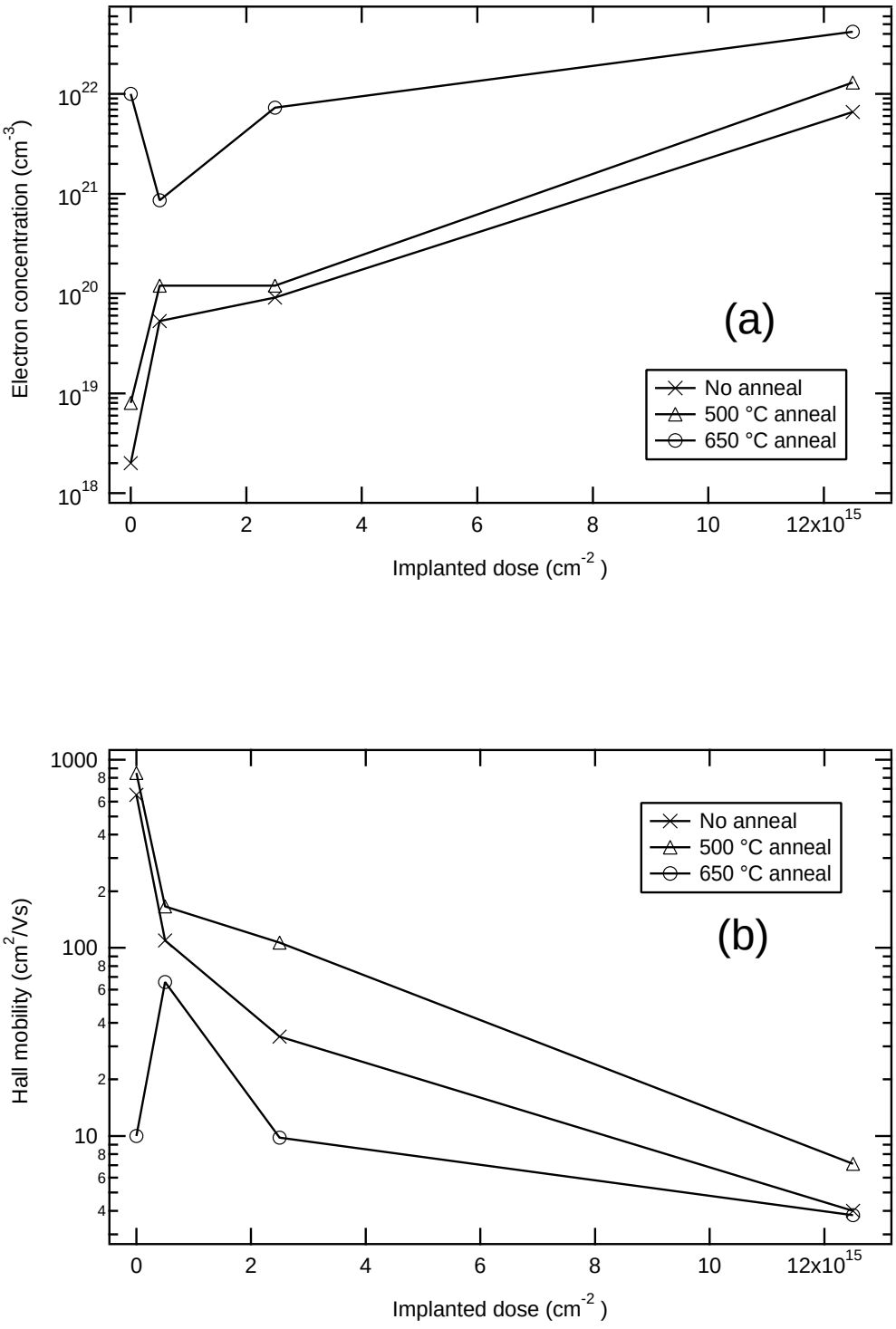

Figure 4.9 (a) The carrier concentration and (b) Hall mobility of InN films implanted with various doses of carbon atoms. Three separate rapid thermal annealing conditions are shown for each series. Each rapid thermal anneal lasted for 45 s in a nitrogen atmosphere. The implantation energy was 100 keV.

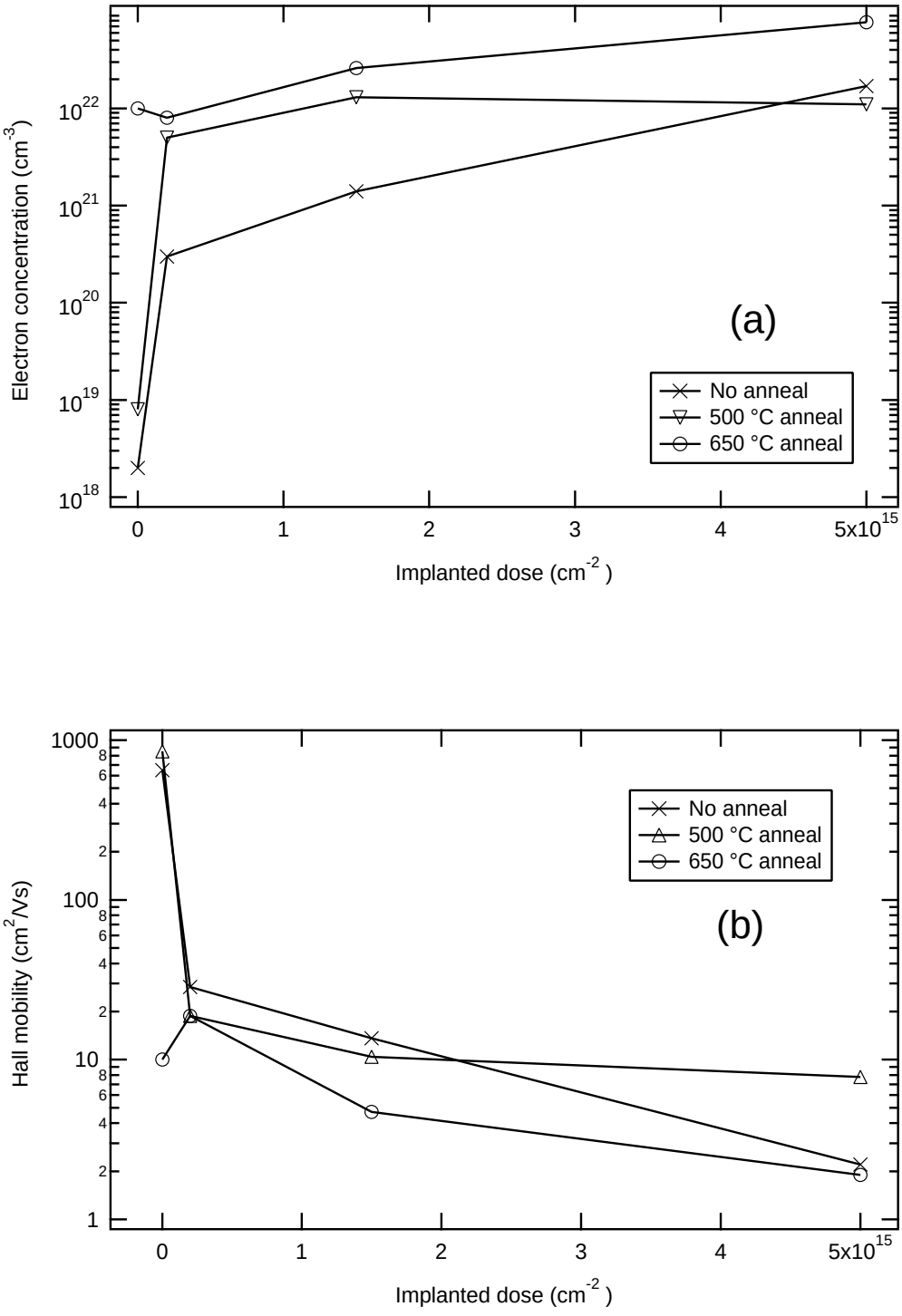

Figure 4.10 (a) The carrier concentration and (b) Hall mobility of InN films implanted with various doses of zinc atoms. Three separate rapid thermal annealing conditions are shown for each series. Each rapid thermal anneal lasted for 45 s in a nitrogen atmosphere. The implantation energy was 400 keV.

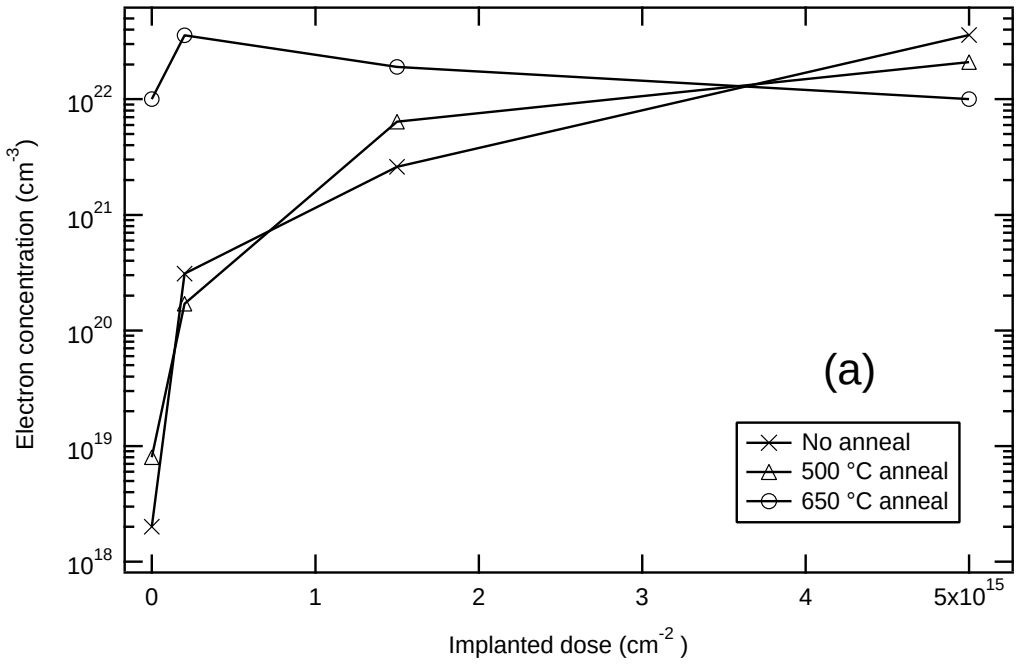

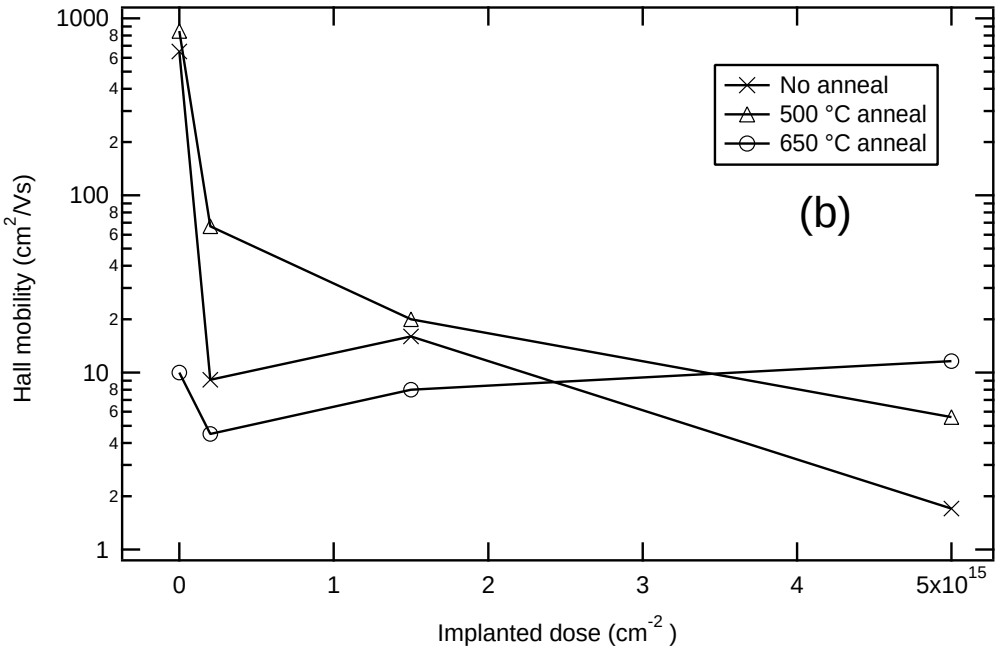

Figure 4.11 (a) The carrier concentration and (b) Hall mobility of InN films implanted with various doses of cadmium atoms. Three separate rapid thermal annealing conditions are shown for each series. Each rapid thermal anneal lasted for 45 s in a nitrogen atmosphere. The implantation energy was 650 keV.

From the increase in n-type conductivity, it appears that the significant damage which is caused to the InN lattice during the implantation results in a significant increase in the native defect density. It is possible that the implanted species may adopt lattice locations which result in the impurities acting as donors (such as interstitials), but, the implanted dose in all three cases is too low to account for the additional n-type carriers, even assuming that all impurities are ionised donors. It is interesting to note that n-type carrier concentration correlates well with implantation energy. Implantation energy is a good indication of how much damage each atom will cause when entering the lattice. For example, the 1.5×10^{15} cm^{-2} dose cadmium samples have considerably higher carrier concentrations than the 2.5×10^{15} cm^{-2} dose carbon samples. The cadmium atoms are implanted at 650 keV compared to only 100 keV for the carbon atoms. This again is consistent with the dominant source of electrons being implantation induced defects in the InN lattice.

It was shown in figure 4.8 how the 650°C anneal lead to dramatically higher carrier concentrations and lower mobility, even for non-implanted films; this trend persisted throughout the three implantation trials. Not inconsistent with the growth related observations, it appears that the dissociation of InN is severe at this temperature. Any added effect of crystal healing at the higher temperature is more than nullified by temperature induced damage. The 500°C anneals show a more promising effect. As with the control sample, carbon and cadmium implantations show a higher mobility after being annealed at 500°C than no anneal at all. This gives some confidence that the rapid thermal annealing step is partially repairing some of the lattice damage caused by the implantation. The zinc implanted film shows similar Hall mobilities between the non annealed and 500°C annealed samples. Also, consistent with figure 4.8 the carrier concentration of the three implanted runs is comparable to or slightly higher than the non-annealed samples.

There is some evidence for partial healing of the InN lattice through rapid thermal annealing. However, the effect is insufficient to make ion implantation a viable processing tool for InN. If ion implantation is to become a doping tool for InN, a more efficient annealing process is required.

4.3.2 Ion damage, the Fermi stabilisation energy, and electron accumulation

The sharp increases in n-type carrier concentrations observed in the implanted InN samples is not a common attribute of semiconductors. Many other semiconductors, including GaN and ZnO, become more insulating as they are damaged by bombarding ions [138, 139]. Li *et* al. have used the concept of a Fermi stabilisation energy to explain the effect [140]. It is argued that due to the average energy of dangling bonds in most semiconductors being comparable, the Fermi energy of highly defective semiconductors approaches a common level 4.9 eV below the vacuum level. For semiconductors such as ZnO and GaN this energy level falls in the forbidden gap, so as these semiconductors are damaged, they tend to become insulating. However, InN has an unusually low conduction band relative to the vacuum level. This leads to the Fermi level stabilising in the conduction band — hence the increase in electron concentration with increasing ion damage. This theory seems to explain the bulk behaviour of InN native defects fairly accurately, and is in good agreement with the ion implantation related damage reported here. Li *et* al. then used this concept to attempt an explanation of the electron accumulation layer. It was proposed that surface states can be treated as a high density of defects and hence become pinned at the Fermi stabilisation energy. The problem with this picture is the tendency of surfaces to adopt a particular chemical state, which will likely dominate most of the surface. The Fermi stabilisation model assumes that on average the dangling bond energies will lead to a Fermi level 4.9 eV below the vacuum level. If a single defect dominates the surface, then the surface is not well represented by the average dangling bond energy. The nature of the dominant defect will determine surface carriers and the Fermi level at the surface. This picture of surface termination determining electron accumulation at the surface is supported by the polarity dependent (and therefore surface termination dependent) accumulation observed in figure 4.7.

4.4 IN-SITU MAGNESIUM DOPING

The most widely used p-type dopant in GaN technology is magnesium. Magnesium doped InN has also attracted attention recently as several groups have intensified work towards producing p-type InN. The first report of Mg doped InN was by Mamutin *et* al. in 1999 [141]. This study found that doping InN with magnesium on the level of 10^{20} cm^{-3} led to an order of magnitude reduction in n-type carrier concentration, and improvements in crystal quality as measured by XRD. It was proposed that these effects could be explained in terms of a surfactant effect provided by Mg on crystal growth. Following this study there was a single report in 2004 by Jasinski *et* al. which showed how Mg doping of InN could lead to polarity inversion domains [142]. The electrical properties of these films was not discussed in detail. However, 2006 has seen a burst of interest in Mg doped InN. Walukiewicz *et* al. showed that the carrier concentration of Mg doped films varied substantially from undoped films after particle irradiation [143]. It was suggested that the discrepancy could result from the compensation of acceptors within the layer. Cimalla *et* al. then showed that there was evidence for a buried p-type layer in Mg doped InN films as revealed by sputter depth profiling [144]. Finally, Jones *et* al. presented capacitance-voltage analysis with further evidence for a buried p-type layer, and reported that their Mg doped films exhibit no PL. It was demonstrated how the PL in Mg doped films could be recovered by irradiating samples with high energy particles.

In this section measurements on a range of Mg doped films grown on both (0001) sapphire/GaN and (0001) Ga-polar GaN templates are presented. All films were grown at the University of Canterbury using MBE. The recipe for the Mg doped films was based on the optimised recipe of section 2.8.3, with a growth temperature of 450°C. Both sapphire and GaN substrates were nitrided for 15 min followed by 150 nm of GaN. A 25 nm InN layer was then grown before the Mg shutter was opened and 500 nm of Mg doped InN was deposited. The cell used to produce Mg flux was only 2 cc in volume, and as such was not capable of producing a flux measurable by the quartz crystal microbalance.

Theoretical flux curves were therefore used to predict the expected Mg flux. Figure 4.12 shows the theoretical curve for Mg flux from a 2 cc crucible in the University of Canterbury MBE system. The Mg concentration has been calculated assuming that all Mg incorporates and an In flux of 1.2×10^{14} atoms.cm^{-2}s^{-1}. A range of cell temperatures were chosen which were calculated to result in Mg content of 6×10^{17}, 2×10^{18}, 6×10^{18}, 6×10^{19}, 3×10^{20} and 1×10^{21} cm^{-3}. The two highest Mg content InN films were then studied by particle induced X-ray emission (PIXE) to confirm the level of Mg doping. PIXE measurements were not possible on all films as the resolution of the technique is $\sim$100 ppm (5×10^{19} cm^{-3}). Figure 4.13 shows the PIXE measurement for the two highest content Mg doped InN films grown on sapphire, and also an undoped InN film grown on sapphire. The Mg K, Al K and In L level transitions are all visible. The amount of Mg within the film is calculated by the relative intensity of the Mg K and In L levels after allowing for the relative likelihood of the two transitions. This approach leads to a cation content of 3% and 0.6% compared for the expected content from the theoretical flux curve of 0.7% (1×10^{21} cm^{-3}) and 0.2% (3×10^{20} cm^{-3}), respectively. Although there is a discrepancy between the two approaches of approximately a factor of 3, the ratio of the two results is consistent with the Mg incorporating in proportion to the Mg flux. Also, precise control of Mg content is not required for this experiment, the goal being to explore a wide range of Mg concentrations over several orders of magnitude.

The motivation for growing the Mg doped layer on both sapphire and Ga-polar GaN templates was to investigate the role film polarity may have on Mg incorporation. Film polarity has been shown to have a dramatic influence on the incorporation of Mg in GaN [145]. Also, Jasinski *et* al. showed that Mg doping of InN can lead to changes in the polarity of the growing film. Growing undoped InN on sapphire substrates with a GaN buffer has been determined to result in N-polar films, while growing undoped InN on Ga-polar GaN templates has been found to result in In-polar InN. The polarity of these layers was determined as described in section 2.7.2, by etching in KOH.

A further series of etching experiments were undertaken on the Mg doped layers to determine the polarity of the layers. Table 4.3 shows the Mg concentration, substrate

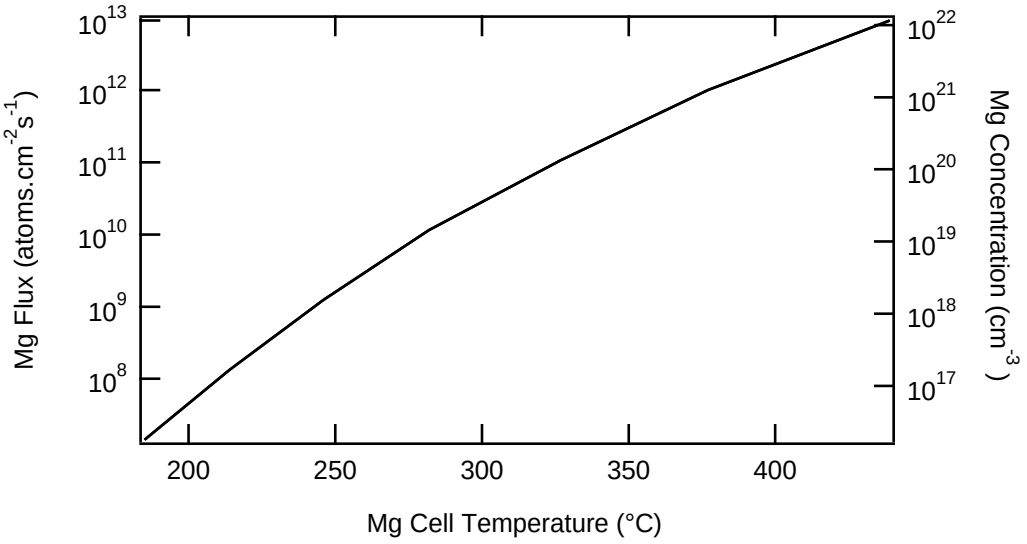

Figure 4.12 The theoretical curve for Mg flux from a 2 cc crucible in the University of Canterbury MBE system. The Mg concentration has been calculated assuming that all Mg incorporates and an In flux of 1.2×10^{14} atoms.cm^{-2}s^{-1}.

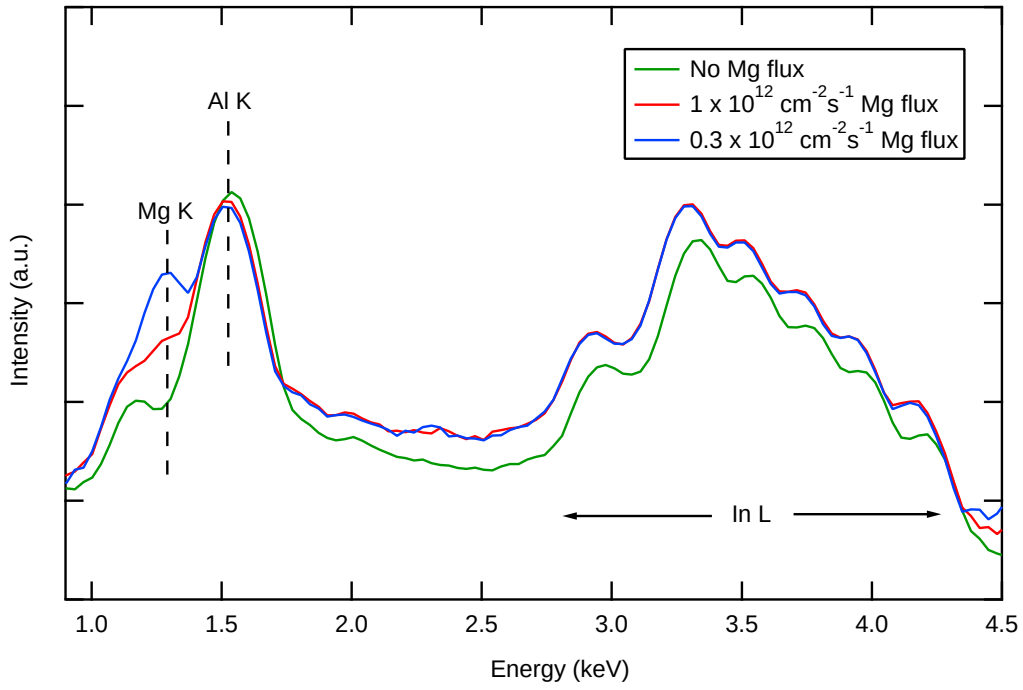

Figure 4.13 PIXE measurement showing the Mg K level, Al K level, and In L level emission for 3 films with varying Mg concentration.

Table 4.3 The polarity of magnesium doped layers grown on substrates of different polarity. The Mg concentration has been calculated from theoretical flux curves after normalising with the PIXE results of figure 4.13.

Mg content (10^{21} cm^{-3})	1	1	0.3	0.3	0.06	0.06	0.006	0.006
Substrate polarity	N	In	N	In	N	In	N	In
Film polarity	In	In	In	In	N	In	N	In

polarity, and the polarity of the resulting film for higher concentration Mg doped films. It is important to note that etching reveals only the dominant polarity; inversion domains as discussed by Jasinski *et* al. would not be detected during etching experiments [142]. At low Mg concentration the polarity of the underlying substrate is preserved, as is evident from the two lowest Mg concentration films (6×10^{18} and 3×10^{19} cm^{-3}). However, at higher Mg concentrations the dominant polarity of all films becomes In-polar, regardless of the polarity of the underlying substrate. This effect may be related to the presence of a Mg surface layer as has been suggested by Mamutin *et* al. [141]. It has been proposed that the presence of a Mg surface layer acts as a surfactant during InN growth, improving crystal order. The presence of such a layer may also result in a preferred growth polarity. At low fluxes there may be insufficient Mg flux to establish a Mg accumulation layer and hence the polarity of the film is preserved in this case.

Figure 4.14 shows the carrier concentration and Hall mobility for Mg doped films grown on both sapphire and GaN. The decrease in Hall mobility as the Mg concentration increases gives confidence that the Mg is indeed incorporating into the layers as anticipated by the Mg flux curve. Additional Mg incorporation can be expected to lead to compensation which will degrade mobility. The carrier concentration of films grown on both substrates shows little dependence on the Mg concentration. Jones *et* al. have argued that the apparent invariance of the carrier concentration of Mg doped InN is related to the dominance of the surface accumulation layer [146].

It has been proposed that although CV measurements provided evidence for a "bulk" p-type layer, the surface remains n-type and dominates Hall effect measurements. The bulk and surface layer are isolated from each other by a depletion region which prevents the bulk contributing to Hall effect measurements. A similar effect re-

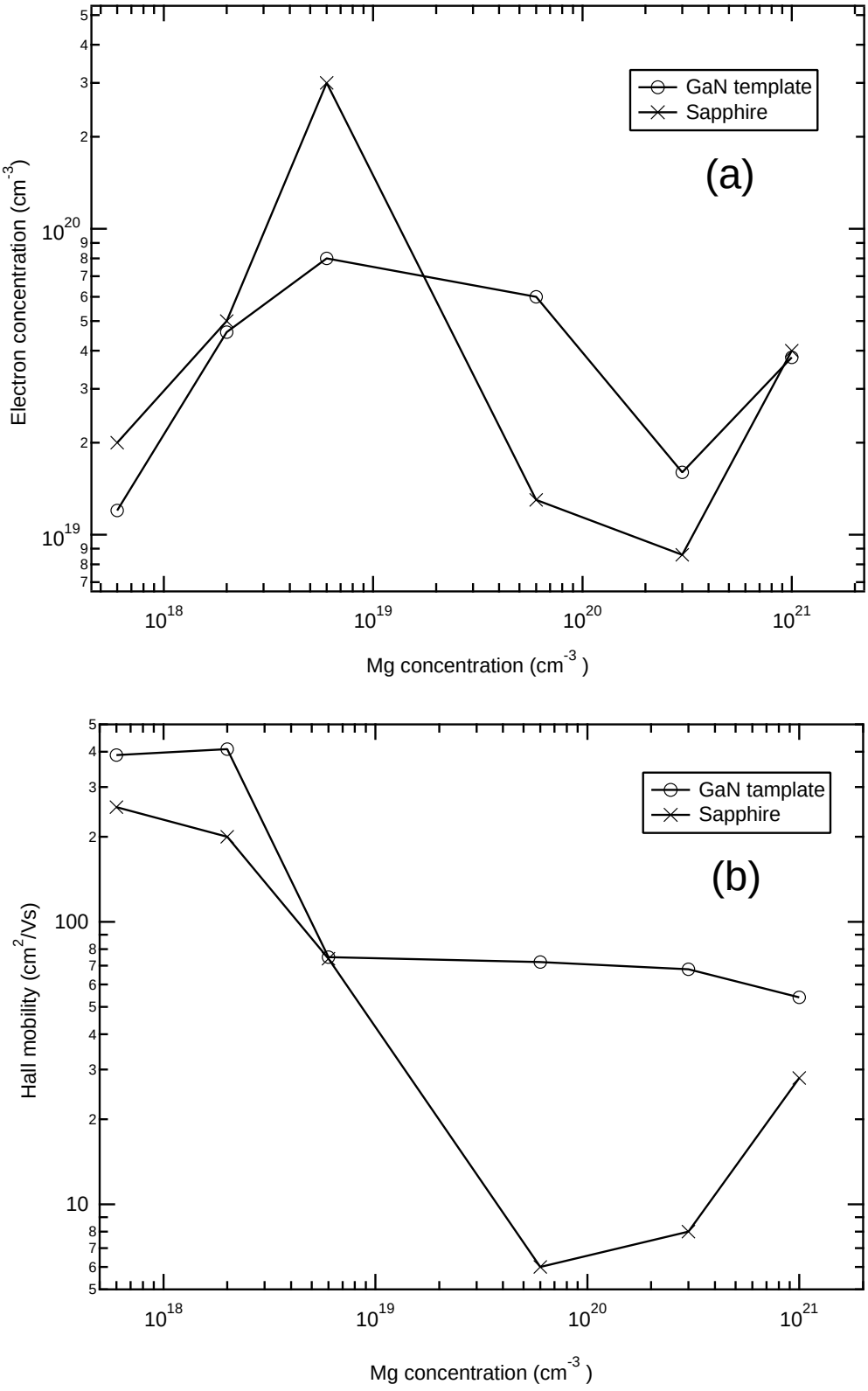

Figure 4.14 (a) The carrier concentration and (b) Hall mobility of Mg doped InN films grown on (0001) sapphire and (0001) Ga-polar GaN templates.

mains a possibility in this case, although the similar electron concentrations measured between the two polarities would suggest that electron accumulation at the surface is comparable for both polarities. This would be in contrast to evidence presented in section 4.2.2 where the electron accumulation was found to vary substantially between In-polar and N-polar films grown on (111) YSZ and sapphire, respectively. Assuming that the Hall effect measurements are a result of only surface conduction, the sheet charge at the surface is in the range of 0.4-4$\times10^{15}$ cm^{-2}. This would require an average electron density on the order of 0.8-8$\times10^{21}$ cm^{-3}, assuming the surface accumulation is spread over 5 nm, a higher level of accumulation than has been reported in previous studies [31, 33]

The deconvolution of the surface and bulk conduction provides a major obstacle to proving the existence of p-type material. The assumptions used here require the existence of unusually high electron accumulation at the surface if the bulk of the material is to be p-type. However, it must be noted that the presence of Mg, and in particular, a surface layer of Mg, may lead to a modification of the surface chemistry which leads to electron accumulation. Therefore the possibility of a buried p-type layer should not be discounted due to the high level of electron accumulation required.

4.4.1 Luminescence quenching

All magnesium doped InN films were studied by photoluminescence in order to search for any optical evidence of acceptor states. Despite intense efforts to obtain PL from all films, only those with Mg content $<10^{19}$ cm^{-3} exhibited any detectable signal. Figure 4.15 shows the luminescence from three such InN films grown on Ga-polar GaN templates. Films grown on sapphire showed a similar trend, but the intensity of the luminescence was approximately an order of magnitude lower. The films with Mg content of 6×10^{17} and 2×10^{18} cm^{-3} are typical of undoped InN luminescence, with peak intensities in the 0.65–0.7 eV region and FWHM of <50 meV.

Contrastingly, the film with Mg content of 6×10^{18} cm^{-3} shows a peak PL energy at much lower energy, around 0.58 eV. The dip observed in the PL spectrum at 0.56 eV is an absorption caused by the spectrometer in this region; accounting for this, the PL

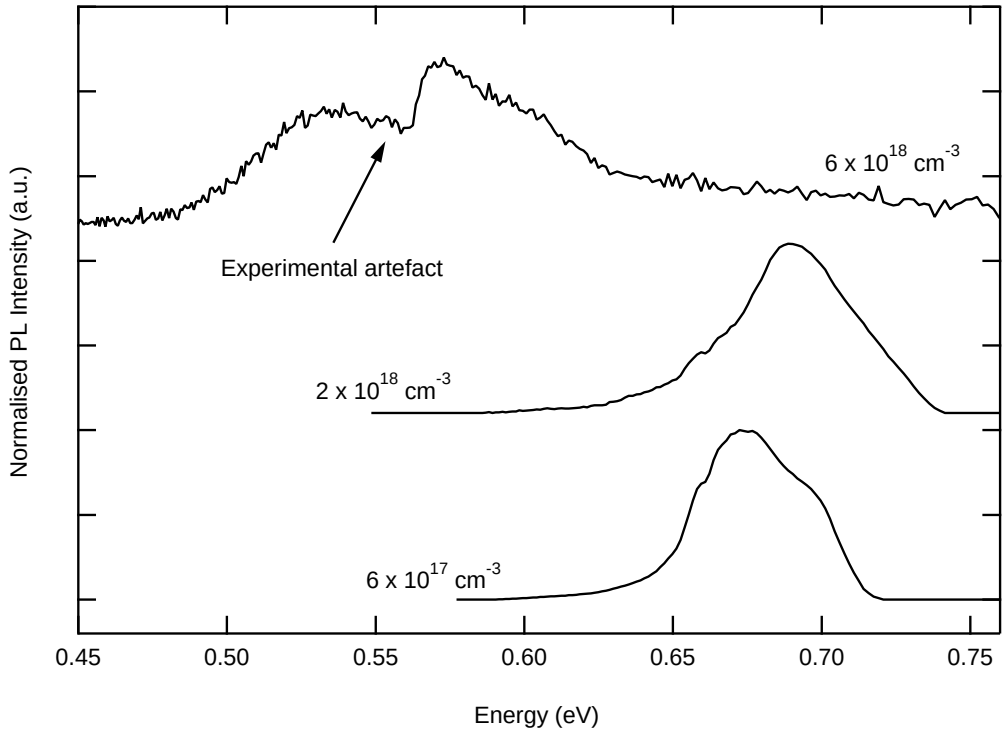

Figure 4.15 Photoluminescence emission from three Mg doped InN films grown on (0001) Ga-polar GaN templates.

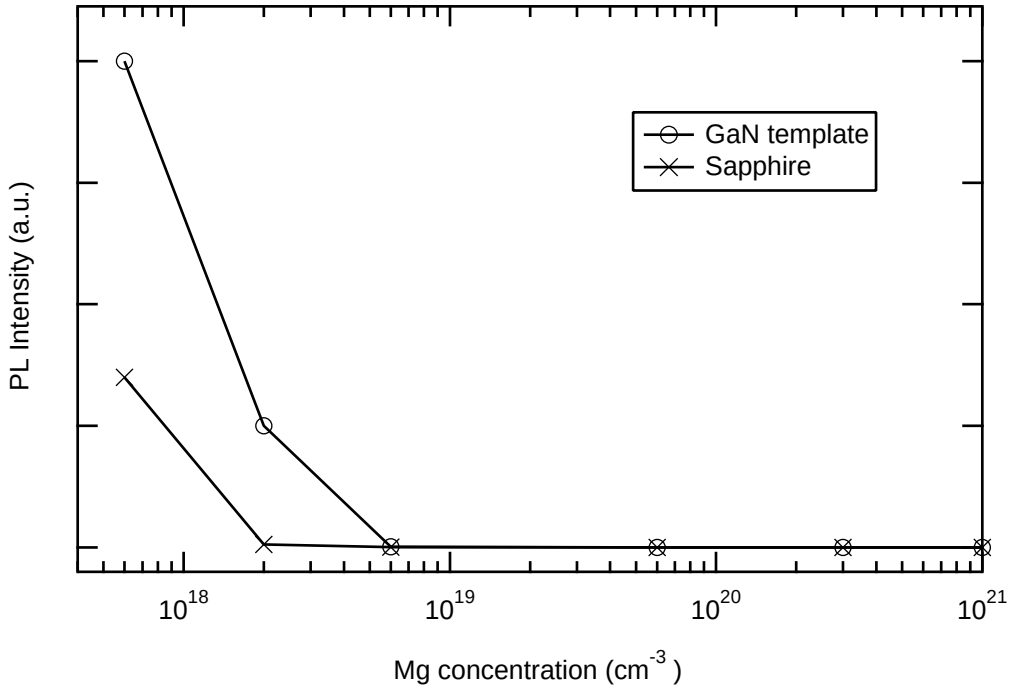

Figure 4.16 The PL peak intensity measured from Mg doped InN films grown on (0001) sapphire and (0001) Ga-polar GaN templates.

signal should actually peak near 0.56 eV. The lineshape of this signal is much broader than the lower Mg concentration samples, with a FWHM of 100 meV. If the 0.56 eV signal is related to the presence of Mg within the film, it is surprising not to see any evidence of the feature within the other two samples. Should this feature be related to transitions between conduction band edge and a Mg acceptor level, it would indicate a Mg acceptor level approximately 110 meV above the valence band edge.

Figure 4.16 shows the PL intensity of InN films grown on both sapphire and GaN templates. As mentioned earlier, the quenching of PL ceases at Mg contents of $\sim 10^{19}$ cm^{-3}. As the Mg content is further reduced, the PL intensity continues to increase until at 6×10^{17} cm^{-3}, the intensity is comparable to that of undoped films. Jones *et* al. also observed similar quenching of PL in Mg doped films, although the 0.56 eV feature was not observed in their study. It was suggested that the quenching could be due to strong electric fields near the surface of the film. Electric fields within the depletion region do offer a plausible explanation for the quenching of PL. Effectively, a buried p-type layer accompanying a surface accumulation layer forms a basic photovoltaic cell. Any electron and holes generated in the vicinity of the depletion region will be pushed in opposite directions and separated, hence radiative recombination will be stifled.

A problem with this model is that if the n-type and p-type layers within the material are not grounded, charging will occur. This would lead to an accumulation of electrons on one side of the junction and holes on the other side. Eventually, the field caused by this charging would cancel out the field in the depletion region and there would be no net force separating electron hole pairs. Although the samples are not intentionally grounded during PL, the samples are mounted with silver paste which could conceivably circumvent this problem.

4.5 SUMMARY OF DEFECTS AND DOPANTS IN INDIUM NITRIDE

Of the experimental techniques and dopants explored in this chapter, in-situ magnesium doping has shown the most promise as a potential route to achieving p-type InN. Indeed, there is already preliminary evidence that buried p-type layers may exist within some of the Mg doped layers studied. Ion implantation is a very versatile tool for exploring a wide range of potential dopants, but in the case of InN, it appears to be largely incompatible. This is due to the low dissociation temperature of InN preventing rapid thermal annealing at sufficient temperatures to repair implantation induced lattice damage. The behaviour of native defects in InN may also prevent ion induced damage assisting with device isolation as in common with other materials. Nitrogen related native defects in InN were explored via NEXAFS. Several donor states were identified, although the levels were visible only after nitrogen bombardment, and did not seem to account for the background carrier concentration. Indium related native defects, and in particular nitrogen vacancies remain the main candidates for the intrinsic n-type behaviour. The source of donors resulting in the surface electron accumulation layer was explored via variable field Hall effect. In-polar films grown on (111) YSZ exhibited significantly different accumulation profiles than N-polar films grown on sapphire. This observation was related to the likely termination conditions of the different surfaces.

Chapter 5

MAGNETIC AND OPTICAL PROPERTIES OF INDIUM CHROMIUM NITRIDE ALLOYS

5.1 MAGNETIC ORDER IN THE SOLID STATE

5.1.1 Electrons, magnetism and the spin degree of freedom

Elementary particles such as electrons, protons and neutrons are classified as either bosons or fermions. The key difference between the two types of particles is how they behave when they interact with other identical particles. Bosons form symmetric composite wave functions, while fermions form antisymmetric composite wave functions. A consequence of this is that two bosons may occupy the same quantum state, but fermions may not. This is known as the Pauli exclusion principle and lies at the heart of magnetic order in materials.

Most people are familiar with the common attributes of mass and charge which characterise fermions and bosons. Less familiar is the equally intrinsic property of spin. Spin describes the inherent magnetic dipole which is associated with electrons and certain other elementary particles. Spin is represented by the quantum number S; for electrons, S can be 1/2 or -1/2. When electrons combine with nuclei to form atoms, they can fill each available energy level with two electrons — the two electrons have opposite spin, which prevents a breach of the Pauli exclusion principle. This tendency for electrons to fill each energy level twice, with two electrons of equal and opposite spin, results in the magnetic dipole contribution from most electrons being cancelled out (often referred to as electron pairs). However, when atoms contain an

odd number of electrons, or the filling sequence is altered by spin interactions, an atom may have a net spin magnetic dipole associated with it. Hund's rule describes how some atoms adopt lower energy states by having a number of unpaired electrons and hence a net magnetic dipole [147]. The phenomenon arises from the interaction of electron spins in the d-shell and therefore often occurs in transition metal atoms (which have partially filled d-shells). The rare earth metals also exhibit a similar effect from partially filled f-shells, however, they are not considered in detail here. This is why many of the transition metals (and rare earths) form ferromagnetic, ferrimagnetic or antiferromagnetic materials. These three types of magnetic order describe how nearby atoms, with net magnetic moments, interact.

5.1.2 Types of magnetic order

Figure 5.1 illustrates three different types of magnetic order. The diagrams present a simplistic two-dimensional description of the phenomenon but the concepts are extendable to three-dimensions. Figure 5.1(a) shows the atomic level order characteristic of a ferromagnetic material. Dipoles of nearby atoms align to form magnetic domains (not shown); the moments of the individual atoms add together to form a total domain moment. Different domains will have magnetic dipoles pointing in different directions, but under the influence of a critical magnetic field these domains become aligned, and remain aligned after the field is removed.

Figure 5.1(b) shows the atomic level order characteristic of antiferromagnetism. In this case, nearby lattice sites couple with magnetic dipoles in opposite directions. This has the net effect of canceling out magnetic moments, and hence there is no net dipole. There are a number of different short range orders possible for antiferromagnetism; the common attribute is that the net magnetic moment is always zero. Figure 5.1(c) shows a possible short range order arrangement for a ferrimagnetic film. In ferrimagnetic order some nearby atoms couple with dipoles parallel and others with antiparallel dipoles. This form of magnetism is more common in compounds of two or more different magnetic elements. All ferrimagnetic films result in a net magnetic dipole, and like ferromagnetic films form magnetic domains.

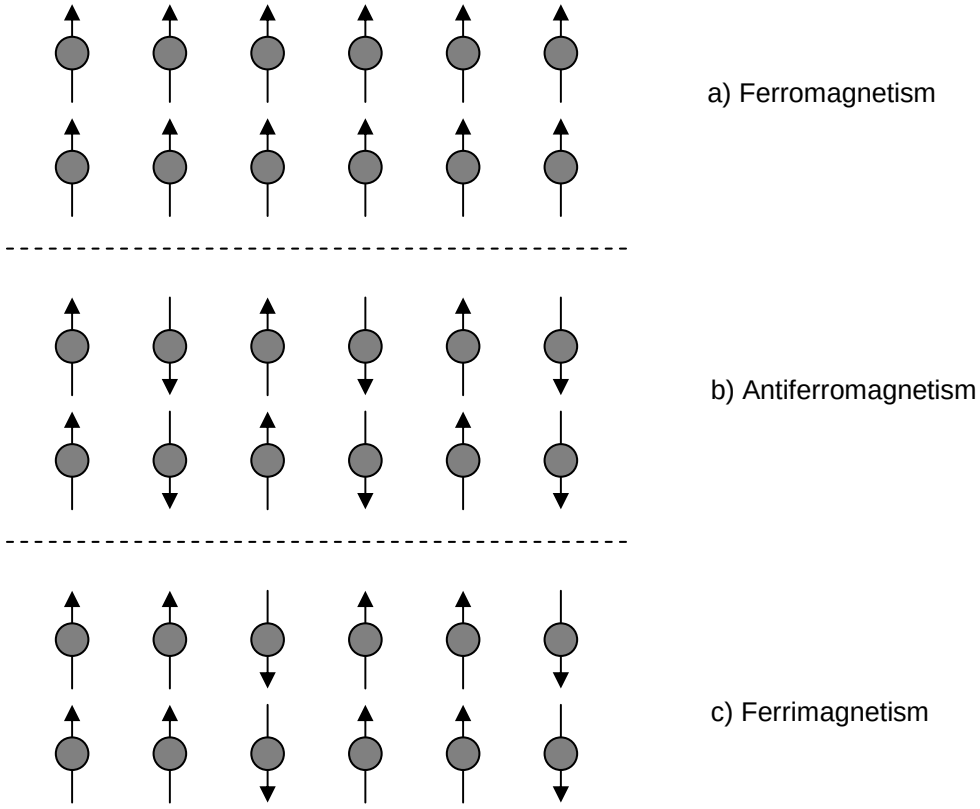

Figure 5.1 A description of how short range magnetic order influences which form of magnetism manifests itself in a magnetic material. The circles and arrows represent atoms with the corresponding magnetic moment. (a) Ferromagnetism. (b) Antiferromagnetism. (c) Ferrimagnetism.

5.2 MAGNETISM AND SEMICONDUCTORS

5.2.1 Spin injection layers

As discussed in section 1.5, an emerging area of interest is the use of the spin degree of freedom within conventional electronics [34]. One of the major obstacles to be overcome in this area dubbed, "spintronics," is the development of efficient spin injecting layers. For a material to be useful as a spin injecting layer, the material must provide some mechanism which forces carriers within the material to have a degree of spin correlation. In conventional ferromagnets, the intrinsic magnetic field serves to align the spin of carriers. However, conventional ferromagnets are metals and passing current through metal-semiconductor interfaces is a strongly depolarising process [35]. As a result, most electrons lose their spin alignment when injected across a metal-semiconductor interface.

This problem can be avoided by using a semiconductor as the spin injection layer. The problem now becomes engineering a material which is both semiconducting and ferromagnetic. A diluted magnetic semiconductor is such a material. In a diluted magnetic semiconductor, the potential for magnetic order is created by replacing a fraction of the host semiconductor with transition metal atoms. Under certain circumstances, the transition metal atoms within the semiconductor host will couple magnetically to form one of the orderings outlined in figure 5.1. If this order is ferromagnetism, then carriers may be polarised and the DMS could be suitable as a spin injection layer.

Another approach to spin injection layers has been the use of the half-metal double perovskites [34, 148]. The name "half-metal" arises as carriers of one spin polarisation have a forbidden gap, while those of the other spin polarisation do not. This effectively means that carriers of one spin are semiconducting while the other spin is metallic. It has been proposed by many that this property could be exploited to provide spin injection into semiconductors. This family of materials is still in its infancy, and is mentioned here for completeness only. This chapter focuses on the use of diluted magnetic semiconductors as spin injection layers and in particular an experimental investigation of the potential DMS $In_{1-x}Cr_xN$.

Incorporating magnetic ions into a semiconducting host to produce diluted magnetic semiconductors was first explored extensively in the II-VI semiconductors. In particular, $Zn_{1-x}Mn_xTe$ and $Cd_{1-x}Mn_xSe$ were heavily studied. Unfortunately from a spin injection point of view, these material systems emerged as having exclusively antiferromagnetic ordering [149]. More recently $Ga_{1-x}Mn_xAs$ and $In_{1-x}Mn_xAs$ have received considerable attention as the magnetic order in these materials was found to be ferromagnetic, although, the Curie temperatures of both remain well below room temperature. As mentioned in section 1.5 a range of wide bandgap magnetic semiconductors have been recently reported to exhibit ferromagnetic order. These materials include $Ga_{1-x}Mn_xN$ [39], $Ga_{1-x}Cr_xN$ [40], $Al_{1-x}Cr_xN$ [41], $Zn_{1-x}Co_xO$, $Ti_{1-x}Co_xO_2$ [42] and $Sn_{1-x}Co_xO_2$ [43].

The origin of ferromagnetism in many of these apparently high Curie temperature DMS has been the subject of debate. Clustering of magnetic atoms within a semiconductor can lead to "pockets" of ferromagnetic material within the layer. Although these regions may make the layer exhibit characteristics typical of a DMS, they cause little or no polarisation of free carriers, and hence the material will not be suitable for spin injection layers. No obvious source of clustering has been identified in these layers, however, clusters of only several atoms are difficult to detect. Such clusters have the potential to produce ordering with high Curie temperatures. There are also inconsistencies between the theoretically predicted and experimentally observed Curie temperatures, given the free carrier concentrations of the layers [38].

5.2.2 Modeling magnetisation in dilute magnetic layers

The common quantity measured in magnetic experiments is magnetisation. The magnetisation of a material represents the contribution made to magnetic field strength by dipoles within a material. Magnetisation is related to magnetic field strength by:

$$\vec{M} = \chi \vec{H} \tag{5.1}$$

where $\vec{M}$ is the magnetisation, χ is the magnetic susceptibility and $\vec{H}$ is the magnetic field strength. Measuring the magnetisation as a function of temperature and magnetic field strength are common approaches to distinguish paramagnetic and ferromagnetic responses, which are typically the dominant responses in a dilute magnetic system such as a DMS. This section considers the theoretical temperature dependent magnetisation of paramagnetic and ferromagnetic materials.

To derive the temperature dependence of a dilute paramagnetic system containing N identical magnetic dipoles we start by noting that the energy of a single dipole in a magnetic field is given by:

$$E = \vec{d} \cdot \vec{B} \tag{5.2}$$

where E is the potential energy, $\vec{d}$ is the magnetic dipole moment and $\vec{B}$ is the magnetic field (defined as $\vec{B} = \mu\vec{H}$ where μ is the magnetic permeability). In order to create an expression for a paramagnetic response of a group of such dipoles we need to construct an expression for the expected value of the dipole under an applied field. From equation 5.2 we note that the minimum and maximum energies of the system are $E_{min} = -dB$ and $E_{max} = dB$, respectively. As the transition between these two energy levels is well behaved, we can approximate the system as two discrete levels by assuming that each magnetic dipole adopts either E_{min} or E_{max}. With this assumption we can write the expected value for the potential energy as:

$$\langle E \rangle = E_{min}P(E_{min}) + E_{max}P(E_{max}) \tag{5.3}$$

where $\langle E \rangle$ is the expected value of E, $P(E_{min})$ is the probability that a single dipole adopts E_{min}, and $P(E_{max})$ is the probability that a single dipole adopts E_{max}. An expression for each of the probabilities can be constructed by using the Boltzmann factor [150] which describes the relative probability of occupation for systems in ther-

modynamic equilibrium as:

$$f(T, E) = e^{-\frac{E}{kT}} \tag{5.4}$$

where T is the temperature, E is the potential energy and k is the Boltzmann constant. Applying this to E_{min} and E_{max} we get $f(T, E_{min}) = e^{\frac{dB}{kT}}$ and $f(T, E_{max}) = e^{-\frac{dB}{kT}}$ as the relative probabilities the two states will be occupied. To turn these factors into an absolute probability the two expressions must be normalised so that the sum of the two probabilities is 1:

$$Ze^{\frac{dB}{kT}} + Ze^{-\frac{dB}{kT}} = 1 \tag{5.5}$$

$$Z = \frac{1}{e^{\frac{dB}{kT}} + e^{-\frac{dB}{kT}}} \tag{5.6}$$

$$Z = \frac{1}{cosh(\frac{dB}{kT})} \tag{5.7}$$

where Z is the normalising factor and is also known as the "partition function". Applying Z to normalise $f(T, E_{min})$ and $f(T, E_{max})$ lets us rewrite equation 5.3 as:

$$\langle E \rangle = \frac{-dB}{cosh(\frac{dB}{kT})} e^{\frac{dB}{kT}} + \frac{dB}{cosh(\frac{dB}{kT})} e^{\frac{-dB}{kT}} \tag{5.8}$$

$$\langle E \rangle = \frac{dB sinh(\frac{dB}{kT})}{cosh(\frac{dB}{kT})} \tag{5.9}$$

$$\langle E \rangle = dB tanh(\frac{dB}{kT}) \tag{5.10}$$

and finally by using equation 5.2 we can write the magnetisation of N dipoles as:

$$M = dN tanh(\frac{dB}{kT}) \tag{5.11}$$

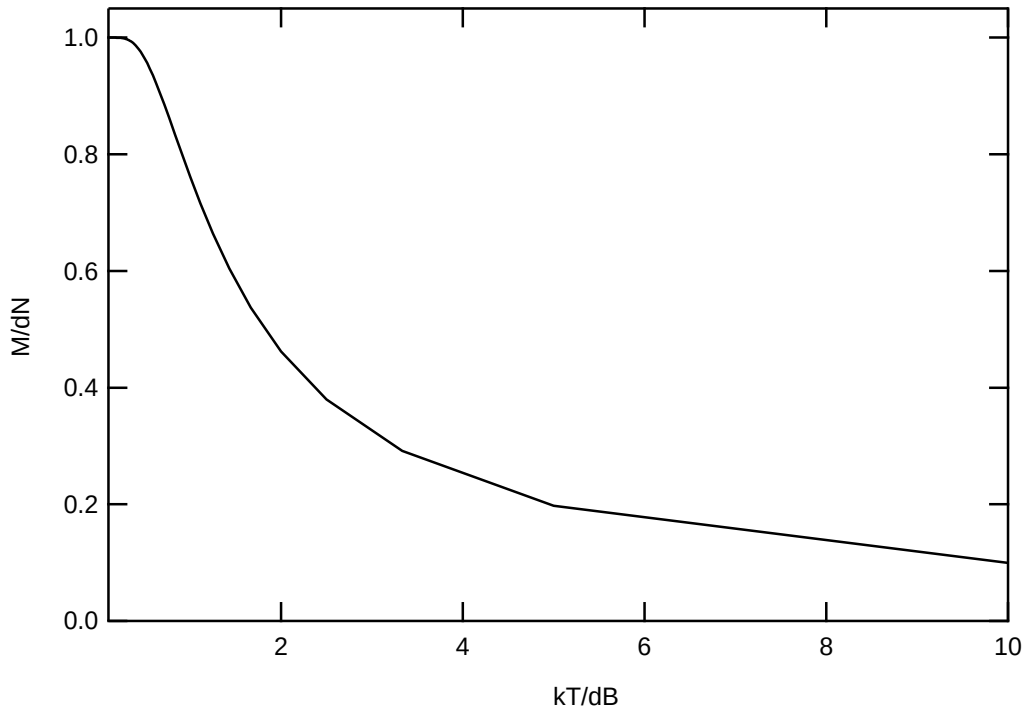

Figure 5.2 The temperature dependent magnetisation of a paramagnetic material relative to its 0 K magnetisation.

Figure 5.2 shows the temperature dependent magnetisation of a paramagnetic material relative to its 0 K magnetisation. A paramagnetic material is characterised by the strong enhancement in magnetisation at low temperatures. Typically the saturation observed when kT/dB <1 will occur at <5 K. For many common regimes $\frac{dB}{kT} >> 1$, so that $tanh(\frac{dB}{kT}) \approx \frac{dB}{kT}$ and the expression can be approximated by the commonly used Curie's law:

$$M = \frac{d^2NB}{kT} \tag{5.12}$$

Which shows that the magnetisation is inversely proportional to temperature. It is this strong enhancement of magnetisation at low temperature which can be used to distinguish paramagnetism from other magnetic phenomena. Having developed an expression to describe the temperature dependent magnetisation of a paramagnetic system we now turn our attention towards the ferromagnetic case. Ferromagnetic

order is a cooperative phenomenon, as such a complete solution requires the evaluation of the interaction of each electrons with every other electron. Computationally this is not a feasible approach and simplifications are routinely made. A common approach is the mean field approximation [151] which assumes that the field at any lattice site can be approximated by $B_{eff} = B_{loc} + B_{mag}$, where B_{loc} represents the local field at the atom and B_{mag} the field due to all other atoms within the lattice. This assumption allows us to use the approach adopted when calculating the paramagnetic response, but B is replaced by B_{eff} so that:

$$M = dNtanh(\frac{dB_{eff}}{kT}) \tag{5.13}$$

now by assuming $\frac{dB_{eff}}{kT} >> 1$ we can write:

$$M = \frac{d^2N}{kT}(B_{loc} + B_{mag}) \tag{5.14}$$

$$M = \frac{d^2N}{kT}(B_{loc} + \mu_0\lambda M) \tag{5.15}$$

or, more simply,

$$M = \frac{C}{T - T_C}B \tag{5.16}$$

where λ is a constant representing the portion of the relative permeability which corresponds to M, $T_C = Nd^2\lambda\mu_0/k$ is the Curie temperature and $C = Nd^2/k$. This is the Curie-Weiss law and is commonly used to define the temperature dependence of a ferromagnetic material above the Curie temperature. In order to obtain a complete solution below the Curie temperature we adopt a graphical approach to solve the transcendental function of equation 5.13; by setting $y = M/Nd$ and $x = dB_{eff}/kT$ we can write the solution as the intercepts between the curves [152]:

$$x = \frac{T_C}{T} y \tag{5.17}$$

$$y = tanh(x) \tag{5.18}$$

Figure 5.3 shows the graphical solution for $T/T_C = 1$, $T/T_C = 3/4$ and $T/T_C = 1/2$. The M/dN value of each intercept is then plotted against T/T_C to give the temperature dependent magnetisation relative to the 0 K magnetisation as a function of temperature as shown in figure 5.4.

The temperature dependent magnetisation of a ferromagnetic material is typified by a sharp turn-on in the observed magnetisation at the Curie temperature. Above T_C the magnetisation can be expected to be relatively constant with temperature. On an atomic level the Curie temperature signals the point at which the available thermal energy (kT) exceeds the energy gain electrons achieve by adopting an ordered magnetic state.

5.2.3 Carrier mediated exchange interactions

The mean field approach adopted in section 5.2.2 assumes only that there are interactions between spins which can be approximated by an average field; the nature of these interactions is not considered. Many different exchange interactions occur in materials, and determining which type of magnetic order a material will adopt often involves evaluating the influence of several different, possibly competing, exchange interactions. For example, in elemental chromium, the exchange integral is dominated by direct interactions between nearest neighbour d-shell electrons (superexchange), which results in antiferromagnetic order. However, second nearest neighbour atoms interact via an indirect exchange which favours ferromagnetic order. As the second nearest neighbour interaction is weak relative to the nearest neighbour, the material is antiferromagnetic. In DMS materials the direct interaction is thought to be small, the exchange integral dominated by an indirect carrier mediated exchange involving holes [38]. Figure 5.5 shows a diagram of two different exchange interactions occurring in a DMS. The direct

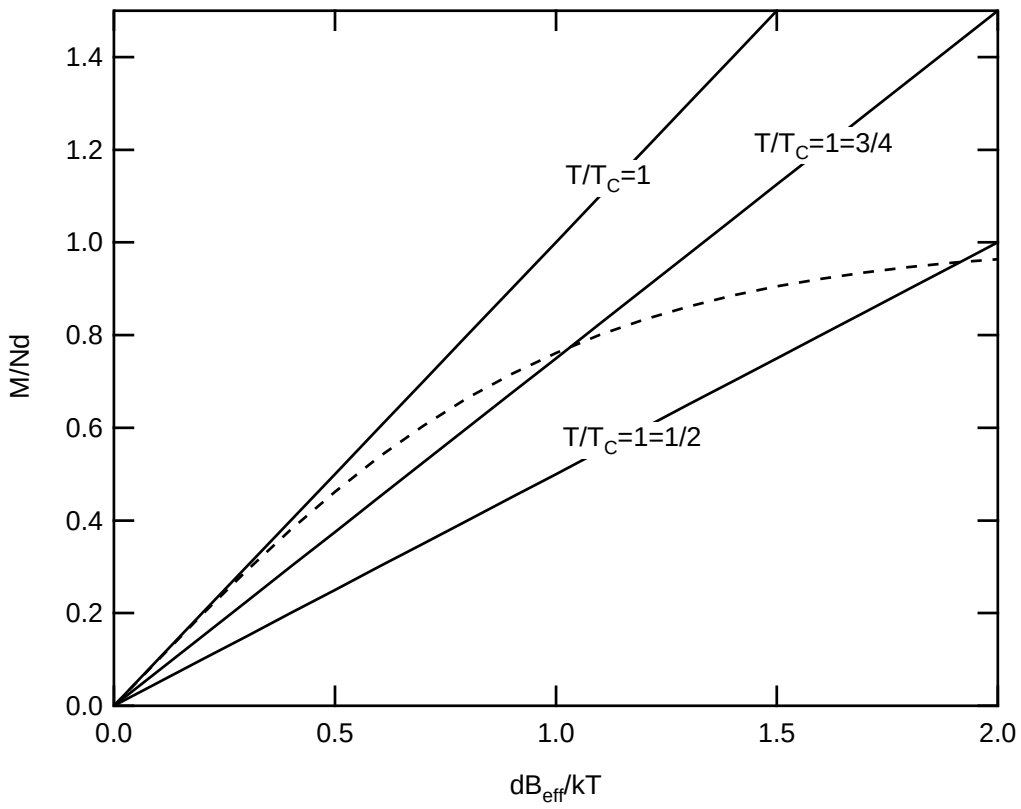

Figure 5.3 A graphical approach to solving the transcendental function of equation 5.13. For a given line $x = \frac{T_c}{T}y$ the intercept with $y = tanh(x)$ (dashed curve) gives the magnetisation as a function of $\frac{T_c}{T}$.

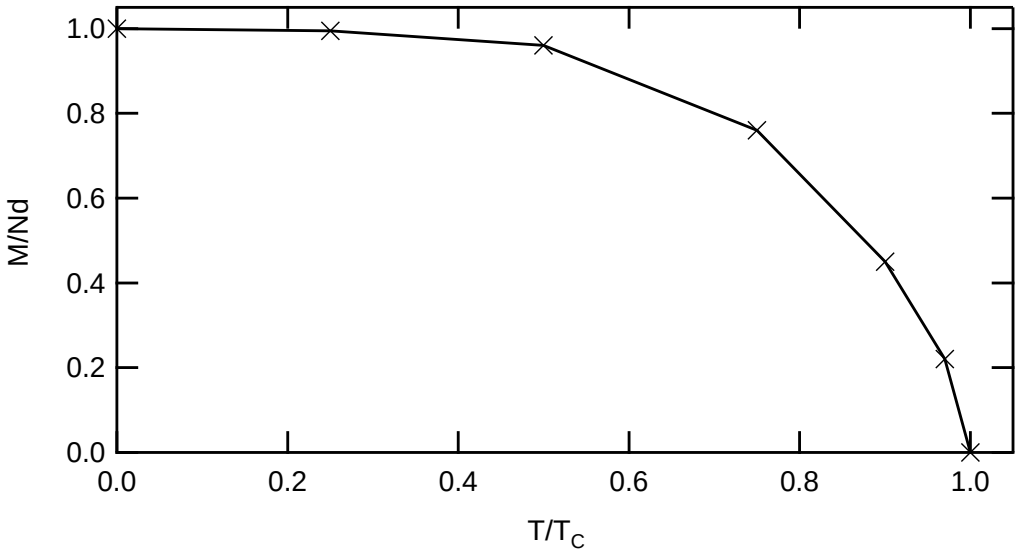

Figure 5.4 The temperature dependent magnetisation of a ferromagnetic material relative to its 0 K magnetisation.

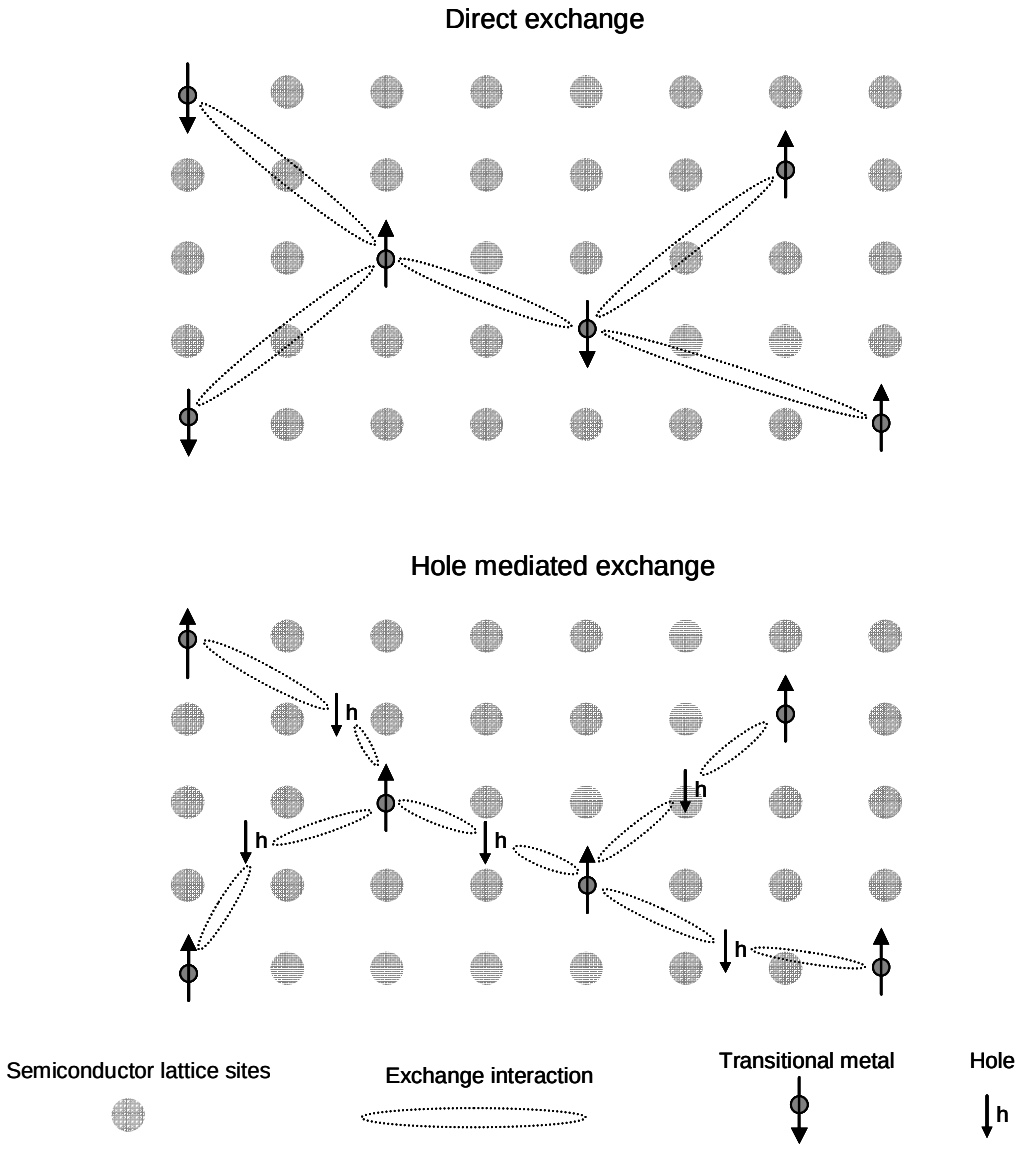

Figure 5.5 Two different exchange interactions that can lead to magnetic order in diluted magnetic semiconductors. The direct exchange, also known as the superexchange (top), and hole mediated exchange (bottom).

exchange depicts an interaction resulting in antiferromagnetic order. The hole mediated interaction shows an interaction resulting in ferromagnetic order. Other exchange interactions may involve multiple carriers and combinations of electrons and/or holes.

Several models exist which attempt to describe carrier mediated ferromagnetism in dilute magnetic semiconductors. The recent work by Dietl *et* al. proposes a mean field model of hole mediated ferromagnetism in wide bandgap semiconductors [38]; this work predicts that room temperature ferromagnetism could occur in a number of heavily p-type Mn-doped semiconductors. The most widely applied theory to explain DMS behaviour has been the Ruderman, Kittel, Kasuya and Yosida (RKKY) approach [153, 154], which also suggests that high p-type carrier concentrations are required for mediated exchange to take place. The RKKY interaction has been used to accurately describe the Curie temperatures observed in $Ga_{1-x}Mn_xAs$, and has also predicted the transition to paramagnetism which $Ga_{1-x}Mn_xAs$ undergoes when the hole concentration is reduced. No well developed carrier mediated exchange model exists to explain ferromagnetism in n-type DMS. For this reason, there remain many opinions in the scientific community as to how clustering may be responsible for observed ferromagnetism in n-type materials such as $Ga_{1-x}Mn_xN$.

5.3 DISTINGUISHING CLUSTERING EFFECTS AND CARRIER MEDIATED EXCHANGE

With the origins of magnetism in some apparently high Curie temperature DMS remaining unclear, considerable effort has been made to search for clusters in DMS. Although the bulk phase of many of the transition metals is antiferromagnetic, nanoscale clusters of the materials may adopt ferromagnetic order. This arises as clusters of up to several hundred atoms often adopt different crystal structures, and hence possibly different magnetic states from the bulk form of the material. If a semiconductor contains nanoscale inclusions of a ferromagnetic material, the cluster based ferromagnetism may be difficult to distinguish from the carrier mediated case, particularly if the clusters contain only a few tens of atoms. Common structural analysis techniques have difficulty detecting structures of this size. Clusters may also include transition metal rich alloys

with the host constituents — for example, $GaMn_3N$ clusters in $Ga_{1-x}Mn_xN$ [155].

5.3.1 X-ray diffraction

The most common and accessible structural analysis technique which is applied to DMS is X-ray diffraction (XRD). XRD is a good technique for exploring bulk crystal structures and major secondary phases, but the sensitivity of the technique when detecting small clusters is limited by Scherrer's law. The law describes how the FWHM of a two theta XRD peak broadens as the cluster size becomes smaller:

$$FWHM = \frac{0.94\lambda}{Dcos\theta} \tag{5.19}$$

where λ is the wavelength of the X-rays used, D is the diameter of the cluster, and θ is the angle at which the peak is measured (taken from the surface normal to the incident beam). If we apply this to a 10 nm cluster, measured at 80° with 0.151 nm X-rays, the FWHM is 4.8°. This is a very broad peak, which would likely be close to the detection limit of common XRD systems, given that the cluster would likely make up $< 1\%$ of the vloume [156]. Aghamalyan *et* al. used XRD to detect 25 nm diameter gallium clusters within a zinc oxide crystal which comprised $\sim$2% of the cation atoms [157]. All factors considered, this size of cluster is approaching the limit of the XRD technique in a diluted system. However, a 20 nm diameter cluster is relatively large on an atomic level and would contain on the order of 50,000 atoms. It has been suggested that clusters with less than 10 atoms (diameters $\sim$1 nm) could result in the observed magnetic responses of apparently high Curie temperature DMS [158]. As a result, XRD can be expected to detect major phase segregation within a DMS material but not atomic scale clusters.

5.3.2 Transmission electron microscopy

An alternative technique which can resolve atomic level detail is transmission electron microscopy (TEM). As such TEM does have the potential to detect small clusters

within DMS, particularly if the clusters adopt an alternative crystal structure to the host crystal. If however the clusters adopt the crystal structure of the host, they are difficult to detect. Detection may also be problematic if the clusters tend to accumulate in areas of high disorder, such as threading dislocations. The other major drawback to TEM is time and resources. Making a TEM measurement requires a great deal of sample preparation and it is not trivial to examine large areas of the crystal under high resolution. Therefore, if clusters are sparse they may fall outside the area of investigation. Nonetheless, TEM does offer a complimentary tool to XRD for exploring the presence of clusters in DMS. An added advantage of the TEM technique is the compositional X-ray techniques which can be combined with the TEM measurement. In particular, secondary X-rays detected during scanning measurements may allow some compositional profiles to be obtained. This technique is known as electron induced X-ray emission (EIXE) and is useful for determining where magnetic dopants reside in DMS layers.

5.4 GROWTH OF INDIUM CHROMIUM NITRIDE ALLOYS

The University of Canterbury MBE system as described in section 2.2 was used for the growth of $In_{1-x}Cr_xN$ and CrN thin films. The RF plasma source was operated at 1.25 sccm and 250 W, and the indium flux was kept constant at 1.2×10^{14} atoms.cm^{-2}s^{-1} for all $In_{1-x}Cr_xN$ film growths. This In:N flux ratio resulted in growth in the N-rich regime for InN films. The chromium flux was varied in the range of 2×10^{11}-5×10^{12} atoms.cm^{-2}s^{-1} for $In_{1-x}Cr_xN$ growth, as calculated from theoretical flux tables after calibration at high flux with the quartz crystal microbalance. Although the total metal to nitrogen flux ratio does change with the varying chromium fluxes, the film growth regime is expected to remain in the N-rich regime for all $In_{1-x}Cr_xN$ films. For CrN growth, the Cr flux was kept fixed at 1×10^{14} atoms.cm^{-2}s^{-1}. (0001) sapphire substrates were used for all film growth experiments after nitriding for 15 min at 650°C. For $In_{1-x}Cr_xN$ growth a 150 nm GaN buffer layer was deposited at 650°C, followed by 150 nm of InN at 450°C, and finally 600 nm of $In_{1-x}Cr_xN$ at 450°C. CrN films were deposited directly on nitrided sapphire and were 500 nm thick. Growth rates for InN,

$In_{1-x}Cr_xN$, CrN and GaN were ∼250 nm/h. Growth was monitored in-situ by 20 kV reflection high energy electron diffraction (RHEED).

The $In_{1-x}Cr_xN$ films, having x ranging from 0.0005 to 0.04, each exhibited a total metal to nitrogen ratio of essentially unity as determined by ion beam analysis. The elemental concentrations were obtained with three different ion beam techniques. NRA was used to determine the total amount of nitrogen in the films, which in turn was used to verify the nitrogen content obtained from RBS. Further, the chromium concentrations measured with PIXE confirmed the values obtained by RBS. Figure 5.6 shows the RHEED patterns for three films of varying Cr content after 30 and 180 minutes into growth. Increased Cr content was found to lead to progressively degraded crystal quality as indicated by RHEED patterns which changed from streaky for x <0.025, to spotty with weak arcs visible in the case of $x = 0.025$ and 0.04. This suggests that there is some a-plane rotation between crystal domains in these films, whereas the lower chromium concentration films have good alignment between domains in the a-plane. The film grown with $x = 0.04$ partially delaminated from the GaN buffer layer, signalling the high level of stress present in the film. This observation is surprising as the lattice match between $In_{1-x}Cr_xN$ and GaN improves with increasing Cr content, assuming that chromium occupies the cation lattice site.

5.5 SEARCHING FOR CLUSTERING

5.5.1 Structural analysis

Atomic force microscopy (AFM), electron backscatter diffraction (EBSD), X-ray diffraction (XRD) and transmission electron diffraction (TEM) were used to search for any evidence of phase separation within the $In_{1-x}Cr_xN$ films. AFM revealed the film surfaces contained plateaus exhibiting hexagonal symmetry which covered increasing proportions of the surface with higher film chromium content, as shown in figure 5.7. The film morphology quickly departs from the smooth appearance of InN with rms roughness <5 nm, to the highly plateaued surfaces of the higher Cr content films with rms roughness >50 nm. EBSD is a structurally sensitive technique which can map the

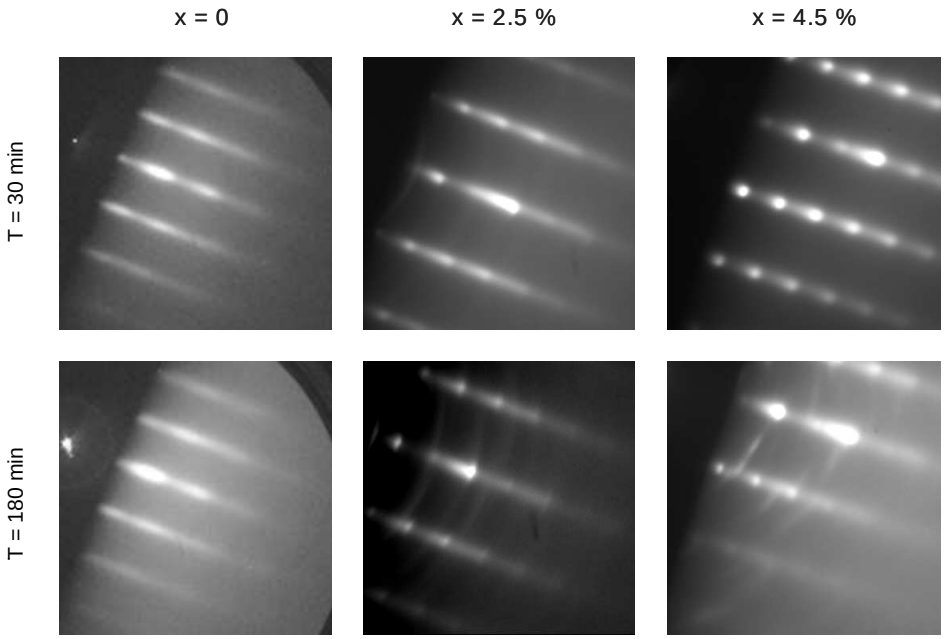

Figure 5.6 RHEED images taken after thirty minutes and at the end of growth (180 min) for three $In_{1-x}Cr_xN$ films, grown under identical conditions except for the Cr content.

crystal structure of the near surface region. EBSD showed that the hexagonal plateaus were the same crystal structure and orientation as the rest of the film, suggesting that they are not precipitates but a product of the growth mode of the films. We have also observed this growth behaviour in InN grown at low substrate temperatures.

Figure 5.8 shows the two theta XRD curves for three high Cr content films. Only features expected from a c-axis oriented wurtzite structure are observed. The weak indium metal peak at 33° originates from In on the backside of the substrate, used to mount the sample. As discussed in section 5.3 this does not exclude atomic scale clusters. However, it does confirm that there is no significant cluster content with diameters >20 nm. The $\alpha(0002)$ peak positions for $x = 0.01$, 0.025 and 0.04 correspond to diffraction plane spacings of 2.9594 Å, 2.9644 Å and 2.9610 Å respectively. For x>0.025 the spacings indicate that the c-axis lattice constant is actually increasing with the addition of the much smaller Cr atoms, contrary to the expected dependence of Vegard's law. This is likely due to a significant amount of the Cr occupying interstitial sites. However, the diffraction spacing for the x=0.04 film is less than that of the x=0.025 film, suggesting that there are two competing processes. It seems likely that

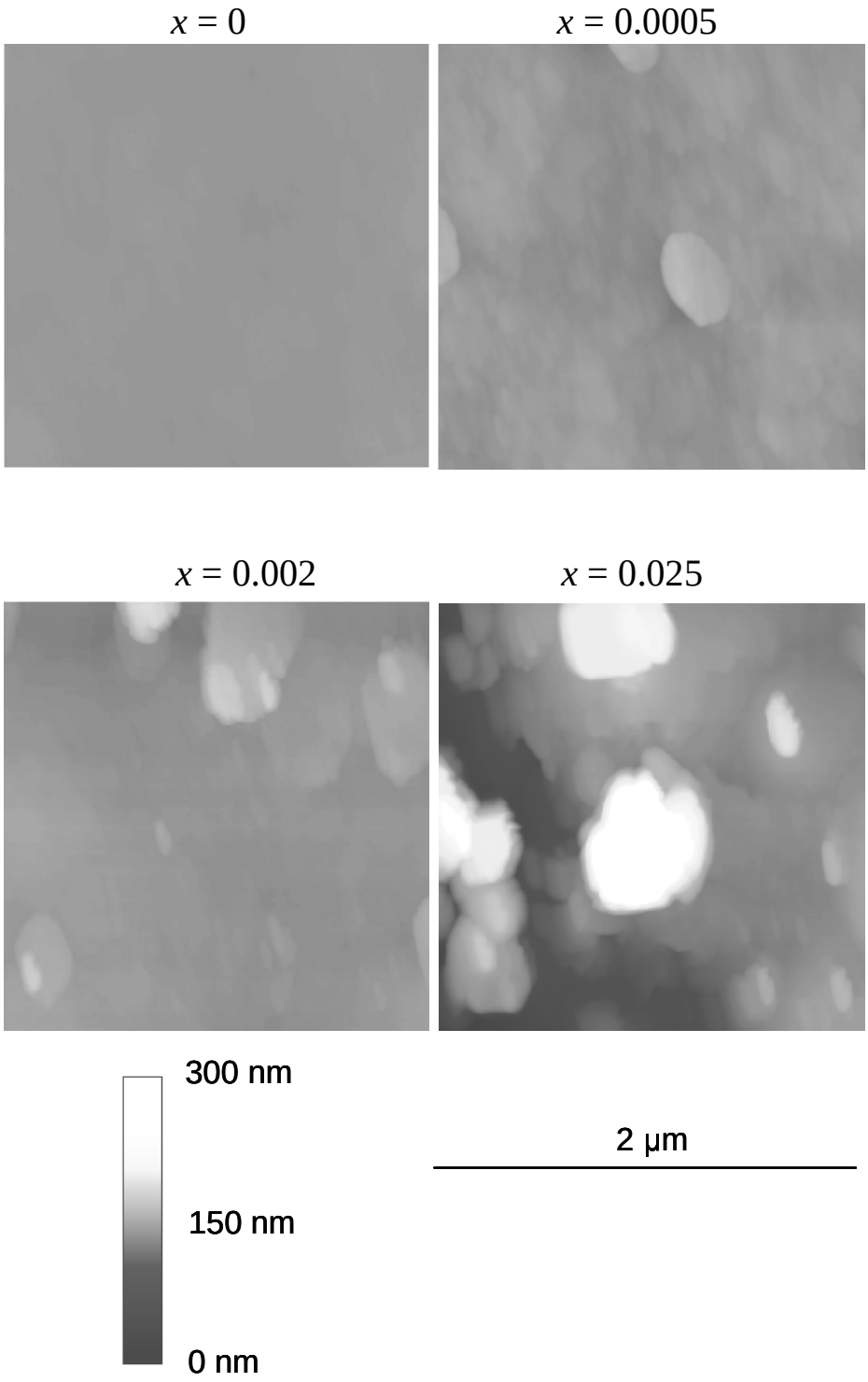

Figure 5.7 AFM images of four $In_{1-x}Cr_xN$ films with varying chromium content.

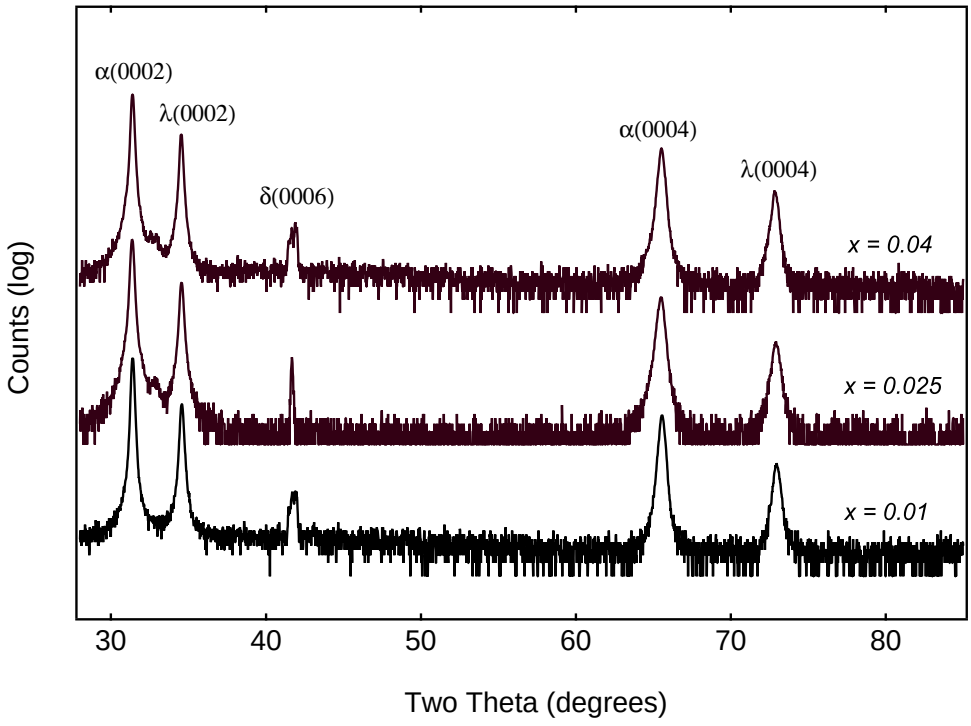

Figure 5.8 Two theta X-ray diffraction scans for $In_{1-x}Cr_xN$ films with $x = 0.01$, 0.025 and 0.04; α denotes InN, λ denotes GaN and δ denotes sapphire peaks. Curves are displaced from each other for clarity.

Cr is occupying both substitutional and interstitial sites with the different locations having competing effects on the measured lattice constant.

With XRD excluding the presence of large clusters, TEM was used to explore whether smaller scale clusters may be present within the films. Figure 5.9 shows high resolution TEM images of an $In_{0.975}Cr_{0.025}N$ film within the magnetic layer (figure 5.9.a) and at the interface between the InN and GaN buffer layer (figure 5.9.b). No evidence of Cr clusters on any level is identifiable within figure 5.9(a) which shows a region of the $In_{0.975}Cr_{0.025}N$ layer 200 nm from the surface. Atomic planes are clearly visible indicating the reasonably high level of short range crystal order in the layer. It must be noted that clusters would only be easily distinguished in this image if they adopted a crystal structure that varied from the InN lattice; small clusters which are substituting for regions of the InN lattice will not be distinguished. The interface region is also explored here as clusters often show a tendency to form at areas of high crystal stress. In such areas the formation of clusters can sometimes assist lattice re-

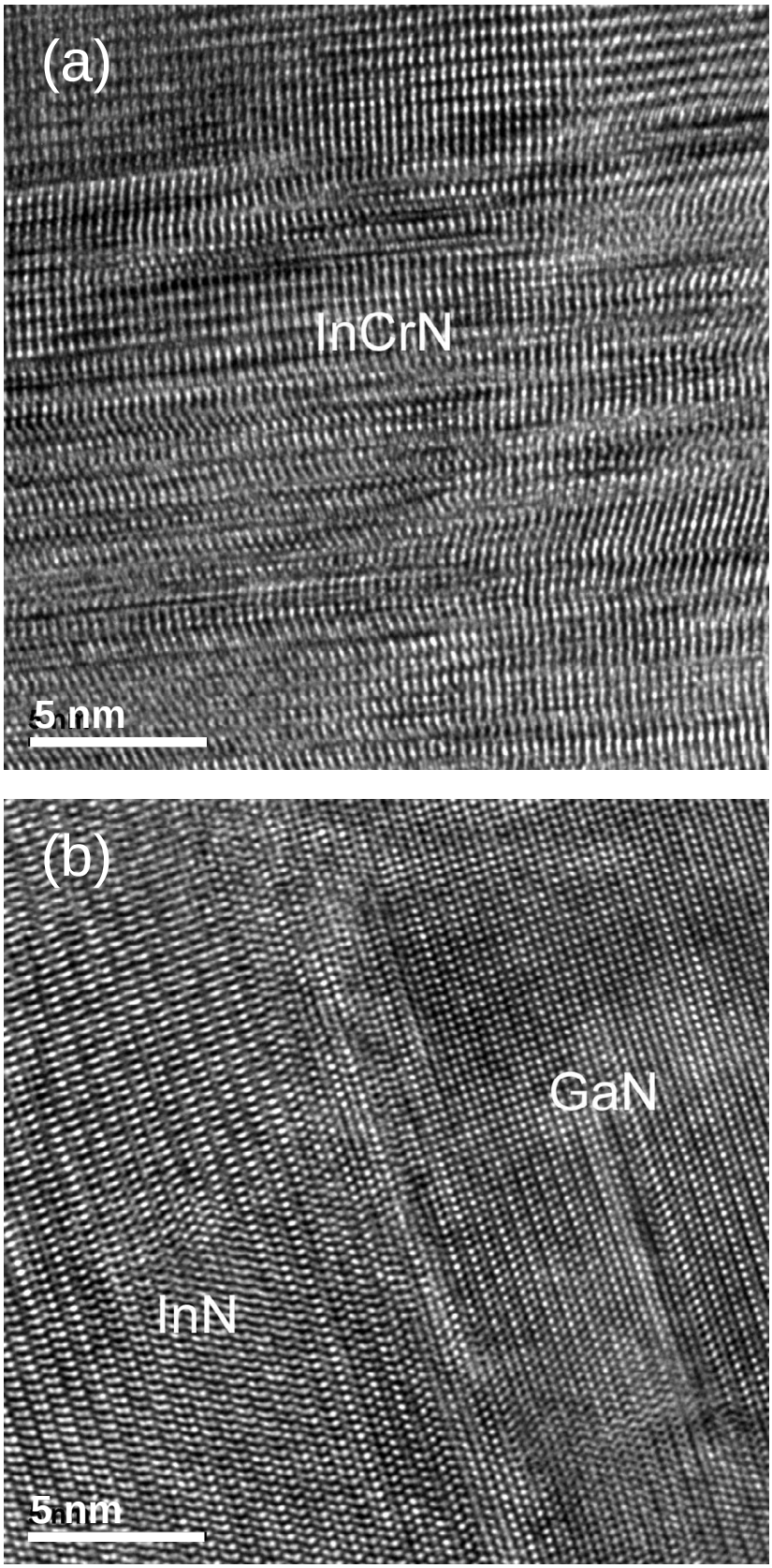

Figure 5.9 High resolution transmission electron microscopy images of an $In_{0.975}Cr_{0.025}N$ film: (a) mid film area of $In_{0.975}Cr_{0.025}N$; (b) the interface between the GaN and InN buffers.

laxation. Figure 5.9(b) shows no evidence for any secondary phases clustering at the interface. Indeed, the crystal order in this region of the film appears greater than that of the presumably more relaxed $In_{0.975}Cr_{0.025}N$ layer. Atomic planes are clearly visible extending unbroken over the full 20 nm of this image. TEM reveals no evidence for any secondary phases in the bulk or at the InN/GaN interface.

5.5.2 Compositional analysis

When scanning TEM is combined with EIXE, it allows a compositional map of a layer to be created. Cross-sectional images of the $In_{0.975}Cr_{0.025}N$ described in figure 5.9 were studied using this technique, the goals being to identify any interdiffusion that was occurring between the various layers, and to measure how chromium was incorporating. Figure 5.10 shows scanning TEM/EIXE images of the $In_{0.975}Cr_{0.025}N$ with characteristic In and Ga X-rays detected by a secondary X-ray probe. The scan reveals that the In and Ga atoms are located almost exclusively in the intended layers — there is little or no mixing occurring between the InN and GaN layers.

Figure 5.11 shows the same measurement made with characteristic Cr X-rays being detected. Although the Cr shutter is only open during the final $In_{0.975}Cr_{0.025}N$ layer, there is significant Cr content in both the InN and GaN layers. This shows that the Cr is very mobile within both lattices. The chromium atom is significantly smaller than both the indium and gallium atoms which may partly explain the high mobility of the element within both lattices. Also, as the films are c-axis oriented, channels within the crystal lattice offer a direct diffusion pathway between layers along the (0001) direction. The evidence for interstitial Cr as determined by XRD also supports this picture. Any Cr atoms diffusing along (0001) channels would occupy a series of interstitial lattice locations. The high mobility of the Cr within both InN and GaN does suggest that migration and clustering of small Cr precipitates is a very real possibility. Figure 5.11 shows no evidence for clustering, although the resolution of this technique is at best ~ 5 nm.

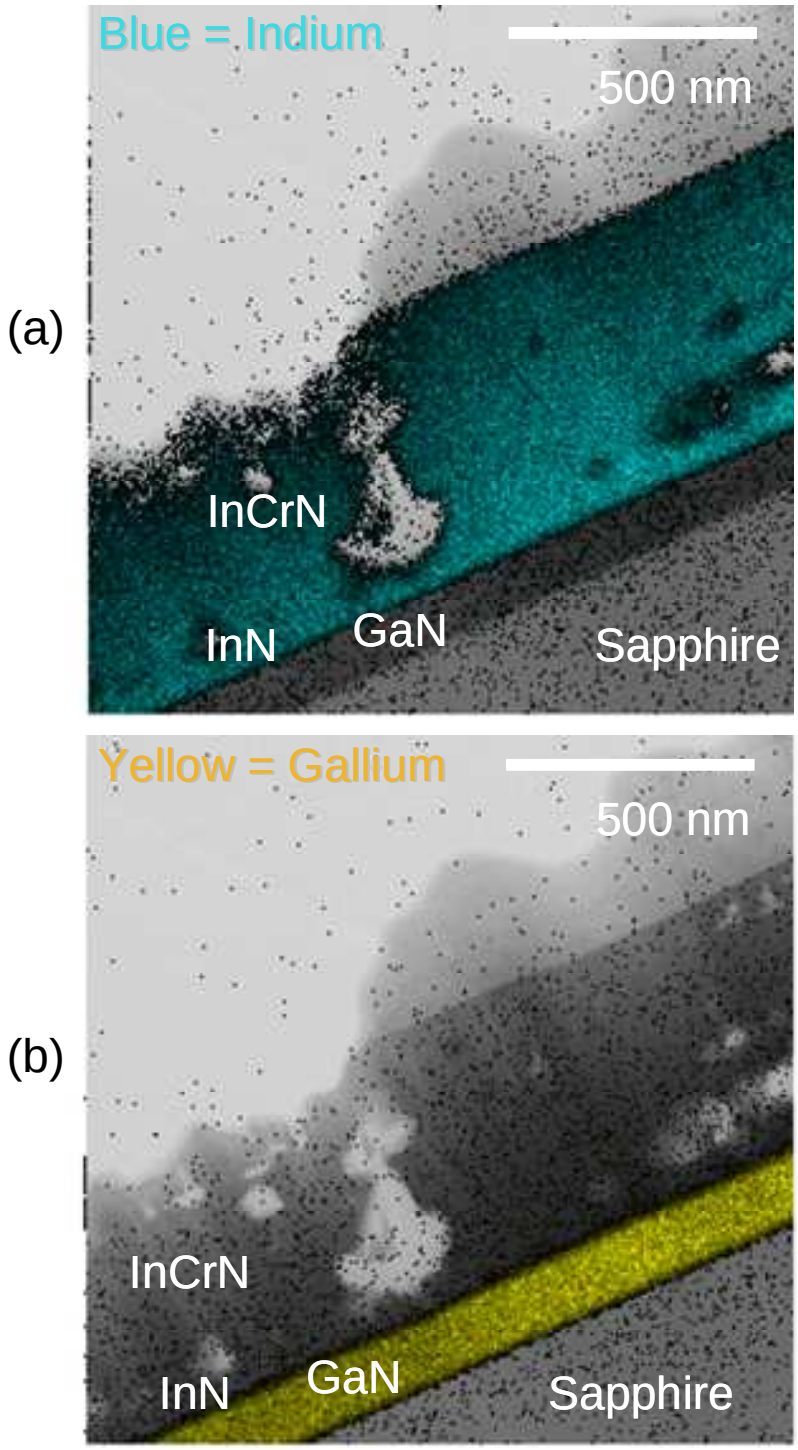

Figure 5.10 Scanning TEM EIXE images of the (a) indium and (b) gallium content within a $In_{0.975}Cr_{0.025}N$ film.

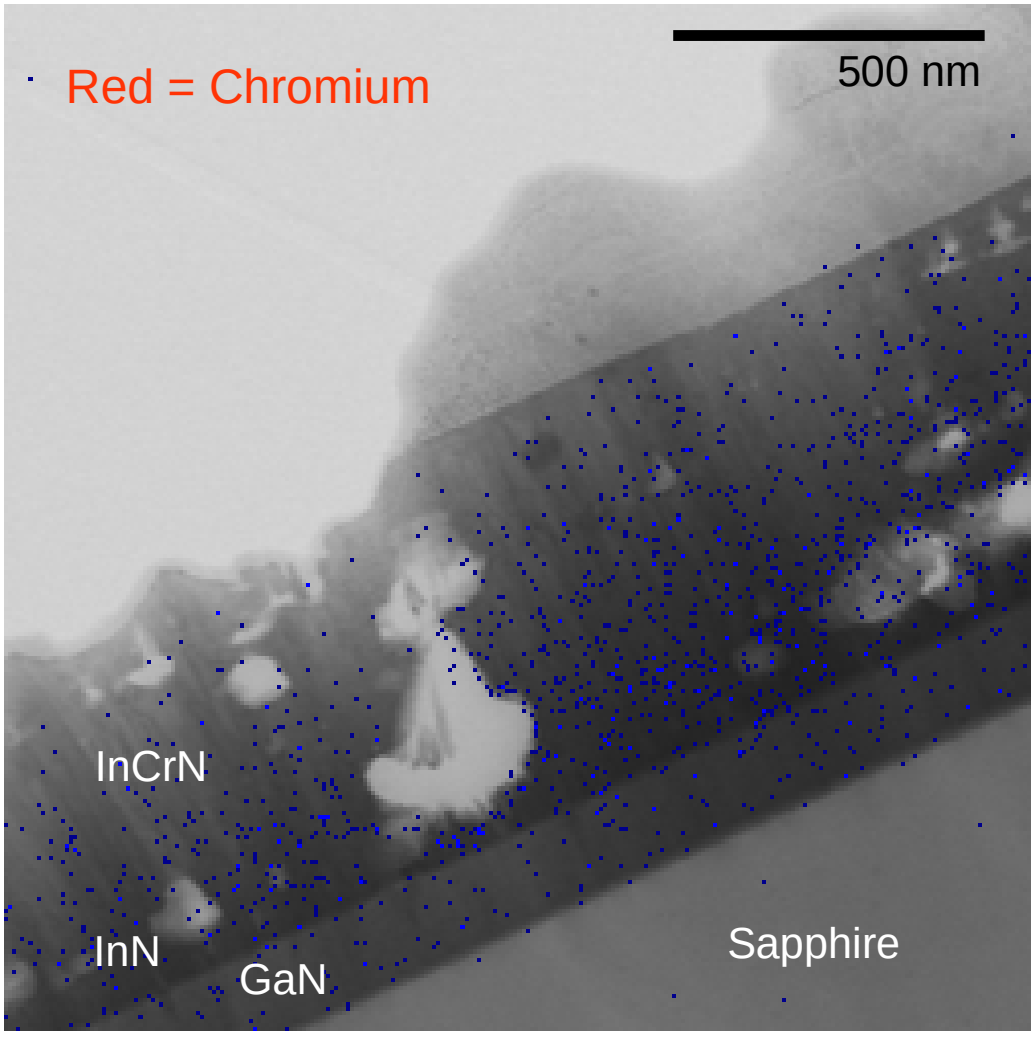

Figure 5.11 Scanning TEM EIXE images of the chromium content within a $In_{0.975}Cr_{0.025}N$ film.

5.6 MAGNETIC ORDER: ORIGINS OF THE EXCHANGE INTERACTION

Temperature dependent magnetisation measurements taken at 20 mT after samples have been demagnetised (dashed curves), and then again with the samples magnetised (solid curves) are shown in figure 5.12. The displacement between each pair of curves persists throughout the temperature range indicating that ferromagnetism remains in all samples at 300 K. A comparison of the four sets of curves with the theoretical temperature dependent magnetisation of figure 5.4 shows that each is consistent with $T<<T_C$. Further investigation of the $x = 0.025$ and 0.04 samples by vibrating sample magnetometer (VSM) revealed hysteresis persisting to 470 K; above this temperature, the signal to noise level in the system prevented further exploration. Interestingly, all of the films show little increase in magnetic moment at low temperatures. This effect is common among DMS materials and arises from enhancements in the magnetic susceptibility of paramagnetic ions within the film as described in figure 5.2. There is evidence of a weak paramagnetic response in the x=0.04 sample. The absence of a strong paramagnetic component indicates that ordered magnetic states are dominating the response in this case. In ordered states the localised moments are not as free to realign under an applied field as is the case for isolated moments (e.g. paramagnetic moments). The interactions with nearby moments essentially lock the moment in place in ferromagnetic and antiferromagnetic coupling, preventing the paramagnetic enhancement in magnetic moment at low temperatures. The maximum magnetic moment is observed in the $x = 0.025$ sample, with lower Cr concentrations displaying very weak ferromagnetism.

Figure 5.13 shows the room temperature hysteresis loop for the film with $x = 0.025$. The measured saturation moment of 7 emu/cm^3 corresponds to a moment of 1 Bohr magneton per Cr atom, and the remnant moment of 0.7 emu/cm^3 and coercive field of 7 mT are both comparable with other nitride based DMS at room temperature, including the $In_{0.98}Cr_{0.02}N$ examined by Chen *et al.* [45, 159].

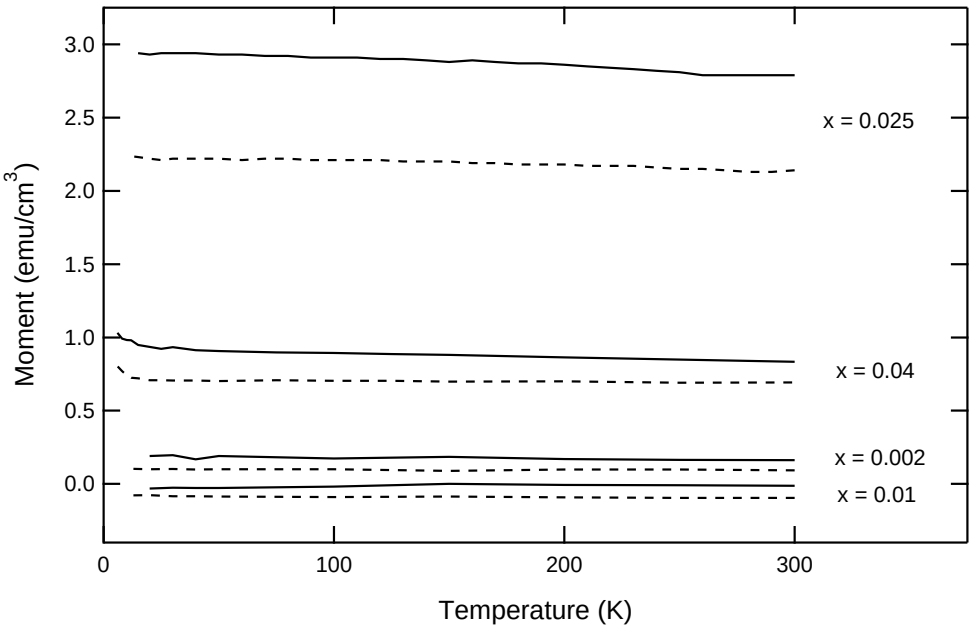

Figure 5.12 Magnetisation vs. temperature measurements at 20 mT for $In_{1-x}Cr_xN$ films grown under identical conditions, except for the Cr content. The films were either demagnetised (dashed curves) or poled at 1 Tesla (solid curves) before beginning the temperature sweep. Displacement between the two curves indicates the level of ferromagnetic component.

5.6.1 Evidence for an electron assisted exchange interaction

Electrical measurements on the films revealed an increase in the n-type carrier concentration from $\sim 10^{19}$ cm^{-3} for undoped InN to 0.8-9$\times 10^{20}$ cm^{-3} for the Cr doped films. Transition metals typically occupy the cation lattice site and act as an effective mass acceptor in III-V semiconductors [159]. However, 3-d shell energy estimates by Dietl *et al.* using the Vonsovskii model suggest Cr may act as a donor in InN [160]. Alternatively, the increased carrier concentrations may be related to interstitial Cr. This hypothesis is supported by XRD measurements which show a significant amount of the Cr is incorporating interstitially. Additionally, the n-type carrier concentration is found to be highest in the films with the largest c-axis lattice constant and hence greatest number of interstitial chromium atoms, again supporting interstitial Cr acting as a donor. Consistent with the degradation of the RHEED patterns, the Hall mobility decreased with increasing Cr content, from 250 cm^2/Vs for $x = 0$, to 35 cm^2/Vs for

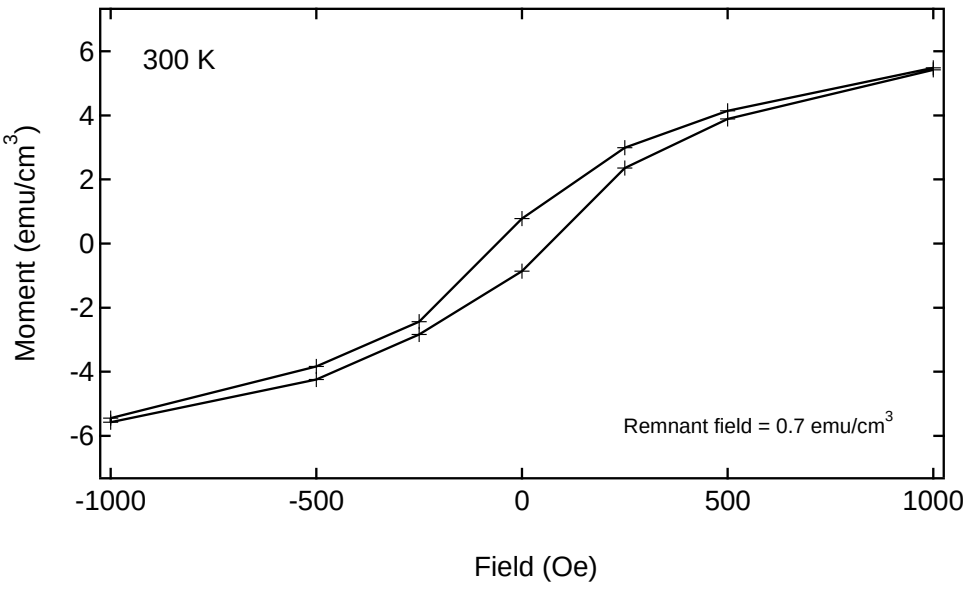

Figure 5.13 Magnetisation vs. applied field measurement at 300 K for an $In_{0.975}Cr_{0.025}N$ film. The field was set at ± 1 Tesla in order to saturate the magnetisation of the sample before beginning the magnetic field sweeps.

$x = 0.04$. Figure 5.14 shows the moment between the magnetised and demagnetised curves of figure 5.12 as a function of carrier concentration. A clear correlation between n-type carrier concentration and magnetic moment is observed. This is a surprising result as most theoretical treatments of III-V DMS predict that holes are required to mediate the exchange interaction as discussed in section 5.2.1. The enhancement in ferromagnetism is similar to observations by Story *et al.* who found a change in magnetic ordering in PbSnMnTe at comparable p-type carrier concentrations [153]. Comparable changes in the magnetic state of InMnAs have been shown to occur at the lower p-type carrier concentrations around 10^{19} cm^{-3} [161].

The observation of strong room temperature ferromagnetism accompanying the high n-type conductivity is in conflict with most theoretical frameworks for DMS materials. In this case, considerable effort has been made to search for clustering and no evidence of precipitates has been uncovered. However, the Cr atoms were shown to be highly mobile within both the GaN and InN lattices suggesting that Cr atoms could easily migrate to form clusters. If clusters are present they must be <10 nm in diameter to elude detection by the techniques employed. With significant Cr migrating into

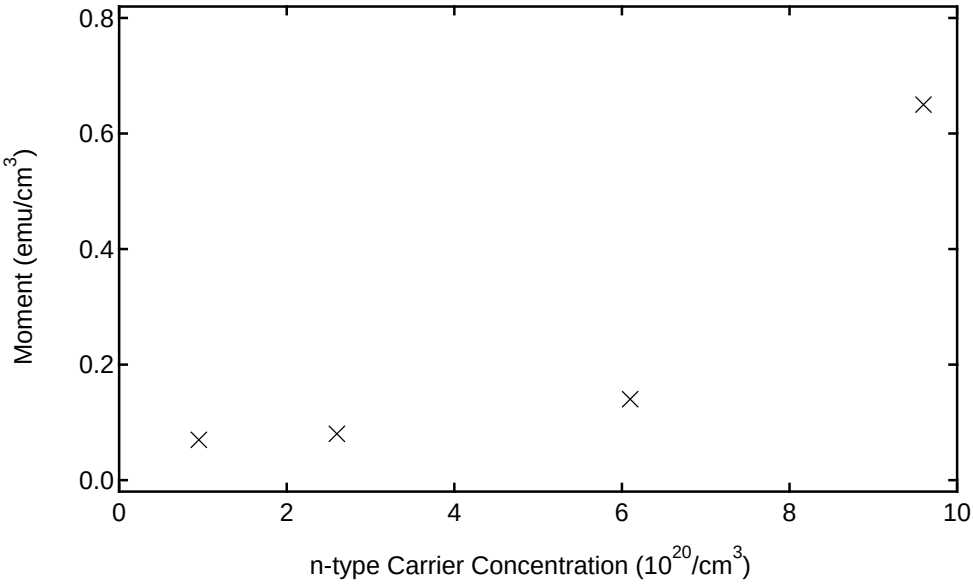

Figure 5.14 Ferromagnetic component of figure 5.12 at 300 K versus the corresponding carrier concentrations of the films.

the GaN buffer layer magnetic effects occurring within the GaN layer can not be ruled out. The $In_{1-x}Cr_xN$ cannot yet be declared a true carrier mediated DMS. Nonetheless, a number of materials have now exhibited ferromagnetism with accompanying n-type carrier concentrations without the detection of any clusters [39, 40, 41, 42, 43]. Also, the correlation between electron concentration and magnetic moment observed in this work is suggestive that electrons could be playing a role in a mediated exchange. Recent work by Litvinov *et* al. questions the ability of the RKKY interaction to explain ferromagnetism in many of the recently reported DMS materials [162]. They also suggest several other mediated exchanges which involve electrons, thus the theoretical framework describing DMS materials is still evolving. It would be premature to discount the observed magnetic properties of these apparent n-type DMS materials based on early theoretical predictions.

5.7 THE BANDGAP OF CHROMIUM NITRIDE

The binary endpoints of the alloy — CrN and InN — were studied along with the $In_{1-x}Cr_xN$ films in order to gain an understanding of the optical properties of the

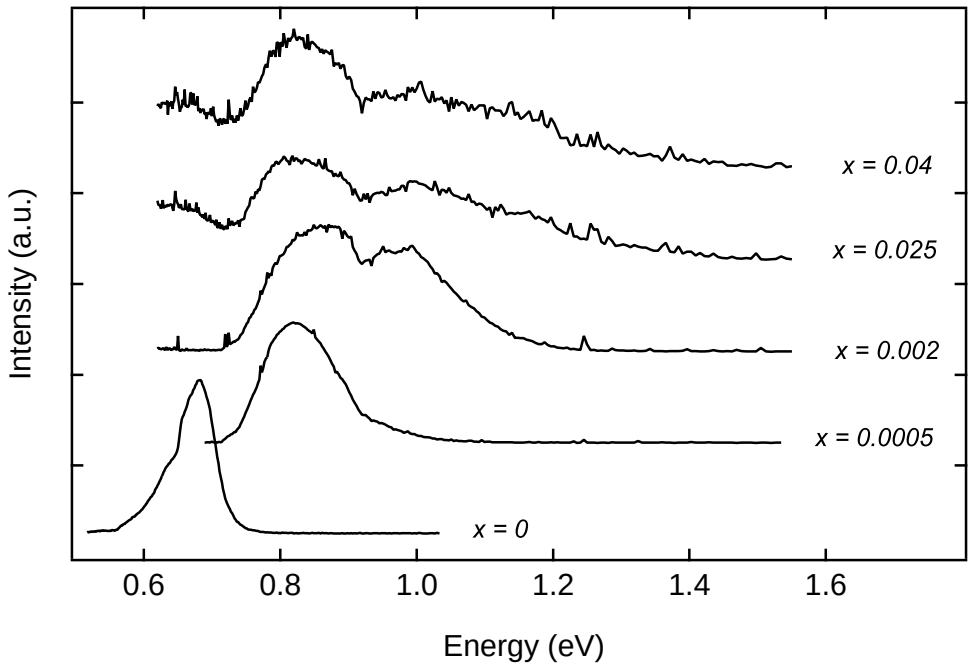

Figure 5.15 Photoluminescence signals obtained from $In_{1-x}Cr_xN$ films with varying values of x. Curves are displaced from each other for clarity.

material system. CrN films were grown on (0001) sapphire at substrate temperatures in the range of 250-650 °C. 650 °C was found to give the lowest electron concentration and highest mobility of 9×10^{18} cm^{-3} and 70 cm^2/Vs, respectively. The films were identified as (111) oriented rocksalt phase CrN by XRD. SQUID measurements confirmed that the material was antiferromagnetic with a Neel temperature near 280 K.

InN luminesces brightly near 0.7 eV, which is now tentatively believed to reflect a bandgap energy of comparable value. Addition of Cr to the InN matrix was found to reduce the PL intensity and lead to multiple features at higher energies as shown in figure 5.15. Attempts were made to obtain a PL signal from CrN but nothing above background noise was observed.

With PL failing to reveal any meaningful information on the band structure of CrN, temperature dependent resistivity and optical transmission and reflection measurements were performed as alternative approaches. Figure 5.16 shows the temperature dependent resistivity of a CrN film grown at 650 °C. The resistivity increases slowly with decreasing temperature, suggesting some semiconductor-like carrier freeze

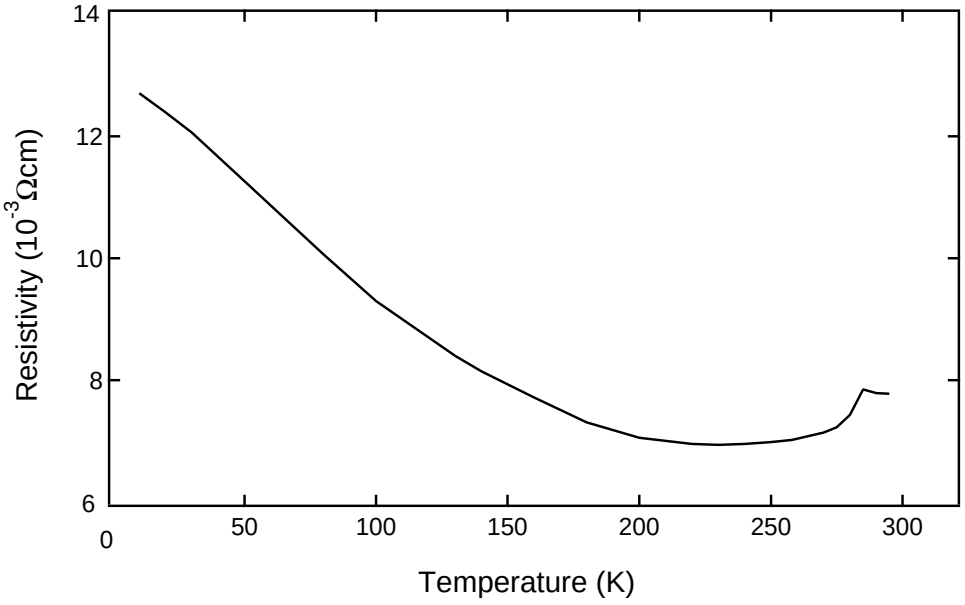

Figure 5.16 The temperature dependent resistivity of a CrN film.

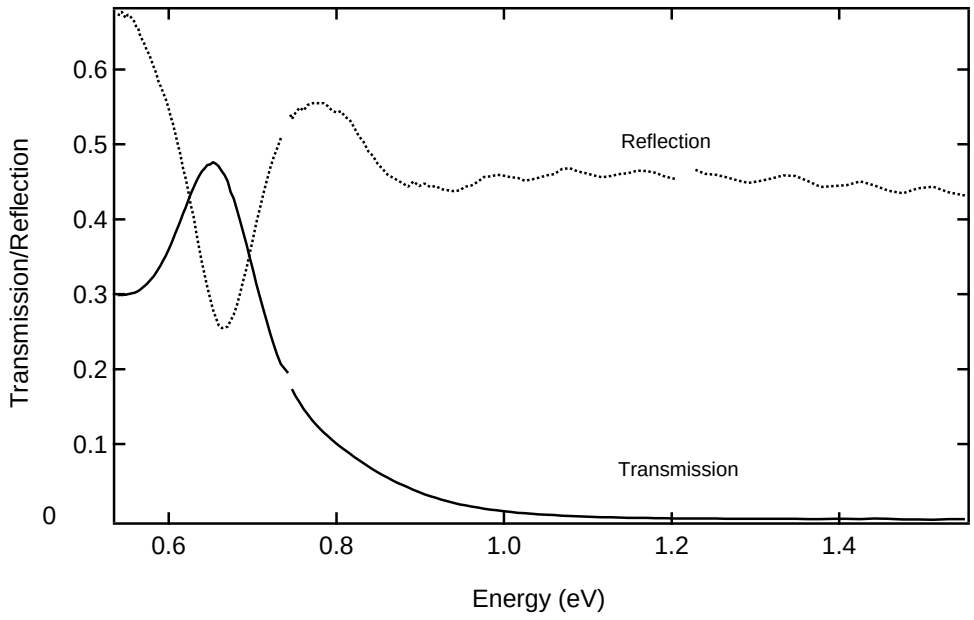

Figure 5.17 Transmission and reflection of a CrN film showing a band edge like feature near 0.7 eV.

out, although there appears to be a large degenerate background concentration which is not unreasonable considering the measured carrier concentrations. A step in the resistivity is observed at the Neel temperature, confirming earlier reports on bulk samples which identified a change in the electrical properties of the material at a comparable temperature [163, 164]. The temperature dependent resistivity measurements are consistent with the CrN film being a semiconductor with a high carrier concentration.

Optical transmission and reflection spectra of CrN are shown in figure 5.17. These results confirm observations by Gall *et al.* who saw a similar bandgap-like feature near 0.7 eV [165]. The reduction in transmission from 0.48 to less than 0.01, coupled with the temperature dependent resistivity measurements, point to CrN being semiconducting with a bandgap close to 0.7 eV. The lack of PL from the material suggests that the fundamental bandgap is indirect. A Γ-valley gap of >0.7 eV with an indirect gap near 0.7 eV can be used to explain the PL results and infrared absorption data. Upon addition of Cr to the InN matrix, the direct gamma valley gap increases, which explains the appearance of the higher energy components in figure 5.15. Further, momentum conservation results in a rapid dampening of radiative recombination and hence PL. However, creation of electron hole pairs via absorption is not inhibited to the same extent by the momentum constraint, and hence CrN still exhibits strong transmission and reflection features near 0.7 eV.

5.8 SUMMARY OF THE INDIUM CHROMIUM NITRIDE SYSTEM

In conclusion, $In_{1-x}Cr_xN$ films with x ranging from 0.0005 to 0.04, as well as the binary endpoints InN and CrN, have been grown on sapphire using a PAMBE technique. Cr doping was found to lead to a high concentration of n-type carriers, and a degradation of the crystal quality as observed by RHEED. Magnetic characterisation revealed room temperature ferromagnetism in all InCrN films, with the magnitude of the ferromagnetic signal increasing with n-type carrier concentration. The highest saturation and remnant moment achieved were 7 and 0.7 emu/cm^3 for a film with $x = 0.025$, and an electron concentration of 9×10^{20} cm^{-3}, respectively. Increasing the Cr concentration in

$In_{1-x}Cr_xN$ led to a shift in PL to higher energy and a reduction in PL intensity. Transmission and reflection results showed a bandgap like feature near 0.7 eV within CrN films and no distinguishable PL, consistent with an indirect gap near 0.7 eV for CrN. The magnetic properties of $In_{1-x}Cr_xN$ compare well with other nitride based DMS and the possibility of electron mediated ferromagnetism makes these unintentionally n-type materials promising candidates for future devices.

Chapter 6

CONCLUSIONS AND RECOMMENDATIONS FOR FUTURE RESEARCH

6.1 KEY RESULTS AND FUTURE PROSPECTS FOR INDIUM NITRIDE

Indium nitride has been a very challenging material to grow with structural and electrical characteristics considered "high quality" by the electronics community. In particular, the limitations on growth temperature imposed by the dissociation of the material is a major hinderance. The growth regimes of the material were found to follow similar trends to the closely related GaN material system, with growth close to the "In-rich" regime preferred over growth at low In:N ratios. Perhaps the most striking observation of the growth investigation was the strong dependence of electrical characteristics on the active nitrogen species used during growth. The active nitrogen species should be a major consideration when selecting a nitrogen source and operating regime for InN growth. The use of the closely lattice matched (111) YSZ substrate was demonstrated as a promising alternative to sapphire. InN films grown on (111) YSZ exhibited electron concentrations comparable to optimised films grown on sapphire with multiple buffer layers. Such substrates may in the future offer a viable alternative if effective buffer layer steps can be developed for the substrate.

A large number of indium nitride layers were studied by photoluminescence (PL) in this work. The ~0.7 eV feature commonly observed in PL from MBE and MOCVD grown InN was the only reliably reproduced PL feature. No PL was ever detected above 1.1 eV and the brightest PL signals were detected near 0.67 eV. The photoconductivity

measurements presented here are, to the author's knowledge, the first such measurements reported on InN layers and represent further compelling evidence for a wurtzite bandgap near 0.67 eV. The discrepancy between the ∼0.7 and ∼1.9 eV features was discussed in terms of quantum size effects, alloying and the Burstein-Moss effect. In the author's opinion the single most important factor in the higher apparent bandgap material is the Burstein-Moss shift. It has been argued that the shift cannot explain a large number of reported films given the measured electron concentration, however, determination of electron density in indium nitride films is highly problematic, and is likely a major source of error. The optical properties of mixed phase indium nitride films with substantial zincblende content were explored. A PL feature near 0.61 eV was routinely measured from the mixed phase films and the temperature and power dependence of the peak was suggestive of a band edge related transition for zincblende InN.

Magnesium doping has shown great promise as a possible route towards p-type InN. The quenching of PL observed in Mg doped layers is consistent with a p-n junction separating photo-generated carriers before they can recombine radiatively. The problem of electron accumulation at InN surfaces is a major obstacle to measuring a p-type layer electrically, and techniques which can lead to minimisation of this electron accumulation will be valuable in any future InN device research. The origins of electron accumulation were discussed with donor states at the film surface identified as the likely origin. Film polarity was demonstrated to influence surface termination conditions and as a result may prove to be a valuable tool in controlling electron accumulation. Ion implantation was investigated as a doping mechanism, however, the low temperatures to which rapid thermal annealing was limited prevented adequate lattice healing and may render the material unsuitable for ion implantation processing.

The potential DMS $In_{1-x}Cr_xN$ was shown to exhibit ferromagnetism with a remnant moment of 0.7 emu/cm^3 at 300 K. X-ray diffraction and TEM could find no evidence of clustering within the films, although nanoscale clustering could not be ruled out. An interesting relationship between n-type carrier concentration and remnant moment was presented which was suggestive of electrons playing a role in magnetic

exchange. Experimentally, a number of potential DMS materials have now been shown to exhibit high Curie temperatures with no apparent clustering. No theoretical framework exists to explain ferromagnetic order in n-type DMS, but the theory is still being developed and it remains to be seen whether electrons will emerge as a viable exchange mediating carrier. The optical properties of the related endpoint compound CrN were explored and evidence for an indirect bandgap of 0.7 eV was presented. CrN films showed a strong optical absorption feature near 0.7 eV but exhibited no PL. It was shown that PL from $In_{1-x}Cr_xN$ alloys quickly quenched with increasing Cr content, consistent with an indirect gap.

6.2 THE ROLE OF ACTIVE NITROGEN IN III-NITRIDE GROWTH

During the initial stages of this research project a different plasma source was used to grow III-nitride layers. This source was an MDP-21 plasma source made by Oxford Applied Research. This source was ∼10 years old and at the end of 2003 degradation of the plasma cavity (pyrolytic boron nitride) led to the purchase of a new source — an HD-25, also made by Oxford Applied Research. Upon installing the new plasma source we then attempted to grow a standard InN layer which had been optimised with the earlier plasma source. It was found the InN layer grown with the new plasma source had significantly inferior electrical properties compared to the same film grown with the old plasma source. Initially it was suspected that the new source may have produced more active nitrogen than the old, and that we needed to retune our indium flux to restore the In:N ratio. However, after several months of grappling with the problem and being unable to produce InN layers with comparable electrical properties as achieved with the MDP-21, attention was turned to the active nitrogen species taking part in growth. This led to the investigation of section 2.7, where the electrical properties of InN layers were found to vary significantly depending on the plasma operating conditions. The influence of the plasma operating conditions was found to be more significant than the relative In:N ratio for InN growth. The general conclusions of this investigation were that by operating at low plasma power, the relative production of excited molecular

nitrogen is enhanced. This specie is believed to be preferred for InN growth as has been suggested for GaN growth [78].

While undertaking these investigations it was very surprising to find out how little was actually known about the active species produced by nitrogen plasma sources. There are three main RF nitrogen plasma sources sold to the nitrides community, made by Oxford Applied Research, Veeco and SVT Associates. All three of these companies were approached with requests for details of the nitrogen species produced by their sources. The only meaningful data which was supplied was in the form of the optical spectrum produced by the source. Optical spectrum analysis of the plasma source does provide a good description of species produced in the cavity, but it tells us little about which species arrive at the growth location. Many of the species which dominate the optical spectrum of a nitrogen plasma have short lifetimes and exist only within the cavity. Ptak *et* al. have also shown that aperture and cavity design can influence the likelihood of particular species leaving the cavity. It seems that the manufacturers of these plasma sources have paid limited attention to many of these issues and have simply stuck to a design they know works.

The motivation for optimising the species produced by RF plasma sources is great. At present, III-nitrides manufacturing is dominated by MOCVD technology. This is due to the fact that MOCVD growth can produce nitride layers with moderately improved film properties. In many respects MBE is more suited to low cost manufacturing. Although MBE requires a UHV vacuum it uses source material more efficiently; MOCVD often has large costs associated with carrier gases. At present, MBE is the technology of choice for phosphide and arsenide growth. If further development of active nitrogen sources are successful, MBE manufacture may offer a path to cheaper and improved devices for nitrides as well.

It is not trivial to measure the active nitrogen species produced by a plasma source. The two approaches which have been used to date are quadrupole mass spectroscopy (QMS) and optical emission spectroscopy. In the author's opinion, of these two approaches, mass spectrometry provides the most potential as a tool for the advancement of new active nitrogen source technology. The development of a plasma source test

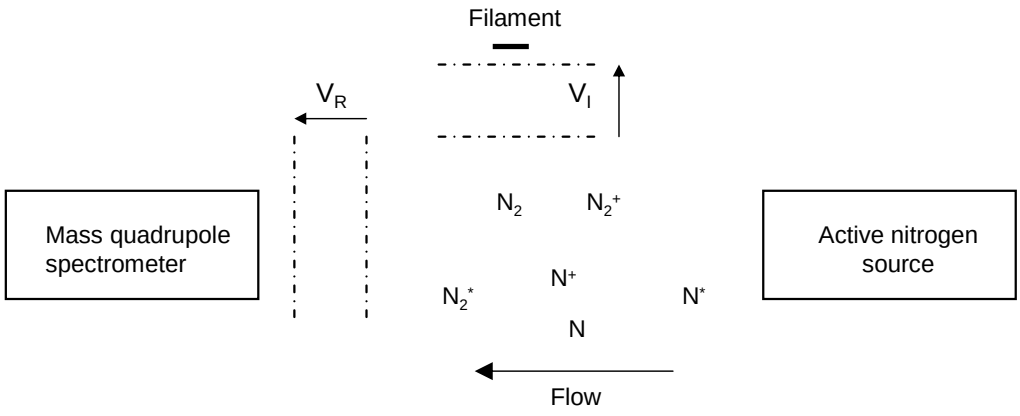

Figure 6.1 A proposed test structure for active nitrogen source characterisation. V_I represents the ionisation voltage and V_R the retarding voltage.

structure which combines QMS, variable ionisation conditions, and a controllable retarding potential could provide valuable information for modification and optimisation of a nitrogen source. Figure 6.1 shows a proposed structure. The key requirement is the selective ionisation of species entering the QMS. This is achieved by having fine control over the ionising voltage (V_I). Although many 'off the shelf' residual gas analysers (RGA) allow some choice in the ionising voltage, they are not designed to distinguish between electronic energy levels of the same species. This means that ionising voltages are typically allowable only over a certain threshold. For example, UTI and Stanford Research Systems models used in this thesis were limited to above 20 V. For nitrogen species investigation an ionising voltage in the 0-25 V range with resolution of $\sim$0.1 V would be ideal. Ptak *et* al. showed that such an approach was possible by using a customisable QMS [78].

Another parameter which, to the author's knowledge, has never been investigated, is the kinetic energy of species leaving the nitrogen source. The kinetic energy of species within the plasma is significant but the state of species when they reach the growth position is unknown. By applying a retarding potential (V_R in figure 6.1) only species with the required kinetic energy will overcome the barrier and enter the QMS. This approach would allow the influence of kinetic species on growth to be determined. Again, this measurement is partially allowed for in 'off the shelf' RGA systems. The series of cages involved with ionisation can sometimes be selectively biased. Establishing a

test system capable of both these measurements could be achieved by modifying an RGA to allow the added bias conditions. Such a system would allow comprehensive diagnosis of plasma sources of nitrogen, and other species, such as oxygen which is becoming increasingly popular. The system would also allow the exploration of other active nitrogen sources such as the use of a vacuum ultra violet (VUV) lamp to excite nitrogen molecules.

6.3 MAGNESIUM DOPING AND CIRCUMVENTING THE ACCUMULATION PROBLEM

The development of an efficient p-type doping mechanism for InN is of central importance if the material is to become viable for use in devices. Mg doping appears to offer the most promising way forward in this respect[1]. One of the main complications with accessing a potentially p-type layer is the electron accumulation layer which dominates most InN surfaces as discussed in section 4.4. Capping layers on InN films may provide a means to modify the effect of the accumulation layer. A capping layer would eliminate many of the dangling bonds at InN surfaces which are a likely source of electrons. An investigation of different capping layers and the influence they have on electron accumulation may provide a route for a more thorough investigation of the electrical characteristics of Mg doped InN. In, Ga, Al, GaN and AlN are all capping layers which could be easily incorporated onto InN surfaces. Capping layers may also minimise the effect of oxygen contamination at surfaces of which the effect is largely unknown.

As far as Mg doping is concerned, there remains much scope for investigation of how the dopant behaves in InN. In GaN, Mg is known to be passivated by hydrogen, but no study has yet been undertaken to determine if similar effects are observed in InN. Mg doped InN is poised to become a topic of increased interest as the recent flurry of reports shows. The University of Canterbury is well placed to be a leading contributor to the topic as the knowledge base of InN and Mg doping is well established.

[1]Since the time of writing compelling evidence has emerged that the heavily Mg-doped layers studied in this work do indeed contain buried p-type layers. Variable field Hall effect measurements made in collaboration with West Virginia University have allowed the first direct measurement of p-type conduction in InN layers.

Particular areas of interest will be: the Mg acceptor level relative to the valence band edge, clustering of Mg within the lattice, the role of interstitial Mg, polarity dependence of Mg incorporation. If Mg doped films are confirmed to contain buried p-type layers there will be a great deal of interest in the demonstration of an infrared LED based on InN, and even laser diodes.

6.4 TRANSISTORS BASED ON INDIUM NITRIDE

One of the first devices to be realised in GaN technology was the high electron mobility transistor (HEMT). Nitride based HEMTs consist of a remarkably simple device structure and may also offer one of the first realisable devices based on InN. The presence of the electron accumulation layer provides a problem here as it lies within the first several nanometers from the surface, a crucial region for HEMT operation. However, this may also prove to be of assistance in HEMT design, as this effect may assist high sheet charge levels. The basic structure of a nitride based HEMT was outlined in section 1.4. As InN has a considerably higher electron mobility than GaN, an initial approach may be to alloy a small amount of InN into a proven device in order to improve carrier drift velocities. This will also reduce the high voltage capacity of the HEMT due to the reduced bandgap of the alloy layer, but it does provide another degree of design freedom. If devices become more In-rich problems with creating a low carrier concentration bulk layer may arise. The operation of a HEMT relies on the ability to achieve a high resistance off state. Future research in transition metal doped InN which is insulating, while still maintaining high carrier mobility may provide solutions in this respect. Transition metals have been found to act as electron traps in some semiconductors: Fe doped GaN is now commonly used as an insulating bulk layer for GaN based HEMTs.

REFERENCES

[1] G. E. Moore, "Cramming more components onto integrated circuits," *Electronics magazine*, vol. 38, p. 114, 1965.

[2] S. C. Jain, M. Willander, J. Narayan, and R. V. Overstraeten, "III–nitrides: Growth, characterization, and properties," *J. Appl. Phys.*, vol. 87, p. 965, 2000.

[3] R. Juza and H. Hahn, "Uber die kristallstrukturen von Cu_3N, GaN und InN metallamide und metallnitride," *Anorg. Allgem. Chem.*, vol. 234, p. 282, 1938.

[4] H. P. Maruska and J. J. Tietjen, "The preparation and properties of vapor–deposited single–crystal–line GaN," *Appl. Phys. Lett.*, vol. 15, p. 327, 1969.

[5] H. Amano, I. Akasaki, T. Kozowa, H. Hiramatsu, N. Sawak, K. Ikeda, and Y. Ishii, "Electron beam effects on blue luminescence of zinc–doped GaN," *J. Luminescence*, vol. 40, p. 121, 1988.

[6] S. Nakamura, M. Senoh, N. Iwasa, and S. Nagahama, "High–brightness InGaN blue, green and yellow light–emitting diodes with quantum well structures," *Jpn. J. Appl. Phys.*, vol. 34, p. L797, 1995.

[7] I. Akasaki and H. Amano, *GaN*, vol. 1. Academic, New York, 1998.

[8] S. Nakamura, M. Senoh, S. ichi Nagahama, N. Iwasa, T. Yamada, T. Matsushita, H. Kiyoku, and Y. Sygimoto, "InGaN multi–quantum–well structure laser diodes grown on $MgAl_2O_4$ substrates," *Appl. Phys. Lett.*, vol. 68, p. 2105, 1996.

[9] A. J. Sierakowskia and L. F. Eastman, "Analysis of schottky gate electron tunneling in polarization induced AlGaN/GaN high electron mobility transistors," *J. Appl. Phys.*, vol. 86, p. 3398, 1999.

[10] J. I. Pankove, *GaN and related meterials*, vol. 2. Gordon and Breach, Amsterdam, 1997.

[11] Y. Narukawa, Y. Kawakami, M. Funato, S. Fujita, S. Fujita, and S. Nakamura, "Role of self–formed InGaN quantum dots for exciton localization in the purple laser diode emitting at 420 nm," *Appl. Phys. Lett.*, vol. 70, p. 981, 1996.

[12] Y.-H. Kwon, G. H. Gainer, S. Bidnyk, Y. H. Cho, J. J. Song, M. Hansen, and S. P. DenBaars, "Structural and optical characteristics of $In_xGa_{1x}N$/GaN multiple quantum wells with different In compositions," *Appl. Phys. Lett.*, vol. 75, p. 2545, 1999.

[13] M. Sumiya, N. Ogusu, Y. Yotsuda, M. Itoh, , S. Fuke, T. Nakamura, S. Mochizuki, T. Sano, S. Kamiyama, H. Amano, and I. Akasaki, "Systematic analysis and control of low–temperature GaN buffer layers on sapphire substrates," *J. Appl. Phys.*, vol. 93, p. 1311, 2003.

[14] T. L. Tansley and C. P. Foley, "Optical band gap of indium nitride," *J. Appl. Phys.*, vol. 59, p. 3241, 1986.

[15] K. L. Westra, R. P. W. Lawson, and M. J. Brett, "The effects of oxygen contamination on the properties of reactively sputtered indium nitride films," *J. Vac. Sci. Technol. A*, vol. 6, p. 1730, 1988.

[16] K. Kubota, Y. Kobayashi, and K. Fujimoto, "Preparation and properties of III–V nitride thin films," *J. Appl. Phys.*, vol. 66, p. 2984, 1989.

[17] V. Y. Davydov, A. A. Klochikhin, R. P. Seisyan, V. V. Emtsev, S. V. Ivanov, F. Bechstedt, J. Furthmuller, H. Harima, A. V. Mudryi, J. Aderhold, O. Semchinova, and J. Graul *Phys. Stat. Sol. B*, vol. 229, p. R1, 2001.

[18] J. Wu, W. Walukiewicz, K. M. Yu, J. W. Ager III, E. E. Haller, H. Lu, W. J. Schaff, Y. Saito, and Y. Nanishi, "Unusual properties of the fundamental band gap of InN," *Appl. Phys. Lett.*, vol. 80, p. 3967, 2002.

[19] T. Matsuoka, H. Okamoto, M. Nakao, H. Harima, and E. Kurimoto, "Optical bandgap energy of wurtzite InN," *Appl. Phys. Lett.*, vol. 81, p. 1246, 2002.

[20] K. S. A. Butcher and T. L. Tansley, "InN, latest developement and a review of the band–gap controversy," *Superlatices Microstruct.*, vol. 38, p. 1, 2005.

[21] T. V. Shubina, S. V. Ivanov, V. N. Mjerik, D. D. Solnyshkov, V. A. Vekshin, P. S. Kopev, A. Vasson, J. Leymarie, A. Kavokin, H. Amano, K. Shimono, A. Kasic, and B. Monemar, "Mie resonances, infrared emission, and the band gap of InN," *Phys. Rev. Lett.*, vol. 92, art. 117407, 2004.

[22] P. Specht, J. C. Ho, X. Xu, R. Armitage, E. R. Weber, R. Erni, and C. Kisielowski, "Band transitions in wurtzite GaN and InN determined by valence electron energy loss spectroscopy," *Sol. State Comm.*, vol. 135, p. 340, 2005.

[23] K. S. Butcher, M. Winterbert-Fouquet, P. P. T. Chen, K. E. Prince, H. Timmers, S. K. Shrestha, T. V. Shubina, S. V. Ivanov, R. Wuhurer, M. R.

Phillips, and B. Monemar, "Non–stoichiometry and non–homogeneity in InN," *Phys. Stat. Sol. C*, vol. 2, p. 2263, 2005.

[24] J. Wu, W. Walukiewicz, W. Shan, K. M. Yu, J. W. Ager III, E. E. Haller, H. Lu, and W. J. Schaff, "Effects of the narrow band gap on the properties of InN," *Phys. Rev. B*, vol. 66, art. 201403, 2002.

[25] V. Y. Davydov, A. A. Klochikhin, V. V. Emtsev, D. A. Kurdyukov, S. V. Ivanov, V. A. Vekshin, F. Bechstedt, J. Furthmuller, J. Aderhold, J. Graul, A. V. Mudryi, H. Harima, A. Hashimoto, A. Yamamoto, and E. E. Haller, "Band gap of hexagonal InN and InGaN alloys," *Phys. Stat. Sol. B*, vol. 234, p. 787, 2002.

[26] I. Hamberg and C. G. Granqvist, "Evaporated Sn–doped In_2O_3 films: Basic optical properties and applications to energy–efficient windows," *J. Appl. Phys.*, vol. 60, p. 123, 1986.

[27] M. Yoshimoto, H. Yamamoto, W. Huang, H. Harima, J. Saraie, A. Chayahara, and Y. Horino, "Widening of optical bandgap of polycrystalline InN with a few percent incorporation of oxygen," *Appl. Phys. Lett.*, vol. 83, p. 3480, 2003.

[28] A. G. Bhuiyan, K. Sugita, K. Kasashima, A. Hashimoto, A. Yamamoto, and V. Y. Davydov, "Single–crystalline InN films with an absorption edge between 0.7 and 2 eV grown using different techniques and evidence of the actual band gap energy," *Appl. Phys. Lett.*, vol. 83, p. 4788, 2003.

[29] M. S. Shur and M. A. Khan, *GaN and related meterials*, vol. 7. Gordon and Breach, Amsterdam, 2000.

[30] B. E. Foutz, S. K. Oleary, M. S. Shur, and L. F. Eastman, "Transient electron transport in wurtzite GaN, InN, and AlN," *J. Appl. Phys.*, vol. 85, p. 7727, 1999.

[31] H. Lu, W. J. Schaff, , and L. F. Eastman, "Surface charge accumulation of InN films grown by molecular–beam epitaxy," *Appl. Phys. Lett.*, vol. 82, p. 1736, 2003.

[32] I. Mahboob, T. D. Veal, C. F. McConville, H. Lu, and W. J. Schaff, "Intrinsic electron accumulation at clean InN surfaces," *Phys. Rev. Lett.*, vol. 92, art. 036804, 2004.

[33] I. Mahboob, T. D. Veal, L. F. J. Piper, C. F. McConville, H. Lu, W. J. Schaff, J. Furthmller, and F. Bechstedt, "Origin of electron accumulation at wurtzite InN surfaces," *Phys. Rev. B*, vol. 69, art. 201307, 2004.

[34] S. A. Wolf, D. D. Awschalom, R. A. Buhrman, J. M. Daughton, S. von Molnar, M. L. Roukes, A. Y. Chtchelkanova, and D. M. Tregger, "Spintronics: A spin–based electronics vision for the future," *Science*, vol. 294, p. 1488, 2001.

[35] V. F. Motsnyi, J. D. Boek, J. Das, W. V. Roy, and G. Borghs, "Electrical spin injection in a ferromagnet/tunnel barrier/semiconductor heterostructure," *Appl. Phys. Lett.*, vol. 81, p. 265, 2002.

[36] H. Ohno, A. Shen, F. Matsukura, A. Oiwa, A. Endo, S. Katsumoto, and Y. Lye, "(Ga,Mn)As: A new diluted magnetic semiconductor based on GaAs," *Appl. Phys. Lett.*, vol. 69, p. 363, 1996.

[37] H. Ohno, H. Munekata, T. Penney, S. von Molnar, and L. L. Chan, "Magnetotransport properties of p–type (In,Mn)As diluted magnetic III–V semiconductors," *Phys. Rev. Lett.*, vol. 68, p. 2664, 1993.

[38] T. Dietl, H. Ohno, and F. Matsukura, "Hole–mediated ferromagnetism in tetrahedrally coordinated semiconductors," *Phys. Rev. B*, vol. 63, art. 195205, 2001.

[39] K. H. Kim, K. J. Lee, D. J. Kim, H. J. Kim, and Y. E. Ihm, "Enhanced carrier–mediated ferromagnetism in GaMnN by codoping of Mg," *Appl. Phys. Lett.*, vol. 82, p. 4755, 2003.

[40] A. F. Hebard, R. P. Rairigh, J. G. Kelly, S. J. Pearton, C. R. Abernathy, S. N. G. Chu, and R. G. Wilson, "Mining for high T_c ferromagnetism in ion–implanted dilute magnetic semiconductors," *J. Phys. D*, vol. 37, p. 511, 2004.

[41] D. Kumar, J. Antifakos, M. G. Blamire, and Z. H. Barber, "High curie temperatures in ferromagnetic Cr–doped AlN thin films," *Appl. Phys. Lett.*, vol. 84, p. 5004, 2004.

[42] W. K. Park, R. J. Ortega-Hertogs, and J. S. Moodera, "Semiconducting and ferromagnetic behaviour of sputtered Co–doped TiO_2 thin films above room temperature," *J. Appl. Phys.*, vol. 91, p. 8093, 2002.

[43] S. B. Oagle, R. J. Choudhary, J. P. Buban, S. E. Lofland, S. R. Shinde, S. N. Kale, V. N. Kulkarni, J. Higgins, C. Lanci, J. R. Simpson, N. B. Browning, S. D. Sarma, H. D. Drew, R. L. Greene, and T. Venekatesan, "High temperature ferromagnetism with a giant magnetic moment in transparent Co–doped $SnO_{2-\Gamma}$," *Phys. Rev. Lett.*, vol. 91, art. 077205, 2003.

[44] P. P. Chen, H. Makino, and T. Yao, "InMnN: a nitride–based diluted magnetic semiconductor," *Sol. State Comm.*, vol. 130, p. 25, 2004.

[45] P. P. Chen, H. Makino, and T. Yao, "MBE growth and properties of InN–based dilute magnetic semiconductors," *J. Crys. Growth*, vol. 269, p. 66, 2004.

[46] L. M. Sandratskii and P. Bruno, "The influence of the clustering of Mn impurities on the magnetic properties of (GaMn)As," *J. Phys. Condens. Matter*, vol. 16, p. 523, 2004.

[47] T. L. Tansley and C. P. Foley, "Electron mobility in indium nitride," *Electron. Lett.*, vol. 20, p. 1066, 1984.

[48] R. D. Vispute, V. Talyansky, R. P. Sharma, S. Choopun, M. Downes, T. Venkatesan, K. A. Jones, A. A. Iliadis, M. A. Khan, and J. W. Yang, "Growth of epitaxial GaN films by pulsed laser deposition," *Appl. Phys. Lett.*, vol. 71, p. 102, 1997.

[49] X. Wang and A. Yoshikawa, "Molecular beam epitaxy growth of GaN, AlN and InN," *Prog. Crystal Growth Char. Mat.*, vol. 48, p. 42, 2004.

[50] W. Braun, *Applied RHEED.* Springer, New York, 1999.

[51] H. Xia, Q. Xia, and A. L. Ruoff, "High–pressure structure of gallium nitride: Wurtzite–to–rocksalt phase transition," *Phys. Rev. B*, vol. 47, art. 12925, 1993.

[52] A. Dadgar, M. Poschenrieder, J. Blsing, K. Fehse, A. Diez, and A. Krost, "Thick, crack–free blue light–emitting diodes on Si(111) using low–temperature AlN interlayers and in situ Si_xN_y masking," *Appl. Phys. Lett.*, vol. 80, p. 3670, 2002.

[53] R. W. Cahn, *Concise encyclopedia of materials characterization.* Elsevier, Amsterdam, 2nd ed., 2005.

[54] B. Heying, R. Averbeck, L. F. Chen, E. Haus, H. Riechert, and J. S. Speck, "Control of GaN surface morphologies using plasma–assisted molecular beam epitaxy," *J. Appl. Phys.*, vol. 88, p. 1855, 2000.

[55] J.-K. Tsai, I. Lo, K.-L. Chuang, L.-W. Tu, J.-H. Huang, C.-H. Hsieh, and K.-Y. Hsieh, "Effect of N to Ga flux ratio on the GaN surface morphologies grown at high temperature by plasma–assisted molecular–beam epitaxy," *J. Appl. Phys.*, vol. 95, p. 460, 2004.

[56] J. Neugebauer, T. K. Zywietz, M. Scheffler, J. E. Northrup, H. Chen, and R. M. Feenstra, "Adatom kinetics on and below the surface: The existence of a new diffusion channel," *Phys. Rev. Lett.*, vol. 90, art. 056101, 2003.

[57] S. K. Davidsson, J. F. Falth, X. Y. Liu, H. Zirath, and T. G. Andersson, "Effect of AlN nucleation layer on the structural properties of bulk GaN grown on sapphire by molecular–beam epitaxy," *J. Appl. Phys.*, vol. 98, art. 016109, 2005.

[58] F. Widmann, G. Feuillet, B. Daudin, and J. L. Rouvie're, "Low temperature sapphire nitridation: A clue to optimize GaN layers grown by molecular beam epitaxy," *J. Appl. Phys.*, vol. 85, p. 1550, 1999.

[59] C. Kruse, S. Einfeldt, T. Bottcher, and D. Hommel, "In as a surfactant for the growth of GaN (0001) by plasma–assisted molecular–beam epitaxy," *Appl. Phys. Lett.*, vol. 79, p. 3425, 2001.

[60] W.-L. Chen, R. L. Gunshor, J. Han, K. Higashimine, and N. Otsuka, "Growth of InN by MBE," *MRS Internet J. Nitride Semicond. Res.*, vol. 5S1, art. W3.30, 2000.

[61] K. Xu and A. Yoshikawa, "Effects of film polarities on InN growth by molecular–beam epitaxy," *Appl. Phys. Lett.*, vol. 83, p. 251, 2003.

[62] M. A. Herman and H. Sitter, *Molecular Beam Epitaxy Fundamentals and Current Status*. Springer, Verlag, 2nd ed., 1996.

[63] E. Dimakis, E. Iliopoulos, K. Tsagaraki, T. Kehagias, P. Komninou, and A. Georgakilas, "Heteroepitaxial growth of In–face InN on GaN (0001) by plasma–assisted molecular–beam epitaxy," *J. Appl. Phys,*, vol. 97, art. 113520, 2005.

[64] R. Held, G. Nowak, B. E. Ishaug, S. M. Seutter, A. Parkhomovsky, A. M. Dabiran, P. I. Cohen, I. Grzegory, and S. Porowski, "Structure and composition of GaN(0001) A and B surfaces," *J. Appl. Phys.*, vol. 85, p. 7697, 1999.

[65] T. Honke, H. Fujioka, J. Ohta, and M. Oshima, "InN epitaxial growths on yttria stabilized zirconia (111) step substrates," *J. Vac. Sci. Technol. A*, vol. 22, p. 2487, 2004.

[66] V. Cimilla, J. Pezoldt, G. Ecke, E. Koshiba, O. Ambacher, L. Spieß, G. Teichert, H. Lu, and W. J. Schaff, "Growth of cubic InN on r–plane sapphire," *Appl. Phys. Lett.*, vol. 83, p. 3468, 2003.

[67] A. Tabata, A. P. Lima, L. K. Teles, L. M. R. Scolfaro, J. R. Leite, V. Lemos, B. Schotker, T. Frey, D. Schikora, and K. Lischka, "Structural properties and raman modes of zinc blende InN epitaxial layers," *Appl. Phys. Lett.*, vol. 74, p. 362, 1999.

[68] H. Liu, A. C. Frenkel, J. G. Kim, and R. M. Park, "Growth of zinc blende–GaN on β–SiC coated (001) Si by molecular beam epitaxy using a radio frequency plasma," *J. Appl. Phys.*, vol. 74, p. 6124, 1993.

[69] J. M. V. Hove, G. J. Cosimini, E. Nelson, A. M. Wowchak, and P. P. Chow, "GaN growth by a controllable RF–excited nitrogen source," *J. Cryst. Growth*, vol. 150, p. 908, 1995.

[70] S. E. Hooper, C. T. Foxon, T. S. Cheng, L. C. Jenkins, D. E. Lacklison, J. W. Orton, T. Bestwick, A. Kean, M. Dawson, and G. Duggan, "Some aspects of GaN growth on GaAs(100) substrates using molecular beam epitaxy with an RF activated nitrogen–plasma source," *J. Cryst. Growth*, vol. 155, p. 157, 1995.

[71] R. J. Molnar and T. D. Moustakas, "Growth of gallium nitride by electron–cyclotron resonance plasma–assisted molecular–beam epitaxy: The role of charged species," *J. Appl. Phys.*, vol. 76, p. 4587, 1994.

[72] W. C. Hughes, W. H. Rowland Jr., M. A. L. Johnson, S. Fujita, J. W. Cook Jr., J. F. Schetzina, J. Ren, and J. A. Edmond, "Molecular beam epitaxy growth and properties of GaN films on GaN/SiC substrates," *J. Vac. Sci. Tech. B*, vol. 13, p. 1571, 1995.

[73] S.-H. Cho and H. Okumura, "Comparison of excited nitrogen sources for molecular–beam–epitaxy GaN growth: Radio frequency and electron cyclotron resonance plasma sources," *Appl. Phys. Lett.*, vol. 76, p. 3861, 2000.

[74] H. Carrere, A. Arnoult, A. Ricard, and E. Bedel-Pereira, "RF plasma investigations for plasma–assisted MBE growth of (Ga,In)(As,N) materials," *J. Cryst. Growth*, vol. 243, p. 295, 2002.

[75] A. Georgakilas, H. Min, and P. Komninou, *Nitride Semiconductors: Handbook on materials and devices.* Wiley–VCH, Weinheim, 2003.

[76] R. P. Vaudo, J. W. Kook Jr, and J. F. Schetzina, "Atomic nitrogen production in a molecular–beam epitaxy compatible electron cyclotron resonance plasma source," *J. Vac. Sci. Tech. B*, vol. 12, p. 1232, 1994.

[77] A. N. Wright and C. A. Winkler, *Active Nitrogen.* Academic Press, New York, 1968.

[78] A. J. Ptak, M. R. Millecchia, T. H. Myers, K. S. Ziemer, and C. D. Stinespring, "The relation of active nitrogen species to high–temperature limitations for $(000\bar{1})$ GaN growth by radio–frequency–plasma–assisted molecular beam epitaxy," *Appl. Phys. Lett.*, vol. 74, p. 3836, 1999.

[79] A. J. Ptak, K. S. Ziemer, M. R. Millecchia, C. D. Stinespring, and T. H. Myers, "Influence of active nitrogen species on the nitridation rate of sapphire," *MRS Internet J. Nitride Semicond. Res.*, vol. 4S1, art. G3.10, 1999.

[80] A. Kikuchi, H. Hoshi, and K. Kishino, "Substrate nitridation effects on GaN grown on GaAs substrates by molecular beam epitaxy using RF–radical nitrogen source," *Jpn. J. Appl. Phys.*, vol. 33, p. 688, 1994.

[81] H. Lu, W. J. Schaff, L. F. Eastman, J. Wu, W. Walukiewicz, D. C. Look, and R. J. Molnar, "Growth of thick InN by molecular beam epitaxy," *Mat. Res. Soc. Symp. Proc.*, vol. 743, art. L4.10.1, 2003.

[82] Y. Nanishi, Y. Saito, T. Yamaguchi, F. Matsuda, T. Araki, H. Naoi, A. Suzuki, H. Harima, and T. Miyajima, "Band–gap energy and physical properties of

InN grown by RF–molecular beam epitaxy," *Mat. Res. Symp. Proc.*, vol. 798, art. Y12.1.1, 2004.

[83] C. Adelmann, J. Brault, D. Jalabert, P. Gentile, H. Mariette, and G. Mula, "Dynamically stable gallium surface coverages during plasma–assisted molecular–beam epitaxy of (0001) GaN," *J. Appl. Phys.*, vol. 91, p. 9638, 2002.

[84] P. A. Anderson, C. E. Kendrick, T. E. Lee, W. Diehl, R. Reeves, V. J. Kennedy, A. Markwitz, R. J. Kinsey, and S. M. Durbin, "Optical and microstructural characterisation of InN grown by PAMBE on (0001) sapphire and (001) YSZ," *Mat. Res. Symp. Proc.*, vol. 798, art. Y12.3.1, 2003.

[85] D. Muto, T. Araki, H. Naoi, F. Matsuda, and Y. Nanishi, "Polarity determination of InN by wet etching," *Phys. Stat. Sol. A*, vol. 202, p. 773, 2005.

[86] Y. Ng, Y. G. Cao, M. H. Xie, W. L. . Wang, and S. Y. Tong, "Growth mode and strain evolution during InN growth on GaN(0001) by molecular–beam epitaxy," *Appl. Phys. Lett.*, vol. 81, p. 3960, 2002.

[87] Y. Saito, N. Teraguchi, A. Suzuki, T. Araki, and Y. Nanishi, "Growth of high–electron–mobility InN by RF molecular beam epitaxy," *Jpn. J. Appl. Phys.*, vol. 40, p. L91, 2002.

[88] X. Zhu and S. G. Louie, "Quasiparticle band structure of thirteen semiconductors and insulators," *Phys. Rev. B*, vol. 43, art. 14142, 1991.

[89] A. Rubio, J. L. Corkill, M. L. Cohen, E. L. Shirley, and S. G. Louie, "Quasiparticle band structure of AlN and GaN," *Phys. Rev. B*, vol. 48, art. 11810, 1993.

[90] S.-H. Wei, X. Nie, I. G. Batyrev, and S. B. Zhang, "Breakdown of the band–gap–common–cation rule: The origin of the small band gap of InN," *Phys. Rev. B*, vol. 67, art. 165209, 2003.

[91] A. Sher, M. van Schifgaarde, M. A. Berding, S. Krishnamurthy, and A. B. Chen, "Computational materials science, an increasingly reliable engineering tool: Anomalous nitride band structures and device consequences," *MRS Internet J. Nitride Semicond. Res.*, vol. 4S1, art. G5.1, 1999.

[92] K. A. Johnson and N. W. A. and, "Corrections to density–functional theory band gaps," *Phys. Rev. B*, vol. 58, art. 15548, 1998.

[93] F. Bechstedt, J. Furthmuller, M. Ferhat, L. K. Teles, L. M. R. Scolfaro, J. R. Leite, V. Y. Davydov, O. Ambacher, and R. Goldhahn, "Energy gap and optical properties of $In_xGa_{1-x}N$," *Phys. Stat. Sol. A*, vol. 195, p. 628, 2003.

[94] J. I. Pankove, *Optical Processes in Semiconductors.* Prentice Hall, New Jersey, 1st ed., 1971.

[95] T. H. Keil, "Theory of the Urbach rule," *Phys. Rev.*, vol. 144, p. 582, 1965.

[96] F. Urbach, "The long–wavelength edge of photographic sensitivity and of the electronic absorption of solids," *Phys. Rev.*, vol. 92, p. 1324, 1953.

[97] S. O. Kucheyev, M. Toth, M. R. Phillips, J. S. Williams, C. Jagadish, and G. Li, "Chemical origin of the yellow luminescence in GaN," *J. Appl. Phys.*, vol. 91, p. 5867, 2002.

[98] A. Armstrong, A. R. Arehart, D. Green, U. K. Mishra, J. S. Speck, and S. A. Ringel, "Impact of deep levels on the electrical conductivity and luminescence of gallium nitride codoped with carbon and silicon," *J. Appl. Phys.*, vol. 98, art. 053704, 2005.

[99] J. S. Colton, P. Y. Yu, K. L. Teo, E. R. Weber, P. Perlin, I. Grzegory, and K. Uchida, "Selective excitation and thermal quenching of the yellow luminescence of GaN," *Appl. Phys. Lett.*, vol. 75, p. 3273, 1999.

[100] H. Teisseyre, P. Perlin, T. Suski, I. Grzegory, S. Porowski, and J. Jun, "Temperature dependence of the energy gap in GaN bulk single crystals and epitaxial layer," *J. Appl. Phys.*, vol. 76, p. 2429, 1994.

[101] Y. P. Varshni, "Temperature dependence of the energy gap in semiconductors," *Physica*, vol. 34, p. 149, 1967.

[102] H. Yaguchi, G. Biwa, S. Miyoshi, D. Aoki, K. Arimoto, K. Onabe, R. Ito, and Y. Shiraki, "Temperature dependence of photoluminescence of $GaP_{1-x}N_x$ alloys," *J. Cryst. Growth*, vol. 189, p. 496, 1998.

[103] S. O. Kasap, *Electronic materials and devices.* McGraw Hill, Boston, 3rd ed., 2006.

[104] L. Williams, "Photoconductivity and photoluminescence of indium nitride," Master's thesis, University of Canterbury, 2005.

[105] O. Katz, G. Bahir, and J. Salzman, "Persistent photocurrent and surface trapping in GaN schottky ultraviolet detectors," *Appl. Phys. Lett.*, vol. 84, p. 4092, 2004.

[106] Z. H. Lan, W. M. Wang, C. L. Sun, S. C. Shi, C. W. Hsu, T. T. Chen, K. H. Chen, C. C. Chen, Y. F. Chen, and L. C. Chen, "Growth mechanism, structure and IR photoluminescence studies of indium nitride nanorods," *J. Cryst. Growth*, vol. 269, p. 87, 2004.

[107] B. Monemar, P. P. Paskov, and A. Kasic, "Optical properties of InN—the bandgap question," *Superlatices Microstruct.*, vol. 38, p. 38, 2005.

[108] J. Wu, W. Walukiewicz, W. Shan, K. M. Yu, J. W. Ager III, S. X. Li, E. E. Haller, H. Lu, and W. J. Schaff, "Temperature dependence of the fundamental band gap of InN," *J. Appl. Phys.*, vol. 94, p. 4457, 2003.

[109] I. Vurgaftman, J. R. Meyer, and L. R. Ram-Mohan, "Band parameters for III-V compound semiconductors and their alloys," *J. Appl. Phys.*, vol. 89, p. 5815, 2001.

[110] A. A. Klochikhin, V. Y. Davydov, V. V. Emstev, A. V. Sakharow, V. A. Kapitonov, B. A. Andreev, H. Lu, and W. J. Schaff, "Acceptor states in the photoluminescence spectra of n–InN," *Phys. Rev. B*, vol. 71, art. 195207, 2005.

[111] B. Arnaudov, T. Paskova, B. Magnusson, E. Valcheva, and B. Monemar, "Energy position of near–band–edge emission spectra of InN epitaxial layers with different doping levels," *Phys. Rev. B*, vol. 69, art. 115216, 2004.

[112] M. Pan and A. J. Steckl, "Red emission from Eu–doped GaN luminescent films grown by metalorganic chemical vapor deposition," *Appl. Phys. Lett.*, vol. 83, p. 9, 2003.

[113] R. Rosenbaum, "Crossover from Mott to Efros–Shklovskii variable–range–hopping conductivity in In_xO_y films," *Phys. Rev. B*, vol. 44, p. 3599, 1991.

[114] K. M. Itoh, "Variable range hopping conduction in neutron–transmutation–doped 70Ge:Ga," *Phys. Stat. Sol. B*, vol. 218, p. 211, 2000.

[115] J. R. Friedman, Y. Zhang, P. Dai, and M. P. Sarachik, "Magnetic–field–induced crossover from Mott variable–range hopping to weakly insulating behavior," *Phys. Rev. B*, vol. 53, p. 9528, 1996.

[116] D. Feiler, R. S. Williams, A. A. Talin, H. Yoon, and M. S. Goorsky, "Pulsed laser deposition of epitaxial AlN, GaN, and InN thin films on sapphire(0001)," *J. Cryst. Growth*, vol. 171, p. 12, 1997.

[117] S. O. Kasap, *Electronic materials and devices.* McGraw Hill, Boston, 3rd ed., 2006.

[118] C. H. Swartz, R. P. Tompkins, N. C. Giles, T. H. Myers, H. Lu, W. J. Schaff, and L. F. Eastman, "Investigation of multiple carrier effects in InN epilayers using variable magnetic field hall measurements," *J. Cryst. Growth*, vol. 269, p. 29, 2004.

[119] J. Wu, W. Walukiewicz, S. X. Li, R. Armitage, J. C. Ho, E. R. Weber, E. E. Haller, H. Lu, W. J. Schaff, A. Barcz, and R. Jakiela, "Effects of electron concentration on the optical absorption edge of InN," *Appl. Phys. Lett.*, vol. 84, p. 2805, 2004.

[120] V. A. Tyagai, A. M. Evstigneev, A. N. K. A. F. Andreeva, and V. Y. Malakhov, "Optical properties of indium nitride films," *Sov. Phys. Semicond.*, vol. 11, p. 1257, 1977.

[121] V. Y. Davydov, A. A. Klochikhin, V. V. Emtsev, S. V. Ivanov, V. V. Vekshin, F. Bechstedt, J. Furthmller, H. Harima, A. V. Mudryi, A. Hashimoto, A. Yamamoto, J. Aderhold, J. Graul, and E. E. Haller, "Band gap of InN and In–rich $In_xGa_{1-x}N$ alloys (0.36<x<1)," *Phys. Stat. Sol. B*, vol. 230, p. R4, 2002.

[122] D. Fritsch, H. Schmidt, and M. Grundmann, "Band dispersion relations of zinc–blende and wurtzite InN," *Phys. Rev. B*, vol. 69, art. 165204, 2004.

[123] E. O. Kane, "Band structure of indium antimonide," *J. Phys. Chem. Solids*, vol. 1, p. 249, 1957.

[124] P. Bhattacharya, T. K. Sharma, S. Singh, A. Ingale, and L. M. Kukreja, "Observation of zincblend phase in InN thin films grown on sapphire by nitrogen plasma–assisted pulsed laser deposition," *J. Cryst. Growth*, vol. 236, p. 5, 2002.

[125] C. G. V. de Walle and J. Neugebauer, "First–principles calculations for defects and impurities: Applications to III–nitrides," *J. Appl. Phys.*, vol. 95, p. 3851, 2004.

[126] S.-G. Lee and K. J. Chang, "Atomic model for blue luminescences in Mg–doped GaN," *Semicond. Sci. Technol.*, vol. 14, p. 138, 1998.

[127] M. E. Zvanut, D. M. Matlock, R. L. Henry, D. Koleske, and A. Wickenden, "Thermal activation of Mg–doped GaN as monitored by electron paramagnetic resonance spectroscopy," *J. Appl. Phys.*, vol. 95, p. 1884, 2004.

[128] L. Eckey, U. von Gfug, J. Holst, A. Hoffmann, A. Kaschner, H. Siegle, C. Thomsen, B. Schineller, K. Heime, M. Heuken, O. Schon, and R. Beccard, "Photoluminescence and raman study of compensation effects in Mg–doped GaN epilayers," *J. Appl. Phys.*, vol. 84, p. 5828, 1998.

[129] E. G. Guk and N. M. Shmidt, *Introduction to Semiconductor Technology.* Wiley, New York, 1st ed., 1997.

[130] D. C. Look, H. Lu, W. J. Schaff, J. Jasinski, and Z. Liliental-Weber, "Donor and acceptor concentrations in degenerate InN," *Appl. Phys. Lett.*, vol. 80, p. 258, 2002.

[131] I. J. Lee, J.-Y. Kim, and H.-J. Shin, "Near–edge X–ray absorption fine structure and X–ray photoemission spectroscopy study of the InN epilayers on sapphire (0001) substrate," *J. Appl. Phys.*, vol. 95, p. 5540, 2004.

[132] M. Petravic, P. N. K. Deenapanray, M. D. Fraser, A. V. Soldatov, Y.-W. Yang, P. A. Anderson, and S. M. Durbin, "Direct observation of defect levels in InN by soft X–ray absorption spectroscopy," *J. Phys. Chem.*, vol. 110, p. 2984, 2006.

[133] K. Lawniczak-Jablonska, T. Suski, I. Gorczyca, N. E. Christensen, K. E. Attenkofer, R. C. C. Perera, E. M. Gullikson, J. H. Underwood, D. L. Ederer, and Z. L. Weber, "Electronic states in valence and conduction bands of group–III nitrides: Experiment and theory," *Phys. Rev. B.*, vol. 61, art. 16623, 2000.

[134] C. Stampfl, C. G. V. de Walle, D. Vogel, P. Kruger, and J. Pollmann, "Native defects and impurities in InN: First–principles studies using the local–density approximation and self–interaction and relaxation–corrected pseudopotentials," *Phys. Rev. B*, vol. 61, p. 7846, 2000.

[135] J. L. Rouviere, J. L. Weyher, M. Seelmann-Eggebert, and S. Porowski, "Polarity determination for GaN films grown on (0001) sapphire and high pressure grown GaN single crystals," *Appl. Phys. Lett.*, vol. 73, p. 668, 1998.

[136] I. Vurgaftman, J. R. Meyer, C. A. Hoffman, D. Redfern, J. Antoszewski, L. Faraone, and J. R. Lindemuth, "Improved quantitative mobility spectrum analysis for Hall characterization," *J. Appl. Phys.*, vol. 84, p. 4966, 1998.

[137] J. Ziegler. SRIM ion implantation simulation package, version 2003.26, www.SRIM.org, accessed 1/12/2005.

[138] S. O. Kucheyev, H. Boudinov, J. S. Williams, C. Jagadish, and G. Li, "Effect of irradiation temperature and ion flux on electrical isolation of GaN," *J. Appl. Phys.*, vol. 91, p. 4117, 2002.

[139] S. O. Kucheyev, C. Jagadish, J. S. Williams, P. N. K. Deenapanray, M. Yano, K. Koike, S. Sasa, and M. Inoue, "Implant isolation of ZnO," *J. Appl. Phys.*, vol. 93, p. 2972, 2003.

[140] S. X. Li, K. M. Yu, J. Wu, R. E. Jones, W. Walukiewicz1, J. W. Ager III, W. Shan, E. E. Haller, H. Lu, and W. J. Schaff, "Fermi–level stabilization energy in group III nitrides," *Phys. Rev. B*, vol. 71, art. 161201, 2005.

[141] V. V. Mamutin, V. A. Vekshin, V. Y. Davydov, V. V. Ratnikov, Y. A. Kudriavtsev, B. Y. Ber, V. V. Emtsev, and S. V. Ivanov, "Mg–doped hexagonal InN/Al_2O_3 films grown by MBE," *Phys. Stat. Sol. A*, vol. 176, p. 373, 1999.

[142] J. Jasinski and Z. Liliental-Weber, "V–shaped inversion domains in InN grown on c–plane sapphire," *Appl. Phys. Lett.*, vol. 85, p. 233, 2004.

[143] W. Walukiewicz, R. E. Jones, S. X. Li, K. M. Yu, J. W. Ager III, E. E. Haller, H. Lu, and W. J. Schaff, "Dopants and defects in InN and InGaN alloys," *J. Crys. Growth*, vol. 288, p. 278, 2006.

[144] V. Cimalla, M. Niebelschutz, G. Ecke, V. Lebedev, O. Ambacher, M. Himmerlich, S. Krischok, J. A. Schaefer, H. Lu, and W. J. Schaff, "Surface band bending at nominally undoped and Mg–doped InN by Auger electron spectroscopy," *Phys. Stat. Sol. A*, vol. 203, p. 59, 2006.

[145] A. J. Ptak, T. H. Myers, L. T. Romano, C. G. V. de Walle, and J. E. Northrup, "Magnesium incorporation in GaN grown by molecular–beam epitaxy," *Appl. Phys. Lett.*, vol. 78, p. 285, 2001.

[146] R. E. Jones, K. M. Yu, S. X. Li, W. Walukiewicz, J. W. Ager, E. E. Haller, H. Lu, and W. J. Schaff, "Evidence for p–type doping of InN," *Phys. Rev. Lett.*, vol. 96, art. 125505, 2006.

[147] J. Smit, *Magnetic properties of materials.* McGraw Hill, New York, 1st ed., 1971.

[148] J. B. Philipp, P. Majewski, L. Alff, A. Erb, R. Gross, T. Graf, M. S. Brandt, J. Simon, T. Walther, W. Mader, D. Topwal, and D. D. Sarma, "Structural and doping effects in the half–metallic double perovskite A_2CrWO_6 (A = Sr, Ba, and Ca)," *Phys. Rev. B*, vol. 68, art. 144431, 2003.

[149] M. Jain and J. L. Robins, *Diluted Magnetic Semiconductors.* McGraw Hill, New York, 1st ed., 1991.

[150] W. A. Harrison, *Solid State Theory.* McGraw-Hill, New York, 1st ed., 1970.

[151] J. R. Hook and H. E. Hall, *Solid State Theory.* McGraw-Hill, New York, 2nd ed., 1991.

[152] J. R. Hook and H. E. Hall, *Solid State Theory.* McGraw-Hill, New York, 2nd ed., 1991.

[153] T. Story, R. R. Gatazka, R. B. Frankel, and P. A. Wolff, "Carrier–concentration-induced ferromagnetism in PbSnMnTe," *Phys. Rev. Lett.*, vol. 56, p. 777, 1986.

[154] H. Ohno, "Making nonmagnetic semiconductors ferromagnetic," *Science*, vol. 1998, p. 110, 1998.

[155] R. Giraud, S. Kuroda, S. Marcet, E. Bellet-Amalric, X. Biquard, B. Barbara, D. Fruchart, D. Ferrand, J. Cibert, and H. Mariette, "Ferromagnetic $Ga_{1-x}Mn_xN$

epilayers vs. antiferromagnetic $GaMn_3N$ clusters," *Europhys. Lett.*, vol. 65, p. 553, 2004.

[156] B. E. Warren, *X–ray Diffraction*. Dover, New York, 1st ed., 1990.

[157] N. R. Aghamalyan, E. A. Kafadaryan, R. K. Hovsepyan, and S. I. Petrosyan, "Absorption and reflection analysis of transparent conductive Ga–doped ZnO films," *Semicond. Sci. Technol.*, vol. 20, p. 80, 2005.

[158] T. Hynninen, H. Raebiger, and J. von Boehm, "High curie temperatures in (Ga,Mn)N from Mn clustering," *Appl. Phys. Lett.*, vol. 88, art. 122501, 2006.

[159] S. J. Pearton, C. R. Abernathy, M. E. Overberg, G. T. Thaler, D. P. Norton, N. Theodoropoulou, A. F. Hebard, Y. D. Park, F. Ren, J. Kim, and L. A. Boatner, "Wide band gap ferromagnetic semiconductors and oxides," *J. Appl. Phys.*, vol. 93, p. 1, 2003.

[160] T. Dietl and H. Ohno, "Ferromagnetic III-V and II-VI semiconductors," *MRS Bulletin*, p. 714, 2003. October issue.

[161] S. Koshihara, A. Oiwa, M. Hirasawa, S. Katsumoto, Y. Iye, C. Urano, and H. Takagi, "Ferromagnetic order induced by photogenerated carriers in magnetic III–V semiconductor heterostructures of (In,Mn)As/GaSb," *Phys. Rev. Lett.*, vol. 78, p. 4617, 1997.

[162] V. I. Litvinov and V. K. Dugaev, "Ferromagnetism in magnetically doped III–V semiconductors," *Phys. Rev. Lett.*, vol. 86, p. 5593, 2001.

[163] Y. Tsuchiya, K. Kosuge, Y. Ikeda, T. Shigematsu, S. Yamaguchi, and N. Nakayama, "Non–stoichiometry and antiferromagnetic phase transition of NaCl–type CrN thin films prepared by reactive sputtering," *Matter Trans.*, vol. 37, p. 121, 1996.

[164] J. D. Browne, P. R. Liddell, R. Street, and T. Mills, "An investigation of the antiferromagnetic transition of CrN," *Phys. Stat. Sol.*, vol. 1, p. 715, 1970.

[165] D. Gall, C.-S. Shin, R. T. Haasch, I. Petrov, and J. E. Greene, "Band gap in epitaxial NaCl–structure CrN(001) layers," *J. Appl. Phys.*, vol. 91, p. 5882, 2002.

APPENDIX A: IDENTIFICATION OF FILMS

Films grown at the University of Canterbury were identified with a code of the following form:

$$A - B/C - D \tag{A-1}$$

where A is a unique number representing the total number of films grown in the University of Canterbury MBE systems after the growth of this film, B is the chemical symbol for the grown material, C is the substrate used and D is the the number of films grown within this particular series. For example:

$$283 - InN/Sa - 59 \tag{A-2}$$

represents the 283rd film grown within the University of Canterbury MBE research group, the film is InN grown on sapphire and is the 53rd film of this kind grown at Canterbury. The abbreviations for substrates are Sa=sapphire, Q=quartz, YSZ=yttrium stabilised zirconia, GaNT=MOCVD GaN template on sapphire, and GR=growth rate experiment on sapphire. Table A-1 shows the identification codes for films discussed in this thesis.

Table A-1 Identification codes for films discussed in this thesis.

Figure/Table Number	**Identifier**	**Film**
Fig. 2.7	(a)	368-GaN/GR-02
Fig. 2.7	(b)	370-GaN/GR-04
Fig. 2.8	Ga-rich, N-polar	372-GaN/Sa-34
Fig. 2.8	Ga-rich, Ga-polar	373-GaN/GaNT-01
Fig. 2.8	N-rich, N-polar	374-GaN/Sa-35
Fig. 2.8	N-rich, Ga-polar	375-GaN/Sa-02
Fig. 2.9	Indium cell hot	254-InN/Sa-49
Fig. 2.9	Indium cell cold	256-GaN/Sa-29
Fig. 2.11	5×10^{13} atoms.cm^{-2}s^{-1}	139-InN/Sa-29
Fig. 2.11	8×10^{13} atoms.cm^{-2}s^{-1}	140-InN/Sa-30
Fig. 2.11	1.2×10^{14} atoms.cm^{-2}s^{-1}	141-InN/Sa-31
Fig. 2.11	1.8×10^{14} atoms.cm^{-2}s^{-1}	142-InN/Sa-32

Fig. 2.11	3×10^{14} atoms.cm^{-2}s^{-1}	343-InN/Sa-68
Fig. 2.12	(a)	139-InN/Sa-29
Fig. 2.12	(b)	143-InN/Sa-33
Fig. 2.13	200°C	40-InN/Sa-02
Fig. 2.13	400°C	39-InN/Sa-01
Fig. 2.13	550°C	42-InN/Sa-03
Fig. 2.14	5×10^{13} atoms.cm^{-2}s^{-1}	139-InN/Sa-29
Fig. 2.14	8×10^{13} atoms.cm^{-2}s^{-1}	140-InN/Sa-30
Fig. 2.14	3×10^{14} atoms.cm^{-2}s^{-1}	143-InN/Sa-33
Fig. 2.15	(a)	109-InN/(111)YSZ-01
Fig. 2.15	(a)	71-InN/(100)YSZ-03
Fig. 2.16	-	71-InN/(100)YSZ-03
Fig. 2.17	-	77-InN/(100)YSZ-05
Fig. 2.18	(a) 400°C	109-InN/(111)YSZ-01
Fig. 2.18	(a) 450°C	148-InN/(111)YSZ-02
Fig. 2.18	(a) 550°C	170-InN/(111)YSZ-06
Fig. 2.18	(b) 350°C	70-InN/(111)YSZ-03
Fig. 2.18	(b) 400°C	69-InN/(111)YSZ-02
Fig. 2.18	(b) 450°C	68-InN/(111)YSZ-01
Fig. 2.22	Sapphire	283-InN/Sa-59
Fig. 2.22	YSZ	267-InN/(111)YSZ-09
Fig. 2.23	(a)	254-InN/Sa-49
Fig. 2.23	(b)	253-InN/Sa-48
Fig. 2.24	550°C	257-InN/Sa-51
Fig. 2.24	450°C	254-InN/Sa-49
Fig. 3.8	(a)	38-InN/Q-01
Fig. 3.8	(b)	38-InN/Q-01
Fig. 3.9	-	38-InN/Q-01
Fig. 3.10	-	38-InN/Q-01
Fig. 3.11	(a)	139-InN/Sa-34
Fig. 3.11	(b)	217-InN/(111)YSZ-08
Fig. 3.11	(c)	283-InN/Sa-59
Fig. 3.11	(d)	39-InN/Sa-01
Fig. 3.13	(a)	139-InN/Sa-34
Fig. 3.13	(b)	217-InN/(111)YSZ-08
Fig. 3.14	(a)	139-InN/Sa-34
Fig. 3.14	(b)	217-InN/(111)YSZ-08
Fig. 3.15	(a)	217-InN/(111)YSZ-08
Fig. 3.15	(b)	217-InN/(111)YSZ-08
Fig. 3.16	-	123-InN/Sa-27

Fig. 3.17	-	123-InN/Sa-27
Fig. 3.18	(a)	123-InN/Sa-27
Fig. 3.18	(b)	116-InN/Sa-22
Fig. 3.19	(a)	117-InN/Sa-23
Fig. 3.19	(b)	120-InN/Sa-25
Fig. 3.19	(c)	123-InN/Sa-27
Fig. 3.20	9×10^{18} cm^{-3}	117-InN/Sa-23
Fig. 3.20	2.8×10^{19} cm^{-3}	120-InN/Sa-25
Fig. 3.20	3.2×10^{19} cm^{-3}	123-InN/Sa-27
Fig. 3.20	5×10^{19} cm^{-3}	38-InN/Q-01
Fig. 3.20	1.8×10^{20} cm^{-3}	226-InN/Q-05
Fig. 3.20	2.2×10^{20} cm^{-3}	413-InN/Q-09
Fig. 3.22	(a)	139-InN/Sa-34
Fig. 3.22	(b)	333-InN/(100)-08
Fig. 3.23	(a)	333-InN/(100)-08
Fig. 3.23	(b)	333-InN/(100)-08
Fig. 3.24	(a)	333-InN/(100)-08
Fig. 3.24	(b)	333-InN/(100)-08
Fig. 4.5	-	283-InN/Sa-59
Fig. 4.7	N-polar	283-InN/Sa-59
Fig. 4.7	In-polar	217-InN/(111)-08
Fig. 4.8	-	283-InN/Sa-59
Fig. 4.9	(a)	283-InN/Sa-59
Fig. 4.9	(b)	283-InN/Sa-59
Fig. 4.10	(a)	283-InN/Sa-59
Fig. 4.10	(b)	283-InN/Sa-59
Fig. 4.11	(a)	283-InN/Sa-59
Fig. 4.11	(b)	283-InN/Sa-59
Fig. 4.12	No Mg	379-InN/Sa-68
Fig. 4.12	1×10^{12} atoms.cm^{-2}s^{-1}	387-InN:Mg/Sa-02
Fig. 4.12	0.3×10^{12} atoms.cm^{-2}s^{-1}	384-InN:Mg/Sa-01
Fig. 4.13	GaN Template 6×10^{17} cm^{-3}	436-InN:Mg/GaNT-06
Fig. 4.13	GaN Template 2×10^{18} cm^{-3}	434-InN:Mg/GaNT-05
Fig. 4.13	GaN Template 6×10^{18} cm^{-3}	412-InN:Mg/GaNT-04
Fig. 4.13	GaN Template 6×10^{19} cm^{-3}	394-InN:Mg/GaNT-03
Fig. 4.13	GaN Template 3×10^{20} cm^{-3}	385-InN:Mg/GaNT-01
Fig. 4.13	GaN Template 1×10^{21} cm^{-3}	388-InN:Mg/GaNT-02
Fig. 4.13	Sapphire 6×10^{17} cm^{-3}	435-InN:Mg/Sa-06
Fig. 4.13	Sapphire 2×10^{18} cm^{-3}	433-InN:Mg/Sa-05
Fig. 4.13	Sapphire 6×10^{18} cm^{-3}	411-InN:Mg/Sa-04

Fig. 4.13	Sapphire 6×10^{19} cm^{-3}	395-InN:Mg/Sa-03
Fig. 4.13	Sapphire 3×10^{20} cm^{-3}	384-InN:Mg/Sa-01
Fig. 4.13	Sapphire 1×10^{21} cm^{-3}	387-InN:Mg/Sa-02
Fig. 4.14	6×10^{17} cm^{-3}	436-InN:Mg/GaNT-06
Fig. 4.14	2×10^{18} cm^{-3}	434-InN:Mg/GaNT-05
Fig. 4.14	6×10^{18} cm^{-3}	412-InN:Mg/GaNT-04
Fig. 4.15	GaN Template 6×10^{17} cm^{-3}	436-InN:Mg/GaNT-06
Fig. 4.15	GaN Template 2×10^{18} cm^{-3}	434-InN:Mg/GaNT-05
Fig. 4.15	GaN Template 6×10^{18} cm^{-3}	412-InN:Mg/GaNT-04
Fig. 4.15	GaN Template 6×10^{19} cm^{-3}	394-InN:Mg/GaNT-03
Fig. 4.15	GaN Template 3×10^{20} cm^{-3}	385-InN:Mg/GaNT-01
Fig. 4.15	GaN Template 1×10^{21} cm^{-3}	388-InN:Mg/GaNT-02
Fig. 4.15	Sapphire 6×10^{17} cm^{-3}	435-InN:Mg/Sa-06
Fig. 4.15	Sapphire 2×10^{18} cm^{-3}	433-InN:Mg/Sa-05
Fig. 4.15	Sapphire 6×10^{18} cm^{-3}	411-InN:Mg/Sa-04
Fig. 4.15	Sapphire 6×10^{19} cm^{-3}	395-InN:Mg/Sa-03
Fig. 4.15	Sapphire 3×10^{20} cm^{-3}	384-InN:Mg/Sa-01
Fig. 4.15	Sapphire 1×10^{21} cm^{-3}	387-InN:Mg/Sa-02
Fig. 5.4	x=0	123-InN/Sa-27
Fig. 5.4	x=0.0005	173-InCrN/Sa-07
Fig. 5.4	x=0.002	172-InCrN/Sa-06
Fig. 5.4	x=0.025	162-InCrN/Sa-05
Fig. 5.5	x=0.01	150-InCrN/Sa-03
Fig. 5.5	x=0.025	162-InCrN/Sa-05
Fig. 5.5	x=0.04	158-InCrN/Sa-04
Fig. 5.6	(a)	162-InCrN/Sa-05
Fig. 5.6	(b)	162-InCrN/Sa-05
Fig. 5.7	(a)	162-InCrN/Sa-05
Fig. 5.7	(b)	162-InCrN/Sa-05
Fig. 5.8	-	162-InCrN/Sa-05
Fig. 5.9	x=0.002	172-InCrN/Sa-06
Fig. 5.9	x=0.01	150-InCrN/Sa-03
Fig. 5.9	x=0.025	162-InCrN/Sa-05
Fig. 5.9	x=0.04	158-InCrN/Sa-04
Fig. 5.10	-	162-InCrN/Sa-05
Fig. 5.11	0.8×10^{20} cm^{-3}	172-InCrN/Sa-06
Fig. 5.11	2.5×10^{20} cm^{-3}	150-InCrN/Sa-03
Fig. 5.11	9.6×10^{20} cm^{-3}	162-InCrN/Sa-05
Fig. 5.11	6×10^{20} cm^{-3}	158-InCrN/Sa-04
Fig. 5.12	x=0	123-InN/Sa-27

Fig. 5.12	x=0.002	172-InCrN/Sa-06
Fig. 5.12	x=0.01	150-InCrN/Sa-03
Fig. 5.12	x=0.025	162-InCrN/Sa-05
Fig. 5.12	x=0.04	158-InCrN/Sa-04
Fig. 5.13	-	166-CrN/Sa-03
Fig. 5.14	-	167-CrN/(111)YSZ-01
Tab. 4.1	-	283-InN/Sa-59
Tab. 4.13	In-polar 6×10^{17} cm^{-3}	436-InN:Mg/GaNT-06
Tab. 4.13	In-polar 2×10^{18} cm^{-3}	434-InN:Mg/GaNT-05
Tab. 4.13	In-polar 6×10^{18} cm^{-3}	412-InN:Mg/GaNT-04
Tab. 4.13	In-polar 6×10^{19} cm^{-3}	394-InN:Mg/GaNT-03
Tab. 4.13	In-polar 3×10^{20} cm^{-3}	385-InN:Mg/GaNT-01
Tab. 4.13	In-polar 1×10^{21} cm^{-3}	388-InN:Mg/GaNT-02
Tab. 4.13	N-polar 6×10^{17} cm^{-3}	435-InN:Mg/Sa-06
Tab. 4.13	N-polar 2×10^{18} cm^{-3}	433-InN:Mg/Sa-05
Tab. 4.13	N-polar 6×10^{18} cm^{-3}	411-InN:Mg/Sa-04
Tab. 4.13	N-polar 6×10^{19} cm^{-3}	395-InN:Mg/Sa-03
Tab. 4.13	N-polar 3×10^{20} cm^{-3}	384-InN:Mg/Sa-01
Tab. 4.13	N-polar 1×10^{21} cm^{-3}	387-InN:Mg/Sa-02

APPENDIX B: ION IMPLANTATION SIMULATIONS

The following three figures are the profiles produced by the SRIM simulation package [137] for ion implantation energies of 100, 400 and 650 keV for carbon, zinc and cadmium, respectively.

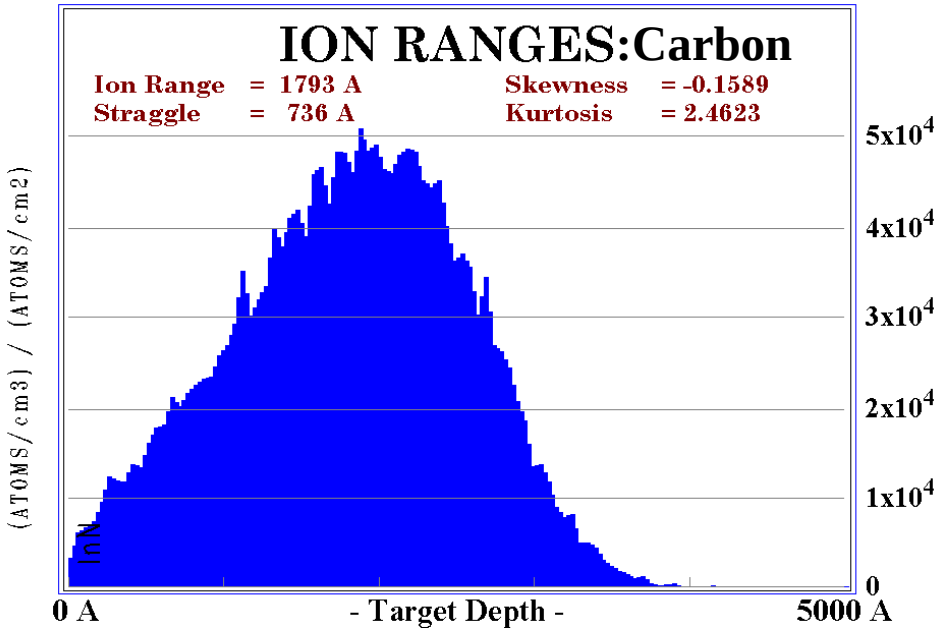

Figure B-1 The implantation profile simulated by the SRIM ion implantation package for 100 keV Carbon species, implanted into wurtzite InN at an incident angle of 7°.

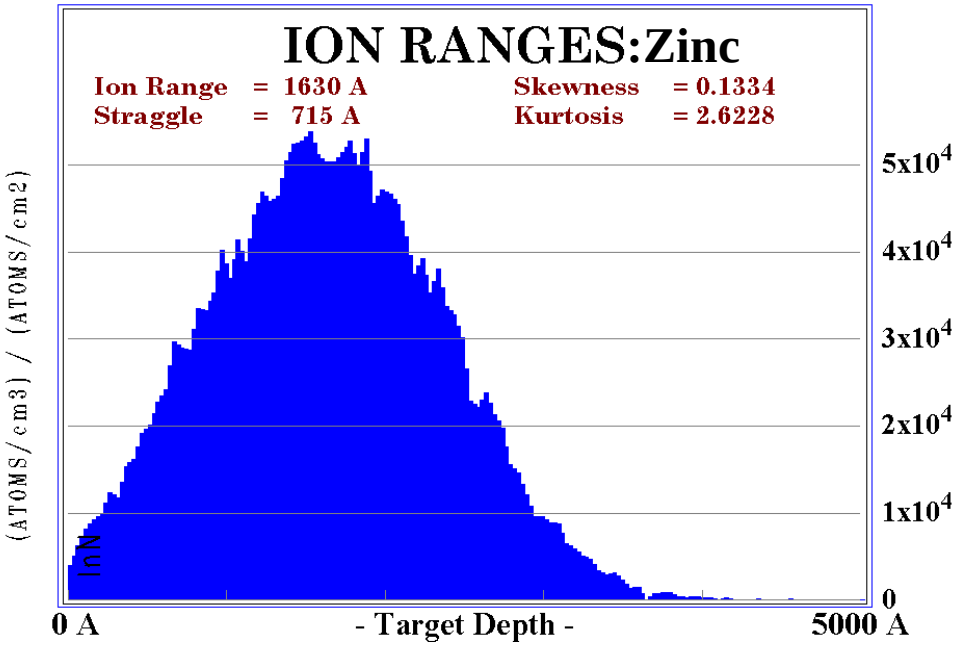

Figure B-2 The implantation profile simulated by the SRIM ion implantation package for 400 keV Zinc species, implanted into wurtzite InN at an incident angle of 7°.

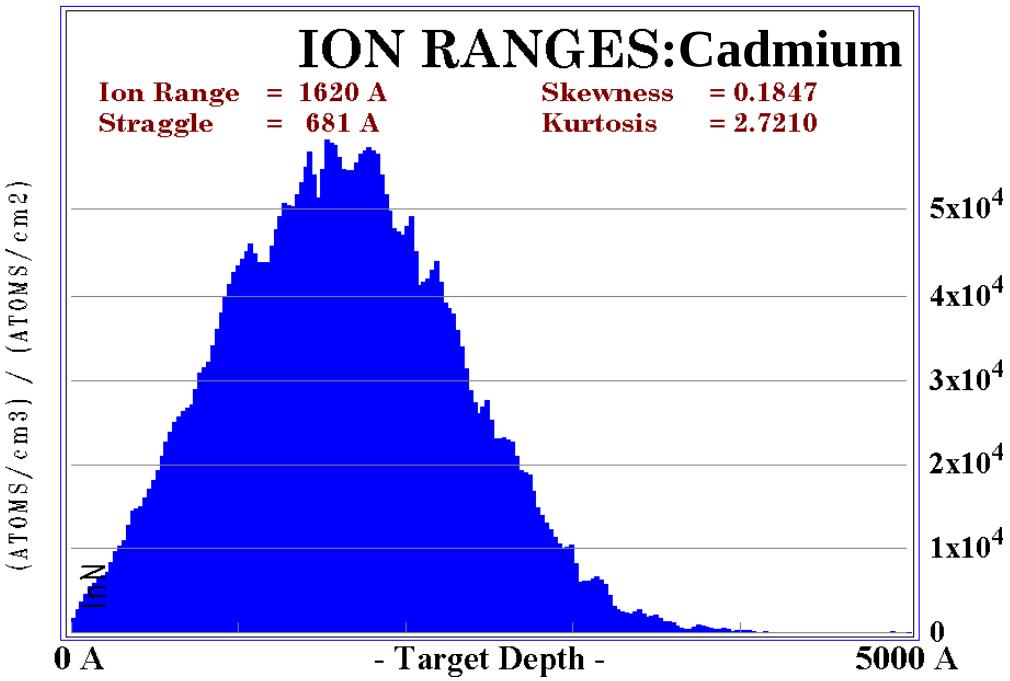

Figure B-3 The implantation profile simulated by the SRIM ion implantation package for 650 keV Cadmium species, implanted into wurtzite InN at an incident angle of 7°.